

Experimental analysis of suprathermal electrons generated by electron cyclotron waves in tokamak plasmas

Présentée le 13 mars 2020

à la Faculté des sciences de base
SPC - Physique du Tokamak TCV
Programme doctoral en physique

pour l'obtention du grade de Docteur ès Sciences

par

Dahye CHOI

Acceptée sur proposition du jury

Prof. F. Mila, président du jury
Dr S. Coda, directeur de thèse
Dr G. Giruzzi, rapporteur
Dr P. Savrukhn, rapporteur
Dr J. Graves, rapporteur

Abstract

This thesis focuses on the physics of suprathermal electrons generated by electron cyclotron (EC) waves in tokamak plasmas, which play an important role in the physics of current drive and energetic particle-driven instabilities. The suprathermal electron dynamics and their effect on the plasma stability have been experimentally studied utilizing high power EC waves, in the TCV tokamak of the Swiss Plasma Center at EPFL, Switzerland. A hard X-ray diagnostic, which measures the bremsstrahlung radiation of the suprathermal electrons in radial and energy spaces, has been mainly used for the analysis, and the measurement has been compared to an estimation made by Fokker-Planck modeling coupled with a hard X-ray synthetic diagnostic.

In order to study the response of the suprathermal electrons to ECCD, ECCD modulation discharges have been developed. The time evolution of the hard X-ray profiles has been measured using coherent averaging techniques in order to observe the creation and relaxation of suprathermal electrons. Time-dependent Fokker-Planck modeling coupled with the hard X-ray synthetic diagnostic has been used to compare the experimental and simulation results, with various suprathermal electron transport models. A dependency of the radial transport of suprathermal electrons on the EC wave power has been demonstrated and a possibility of EC wave scattering has been addressed.

The effect of the suprathermal electron population on the plasma stability has been studied, and in particular the destabilization and dynamics of the electron fishbone mode. The response of hard X-ray profiles to the internal kink mode has been observed directly by the hard X-ray diagnostic for the first time, at the frequency of the mode. The experimental evidence and a solution of a linear fishbone dispersion relation coupled to the Fokker-Planck modeling demonstrate the role of suprathermal electrons in destabilizing the fishbone mode and in particular the interaction of trapped electrons with the mode.

This work provides the framework for a comprehensive understanding of the physics of suprathermal electrons related to ECCD, and explains how ECCD-generated suprathermal electrons behave in real and velocity spaces, and how they interact with and are redistributed by the MHD mode.

Keywords: Hard X-ray measurement, Suprathermal electrons, Electron cyclotron current drive,

Suprathermal electron dynamics, Electron fishbone instability

Résumé

Cette thèse se concentre sur l'étude des électrons suprathermiques générés par les ondes cyclotroniques électroniques (EC) dans les plasmas de tokamak. Cette population d'électrons joue un rôle majeur dans la physique de la génération de courant et dans les instabilités induites par les particules rapides. La dynamique des électrons suprathermiques et leurs effets sur la stabilité du plasma ont été étudiés expérimentalement dans le Tokamak à Configurations Variables (TCV) du Swiss Plasma Center, à l'EPFL en Suisse, à l'aide d'ondes cyclotroniques électroniques injectées à haute puissance dans le plasma. Le principal instrument utilisé pour l'analyse est un spectromètre sensible aux rayons X durs. Ce spectromètre mesure les radiations émises par freinage des électrons rapides dans le champ magnétique (bremsstrahlung) aussi bien dans l'espace réel que dans l'espace des énergies. Les mesures sont comparées à des estimations faites par des simulations Fokker-Planck, couplées à un diagnostic synthétique des rayons X durs.

Des scénarios de décharges comprenant des modulations répétées de puissance cyclotronique injectée ont été développés afin d'étudier la réponse des électrons suprathermiques à la génération de courant cyclotronique électronique (ECCD). Les profils temporels d'émission de rayons X durs ont été mesurés afin d'observer la génération puis la relaxation des électrons suprathermiques. Des simulations Fokker-Planck évoluant dans le temps, incluant divers modèles de transport radial des particules rapides et couplées au diagnostic synthétique, ont été utilisées pour être comparées avec les résultats expérimentaux. Une dépendance en puissance injectée du transport radial a été démontrée, et la question d'une potentielle diffraction de l'onde cyclotronique a été soulevée.

L'étude de l'impact des électrons suprathermiques sur la stabilité du plasma a été menée, en particulier au travers de l'étude de la déstabilisation et de la dynamique des modes « fishbone » électroniques. La réponse des profils d'émission de rayons X durs aux modes de « kink » internes a été observée pour la première fois à la fréquence du mode à l'aide du spectromètre rayons X durs. Les mises en évidence expérimentales, ainsi que la solution de la relation de dispersion linéaire des modes « fishbone » électroniques couplée aux modèles Fokker-Planck a permis de démontrer le rôle des électrons suprathermiques dans la déstabilisation des modes « fishbone », et en particulier l'interaction des électrons piégés avec le mode.

Ce travail présente le cadre pour une compréhension complète de la physique des électrons

suprathermiques liés à la génération de courant au moyen d'ondes cyclotroniques électroniques. Il détaille notamment comment les électrons suprathermiques générés par les ondes cyclotroniques se comportent dans l'espace réel et l'espace des vitesses, comment ils interagissent avec les modes MHD et sont redistribués par ceux-ci.

Mots-clefs : Mesures des rayons X durs, électrons suprathermiques, génération de courant à l'aide d'ondes cyclotroniques électroniques, dynamique des électrons suprathermiques, instabilité « fishbone » électronique.

Contents

Abstract (English/Français)	iii
1 Introduction	1
1.1 Plasma and tokamak	2
1.1.1 Basic plasma description	2
1.1.2 TCV tokamak	5
1.2 Suprathermal electrons in tokamak plasmas	8
1.2.1 Suprathermal electron generation by EC waves	8
1.2.2 Suprathermal electron driven instability: electron fishbone	12
1.3 Measurements of suprathermal electrons	13
1.3.1 Hard X-ray measurement	13
1.3.2 Electron cyclotron emission	16
1.4 Modeling of suprathermal electrons	17
1.4.1 Fokker-Planck modeling of ECCD plasmas	17
1.4.2 Hard X-ray synthetic diagnostic	19
1.5 Thesis goals and outline	20
1.5.1 Thesis goals	20
1.5.2 Thesis outline	20
2 Hard X-ray tomographic spectrometer system (HXRS) in TCV	23
2.1 Overview of the diagnostic	23
2.1.1 Hardware and characteristics	23
2.1.2 Data analysis	25
2.2 Tomography method study for HXRS	29
2.2.1 Tomographic inversion methods for HXRS	30
2.2.2 Comparison of inversion methods	34
2.2.3 Conclusions	39
2.3 Modeling of response function for HXRS	41
2.3.1 Measurement of radioactive sources	41
2.3.2 Modeling the response function	43
2.3.3 Reconstruction of measured spectra	46
2.3.4 Conclusions	49
	vii

3	Suprathermal electron dynamics during ECCD	51
3.1	Introduction	51
3.2	Hard X-ray measurements during ECCD discharges	51
3.2.1	Experimental setup	51
3.2.2	On-axis ECCD	54
3.2.3	Off-axis ECCD	59
3.3	Time-dependent Fokker-Planck modeling	63
3.3.1	Simulation setup	63
3.3.2	On-axis ECCD simulation	64
3.3.3	Off-axis ECCD	67
3.4	Conclusions	69
4	Suprathermal electron driven fishbone instability	71
4.1	Introduction	71
4.2	Experimental setup	71
4.3	Experimental observation of the fishbone oscillation	74
4.3.1	The $m/n = 1/1$ mode excitation during ECCD	74
4.3.2	Conditional averaging of data	76
4.3.3	Abel-inversion of the soft X-ray and hard X-ray profiles	81
4.3.4	The different response of passing and trapped electrons	86
4.4	The effect of ECCD parameters on the onset of the fishbone instability	88
4.4.1	ECCD power scan	88
4.4.2	Magnetic field scan	90
4.5	Numerical analysis of the $m/n = 1/1$ mode	94
4.5.1	Fokker-Planck modeling of the experiment	94
4.5.2	Solving the linear fishbone dispersion relation	98
4.6	Conclusions	102
5	Summary, conclusions, and future work	103
5.1	Summary	103
5.2	Conclusions	104
5.3	Future work	105
A	Analysis of time-varying MHD mode structure	109
A.1	Toroidal mode analysis with magnetic probes	110
A.2	Poloidal mode analysis with soft X-ray array	112
A.3	Toroidal mode analysis with soft X-ray array	115
A.4	Summary	119
B	Study of toroidal asymmetry in the hard X-ray emission	121
B.1	Effect of magnetic equilibrium	121
B.2	Competition between RF waves and toroidal electric field	125
B.3	Conclusions	129

C	Study of non-standard sawtooth related to electron fishbones	131
C.1	Observation of fishbone-like perturbations during non-standard sawteeth . . .	131
C.2	Analysis of the evolution of the electron distribution	133
C.2.1	Evolution of the electron density and temperature profiles: Thomson scattering data analysis	134
C.2.2	Suprathermal electron re-distribution: hard X-ray data analysis and nu- merical analysis	138
C.3	Summary	142
D	Solving the electron fishbone dispersion relation	143
D.1	ECCD discharge with fixed EC power	143
D.2	Study of the ECCD power effect on the onset of the fishbone mode	147
	Bibliography	154
	Acknowledgements	155
	Curriculum Vitae	157

1 Introduction

A plasma is an ionized gas with a high electrical conductivity, in which charged particles exhibit collective behavior. This fourth state of matter is distinguished from the other three states: solid, liquid and gas. The term "plasma" was introduced by I. Langmuir almost a hundred years ago, during research on gas discharge physics [1, 2]. The early plasma research was carried out on low temperature plasmas (electron temperature ~ 2 eV) that fill current-carrying vacuum tubes. Nowadays plasma physics research ranges from naturally occurring terrestrial and astrophysical plasmas to magnetic confinement fusion, to various laboratory plasmas for industrial applications and rocket propulsion engines [3]. This thesis is focused on magnetic fusion plasmas, in particular tokamak plasmas.

Magnetic confinement fusion research [4, 5] aims to generate electricity from the nuclear fusion reaction of deuterium and tritium atoms, which takes place in a magnetically controlled plasma. The fuel plasma is heated and confined to enhance the fusion cross section. The Tokamak¹ is currently the magnetic fusion plasma concept with the highest physics performance. This axisymmetric torus machine confines plasma with a combination of toroidal and poloidal magnetic fields. The poloidal magnetic field is created by a plasma current, which distinguishes it from other concepts, such as the stellarator, where non-axisymmetric coils create poloidal magnetic fields. To this date, the highest record of the power gain Q , which is defined by the ratio of net thermal power output to injected heating power, was achieved by the European tokamak JET in the UK: $Q \sim 0.65$ with over 16 MW of fusion power [6]. Aiming to achieve $Q \geq 10$, the ITER (International Thermonuclear Experimental Reactor) tokamak is being built in France by an international collaboration [7, 8].

One of the main topics in tokamak research is auxiliary heating and current drive, an essential part for non-inductive steady state operation [9]. Currently two main methods are used in several tokamaks: injecting energetic neutral beams (NBI) to collide with the background plasma and/or adding radio frequency (RF) waves to resonate with one of many resonant frequencies of the plasma. Among the RF wave injection methods, electron cyclotron (EC)

¹The word "tokamak" is an acronym of "toroidal chamber with axial magnetic field" in Russian.

resonance heating (ECRH) and current drive (ECCD) have been studied in several tokamaks [10–12] utilizing high-power gyrotrons to generate waves in the range 10 - 300 GHz [13]. ECCD is also used as a controlling tool for shaping plasma profiles and stabilizing instabilities, due to its ability to localize the wave absorption, which is superior to other current drive methods. In the physics of ECRH and ECCD, the dynamics of suprathermal electrons plays a fundamental role. However, the complexity of their dynamics in real and velocity spaces has made it difficult to understand the physics clearly.

This thesis sets out to broaden the understanding of suprathermal electron physics related to ECCD. The present work covers not only the suprathermal electron dynamics related to EC waves, but also fishbone instabilities driven by suprathermal electrons, which degrade ECCD efficiency. The experiments have been conducted on the TCV tokamak in Switzerland. TCV [14] is a medium-sized tokamak (major radius $R = 0.88$ m, minor radius $a = 0.25$ m), featuring a high-power density ECRH/ECCD system. A state-of-the-art hard X-ray spectrometer system has been mainly used to diagnose suprathermal electrons generated by EC waves. The plasma is modeled using the Fokker-Planck equation solver LUKE, coupled with a ray-tracing code and a synthetic diagnostic.

This introduction chapter is arranged as follows: in section 1.1 tokamak plasmas are described. The generation of suprathermal electrons by EC waves and an electron fishbone instability driven by them are explained in section 1.2. Experimental measurement methods of suprathermal electron dynamics are presented in section 1.3. The Fokker-Planck modeling and synthetic diagnostic tools are presented in section 1.4, and the goals and outline of this thesis are given in section 1.5.

1.1 Plasma and tokamak

1.1.1 Basic plasma description

Basic plasma concepts

In general, the plasma state is defined by using the following parameters; the Debye length λ_D and the electron plasma frequency ω_{pe} :

$$\lambda_D = \left(\frac{\epsilon_0 T_e}{e^2 n_e} \right)^{1/2}, \quad \omega_{pe} = \left(\frac{n_e e^2}{m_e \epsilon_0} \right)^{1/2}, \quad (1.1)$$

where T_e , n_e , m_e , and ϵ_0 are the electron temperature, electron density, electron mass and vacuum permittivity, respectively. The Debye length λ_D is a characteristic length that represents the plasma's ability to shield out electric fields applied to it. In the plasma, a short Debye length compared to the physical size of the plasma ($\lambda_D \ll L$) is required to ensure its quasi-neutrality. In addition, the number of particles in the Debye sphere (n_{λ_D} in Figure 1.1) needs to be high enough to statistically guarantee Debye shielding. The electron plasma

frequency ω_{pe} has to be higher than the collision frequency with neutral atoms, in which case the plasma motion is controlled by electromagnetic forces unlike ordinary gases [3].

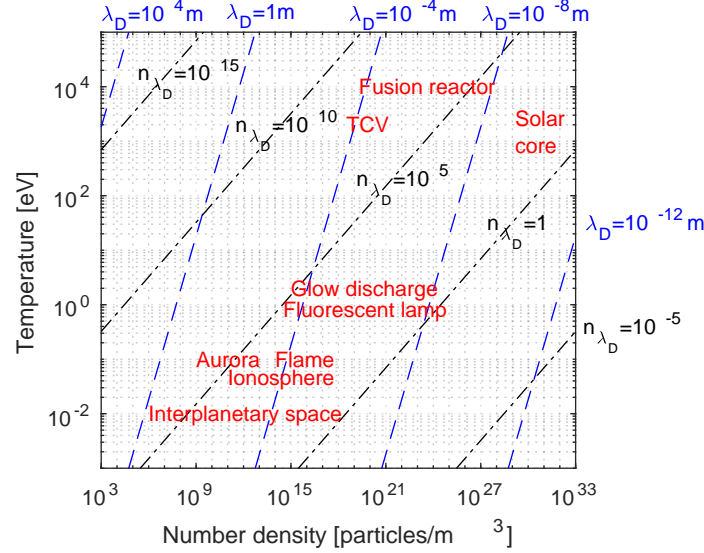


Figure 1.1 – Debye length (λ_D) and number of particles in a Debye sphere (n_{λ_D})

Another important parameter in plasma physics is the cyclotron frequency $\omega_c = eB/m_e$. This describes the gyro motion of charged particles in magnetic fields, which is the key to magnetic confinement. However, due to the spatially varying magnetic field structure in a tokamak ($B \propto 1/R$), charged particles experience drifts across magnetic field lines. In tokamak, this problem is solved by introducing helical magnetic fields with toroidal plasma currents. The spatially varying magnetic field also induces particle trapping phenomena, due to the conservation of magnetic moment $\mu = m_e v_\perp^2 / (2B)$: as the particle moves towards the high field side of tokamak, the perpendicular velocity v_\perp increases to keep μ constant. This reduces the parallel velocity of the particle, and eventually the particle may be reflected back, depending on the initial parallel velocity. This creates a group of particles trapped in the magnetic mirror, which is important in understanding ECCD physics.

As one can notice from Figure 1.1, there are a large number of particles in the plasma of our interest², which makes it practically impossible to describe plasmas by analyzing each single particle. Instead, plasmas can be described as a fluid with electrical charges. Although plasmas generally have low collisionality, the fluid model describes the majority of plasma phenomena. Some phenomena need kinetic treatment by introducing a particle distribution function. For the description of the wave-particle interaction for ECCD, for example, a kinetic description of plasmas is necessary.

²For a typical TCV plasma at $T_e = 2$ keV and $n_0 = 2 \times 10^{19} \text{ m}^{-3}$, $\lambda_D = 0.07$ mm and $n_{\lambda_D} = 3 \times 10^7$.

Fluid description

The two-fluid model describes plasma as a mixture of two types of fluid with opposite charges. For electrons and ions, this model comprises mass, momentum, and energy conservation equations, as well as Maxwell's equations. The complete set of equations and unknowns (density, pressure, velocity of ions and electrons and electric and magnetic fields) gives a self-consistent description of fluid motion and fields.

The two-fluid model can be simplified into the MHD (magnetohydrodynamics) model, which describes the plasma as a single fluid. The set of MHD equations is an important tool in analyzing the stability of plasmas and the plasma equilibrium. Assuming that the plasma quantities are constant in equilibrium ($\partial/\partial t=0$) and static, the magnetic equilibrium properties can be described by the set of equations [13]:

$$\mathbf{J} \times \mathbf{B} = \nabla p, \quad \nabla \times \mathbf{B} = \mu_0 \mathbf{J}, \quad \nabla \cdot \mathbf{B} = 0. \quad (1.2)$$

It is important to observe that the MHD momentum equation yields $\mathbf{B} \cdot \nabla p = 0$. This means that the magnetic field lines are perpendicular to the pressure gradient, therefore the magnetic field lines are confined to the constant pressure surface, called flux surface. From the MHD momentum equation it also follows that $\mathbf{J} \cdot \nabla p = 0$. This implies that the current lines also lie on the constant pressure surfaces.

When the plasma is perturbed from the MHD equilibrium state, it is stable if the plasma recovers back to the original state. The plasma is unstable if the initial perturbation grows. In the MHD stability analysis, the plasma quantities are linearized as $Q(\mathbf{r}, t) = Q_0(\mathbf{r}) + \tilde{Q}_1(\mathbf{r}, t)$, i.e., as a sum of the zeroth-order and a small first-order term ($|\tilde{Q}_1| \ll |Q_0|$) [15]. The perturbation term can be written as $\tilde{Q}_1(\mathbf{r}, t) = \tilde{Q}_1(\mathbf{r}) \exp^{-i\omega t}$. Determining an eigenvalue ω is a key to the stability analysis. An instability is present when $\text{Im}(\omega) > 0$, i.e. when the perturbation grows exponentially.

In general the perturbed quantities in the MHD stability analysis are expressed in terms of a fluid displacement ξ , so the perturbed velocity becomes $\mathbf{v}_1 = \partial \xi / \partial t$. In tokamak plasmas, the displacement is expanded as a Fourier series, in terms of the radial variable r , the poloidal angle θ and the toroidal angle ϕ : $\xi(r, \theta, \phi) = \sum_m \xi^{(m)}(r) \exp^{i(m\theta - n\phi - \omega t)}$. Sawtooth oscillations, one of the most common instabilities in tokamak plasmas, have a dominant $m = n = 1$ MHD mode structure. This type of instability is often excited when the core q (safety factor) value drops below 1 due to increased plasma current. A similar internal kink instability can be triggered by the resonant interaction of the mode with the motion of energetic particles. This interaction often results in a fishbone instability. An adequate analysis requires a kinetic MHD treatment. The fishbone instability was originally observed in NBI-driven plasmas with energetic trapped ions [16]. Recently the effect of energetic electrons has been studied following the observation of a barely trapped electron driven fishbone in an ECCD plasma [17]. In this thesis work, an electron fishbone in TCV is identified and analyzed with the aid of the

electron fishbone dispersion relation solver MIKE [18].

Kinetic theory

In the kinetic treatment of plasma, the plasma is described by its distribution function, $f(\mathbf{x}, \mathbf{v}, t)$. The evolution of the electron distribution function f_e is described by the Fokker-Planck equation [19]

$$\frac{\partial f_e}{\partial t} = \sum_s C(f_e, f_s) - \nabla \cdot \mathbf{S}_w + \frac{e\mathbf{E}}{m_e} \cdot \nabla f_e, \quad (1.3)$$

where $C(f_a, f_b)$ describes Coulomb collisions of species a with species b . The collision term can be expressed as a divergence in velocity space, due to the dominant small-angle scattering, $C(f_a, f_b) = -\nabla \cdot \mathbf{S}_c^{a/b}$. When the RF wave is added, the slow evolution of the distribution function can be also described as velocity space diffusion, more precisely termed quasilinear diffusion [20, 21]. In the Fokker-Planck equation, \mathbf{S}_w represents the quasilinear flux. The ohmic electric field effect can also be represented as a flux,

$$\mathbf{S}_e = \frac{e\mathbf{E}}{m_e} f_e. \quad (1.4)$$

Depending on the physics model, additional source or sink terms can be added to the right hand side of Eq.(1.3). In ECCD plasmas, the radial transport term of suprathermal electrons has been added to describe an anomalous transport effect.

The solution of the Fokker-Planck equation describes changes of the electron distribution function in velocity space. The initial Maxwellian equilibrium distribution diffuses in velocity space towards an asymmetric distribution function due to the RF wave field, Coulomb collisions, and external electric fields. The asymmetry of the distribution function in velocity space is at the root of the externally driven plasma current. Therefore solving the Fokker-Planck equation is the main modeling method for ECCD plasmas in this thesis work. A detailed description of the modeling procedure used in this thesis work is described in section 1.4.

1.1.2 TCV tokamak

This thesis work is conducted on the TCV tokamak. TCV [14] is a medium-sized tokamak ($R = 0.88$ m, $a = 0.25$ m) that features a high-power density ECRH/ECCD system. The original ECRH/ECCD system consisted of six 82.7 GHz gyrotrons and three 118 GHz gyrotrons for heating at the second (X2) and third (X3) harmonic of electron cyclotron resonance. The poloidal angle of each launcher can be changed during the discharge, allowing the sweeping of the power deposition location.

The typical plasma parameters used in this work are: plasma current $I_p \sim 0.1 - 0.2$ MA, toroidal magnetic field $B_\phi \sim 1.4$ T, electron density $n_e \sim 2 \times 10^{19} / m^3$, electron temperature $T_e \sim 2 - 3$

keV, ion temperature $T_i \sim 0.5$ keV, and effective charge $Z_{eff} \sim 1.2$. The plasma equilibrium is reconstructed from the magnetics measurements, by solving the Grad-Shafranov equation with the code LIUQE [22]. Figure 1.2 represents the flux surfaces reconstructed by LIUQE, as well as various coils for generating magnetic field, ohmic current and poloidal shaping fields.

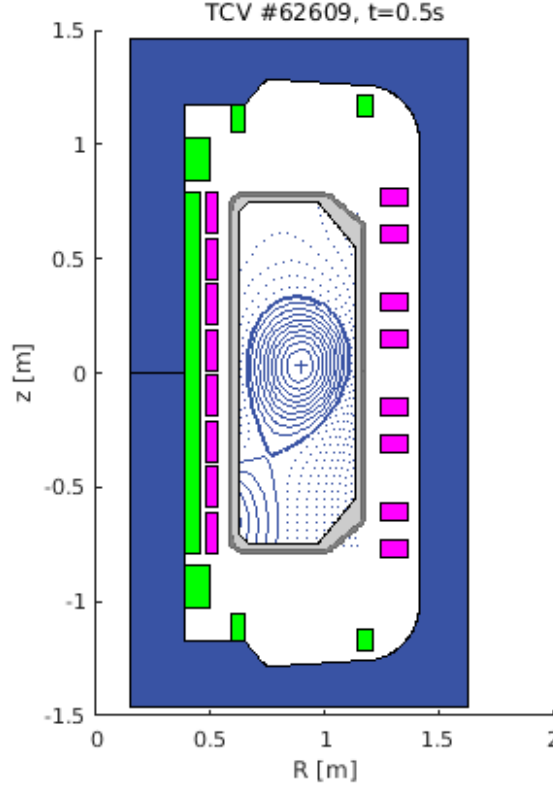


Figure 1.2 – Poloidal view of TCV. Blue: Toroidal magnetic field coil, green: Ohmic current coils, magenta: poloidal field coils. Plasma equilibrium of discharge #62609 at 0.5 s is presented.

Various diagnostics are utilized in the analysis of ECCD plasmas. A recently upgraded Thomson scattering system provides a high spatial resolution (6-12 mm) vertical profile of n_e and T_e at $R = 0.9$ m. This enables observations of the small scale mode structure in the plasma, which will be presented in the MHD mode structure analysis in Chapter 4.

The spatial structure of the thermal plasma is analyzed using a set of soft x-ray diagnostics, XTOMO and DMPX. The soft X-ray tomographic system (XTOMO) consists of 8 pinhole cameras with 20 p-n junction silicon photodiodes each, acquiring data at 100 kHz. The measured signal is used for the tomographic inversion of soft X-ray emission using a finite element grid discretization on the flux surfaces and the minimum Fisher regularization inversion method [23]. The multi-channel soft X-ray detector (DMPX) has a high time resolution of 5 μ s and a high spatial resolution defined by 7.9 mm mean distance between two lines of sight.

Therefore, although this diagnostic does not provide tomographic inversion, it enables soft X-ray profile measurements at high spatial and time resolution. The lines of sight of XTOMO and DMPX are plotted in Figure 1.3. The data from both diagnostics are analyzed using the singular value decomposition (SVD) technique to study the time evolution (chronos) of the spatial mode structure (topos) [23, 24].

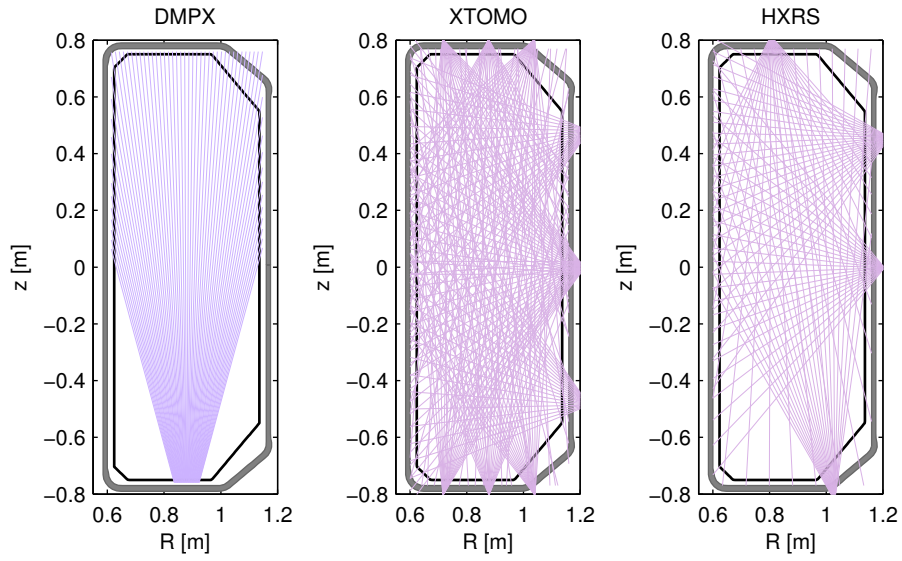


Figure 1.3 – Lines of sight of DMPX, XTOMO, and HXRS

During the MHD mode analysis, a toroidal magnetic probe array is used to analyze the toroidal mode structure. The toroidal magnetic probe array [25] comprises three ($z = -0.23$ m, $z = 0$ m, $z = 0.23$ m) high-field-side arrays of 8 probes each at the inner wall and three ($z = -0.23$ m, $z = 0$ m, $z = 0.23$ m) low-field-side arrays of 16 probes each at the outer wall. The magnetic pick-up coils acquire data at 250 kHz. The mode frequency measured in the laboratory frame is converted to the frequency in the plasma frame using plasma toroidal rotation data acquired from Charge Exchange Recombination Spectroscopy (CXRS), which uses the C_{6+} impurity line assuming $\nu_\phi = \nu_{C_{6+}}$. The CXRS also provides T_i and Z_{eff} .

The fluctuations of thermal electrons are analyzed in detail with the aid of the second harmonic X-mode low field side ECE diagnostic (LFS-ECE), with 24 channels from 65 to 99 GHz [26]. The data is acquired at 200 kHz. Another ECE system, vertical ECE, positioned at the top of the tokamak, can receive electron cyclotron radiation emitted by suprathermal electrons at the third harmonic of the electron cyclotron frequency, with 12 channels from 89 GHz to 114 GHz.

The main diagnostic for the study of suprathermal electron dynamics is a state-of-the-art hard X-ray tomographic spectrometer (HXRS) [27]. This diagnostic detects the bremsstrahlung radiation of energetic electrons, from ~ 15 keV to ~ 200 keV. The system comprises four cameras with 24 CdTe detectors each, therefore 96 lines of sights can cover the poloidal plane for the tomographic inversion of the hard X-ray emission distribution (Figure 1.3). The TCV hard X-ray system features digital pulse processing [28], which enables up to 600,000 photon counts per second. This diagnostic is described in detail in chapter 2, along with the tomographic method study and response function modeling conducted during this thesis work.

1.2 Suprathermal electrons in tokamak plasmas

The ohmic heating of plasma is intrinsically limited due to the nature of collision frequency in plasmas, which is inversely proportional to the plasma temperature. This limitation has been compensated by the RF wave resonance heating, delivering energy from waves to particles without reliance on collisions. Interestingly, the energy can also flow in the opposite way, from particles to waves, driving instabilities in the plasma. In the plasmas studied here, suprathermal electrons are generated by the heating of electrons by the EC resonance, but these same suprathermal electrons may also trigger instabilities through the wave-particle resonance. Suprathermal electron dynamics associated with these events are the main topic of this thesis and are introduced in this section.

1.2.1 Suprathermal electron generation by EC waves

Electron cyclotron wave injection in tokamak

Wave propagation in the plasma can be described by the plasma dispersion relation, by solving the wave equation derived from Maxwell's equations. The dispersion relation in the cold plasma limit can be used to simply describe accessibility of waves in a spatially varying plasma [29]. The dispersion relation for the dimensionless vector $\mathbf{n} = \mathbf{k}c/\omega$ (\mathbf{k} is the wave vector) can be written following the treatment of Stix [21],

$$\tan^2 \theta = -\frac{P(n^2 - R)(n^2 - L)}{(Sn^2 - RL)(n^2 - P)}, \quad (1.5)$$

$$R = 1 - \sum_s \frac{\omega_{ps}^2}{\omega(\omega + \omega_{cs})}, \quad L = 1 - \sum_s \frac{\omega_{ps}^2}{\omega(\omega - \omega_{cs})}, \quad P = 1 - \sum_s \frac{\omega_{ps}^2}{\omega^2}, \quad (1.6)$$

where $S = (R + L)/2$, and the angle θ is between the magnetic field and the wave propagation vector. When the wave propagation is perpendicular to the toroidal magnetic field ($\theta = \pi/2$), the dispersion relation can be reduced to $n^2 = RL/S$ for the extraordinary mode (X-mode) and $n^2 = P$ for the ordinary mode (O-mode). X- or O- mode depends on the wave polarization,

whether the electric field component is parallel or perpendicular to the external magnetic field, respectively.

The limits of wave propagation can be determined depending on n^2 : $n^2 = 0$ and $n^2 = \infty$ correspond to cutoff and resonance, respectively. In order to assess the accessibility of the wave, cutoffs and resonances are plotted in the CMA diagram, Figure 1.4. Compared to O-mode injection, X-mode injection is complicated by the R-cutoff when the wave is launched from the low field side. When the fundamental resonance X-mode wave is launched from the high field side, the density cutoff is twice that of the O-mode. However, wave injection from the high field side is difficult in practice due to the geometry of tokamaks. These limitations can be overcome by adopting second harmonic X-mode, heating from the low field side, by doubling the injection frequency [29]. In TCV, 82.7 GHz and 118 GHz gyrotrons are used to launch X-mode waves at the second and third harmonics.

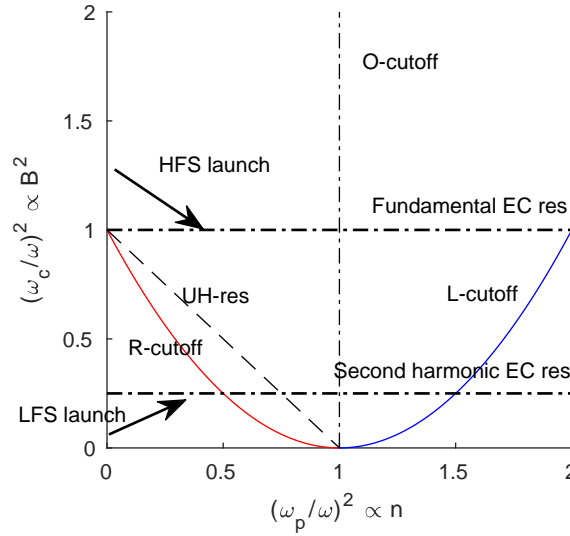


Figure 1.4 – CMA diagram

Electron cyclotron resonance heating of electrons

The interaction of injected waves with electrons can be described by quasilinear theory. Wave-particle interaction induces diffusion of the distribution function in the velocity space. The electron flux S_w in Eq.(1.3) can be written as $S_w = -D_w \cdot \nabla f_e$, where D_w is the quasilinear diffusion tensor. In the simplest case with a single wave, the quasilinear diffusion coefficient is derived by Kennel and Engelmann [30] by assuming a uniform wave E exists in the plasma [19],

Chapter 1. Introduction

$$\mathbf{E}(\mathbf{r}, t) = \text{Re}[\mathbf{E}_w \exp(i\mathbf{k} \cdot \mathbf{r} - i\omega t)],$$

$$D_w = \sum_n \frac{\pi}{2} \frac{e^2}{m^2} \delta(\omega - k_{\parallel} v_{\parallel} - n\omega_c) \mathbf{a}_n^* \mathbf{a}_n, \quad (1.7)$$

$$\mathbf{a}_n = \Theta_n \frac{k_{\parallel}}{\omega} \left[\left(\frac{\omega}{k_{\parallel}} - v_{\parallel} \right) \boldsymbol{\Theta}_{\perp} + v_{\perp} \boldsymbol{\Theta}_{\parallel} \right], \quad \Theta_n = \frac{E_{w+} J_{n-1} + E_{w-} J_{n+1}}{\sqrt{2}} + \frac{v_{\parallel}}{v_{\perp}} J_n E_{w\parallel}, \quad (1.8)$$

where J_n is the n th order Bessel function with the argument $k_{\perp} v_{\perp} / \omega_c$. E_{w+} and E_{w-} correspond to the left- and right- handed components of \mathbf{E}_w . Since the electron velocity in the wave frame $\mathbf{v} - (\omega / k_{\parallel}) \boldsymbol{\Theta}_{\parallel}$ is perpendicular to the \mathbf{a}_n , the diffusion path of the flux S_w is on the wave frame's constant electron energy surface.

This expression can be generalized by including multiple waves and relativistic effects [31]. Then the resonance condition in the delta function in Eq.(1.7) becomes:

$$\omega - k_{\parallel} v_{\parallel} - n\omega_c / \gamma = 0, \quad (1.9)$$

where γ is the relativistic factor, $\gamma = (1 - v_{\perp}^2 / c^2 - v_{\parallel}^2 / c^2)^{-1/2}$. Zero n represents the Landau resonance, and other integers for n correspond to the harmonics of the cyclotron resonance. In other words, the resonance condition is satisfied when the Doppler shifted frequency matches a multiple of the cyclotron frequency ω_c .

Electron cyclotron current drive

The ability of the EC waves to induce wave-particle interaction has been used for driving plasma current. An asymmetry in the velocity distribution function results in plasma current, which is the first moment of the distribution function. The ECCD can be driven by injecting the EC beam obliquely into the plasma, which gives a parallel component to the propagation vector. Current drive is not due to any toroidal momentum transfer. Rather, there are two theories that describe this phenomenon: the Fisch-Boozer [32] and Ohkawa [33] current-drive theories [10, 29].

The Fisch-Boozer current relies on the fact that electrons accelerated by EC waves, which have a preferential parallel velocity consistent with a Doppler-shifted resonance, become less collisional as their velocity increases. Then the pitch angle scattering is less probable compared to the lower energy electrons, inducing slow collisional relaxation. This creates an asymmetry in the velocity space and drives plasma current flowing opposite to the injected wave direction.

The Ohkawa current is often considered in off-axis ECCD, when the trapped electron region is considerable. In that case the resonance curve in velocity space can lie close to the trapping-passing boundary, transferring the accelerated electrons to the trapped region. Then the

collisional flux induced by the detrapping of the electrons appears symmetrically in both toroidal directions. However, since the trapping occurs only in the accelerated electron region, this results in a higher population of energetic electrons on the opposite side. Therefore the Ohkawa current drives current in the injected wave direction.

In the ECCD experiments performed during this thesis work, the ECCD is localized near the magnetic axis, so the main current drive mechanism was the Fisch-Boozer current. However the effect of trapped electrons has been observed during the magnetic field scan experiment in the electron fishbone study. The electron trapping effect decreased the ECCD efficiency due to the fast bounce motion of the trapped electron fraction. This will be discussed in chapter 4.

Previous works on suprathermal electron dynamics

Electron cyclotron current drive (ECCD) induces plasma current by the resonant interaction of EC waves and suprathermal electrons, creating a toroidally asymmetric electron distribution function. Its ability to drive a spatially localized current [34,35] has been used to control plasma instabilities as well, such as the neoclassical tearing mode (NTM) [36, 37] and the sawtooth instability [38]. In ITER, ECCD will be a main stabilization tool for disruptive NTMs [39, 40].

For an estimation of the EC wave driven current, Fokker-Planck modeling of the electron distribution function coupled with a ray tracing code has been a primary tool. Following early research where the plasma current was overestimated in the absence of radial transport of suprathermal electrons [41], the anomalous transport operator in the Fokker-Planck calculation has been a main control parameter [42–45]. The effect of radial transport was further supported by hard X-ray profile measurements, showing that the bremsstrahlung radiation of suprathermal electrons featured a broader profile than the EC wave absorption profile [46].

Recently an effect of EC wave scattering has been addressed as another possible mechanism that degrades the current drive efficiency and localisation [47–52]. Density fluctuations near the edge of the plasma can deflect or scatter the beam, and broaden the driven current profile [53, 54]. However, to this date it is still not clear whether anomalous transport or wave scattering is the dominant cause of the gap between modeling and experiment. This is in part due to the difficulty in observing suprathermal electron dynamics in the real and velocity spaces, which plays an essential role in the physics of ECCD.

The hard X-ray diagnostic has been a main method to analyze the energy spectrum and spatial distribution of suprathermal electrons generated by RF waves [46, 55–57]. However, due to the continuum nature of the bremsstrahlung radiation [58] and the line-integrated nature of the measurement, it is not possible to obtain the electron distribution function directly from the hard X-ray measurement. This limitation can be overcome by resorting to modeling: in particular, a hard X-ray synthetic diagnostic coupled to Fokker-Planck modeling, allows a direct comparison between measurement and simulation [53, 57, 59, 60].

During this thesis work, a state-of-the-art tomographic hard X-ray spectroscopy system of

TCV, equipped with digital pulse detection, has enabled detailed studies of the creation and relaxation of suprathermal electrons. The time evolution of hard X-ray profiles in energy and time has been observed utilizing a minimally perturbative ECCD modulation technique. Time-dependent Fokker-Planck modeling coupled with a hard X-ray synthetic diagnostic has been used for the first time to interpret the experimental results, with various suprathermal electron transport models. The simulation strongly suggests a dependency of the radial transport on the EC wave power and indicates the possibility of EC wave scattering. This will be presented in chapter 3.

1.2.2 Suprathermal electron driven instability: electron fishbone

Fishbone dispersion relation

Suprathermal electrons can drive instabilities in tokamak plasmas [17, 61–65]. The instabilities can induce particle redistribution and may degrade plasma performance. The electron fishbone instability is one of the energetic electron driven instabilities. This is related to the internal kink mode, which was originally observed as an ion driven instability, when the toroidal precessional drift of deeply trapped ions resonates with the mode. In the case of the electron fishbone instability, the internal kink mode, is driven instead by the energetic electrons' resonant interaction with the mode. This was observed in DIII-D for the first time, during off-axis ECCD experiments [17], and was explained by the resonant interaction of barely trapped electrons with the mode, due to the effect of their drift reversal.

The resonance condition for the fishbone mode can be found in the mode dispersion relation [18],

$$\delta I(\omega) = \delta \hat{W}_f + \delta \hat{W}_h(\omega), \quad (1.10)$$

where δI is the inertial term and $\delta \hat{W}_f$ and $\delta \hat{W}_h$ are potential energies from the plasma bulk and suprathermal part, respectively. The suprathermal contribution term $\delta \hat{W}_h = \delta \hat{W}_k(\omega) + \delta \hat{W}_{f,h}$ consists of the kinetic part $\delta \hat{W}_k(\omega)$ and the fluid part $\delta \hat{W}_{f,h}$, which are given by [18]:

$$\delta \hat{W}_k = -\frac{\pi}{2} \frac{\mu_0}{B_0^2} \left\langle E^2 \bar{\Omega}_d^2 \frac{\omega \partial_E \ln f_h - \omega_* \partial_r \ln f_h}{\omega - (q-1)\omega_b \delta_p - \omega_d} \right\rangle_{x,p}, \quad (1.11)$$

$$\delta \hat{W}_{f,h} = \frac{\pi}{2} \frac{\mu_0}{B_0^2} \langle R_p \bar{\Omega}_d E \partial_r \ln f_h \rangle_{x,p}, \quad (1.12)$$

where $\langle \dots \rangle_{x,p} = V^{-1} \int d^3x d^3p f_h$ and the total volume is $V = 2\pi^2 r_s^2 R_p$. f_h is the distribution of suprathermal particles and ω_b and ω_d are their bounce and toroidal drift frequencies, respectively. $\omega_* = q/(e_h B_0 r)$ and $\omega_d = (q E \bar{\Omega}_d)/(e_h B_0 R_p r)$, where e_h is the charge of the suprathermal particle. For trapped particles $\delta_p = 0$. The denominator of Eq.(1.11) gives the resonance condition for the fishbone mode: $\omega = \omega_d$ for trapped electrons and $\omega = \omega_d + (q -$

1) ω_b for passing electrons.

Previous works on electron fishbones

Electron fishbones have been observed in various tokamaks during RF wave heating and current drive experiments: ECRH or ECCD [17, 65–69], LHCD [70–73], and ECRH plus LHCD [66]. The excitation of this internal kink was attributed to the resonant interaction between fast electrons and the mode. In LHCD discharges at high collisionality, the observation of fishbone-like oscillations was explained by non-resonant destabilization due to the suprathermal electron pressure [74, 75].

In the experimental investigation of electron fishbones, diagnosing the suprathermal electron population is a primary goal to assess the stability of the mode and possible loss of energetic electrons. However, the suprathermal electron dynamics related to the fishbone oscillation is still only partially understood. While hard X-ray diagnostics have been the main tool to study the temporal evolution of suprathermal electron energy spectra and spatial structure [67, 68, 71, 72, 76], there has been no detailed analysis at a frequency comparable with the mode frequency, rather only in a few separate time windows during a single fishbone burst [71]. Electron cyclotron emission (ECE) radiated by suprathermal electrons has also showed a correlation between the mode and the fast electron population with higher time resolution, but the measurement lacks spatial resolution [74].

In this thesis work, electron fishbones driven by suprathermal electrons during TCV ECCD discharges are studied. A newly developed ECCD scenario enables collecting hard X-ray photons over regular electron fishbone bursts, allowing high temporal resolution of the hard X-ray measurement. The stability of the mode is assessed by solving the linear fishbone dispersion relation [18], using a realistic electron distribution function modeled by solving the Fokker-Planck equation [77], with the aid of a hard X-ray synthetic diagnostic [57]. This will be presented in Chapter 4.

1.3 Measurements of suprathermal electrons

1.3.1 Hard X-ray measurement

Bremsstrahlung radiation emission

Suprathermal electrons emit bremsstrahlung radiation during their Coulomb collisions with ions. In ECCD plasmas, their energy range lies typically between 20 keV and 200 keV, which corresponds to hard X-rays. Hard X-rays are distinct from soft X-rays, which are emitted from thermal electrons at a few to several keV. Depending on the impurity content of the plasma, the soft X-ray diagnostic can detect not only free-free bremsstrahlung radiation but also free-bound radiation [57]. By contrast, suprathermal electron's bremsstrahlung is generally the

only source of hard X-ray radiation, thus hard X-ray detection clearly serves as a diagnostic for suprathermal electron studies.

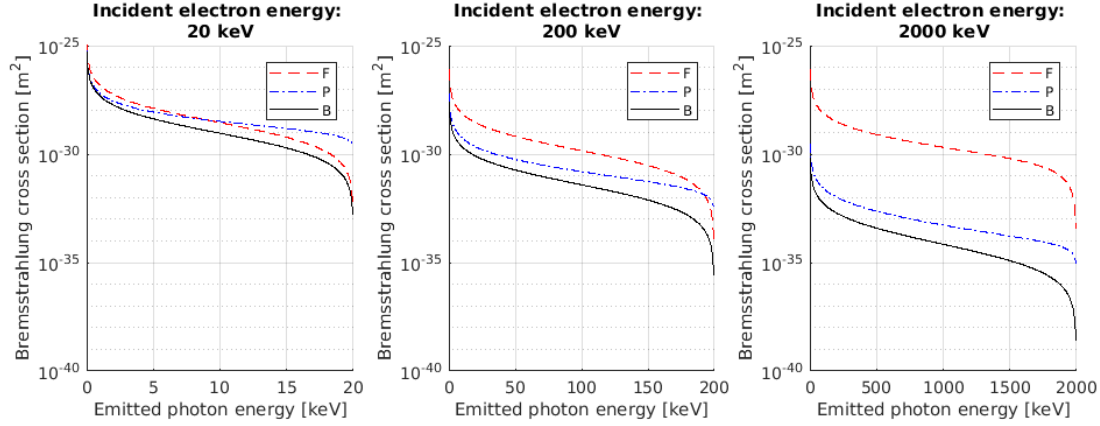


Figure 1.5 – Bremsstrahlung cross section for different incident electron energies. F: forward emission ($\theta = 0$), P: perpendicular emission ($\theta = \pi/2$), B: backward emission ($\theta = \pi$), where θ is the angle between the incoming electron and the bremsstrahlung radiation.

The bremsstrahlung radiation is continuum radiation, since the emitted photon population is continuous in energy. As an example, in Figure 1.5, bremsstrahlung cross sections are plotted for different incident electron energies as a function of emitted photon energy. The bremsstrahlung cross section follows the relativistic Bethe-Heitler formula in combination with the Elwert factor, which is adequate for low impurity plasmas [57, 78, 79]. The cross section is continuous in energy below the incident electron energy. This continuum radiation implies that a direct measurement of the electron distribution function is impossible, unless the electron distribution is mono-energetic, which is hardly the case for plasmas. Therefore in this thesis work, the electron distribution function is modeled using a Fokker-Planck code, which is coupled to a hard X-ray synthetic diagnostic.

In Figure 1.5, forward, perpendicular, and backward emissions (F, P, and B, respectively) are plotted separately. This definition depends on the angle between the incident electron and the emitted photon. In general the emissivity increases from backward to forward emission, and the difference increases with incoming electron energy. In other words, as the incident electron energy increases, emitted photons tend to be increasingly aligned in the forward direction. This so-called relativistic headlight effect [58, 80] is one of the important characteristics of hard X-ray emission. This effect can be used to infer information about the electron distribution in tokamak plasmas, where the suprathermal electron population has an asymmetry in velocity space [55, 81]. For example, passing electrons' forward emission may contribute mainly to the line of sight that is parallel to the toroidal magnetic field line. When the line of sight is perpendicular to the toroidal magnetic field, the bouncing trapped electrons' forward emission may account for a major portion of hard X-ray detection.

Hard X-ray detection

Hard X-ray photon detection is based on light-matter interaction. There are three major interactions that play a role in hard X-ray detection: photoelectric absorption, Compton scattering and pair production [82].

In the photoelectric absorption process, an incident photon is absorbed by the material and an electron, so-called photoelectron, is released. In this process, the bound energy of the photoelectron is consumed, therefore the energy of the photoelectron corresponds to the difference between the energy of the incoming photon and the bound energy. In the hard X-ray range, the bound energy of several eV is negligible compared to the photon energy (thousands of eV). Therefore photoelectrons directly reflect the energy of the incoming photons.

The incident photon can also be scattered by an electron, and the energy is transferred to the electron by Compton scattering. In this case the energy of the recoil electron varies depending on the scattering angle. The recoil electron obtains the most energy from a head-on collision, and this upper energy boundary is defined as “Compton edge”:

$$E_{e,\theta=\pi} = h\nu \left(\frac{2h\nu/m_0c^2}{1 + 2h\nu/m_0c^2} \right), \quad (1.13)$$

where $h\nu$ is the incident photon energy and θ is the scattering angle. The Compton scattering contributes to a hard X-ray detection spectrum below the Compton edge.

Lastly, the pair-production process happens when the energy of the incident photon is above 1.02 MeV, which is twice the rest mass energy of the electron. In this process, the incoming photon disappears and a electron-positron pair is created. The kinetic energy of the electron-positron pair corresponds to the difference between the photon energy and 1.02 MeV, which is usually detected as a delta function as the pair loses their energy in the material. This effect is negligible in the hard X-ray detection of suprathermal electrons from ECCD plasmas, with an energy range far below 1 MeV.

In tokamak plasmas, semiconductor materials are commonly used for hard X-ray detection, for a compact setup comprising multiple detectors [58, 83]. The photon-matter interaction generates many electron-hole pairs in the semiconductor material. The pairs drift to the electrodes by virtue of an externally applied electric field and create a charge pulse.

As an example of the detection process, in Figure 1.6 (bottom), a Monte-Carlo simulation of the photon-matter interaction is presented. EGS (electron gamma shower) software [84] is used to simulate the photon count rate from a cubic CdTe detector of 2 mm side, which is the case of the TCV hard X-ray diagnostic. A photon beam of 60 keV is vertically injected to the detector. EGS computes possible interactions based on its cross section database.

The highest counts are found at the energy of the incident photons, due to the photoelectric

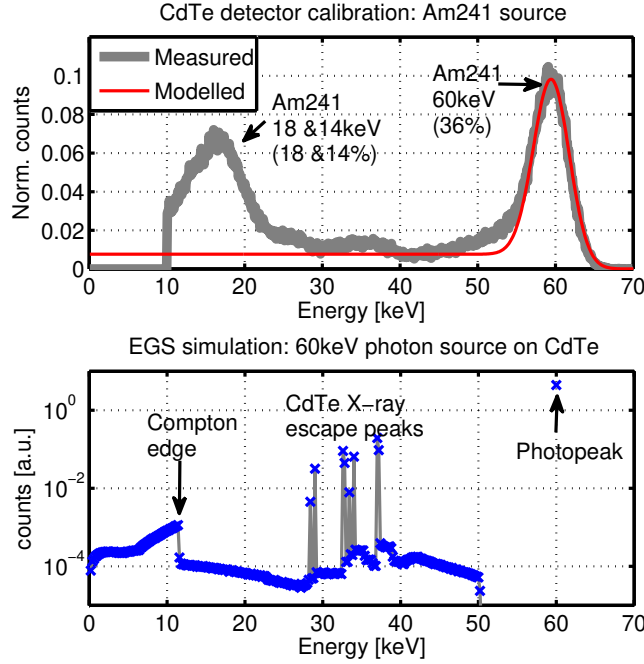


Figure 1.6 – (Top) TCV HXRS CdTe detector measurement of photons emitted from Am-241 source. (Bottom) EGS simulation of 60 keV photon beam incident on the CdTe detector.

effect (“Photopeak”). A continuous spectrum exists below the Compton edge³ from the Compton effect. There are some other peaks, which correspond to escape peaks as the characteristic X-rays of the detector material escape. The energies of these peaks are the differences between the incident photon energy and the characteristic X-ray energies of Cd and Te.

This spectrum is the response function of the detector for one particular energy, which can then be applied to estimating the detection spectrum. This is important in particular in a hard X-ray synthetic diagnostic, where the expected photon count rate is calculated from the modeled electron distribution function. This procedure will be discussed in the next section. In reality, the measured spectrum deviates from the ideal case (Figure 1.6 (top)) due to experimental uncertainty and characteristics of detector. This will be studied in detail for the hard X-ray detectors in TCV, in section 2.3.

1.3.2 Electron cyclotron emission

Another main diagnostic method for the study of suprathermal electron is a detection of electron cyclotron emission (ECE) from suprathermal electrons. In contrast to the continuum bremsstrahlung radiation, the ECE radiation corresponds exclusively to the Doppler-shifted

³Following equation (1.13), the Compton edge of 60 keV photons is 11.41 keV.

EC frequency of electrons with a specific energy. The frequency is in fact the same as the EC wave resonance condition, which was introduced in Eq.(1.9). This can be rewritten in terms of the angle θ in between the wave vector and the magnetic field:

$$\frac{\omega}{\omega_c} = \frac{n\sqrt{1-\beta^2}}{1-\beta_{||}\cos(\theta)}, \quad (1.14)$$

with $\beta = v/c$ and $\beta_{||} = v_{||}/c$.

Following this expression, electrons with high v_{\perp} and $v_{||}$ induce a relativistic downshift and upshift [58]. This property can be used for the ECE detection of high v_{\perp} electrons on the high field side and the ECE detection of high $v_{||}$ electrons obliquely ($\theta \neq \pi/2$) on the low field side. The ECE radiation measurement provides better resolution compared to the hard X-ray photon detection, but the spatial information is limited. In this thesis work, this diagnostic is used as a supplementary measurement for the detection of suprathermal electrons (chapter 4).

1.4 Modeling of suprathermal electrons

1.4.1 Fokker-Planck modeling of ECCD plasmas

Bounce-averaged 3-D Fokker-Planck equation

As introduced in Chapter 1.1, the Fokker-Planck equation is used to describe the effect of RF wave heating on the electron distribution function. In addition to the expression in Eq.(1.3), a transport term is often added to model the effect of anomalous spatial transport, as $\nabla_x \cdot (\mathbf{F}_x f_e - \mathbf{D}_x \cdot \nabla_x f_e)$. \mathbf{F}_x and \mathbf{D}_x describe effects of a convective pinch and diffusion, respectively [85].

There are different orderings used in the derivation of this bounce-averaged Fokker-Planck equation (Eq.(1.3)) to reduce the dimensionality used in solving the problem: 2-D in real space (due to the axisymmetry) and 3-D in velocity space. Firstly, when a strong magnetic field exists, a small Larmor radius assumption can be used. The small parameter $\delta^2 = r_L/a$ is defined, where a is the tokamak minor radius and r_L is the Larmor radius. $\delta^2 \ll 1$ is used to derive the guiding-center Fokker-Planck equation.

In the guiding-center approximation, the electron distribution function is 2-D in real space (flux surface ψ and poloidal angle θ) and 2-D in velocity space (momentum p and pitch angle ξ). This 4-D space can be simplified in the case of low collisionality $\nu^* \ll 1$, where $\nu^* = \nu_{dt}/\nu_b$ is the ratio of the detrapping frequency ν_{dt} to the bounce frequency ν_b . Due to the fast bounce motion, the 3-D Fokker-Planck equation can be obtained by an additional averaging. Therefore the electron distribution function as a solution of the bounce-averaged Fokker-Planck equation is a function of ψ , p and ξ .

LUKE code for TCV

In this thesis work, the LUKE Fokker-Planck code [77] is used to model the electron distribution function in TCV ECCD plasmas. The code is coupled to the ray tracing code C3PO [86], so the damping of the EC rays is calculated self-consistently from the quasilinear diffusion operator.

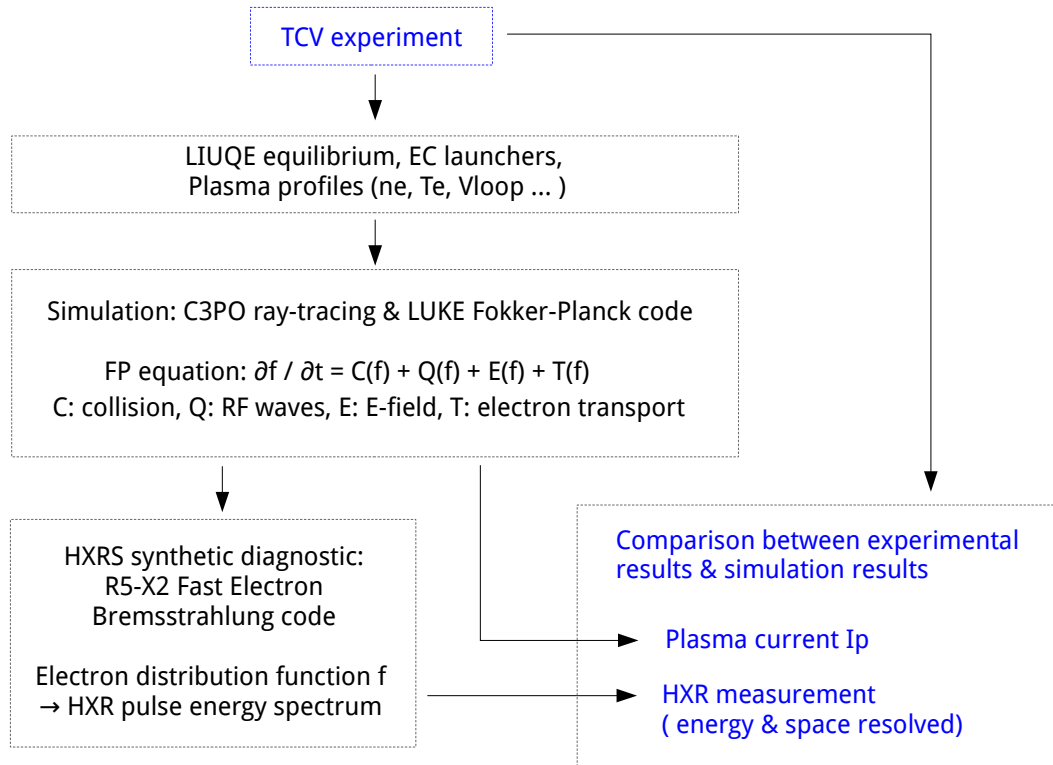


Figure 1.7 – Fokker-Planck modeling scheme in TCV

The structure of the Fokker-Planck modeling of TCV plasmas is presented in Figure 1.7. After the experiment, the plasma equilibrium is reconstructed by the equilibrium code LIUQE [22]. Plasma density and temperature profiles are loaded from the Thomson scattering diagnostic data, and the loop voltage is loaded from the flux loop measurement. Both steady state and time-varying simulations can be performed. In this thesis work, the time-varying simulation is done to model the evolution of the electron distribution function in response to short ECCD pulses. The modeled plasma can be assessed by comparing both the estimated plasma current and the hard X-ray count rate.

1.4.2 Hard X-ray synthetic diagnostic

The hard X-ray synthetic diagnostic calculates the hard X-ray count rate based on the Fokker-Planck modeled electron distribution function. In TCV, the Fast Electron Bremsstrahlung (FEB) module [57] is coupled to the LUKE Fokker-Planck code. The modeled electron distribution function can be directly loaded to the FEB module, as well as the equilibrium structure. Since the distribution function is bounce-averaged, as a first step, the bounce-averaged distribution function is stretched to the 2-D space, using the relation [77]

$$\xi = \text{sign}(\xi_0) \sqrt{1 - \Psi(\psi, \theta) (1 - \xi_0^2)} \quad (1.15)$$

where $\Psi(\psi, \theta) = B(\psi, \theta)/B_0(\psi)$ and ξ is the pitch angle.

The distribution function in 4-D space is then used to calculate the effective photon energy spectrum $dN_k(t, k)/(dt dk)$ using the bremsstrahlung cross section $d\sigma/(dt dk d\Omega)$, where $d\Omega$ is a solid angle and k is a photon energy. Then the photon spectrum arrived at each detector $dN_k(t, k)/(dt dk)$ is used to calculate the pulse energy spectrum $dN_E(t, E)/(dt dE)$,

$$\frac{dN_E(t, E)}{dt dE} = \int_0^\infty \eta_A(k) (1 - \eta_D(k)) G(k, E) \frac{dN_k(t, k)}{dt dk} dk. \quad (1.16)$$

Here, $\eta_A(k)$ is the ratio of photons transmitted on their way to the detector; this can decrease due to the absorption by the window or absorber structures placed in front of the detector. $1 - \eta_D(k)$ describes the fraction of photons stopped inside the detector volume, therefore having a photon-matter interaction. $G(k, E)$ is the normalized detector's response function, $\int_0^\infty G(k, E) dk = 1$. For the hard X-ray diagnostic system in the TCV tokamak, the response function is modeled based on the measured response to various radioactive sources. This will be explained in chapter 2.3.

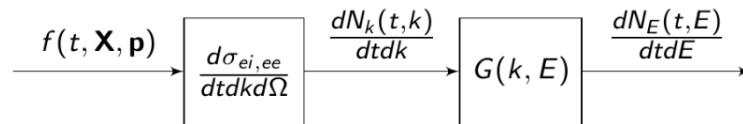


Figure 1.8 – Fokker-Planck modeling scheme in TCV

1.5 Thesis goals and outline

1.5.1 Thesis goals

The goal of this thesis is to advance the understanding of the generation and dynamics (including slowing-down, spatial transport, etc.) of suprathermal electrons and their effect on the plasma stability, primarily in the TCV tokamak of the Swiss Plasma Center at EPFL, Switzerland. This is being done by employing state-of-the-art diagnostics and numerical modeling. The objectives of the research are as follows:

- Development and maintenance of diagnostics and related software tools
 - Oversee the fabrication and installation of the last HXRS camera, perform the calibrations
 - Maintain the general tomographic inversion code (GTI) for HXRS and XTOMO, implement the necessary improvements
- Development of modeling software
 - Improve and optimize the fast electron bremsstrahlung calculator's response function for the TCV HXRS and thus the performance of the synthetic diagnostic for LUKE
 - Optimize the time-varying Fokker-Planck simulation mode of the code LUKE for the ECCD modulation study
- Experimental study and numerical modeling and analysis
 - Study the suprathermal electron population response to ECCD
 - * Characterize the creation and relaxation of the suprathermal electron population using HXRS
 - * Compare the experimental data with modeling using the Fokker-Planck code LUKE and characterize the radial transport
 - Study the interaction between MHD modes and suprathermal electrons
 - * Seek experimental evidence of electron fishbones and document their dynamics
 - * Numerical analysis based on the theoretical model and comparison with the experiment

1.5.2 Thesis outline

The approach to study suprathermal electrons generated by EC waves using hard X-ray diagnostic is outlined below.

- Chapter 2 will introduce a hard X-ray diagnostic (HXRS) in TCV and related studies conducted during this thesis: a tomography method study for HXRS and a model for response function of the CdTe detector, for the HXRS synthetic diagnostic.
- Chapter 3 presents a study of ECCD generated suprathermal electron dynamics, using an ECCD modulation technique and HXRS. Time-varying profiles of hard X-ray emission are presented, which reflect the dynamics of suprathermal electrons. Time-dependent Fokker-Planck modeling, coupled with the synthetic diagnostic, is used to perform a comparison between the experiment and simulation.
- Chapter 4 presents a study of electron fishbones observed during ECCD discharges in TCV. The responses of the thermal and suprathermal electron populations observed during the experiment are presented and the plasma is modeled using the Fokker-Planck code. A linear fishbone dispersion relation is solved based on the modeling, for stability analysis.
- In chapter 5, a summary, conclusions and a future outlook are presented.
- Appendix A presents the MHD mode structure analysis methods used throughout this thesis.
- Appendix B presents a preliminary study of toroidal asymmetry in the hard X-ray emission.
- Appendix C presents a study of non-standard sawteeth, which supports the related observations in chapter 4.
- Appendix D presents a procedure for solving the linear fishbone dispersion relation.

2 Hard X-ray tomographic spectrometer system (HXRS) in TCV

A hard X-ray tomographic spectrometer system (HXRS) has been developed to study the physics of suprathermal electrons in the TCV tokamak [27, 87–89]. This system has been operational for the study of ECRH physics [90] and MHD events [91], with a partial set of cameras. Installation and commissioning of the last camera and pneumatically controllable filters were carried out during this thesis work, which completed the full set of four cameras. In this chapter, an overview of this diagnostic system is given in section 2.1, including its hardware features and data analysis procedures. Section 2.2 presents a study of tomography methods for HXRS, for various hard X-ray emission patterns due to localized EC wave injection or MHD events near rational magnetic flux surfaces. Section 2.3 presents a modeling of the response function of HXRS CdTe detectors based on the detector calibration, which is implemented in the hard X-ray synthetic diagnostic.

2.1 Overview of the diagnostic

2.1.1 Hardware and characteristics

Geometry

The HXRS system consists of four cameras with 24 detectors each, therefore up to 96 lines of sight enable spatially resolved analysis of hard X-ray emission in real space. The two lateral cameras can be rotated by 90 degrees, so that the lines of sight can cover either the toroidal plane, parallel to the magnetic field lines, or the poloidal plane, perpendicular to the magnetic field lines. Since energetic electrons emit hard X-ray radiation preferentially in the direction of travel (relativistic headlight effect, see chapter 1.3.1), trapped and passing electrons contribute differently to the hard X-ray photons received by the camera in different orientations. This fact can be used in studying different behaviors of trapped and passing electrons (chapter 4.3.3).

Figure 2.1 (a) shows the lines of sight of the Equatorial and Upper-lateral cameras (HXRS-E and HXRS-U in the figure), when their lines of sight cover the toroidal plane. The lines of sight

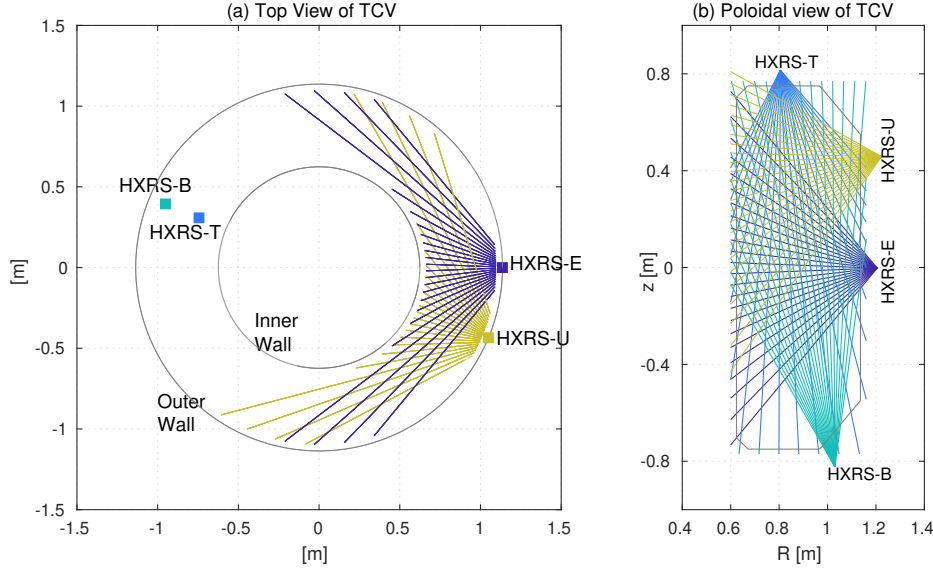


Figure 2.1 – HXRS lines of sight. (a) Top view of TCV. The Equatorial camera (HXRS-E) and Upper-lateral camera (HXRS-U) are oriented horizontally. (b) Poloidal view of TCV. The Equatorial camera (HXRS-E) and Upper-lateral camera (HXRS-U) are oriented vertically.

in the poloidal plane are presented in Figure 2.1 (b). This allows a tomographic inversion of hard X-ray emission in the poloidal plane, which has been performed successfully using three cameras (Top, Equatorial, Bottom) during ECCD discharges [90], for centrally peaked emission profiles. A study of tomography methods for various emission types, such as ring or banana shapes, is presented in the next section.

Hard X-ray detection

During the design process of HXRS [87–89], a CdTe detector was chosen for its good charge collection efficiency, compared to other high Z semiconductor materials, such as CdZnTe or HgI₂. The high Z materials are preferred in the detection of hard X-ray or gamma-rays due to their high probability of photo-electric interaction in the relevant energy range. The cubic CdTe detector of 2 mm side (Figure 2.2 (a)) has an optimum thickness for the detection of photons between ~15 keV and ~200 keV. This semiconductor detector features room-temperature operation and a long-time operational stability. As the detectors and electronics are placed in preliminary vacuum, preventing convective cooling, power to the electronics is turned on only during each discharge.

Camera structure

Each CdTe detector is connected to a preamplifier card. At each photon encounter, electron-hole charges created by the photon-matter interaction in the detector are transformed into a

charge pulse whose height is proportional to the incident photon energy. The electronics are connected to an electronic control module through a SCSI connector. The module in turn is connected to acquisition cards, and the signals are acquired at a sampling rate of 12 MHz.

Each camera has a tungsten fan-type Soller collimator, placed in front of an array of detectors (Figure 2.2). The detectors are shielded by at least 2 cm of tungsten around the camera from uncollimated gamma rays that can be generated in low density inductive discharges. In front of the collimator, two rotatable filters are placed to reduce the incoming photon flux, in order to prevent pile-up events in the pulse detection. 36 filter combinations are enabled by two rotating filter holders with six filters each (Figure 2.2 (c)). The filters are pneumatically controlled remotely by the controller connected to the control module.

2.1.2 Data analysis

After each experiment, a raw time trace of voltage pulses is converted to energy in eV, based on the calibration performed using radioactive sources. Then the time trace is analyzed using the pulse processing method developed for HXRS [28]. This method consists of signal treatment, pulse detection, and pulse height analysis. Among various algorithms developed for the pulse processing, the “opt4na” algorithm has been chosen for HXRS due to its superior detection efficiency in high count rate applications. This algorithm is composed of an optimized finite impulse response (FIR) filter, dynamic threshold pulse detection, and level evaluation for pulse height analysis. The method was implemented in Python and C and parallelized with mpi4py [90]. This digital pulse processing enables up to 600,000 photon counts per second.

After the digital pulse processing, the detected pulse peaks with their time and energy information are stored in the PC dedicated to the HXRS analysis. Then the stored peaks can be sorted into user-set energy and time bins, depending on the physics of interest. As an example, Figure 2.3 shows pulse detection results and the count rate binning procedure. The photon statistics can be enhanced by conditionally averaging photon counts over repetitively occurring events. This has been a main technique in the analysis of hard X-ray data in this thesis. In the ECCD modulation discharge presented in Figure 2.3, the hard X-ray data can be averaged over repetitive ECCD pulses (line in blue in Figure 2.3 (d)) by simply arranging the data according to the time trace of the ECCD pulse.

In case of repetitively occurring MHD events such as sawtooth or fishbones, time points for conditional averaging need to be chosen carefully to reduce the standard deviation, because the amplitude and the length of each event vary. As an example, Figure 2.4 shows repetitive electron fishbone bursts, which will be studied in detail in chapter 4. The selection criteria are applied to the magnetic field fluctuation data, which is presented in Figure 2.4 (a-c). From the Fourier-spectrum (Figure 2.4 (b)) of the magnetic field fluctuation (Figure 2.4 (a)), the maximum spectral power at each time point is plotted in Figure 2.4 (c). A power threshold is applied to the spectral power, which is indicated as a red dashed line in Figure 2.4 (c). In this discharge, the fishbone bursts whose maximum spectral power is above -31 dB are selected

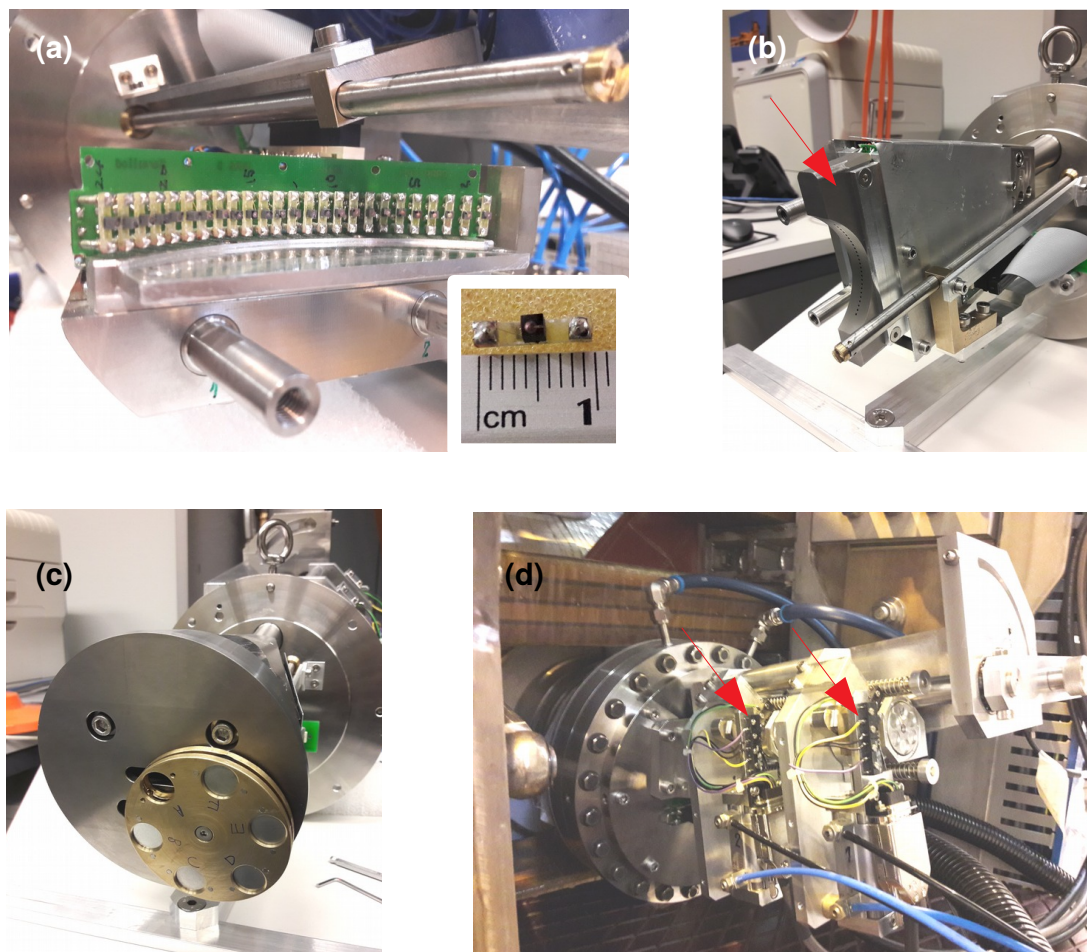


Figure 2.2 – (a) An array of detectors. A single CdTe detector on the supporting structure is shown at bottom right. (b) A Tungsten collimator (red arrow) is placed in front of the array of detectors, which are contained in the cassette with electronics. (c) A front shield and rotating filters are assembled in front of the collimator. Two filter wheels can be separately controlled. (d) Upper-lateral camera as installed on TCV. The two filter controllers are indicated by red arrows.

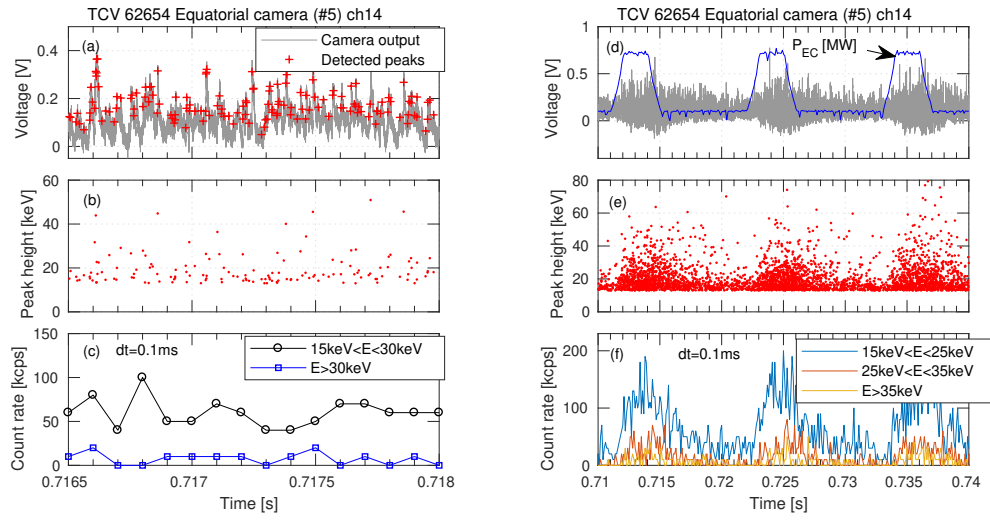


Figure 2.3 – Example of HXRS pulse detection and data analysis. (a,d) Raw signal output from the camera in voltage. (b,e) Detected pulse peak height transformed in keV, after the digital pulse processing. (c,f) Time trace of count rate in thousands of counts per second, after sorting the peak data into energy and time bins.

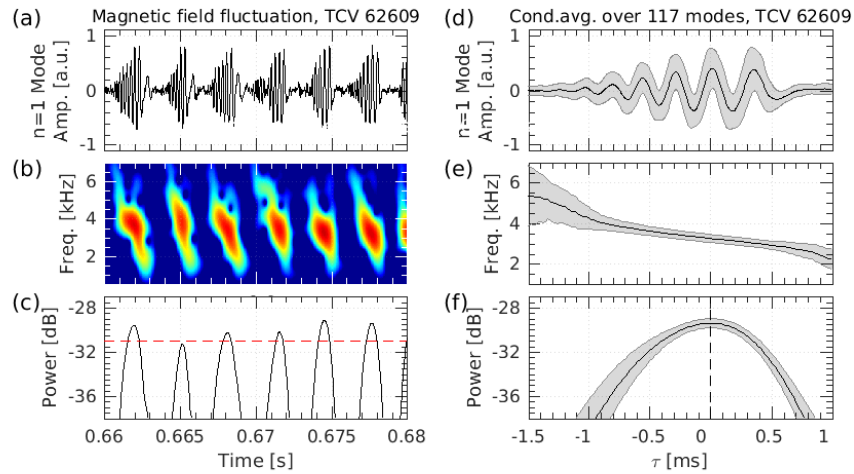


Figure 2.4 – (a) Magnetic field fluctuation in real time and (b) its Fourier spectrogram. (c) The maximum spectral power of (b). (d-f) Conditionally averaged magnetic field fluctuation, mode frequency and spectral power.

for the conditional averaging. The time points of 117 bursts are collected in this discharge. Figures 2.4 (d-f) show the averaged magnetic field fluctuation level, mode frequency, and spectral power. This method is applied to the hard X-ray data analysis in chapter 4.

2.2 Tomography method study for HXRS

Computed tomography methods have been used in tokamak plasma diagnostics [92] in order to derive a 2-D emissivity profile from line-integrated measurements, such as soft X-ray, bolometer, hard X-ray or neutron measurements. The tomography problem aims to invert an integral,

$$f_l = \int_{s_l} g ds, \quad (2.1)$$

where f_l is line-integrated data along s and g is a local emissivity. This problem in the tokamak plasma is basically the same as in the medical application, where these types of methods are intensively studied. However, the application to tokamak plasma is set apart by its limited number of spatial measurement points [92]. In general, the available line-integrated data are of the order of 10^2 in the fusion application and 10^5 in the medical application.

In TCV, the soft X-ray tomography system (XTOMO) comprises 200 lines of sight, all located at the same toroidal position. The system has been routinely used to invert soft X-ray emissivity, in order to investigate the thermal plasma distribution and associated instabilities, with the aid of further analysis such as through singular-value decomposition (SVD) [23]. The minimum Fisher information regularization method is most commonly used to invert centrally peaked soft X-ray profiles. It has also been shown that a ring-shaped emissivity profile can be inverted during the sawtooth crash [93].

This tomographic method was used to invert expected, typical hard X-ray emissivity profiles (“phantoms”) in the process of hard X-ray camera design [89], and to invert a centrally peaked hard X-ray emissivity pattern in ECCD experiments [90]. However, more unusual emissivity patterns such as ring shaped or banana shaped emission have not been considered. The number of lines of sight of HXRS (4 cameras with 24 lines of sight each) is less than half of those of XTOMO (10 cameras with 20 lines of sight each) and the minimum Fisher regularization method is basically a smoothing method, so the quality of the tomographic inversion for the non-centrally-peaked emissivity pattern is questionable. In addition, since two sets of HXRS cameras are toroidally separated by π , if the hard X-ray emissivity is toroidally asymmetric (i.e. helical core that has a $m/n = 1/1$ structure), it could be argued that the number of lines of sight that can be used for an unambiguous inversion is even reduced to 48 (two cameras at each set). Thus it is important to investigate alternative tomographic inversion methods that may be more suitable for the TCV HXRS system, in the study of suprathermal electrons.

In this section, two new tomographic inversion methods are introduced and used to invert various phantoms, based on the geometry of HXRS. These are the maximum likelihood method and the Cormack-Bessel method. In JET neutron tomography with limited measurement data, it has been demonstrated that the maximum likelihood method inverts non-centrally peaked neutron emissivity images successfully [94]. The Cormack-Bessel method is one of the oldest analytic solutions of the tomography problem, and is widely used to invert the emissivity with

a helical structure [95–97].

This section is arranged as follows: in section 2.2.1, the two new tomography methods are introduced as well as the minimum Fisher method. The quality of tomographic inversion is assessed in section 2.2.2 with different emissivity phantoms, and the conclusions are given in section 2.2.3.

2.2.1 Tomographic inversion methods for HXRS

Cormack-Bessel method

One of the first methods applied to the soft X-ray tomography problem in tokamak plasmas is the Cormack method [92, 98, 99], which expands Eq.(2.1) in a series of orthogonal functions. The measured emission f in Eq.(2.1) is represented in terms of p and ϕ , which are the distance between the line of sight and the magnetic axis, and the angle between the horizontal axis and the line of sight [96]. In this scheme, a concentric flux surface structure (r, θ) is necessary, which is often different from the realistic plasma flux surface shape. In the present work, the rotational tomography technique [95] is implemented for non-circular TCV plasmas, which transforms the non-circular flux surfaces into concentric circles, using an elliptic surface approximation and Shafranov shift. Then Eq.(2.1) can be represented as

$$f(p, \phi) = \int_L g(r, \theta) ds. \quad (2.2)$$

The original Cormack technique uses the Zernicke polynomial as a base function in the Fourier expansion. However, it is known that the reconstructed image using the Cormack-Zernicke method has spurious images at the edge [96, 97]. This limitation was improved by implementing the Bessel function as the base function [97, 100]. In this work, the Fourier-Bessel series becomes:

$$g(r, \theta) = \sum_{m=0}^{\infty} \sum_{l=0}^{\infty} [a_m^{(c)l} \cos m\theta + a_m^{(s)l} \sin m\theta] g_m^l(r) \quad (2.3)$$

$$f(p, \phi) = \sum_{m=0}^{\infty} \sum_{l=0}^{\infty} [a_m^{(c)l} f_m^{(c)l}(p, \phi) + a_m^{(s)l} f_m^{(s)l}(p, \phi)] \quad (2.4)$$

$$f_m^{(c,s)l}(p, \phi) = \int_L (\cos m\theta, \sin m\theta) g_m^l(r) ds, \quad (2.5)$$

where $g_m^l(r) = J_m(\gamma_m^{l+1} r)$ and γ_m^l is the l -th zero of the m th order Bessel function $J_m(z)$.

The coefficients $a_m^{(c,s)l}$ are determined by fitting the measurement f using the least-squares fit in Eq.(2.4), then the expected emissivity g is reconstructed using the calculated coefficients in Eq.(2.3). In practice, the expansion is truncated at finite values of l and m .

An example of the tomographic inversion process using the Cormack-Bessel method (CB method) is presented in Figure 2.5. The magnetic equilibrium of TCV shot 62609 at $t = 0.8$ s and the full lines of sight of the four hard X-ray cameras are used (Figure 2.5 (a)). The flux surfaces are approximated as elliptical surfaces (blue dots in Figure 2.5 (a)) and transformed into the circular geometry (blue dots in Figure 2.5 (b)). Then the CB method can be used to invert the emissivity distribution in the transformed geometry (x, y) , which will be transformed back to the original geometry (R, z) after the tomographic inversion. In Figure 2.5 (b), the lines of sight that pass the area of interest (blue dots) are selected for the calculation (red lines).

A banana-shaped emissivity is introduced as a phantom (Figure 2.5 (c)). An array of the line-integrated signals f is calculated for the full set of hard X-ray cameras based on this phantom. Then the CB method is used to obtain the emissivity distribution g . In Figure 2.5 (d-f), the inverted images using different maximum m and l indexes are presented. In general, including a larger number of Fourier-Bessel expansion terms can give a more detailed structure in the image. However, due to the limited number of measurements, increasing the number of expansion terms does not necessarily enhance the quality of the tomographic inversion. In Figure 2.5, the phantom image can be reconstructed with a set up to $m = 2$ and $l = 3$. The root-mean-square (rms in Figure 2.5) difference between the phantom emissivity and the inverted emissivity is calculated as $rms = \sqrt{\sum_i (g_i^{phantom} - g_i^{inverted})^2 / n}$.

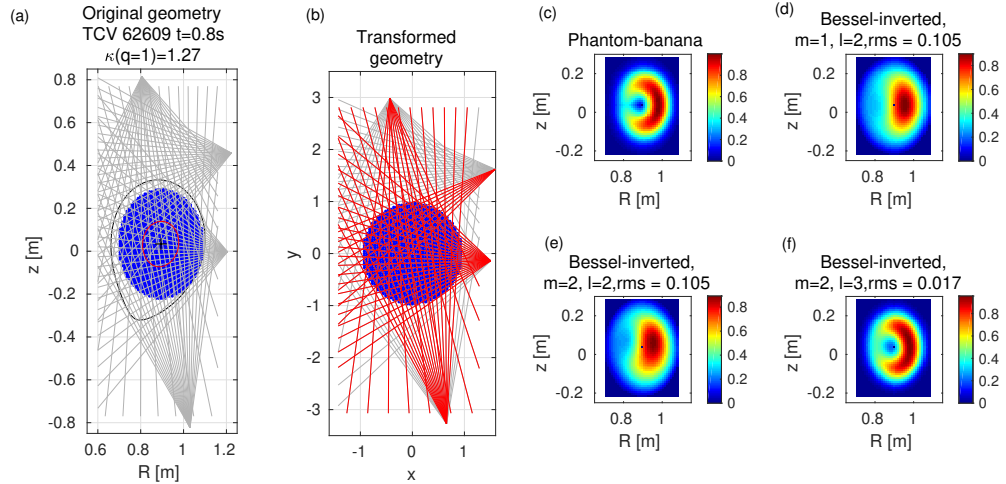


Figure 2.5 – (a) HXRS lines of sight on the poloidal view of the tokamak. (b) The transformed geometry to use the CB method. (c) Banana-shaped emissivity phantom. (d-f) Tomographically inverted emissivity images using the CB method with different number of Bessel expansion.

Minimum Fisher regularization method

The CB method is one of the analytic solution approaches to the tomographic problem. The other approach is to discretize the 2-D area into pixels and perform a numerical inversion of the problem [92]. This assumes that the emissivity is uniform inside each pixel, thus the pixel has to be small enough to justify this assumption. But at the same time the pixel cannot be so small that there are too many pixels to be determined by the numerical inversion. After the discretization, the tomography problem (Eq.(2.1)) can be represented as a sum:

$$f_l = \sum_{i=1}^N T_{il} g_i, \quad (2.6)$$

where T_{il} is a length of a line l in pixel i . The total number of pixels is N . This can also be represented in matrix form, $f = Tg$. Since the number of measurement lines of sight is limited in the tokamak plasma experiments, this problem is generally underdetermined. Even if the number of measurement matches the number of pixels, the matrix T is badly conditioned, so it is almost impossible to obtain a direct inversion of T [23].

One of the well-known regularization methods for this problem is the Tikhonov regularization [23, 101, 102], which minimizes the sum of the residual and the regularization function $O(g)$:

$$\min(\|Tg - f\|^2 + \gamma O(g)), \quad (2.7)$$

where γ is the regularization parameter. In the case of the linear regularization method, the regularization function is chosen as: $O(g) = \|\nabla_x g\|^2 + \|\nabla_y g\|^2$, so that the gradient of g is minimized.

The minimum Fisher (MF) regularization method uses the Fisher information as a regularization function, $O(g) = \int g'(x)^2 / g(x) dx$. This provides a more reliable solution than the linear regularization method, since the smoothness near the core area with high emissivity is weak, so over-smoothing can be prevented [23]. This has been a default tomographic method used for soft and hard X-ray tomography in TCV. In fact, a parameter σ_e that specifies the target error, following the Cramer-Rao inequality $\sigma_e \geq 1/O(g)$, is adjusted to modify the smoothness of the inversion.

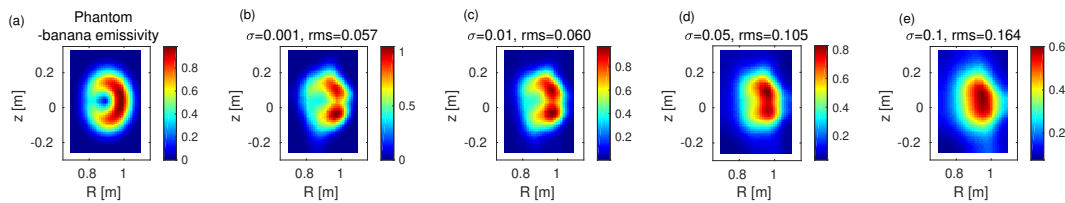


Figure 2.6 – (a) Banana-shaped emissivity phantom, (b-e) Reconstructed emissivity images by the MF method with different parameter σ_e .

An example of the tomographic inversion using the MF method is presented in Figure 2.6. The

banana-shaped phantom image in Figure 2.6 (a) is inverted with varying smoothing parameter value, σ_e (Figure 2.6 (b-e)). A square-pixel discretization is used to divide the area into square pixels of size 1 cm \times 1 cm, and there are 40 pixels horizontally and 60 pixels vertically. The full hard X-ray camera set is implemented: four cameras with 24 detectors each.

Lower σ_e (Figure 2.6 (b)) gives a lower rms error, but the reconstructed image is not smooth; the original banana shape is broken into two pieces. Higher σ_e (Figure 2.6 (e)) smoothes the image but it is difficult to recognize the shape of the phantom.

Maximum Likelihood method

The Maximum Likelihood (ML) method is another method for solving the discretized tomographic problem. The emission g is assumed to represent a Poisson process and the expected value for the measurement is written as $\sum_l T_{il}g_i$. Then the likelihood function of measuring f from the emissivity distribution g is [94]

$$L(f/g) = \prod_l \left(\frac{1}{f_l!} \left(\sum_i T_{il}g_i \right)^{f_l} \times \exp \left(- \sum_i T_{il}g_i \right) \right) \quad (2.8)$$

The ML method consists of finding the f that maximizes the likelihood function. The iterative solution for this problem is given by the formula [103]

$$g_i^{k+1} = g_i^k \left(\sum_l T_{il} \left(f_l / \sum_p T_{jp} f_j^k \right) \right) / \sum_l T_{il}, \quad (2.9)$$

where k is the iteration index [94].

In order to supply additional experimental information, after each iteration, a smoothing operator can be applied to the inverted image g . In this work, the smoothing operator used in the JET neutron tomography [94] is implemented. A sliding window is set at each flux surface, and the emissivity is averaged along the moving window. As an additional smoothing method, virtual lines of sight are added to the hard X-ray lines of sight by interpolating the measurement value f .

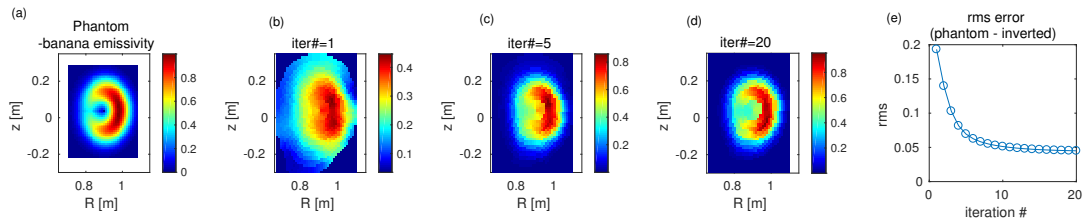


Figure 2.7 – (a) Banana-shaped emissivity phantom. (b-d) Reconstructed emissivity image using the ML method, at different iterations. (e) rms error calculated at each iteration.

An example of tomographic reconstruction using the ML method is shown in Figure 2.7. The spatial discretization used in Figure 2.6 is applied here as well. The length of the sliding window for smoothing is set at 1/8 of each flux surface. Five virtual lines of sight are added to the existing hard X-ray lines of sight, and the measurement f is interpolated using spline interpolation.

Figure 2.7 shows that the reconstructed image gets closer to the phantom image with higher iteration number, as the decreasing rms value shows. However, increasing the iteration number does not guarantee higher accuracy because of a fundamental noise that exists in the ML algorithm, which worsens as the number of iterations increases [94]. In this work with a known phantom image, the process is terminated at the iteration that has the lowest rms value. However, in the real image inversion where the rms error estimation is not possible, it is necessary to introduce a correlation coefficient [94]:

$$corr = \frac{N^2 \sum_i g_i^k g_i^{k-1} - \sum_i g_i^k \sum_i g_i^{k-1}}{[N^2 \sum_i (g_i^k)^2 - (\sum_i g_i^k)^2]^{1/2} [N^2 \sum_i (g_i^{k-1})^2 - (\sum_i g_i^{k-1})^2]^{1/2}}. \quad (2.10)$$

The previous work at JET [94] has shown that the best reconstruction can be obtained when this correlation coefficient reaches the maximum value, so the iteration (k) can be terminated at that point as well.

2.2.2 Comparison of inversion methods

In this section, several emissivity phantoms are used to test the three tomographic methods introduced in the previous section. The phantoms are analytically modeled as centrally peaked, ring and banana structures. In addition, an emissivity profile from a hard X-ray synthetic diagnostic, which is calculated from the Fokker-Planck modeled electron distribution function of ECCD plasma, is also implemented as a phantom, in order to test a more realistic emissivity pattern than the analytic ones.

Centrally peaked emissivity profile

A centrally peaked emissivity profile is the most common type of emissivity pattern observed in soft X-ray tomography, since the plasma pressure decreases monotonically from the core to the edge in general. In the case of hard X-ray emission, this centrally peaked pattern is expected to appear not only during on-axis ECRH, but also during off-axis ECRH, when suprathermal electron transport is sufficiently strong. This type of hard X-ray emissivity profile was reconstructed from TCV ECCD plasmas, using the MF method [90].

The centrally peaked emissivity profile is modeled as a Gaussian shape, $g(r) = \exp(-(r/\sigma_0)^2)$, where $r = [0, 1]$ and $\sigma_0 = 0.5$. This pattern in the circular grid is transformed into the elliptical shape, by stretching the pattern vertically and taking the ellipticity of the plasma equilibrium. The equilibrium used in the previous section (Figure 2.5 (a)) is used in this modeling as well.

The same spatial discretization (40×60) is used in this section as well. The full hard X-ray camera set is used. The number of terms in the series expansion in the CB method (m and l), the smoothing coefficient in the MF method (σ), and the iteration number in the ML method are chosen such as to give the lowest rms value and a reliable reconstruction image.

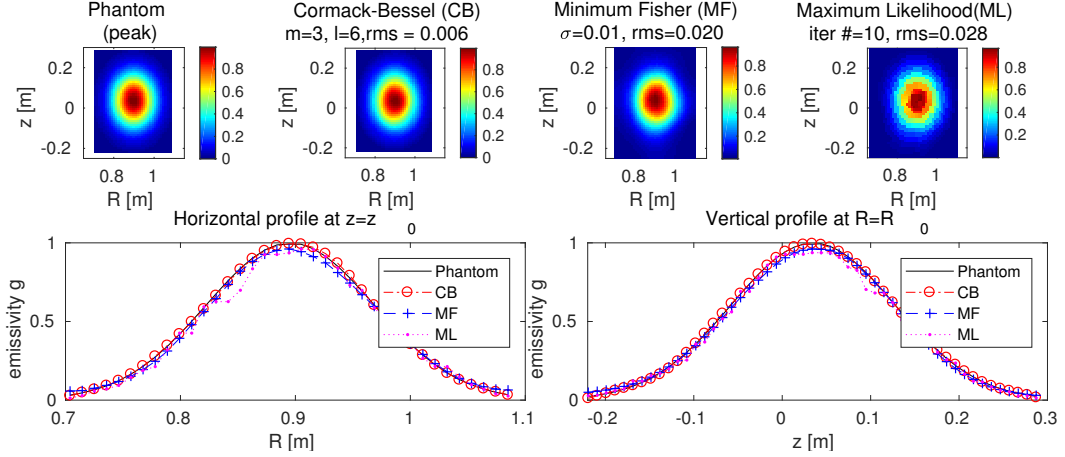


Figure 2.8 – (Top) Central peak emissivity phantom and reconstructed images using different inversion methods. (Bottom) Horizontal and vertical profiles of the phantom and the reconstructed images.

The modeled phantom emissivity is presented in Figure 2.8. The reconstructed images all show the centrally peaked emissivity shape, as can be seen in the horizontal and vertical profiles. The CB method gives the lowest rms error. The reconstructed image from the ML method shows a subtle deviation from the phantom near the center of the peak. This might be due to the size of the pixel and the sliding window for smoothing. An optimization scheme for these sizes is required in the future to enhance the quality of the inversion for the localized emission pattern.

Ring emissivity profile

A ring-shaped emissivity pattern has been observed in the soft X-ray tomography during sawtooth crashes [93]. It might also be possible to observe this in the hard X-ray emissivity profile if the central suprathermal electrons are expelled by the crash. This pattern is also expected to appear during off-axis ECCD, when the driven current is localized far from the magnetic axis and suprathermal electron transport is not strong enough to flatten the profile.

A ring shaped emissivity profile is modeled as a Gaussian shape, $g(r) = \exp(-(r - r_0/\sigma_0)^2)$, where $r = [0, 1]$, $r_0 = 0.4$ and $\sigma_0 = 0.1$. This pattern in the circular grid is transformed to the elliptical shape as was done in the centrally peaked profile case. The discretization method and the free parameter setting in each tomographic method are the same as those in the previous case.

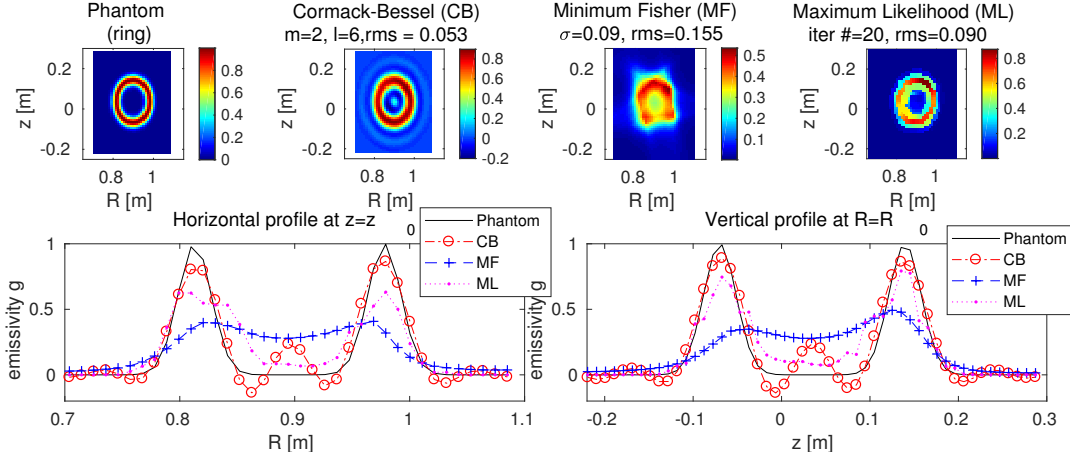


Figure 2.9 – (Top) Ring emissivity phantom and reconstructed images using different inversion methods. (Bottom) Horizontal and vertical profiles of the phantom and the reconstructed images.

The ring-shaped phantom is presented in Figure 2.9. The CB method and ML method reconstruct the ring shape with relatively low rms error. The ML method provides better reconstruction in the core where the emissivity is nearly zero, while the CB method finds a secondary peak near the magnetic axis due to the structure of the Bessel series. The image inverted by the MF method shows some discontinuity, but the ring shape is reconstructed. Increasing the smoothing parameter σ_e in the MF method gives a smoother image but the ring disappears.

Banana emissivity profile

In the hard X-ray tomography, the emissivity image is reconstructed on the poloidal plane. Due to the headlight effect of the bremsstrahlung radiation [58], this emission in the poloidal plane can be dominated by the contribution by trapped electrons, which can result in a banana-shaped emissivity on the low field side. On the other hand, since electrons moving on their own flux surface are slowed down on the high field side due to conservation of the magnetic moment which reduces the parallel energy [104], the hard X-ray emission may have a flipped banana shape.

A banana-shaped emissivity profile is modeled by starting from the ring shaped distribution, then multiplying it by a Gaussian poloidal-angle distribution: $g(r) = g_{ring} \times \exp(-((\theta - \pi)/\sigma_1)^2)$, where $\sigma_1 = 0.5$ rad. This pattern in the circular grid is transformed to the elliptical shape as before. The discretization method and the free parameter setting in each tomographic method are also the same as before.

The CB method and the ML method provide a reliable reconstruction image in Figure 2.10. However, the flat emissivity in the core is underestimated in the case of the CB method, due to the structure of the Bessel function. With the MF method, it is difficult to recognize the

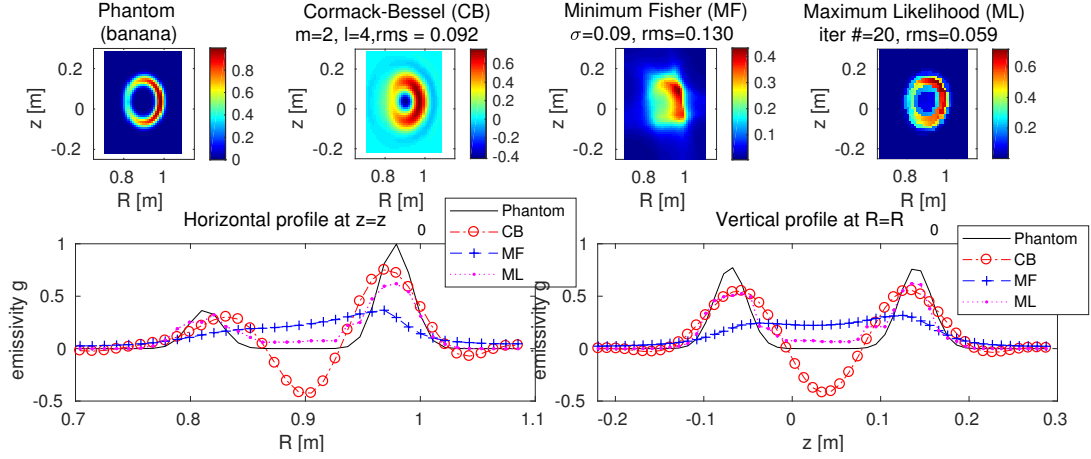


Figure 2.10 – (Top) Banana emissivity phantom and reconstructed images using different inversion methods. (Bottom) Horizontal and vertical profiles of the phantom and the reconstructed images.

original emissivity pattern of the phantom due to the smoothing problem. Therefore it is unlikely that the MF method can provide a reliable result in hard X-ray tomography, where non-centrally-peaked profiles are expected to appear.

The hard X-ray diagnostic system in TCV is equipped with a state-of-the-art digital processing system [28], so up to $\sim 6 \times 10^5$ photons can be counted per second [27]. This enables a study of suprathermal electron related instabilities, which is also a part of this thesis. If suprathermal electrons experience an instability with the $m/n = 1/1$ structure (m and n are the poloidal and toroidal mode numbers, respectively), then the hard X-ray emissivity pattern can possibly have a banana-like structure. In that case, due to the toroidal mode structure, only the lines of sight that lie in the same toroidal location should be considered for the tomographic inversion.

TCV HXRS has two sets of cameras which are toroidally separated. Thus when the frequency varying mode structure is considered, only two cameras at each set can be used for the tomography. In Figure 2.11, the banana-shaped phantom introduced in Figure 2.10 is used again, but only two cameras (camera number #4 and #5) are considered, instead of the full set of four cameras. In this case, the quality of the tomographic inversion results by the CB and MF methods is low, so it is impossible to recognize the shape of the phantom, whereas the ML method still provides a faithful inverted image. It appears therefore that the ML method might provide a reliable solution in particular when limited diagnostic information is available.

Ring and central peak emissivity profile

The ring emissivity phantom is added to the central peak phantom in Figure 2.12, with $r_0 = 0.5$ and $\sigma_0 = 0.1$. This emissivity pattern might appear in a plasma when both on- and off- axis ECCD are added and the suprathermal transport is negligible. As shown in the ring and the

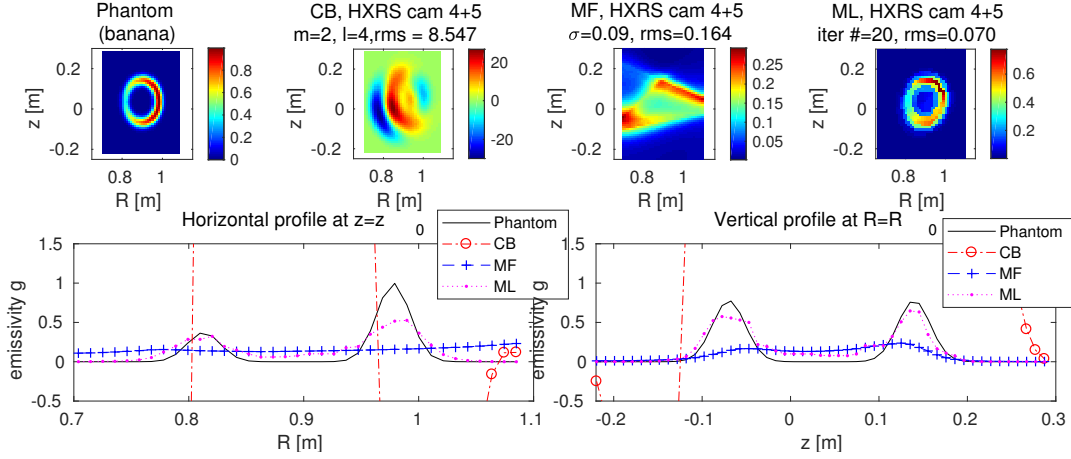


Figure 2.11 – (Top) Banana emissivity phantom and reconstructed images using different inversion methods, using only two hard X-ray cameras (camera #4 and #5). (Bottom) Horizontal and vertical profiles of the phantom and the reconstructed images.

peak phantoms separately, the CB method and the ML method can invert the phantom image well, while the inversion using the MF method does not provide a satisfactory result.

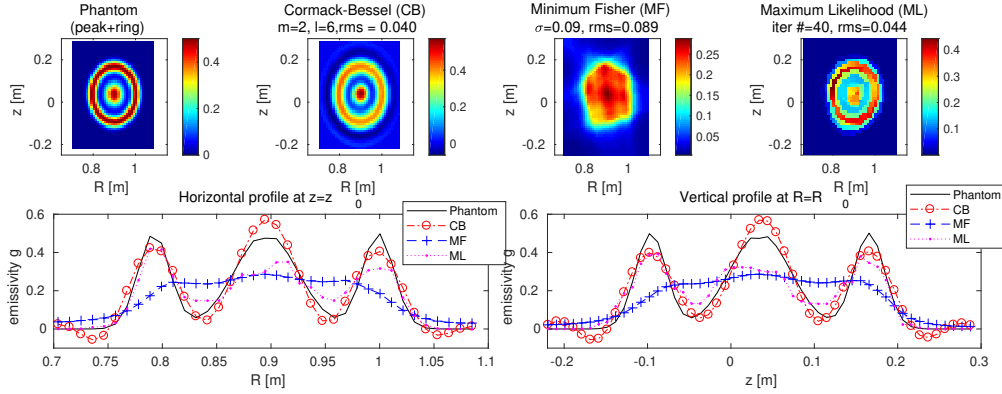


Figure 2.12 – (Top) Ring and peak emissivity phantom and reconstructed images using different inversion methods. (Bottom) Horizontal and vertical profiles of the phantom and the reconstructed images.

Off-axis ECCD synthetic diagnostic emissivity

In order to obtain a realistic hard X-ray emission pattern, a hard X-ray synthetic diagnostic result is used, which is calculated from a plasma with Fokker-Planck modeling of off-axis ECCD. In TCV discharge 49513 (Figure 2.13), EC rays from four launchers are localized near $\rho_{\psi_p} \sim 0.6$ (ρ_{ψ_p} is the square root of the normalized poloidal flux). In the Fokker-Planck modeling using LUKE, the suprathermal transport term is set to zero to simulate a highly localized hard X-ray emission.

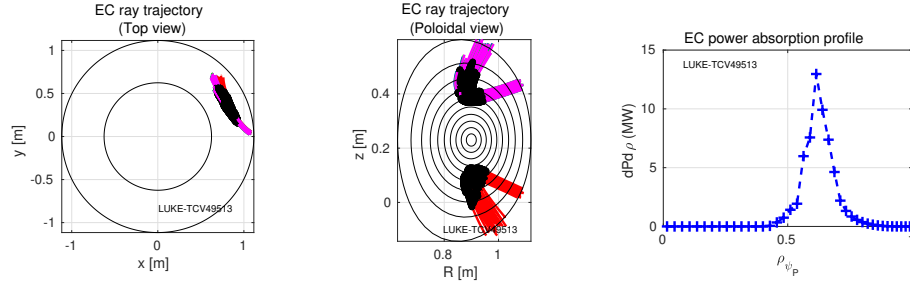


Figure 2.13 – (Left) Top view of the EC ray trajectory (Middle) Poloidal view of the EC ray trajectory (Right) EC power absorption profile

The hard X-ray emissivity phantom from the synthetic diagnostic (Figure 2.14) shows that the emissivity has a ring shape, with an enhanced emissivity on the high field side due to conservation of the magnetic momentum. This phantom is well reconstructed with the CB and ML methods, as observed in the ring and the banana shaped emissivity phantom cases. In the case of the CB method, low-level fluctuations in the horizontal and vertical profiles are observed near the magnetic axis, due to the structure of the Bessel function. The MF method shows that the emissivity is stronger on the high field side, but the continuous emission pattern cannot be reconstructed. When the smoothing parameter σ_e is increased to obtain a smoother image, the ring-shape cannot be reconstructed anymore.

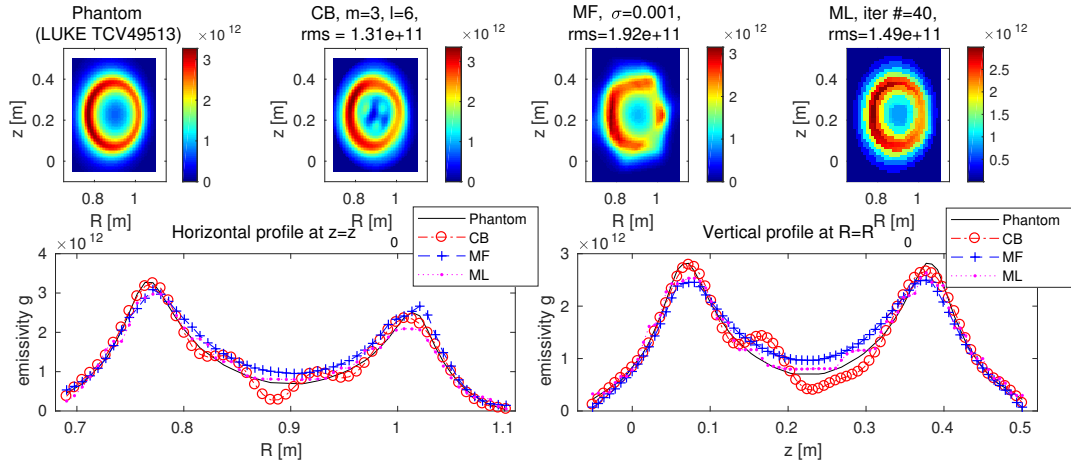


Figure 2.14 – (Top) Emissivity phantom obtained from the LUKE-FEB synthetic diagnostic and reconstructed images using different inversion methods. (Bottom) Horizontal and vertical profiles of the phantom and the reconstructed images.

2.2.3 Conclusions

In this section, two new tomographic inversion methods have been introduced for the TCV hard X-ray diagnostic. The TCV hard X-ray system consists of four cameras with 24 detectors

each, which are considerably fewer than those of the routinely used soft X-ray tomographic system (XTOMO). In addition, the hard X-ray emissivity pattern can be different from the typical centrally peaked profile. Thus various emissivity phantoms have been introduced in this section, to assess the quality of inversion using different tomographic methods.

It is shown that the minimum Fisher regularization method (MF method), which is used as a default inversion method in TCV diagnostics, cannot provide a reliable image reconstruction, except with the centrally peaked emissivity pattern. This is due to the limitations of the MF method, which is basically a smoothing scheme. This limitation may be compensated by introducing an anisotropic smoothing matrix H , as studied in the JET soft X-ray system [105]. The anisotropic smoothing parameter considers that the emissivity gradient is smooth along each flux surface but steep across flux surfaces. In JET, this model gave a reliable emissivity reconstruction compared to the isotropic smoothing matrix model that is currently used in the TCV tomography.

The newly implemented tomographic inversion methods, the Cormack-Bessel method (CB method) and the maximum Likelihood method (ML method), have reconstructed various types of the emissivity phantoms in this section. In particular, the ML method shows that a reliable image reconstruction is possible even when the number of lines of sight is limited (two instead of four cameras).

The CB method can reconstruct a given phantom with low rms error; however, this method is inherently limited to elliptically structured plasmas. Therefore for plasmas with high triangularity, the quality of the inversion might be limited. A further study is needed to assess the limit of the CB method with various emissivity patterns. Adding virtual lines of sight, which is already included in the ML method scheme, can be implemented in this scheme as well. Also a further investigation is required to determine an optimal number of Bessel series expansion terms.

The emissivity phantoms considered in this section are all noise-free, which is not the case in the real experimental data set. A further study that considers experimental noise is desirable, either by adding artificial noise to the analytically modeled phantoms or by considering experimentally measured data.

2.3 Modeling of response function for HXRS

As discussed in the previous chapter, the hard X-ray synthetic diagnostic code [57] estimates the hard X-ray count rates from the Fokker-Planck calculation result, using the response function of the detector. However, the response function currently used in the synthetic diagnostic package [57], which includes only the photopeak and the Compton continuum, which is distant from the photopeak, deviates from the real response of the CdTe detector. The apparent energy spectrum produced by gamma-ray sources observed during detector calibration consists of a photopeak and a long shelf structure below the photopeak due to incomplete charge collection, which is a well-known feature of semiconductor detectors [106–109]. Since the response function depends on each detector's specific characteristics such as structure, geometry, and composition, it appears necessary to put forward a model for the response function.

In this work, a response function model is presented for the CdTe detectors employed in the HXRS apparatus in the TCV tokamak, based on the measurement of the energy spectra from five radioactive sources. Section 2.3.1 overviews the measurement setup and the spectroscopic features of the measured energy spectra. Section 2.3.2 describes the response function model and its coefficients, which are empirically determined from the measurement. Section 2.3.3 demonstrates the ability of the modeled response function to correctly reproduce the measured energy spectra, which is superior to the one which is currently implemented in the synthetic diagnostic module.

2.3.1 Measurement of radioactive sources

Measurement setup

In order to analyze the response of the detector to monochromatic photons with varying energy, five energy spectra are measured using four radioactive isotopes, ^{241}Am , ^{109}Cd , ^{139}Ce , and ^{152}Eu , and a multi-isotope source, which is a liquid mixture of ^{133}Ba , ^{60}Co , and ^{137}Cs . The main gamma-ray and fluorescent X-ray energies of the sources are listed in Table 2.1 with their activities at the measurement date [110].

During the measurement, each source is placed at 1 cm distance in front of a specific detector of one of the HXRS cameras, and the camera is shielded by lead. The detector is a 2 mm \times 2 mm \times 2 mm Ohmic-type CdTe (S.2.2.2U) sensor, produced by Eurorad. The detector is connected to an in-house developed preamplifier card which is included in the camera set. The signal from the camera is processed through an Ortec 571 shaper/amplifier and then sent to Fast ComTec MCA-3, a PC-based, software controlled PCI-bus Multichannel Analyzer (MCA). 8129 channels are used and the threshold voltage is set to 0.4 V. Figure 2.15 shows a mapping from MCA channels to photon energies, by fitting the gamma-ray photopeaks of the measured spectra.

Radioactive source	Activity (kBq)	Gamma-rays (keV)	X-rays (keV)
Cerium-139	33.3	165.9	33.4, 33.0
Cadmium-109	12.7	88.0	22.2, 22.0
Europium-152	22.3	121.8, 244.7, 344.3, 778.9	40.1, 39.5
Americium-241	35.8	59.5	-
Multi-isotope source			
Barium-133	45.6	81.0, 276.4, 302.9, 356.0	31.0, 30.6
Cobalt-60	39.5	1332.5, 1173.2	-
Caesium-137	67.7	661.7	-

Table 2.1 – Main gamma-ray and fluorescent X-ray energies of the radioactive sources.

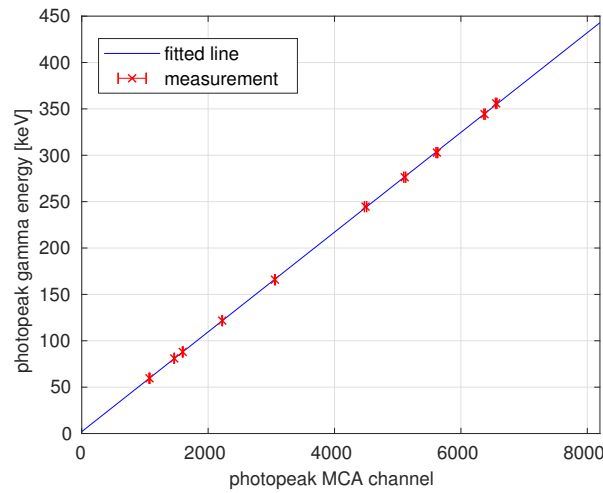


Figure 2.15 – MCA channel - photon energy mapping.

Spectroscopic features

When a monochromatic photon beam with energy k impinges on the CdTe detector, the energy spectrum (counts per energy bin) is observed to have three distinct features: an asymmetric Gaussian photopeak near k , an exponentially inclined shelf structure below k , and escape peaks due to the CdTe material.

As an example, these characteristics can be seen in Figure 2.16, the measured energy spectrum from ^{139}Ce . Firstly, the photopeak deviates from a Gaussian fit at energies less than the gamma-ray energy, 165.9 keV, due to hole tailing that arises from charge trapping events, while the Gaussian curve fits the spectrum well for energies above 165.9 keV. Below the photopeak, an inclined shelf, which is attributed to incomplete charge collection or the interactions between the metal contact and the detector [11], is observed, which can be fitted by an exponential. The CdTe escape peaks are theoretically expected to appear at 142.7 keV and 139.8 keV, which correspond to the differences between the gamma-ray energy and the K_α line emission energies of Cd and Te, 23.2 keV and 26.1 keV. However, these peaks are observed to

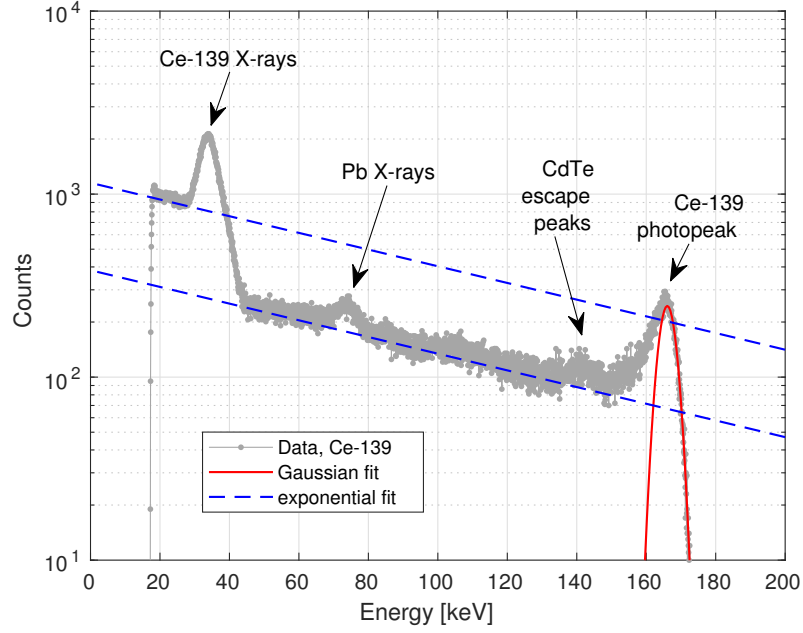


Figure 2.16 – Measured energy spectrum from ^{139}Ce .

have a single broad peak due to their broad Gaussian shapes and the finite detector resolution.

In addition to the spectrum from the monochromatic gamma-ray, the fluorescent X-rays from ^{139}Ce also contribute to the total spectrum. Since the fluorescent X-ray peaks are closely spaced, a broad aggregate peak is observed around 30 keV. An additional inclined shelf structure is formed below the broad peak near 30 keV. Lastly, there is a contribution from the fluorescent X-rays from the lead shielding near 75 keV, which also combine to form a single peak.

2.3.2 Modeling the response function

On the basis of the observed characteristics of the CdTe detector discussed in the previous section, the response function is modeled in this section, based on previous work on the modeling of semiconductor detector response [8-11]. In the case of a photon beam spectrum $\phi(k)$ impinging on the detector, the measured energy spectrum $M(E)$ can be expressed as

$$M(E) = \int_0^\infty \phi(k) \eta(k) G(k, E) dk \quad (2.11)$$

where $\eta(k)$ is the detector efficiency and $G(k, E)$ is the detector's response function. For a monochromatic photon beam with energy k , $G(k, E)$ can be considered as a scaled energy spectrum,

$$M(E) = c_k G(k, E), \quad (2.12)$$

where c_k is a scaling factor. Therefore, the response function can be modeled based on the energy spectra of radioactive sources that emit photons at discrete energy levels.

$G(k, E)$ is modeled using four sub-functions,

$$G(k, E) = G_1(k, E) + G_2(k, E) + G_3(k, E) + G_4(k, E) \quad (2.13)$$

where $G_1(k, E)$ is a Gaussian photopeak, $G_2(k, E)$ describes a broadening of the photopeak below k which contributes to the asymmetry of the photopeak, $G_3(k, E)$ is an inclined shelf structure below the photopeak, and $G_4(k, E)$ describes the CdTe escape peaks. Each function is modeled using empirically determined parameters, such as

$$G_1(k, E) = a_1 \exp\left(-\frac{(E - k)^2}{3.63^2}\right) \quad (2.14)$$

$$G_2(k, E) = 0.29a_1 \exp\left(\frac{E - k}{8.00}\right) \operatorname{erfc}\left(\frac{E - k}{3.63\sqrt{2}}\right) \quad (2.15)$$

$$G_3(k, E) = \frac{a_3(k)}{2} \exp\left(-\frac{E}{95.24}\right) \operatorname{erfc}\left(\frac{E - k}{3.63\sqrt{2}}\right) \quad (2.16)$$

$$G_4(k, E) = 0.06a_1 \left(\exp\left(-\frac{(E - E_{Cd, K_\alpha})^2}{3.63^2}\right) + \exp\left(-\frac{(E - E_{Te, K_\alpha})^2}{3.63^2}\right) \right) \quad (2.17)$$

where erfc is the complementary error function, defined as $\operatorname{erfc}(x) = 1 - \operatorname{erf}(x)$. E_{Cd, K_α} and E_{Te, K_α} are the CdTe escape peak energies: $E_{Cd, K_\alpha} = k - 23.2$ keV and $E_{Te, K_\alpha} = k - 26.1$ keV.

In Eq.(2.16), $a_3(k)$ determines the height of the inclined shelf structure. In the measured spectra, it is observed that this parameter depends on k , as plotted in Figure 2.17. This parameter is modeled by fitting the measured value as

$$a_3(k) = \begin{cases} 0.43a_1 & \text{if } k < 56.14 \\ a_1 (2.01e^{k/196.93} - 2.25) & \text{if } 56.14 \leq k < 315.20 \\ a_1 (1.30 \cdot 10^{-8} e^{k/17.39} + 6.74) & \text{if } k \geq 315.20 \end{cases} \quad (2.18)$$

The height of the Gaussian peak $G_1(k, E)$, a_1 , can be calculated by imposing the normalization condition

$$\int_0^\infty G(k, E) dE = 1. \quad (2.19)$$

An example of the modeled response function for $k = 80$ keV is plotted in Figure 2.18.

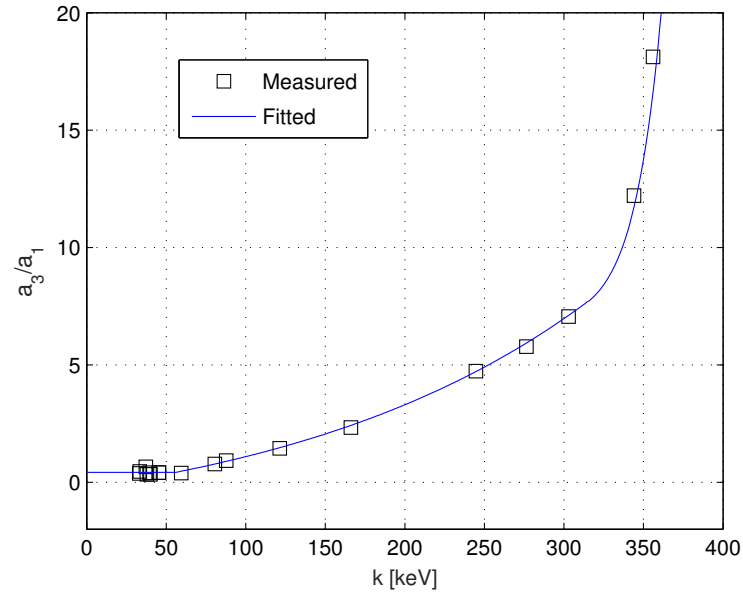


Figure 2.17 – (Squares) the ratio of a_3 to a_1 determined by fitting the measured spectra. (Line) the fitted line described in Eq.(2.18).

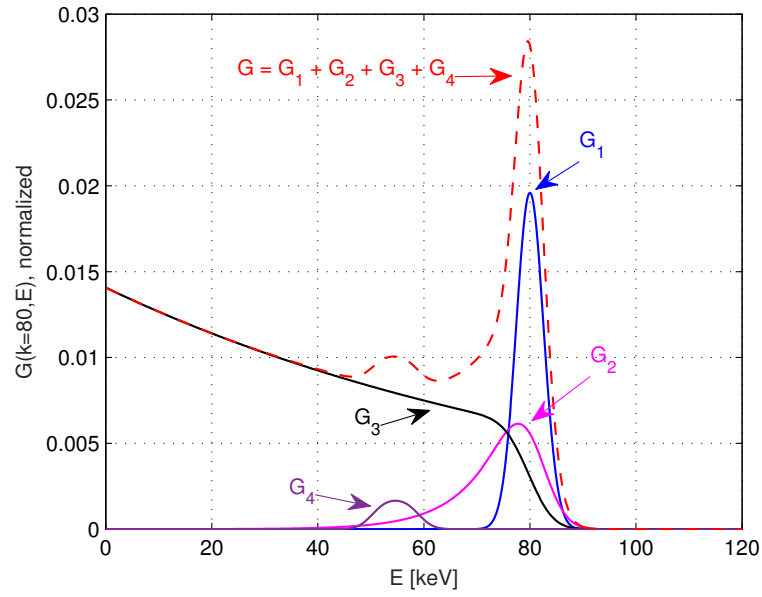


Figure 2.18 – Response function model for $k = 80$ keV, $G(k = 80, E)$.

2.3.3 Reconstruction of measured spectra

In order to demonstrate that the response function modeled in the last section correctly describes the response of the detector, the energy spectra measured in Section 2 are reconstructed. For a radioactive source emitting photons with discrete energy levels, the measured energy spectrum can be reconstructed by adding Eq.(2.12) over all relevant energy photon beams,

$$M(E) = \sum_{i=1}^N c_i G(k_i, E) \quad (2.20)$$

where $M(E)$ is the reconstructed spectrum, c_i is a scaling factor for the photon beam with energy k_i and N is the number of discrete energy levels.

Figure 2.19 presents the reconstruction of the measured spectra using the response function from the R5-X2 synthetic diagnostic module (old, simplified model) [57] and the one modeled in the previous section (new model). Only energy spectra with a single gamma-ray photopeak at k_γ are considered; thus the reconstruction is done by multiplying a single scaling constant by the response function, $M(E) = c_\gamma G(k_\gamma, E)$. Whereas the new model fits well the measured spectra of ^{241}Am , ^{109}Cd , and ^{139}Ce , the old model cannot reproduce the continuous spectrum below the photopeak since it includes only the photopeak and the spectrum below the Compton edge, which is distant from the photopeak.

The energy spectra and the reconstruction of the radioactive sources which have several gamma-ray photopeaks, ^{152}Eu and the multi-isotope source, are plotted in Figure 2.20. The spectra of these sources can be reconstructed as

$$\begin{aligned} M_{tot}(E) &= \sum_{i=1}^{N_\gamma} M_{\gamma i} + M_0 + M_{pb} \\ &= \sum_{i=1}^{N_\gamma} c_{\gamma i} G(k_{\gamma i}, E) + M_0 + c_{pb} G(k_{pb}, E) \end{aligned} \quad (2.21)$$

where $M_{tot}(E)$ is a reconstructed spectrum and M_0 is a flat offset count given by gamma-rays with energies above the measurement limit. M_0 is 4.65 for ^{152}Eu and 7.56 for the multi-isotope source. M_{pb} describes the fluorescent X-rays emitted from the lead shielding at $k_{pb}=75.0$. c_{pb} is $1.37 \cdot 10^3$ for ^{152}Eu and $2.46 \cdot 10^3$ for the multi-isotope source. ^{152}Eu has three significant gamma-ray lines within the measurement limit, thus N_γ is 3 for ^{152}Eu and $k_{\gamma 1}$ is 122.8 with $c_{\gamma 1}=2.05 \cdot 10^4$, $k_{\gamma 2}$ is 244.7 with $c_{\gamma 2}=3.82 \cdot 10^3$, and $k_{\gamma 3}$ is 344.3 with $c_{\gamma 3}=8.47 \cdot 10^3$. The multi-isotope source has four significant gamma-ray lines within the measurement limit, all from ^{133}Ba , thus N_γ is 4 for the multi-isotope source and $k_{\gamma 1}$ is 81.0 with $c_{\gamma 1}=2.36 \cdot 10^4$, $k_{\gamma 2}$ is 276.4 with $c_{\gamma 2}=2.95 \cdot 10^3$, $k_{\gamma 3}$ is 302.9 with $c_{\gamma 3}=5.34 \cdot 10^3$, and $k_{\gamma 4}$ is 356.0 with $c_{\gamma 4}=1.61 \cdot 10^4$.

In figure 2.21, the full spectrum of ^{139}Ce is reconstructed as M_{tot} , including the fluorescent

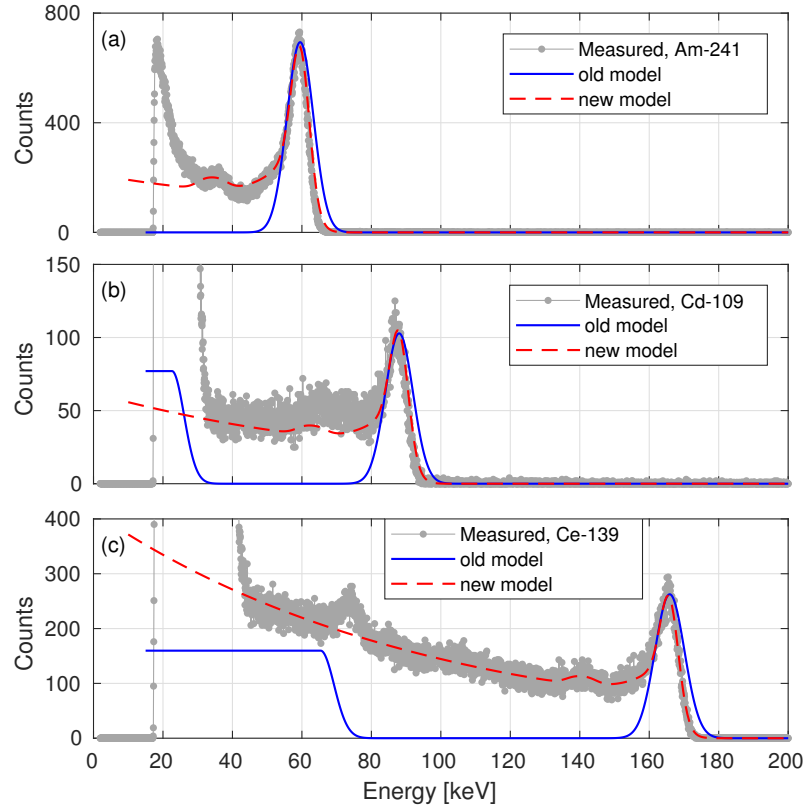


Figure 2.19 – Measured energy spectrum (dot-line) and reconstruction using the default response function from R5-X2 (old model) and the one modeled in this work (new model), for (a) ^{241}Am ($k_\gamma=59.9$, $c_\gamma=1.53 \cdot 10^4$), (b) ^{109}Cd ($k_\gamma=88.0$, $c_\gamma=4.43 \cdot 10^3$), (c) ^{139}Ce ($k_\gamma=159.9$, $c_\gamma=3.45 \cdot 10^4$). Fluorescent X-rays from the lead shielding appear near 75 keV.

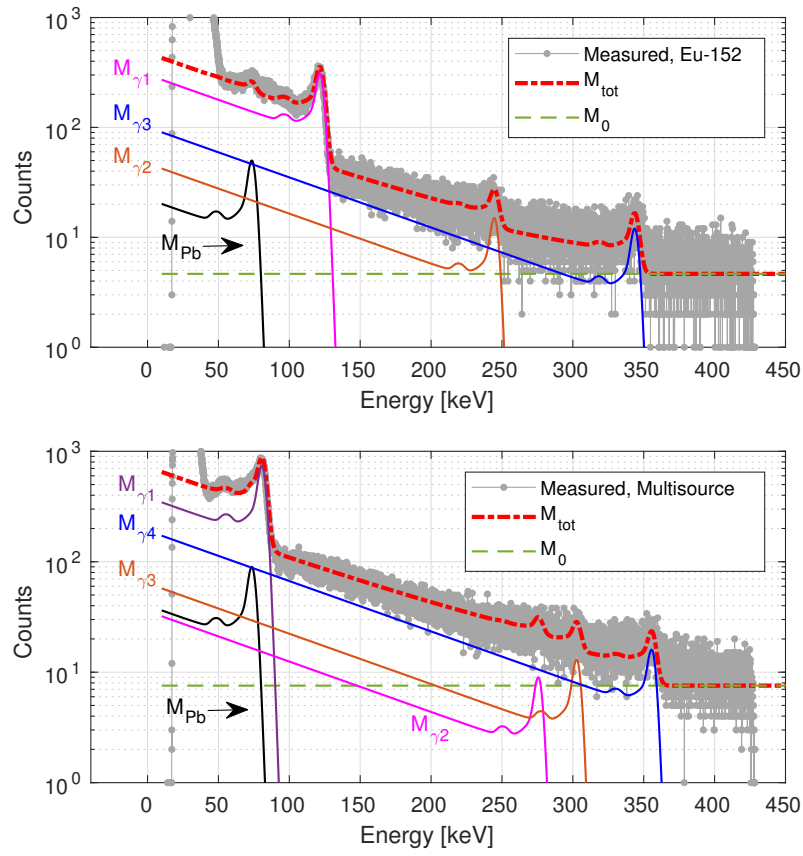
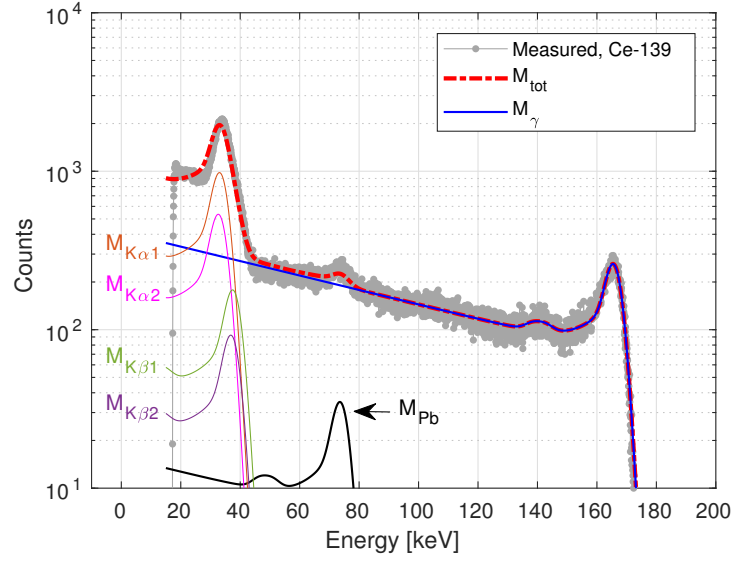


Figure 2.20 – Reconstruction of the energy spectrum of (a) ^{152}Eu and (b) multi-isotope source.


 Figure 2.21 – Reconstruction of the energy spectrum of ^{139}Ce .

X-rays from ^{139}Ce and the lead shielding,

$$\begin{aligned}
 M_{tot}(E) &= M_{\gamma} + M_{K\alpha1} + M_{K\alpha2} + M_{K\beta1} + M_{K\beta2} + M_{Pb} \\
 &= c_{\gamma}G(k_{\gamma}, E) + c_{K\alpha1}G(k_{K\alpha1}, E) + c_{K\alpha2}G(k_{K\alpha2}, E) \\
 &\quad + c_{K\beta1}G(k_{K\beta1}, E) + c_{K\beta2}G(k_{K\beta2}, E) + c_{Pb}G(k_{Pb}, E),
 \end{aligned} \tag{2.22}$$

where k_{γ} is 165.9 with $c_{\gamma}=2.88 \cdot 10^4$, $k_{K\alpha1}$ is 33.4 with $c_{K\alpha1}=1.16 \cdot 10^4$, $k_{K\alpha2}$ is 33.0, $k_{K\beta1}$ is 37.2, and $k_{K\beta2}$ is 37.8. Since the K line emissions of ^{139}Ce are closely spaced and interfere each other, the coefficients of $M_{K\alpha2}$, $M_{K\beta1}$, and $M_{K\beta2}$ are determined using the relative probabilities of these lines to $K\alpha1$ line from the reference [110]: $c_{K\alpha2}/c_{K\alpha1} = 0.55$, $c_{K\beta1}/c_{K\alpha1} = 0.18$, and $c_{K\beta2}/c_{K\alpha1} = 0.09$. k_{Pb} is 75.0 with $c_{Pb}=960.34$.

2.3.4 Conclusions

A realistic response function is modeled for the CdTe detectors used in the HXRS apparatus of the TCV tokamak. The energy spectra of five radioactive sources, ^{241}Am , ^{109}Cd , ^{139}Ce , and ^{152}Eu , and a multi-isotope source, a liquid mixture of ^{133}Ba , ^{60}Co , and ^{137}Cs , are measured and analyzed. The characteristics of the detector observed in the measurement are considered in the response function modeling. The response function consists of four sub-functions: a Gaussian photopeak, an exponential decay at the energies below the photopeak, an inclined shelf structure which is exponentially increasing towards the low energy side, and the escape peaks by the CdTe material. The coefficients of the function are empirically determined based on the measured spectra.

Chapter 2. Hard X-ray tomographic spectrometer system (HXRS) in TCV

In order to demonstrate the ability of the response function to correctly reproduce the response of the detector to photons, the response function is used to reconstruct the measured energy spectra. The reconstructed spectra using the new function fit well the measured spectra, while the default response function model in the synthetic diagnostic module cannot reproduce the continuous shelf structure below the photopeak. Also, the energy spectra which consist of several gamma-rays or fluorescent X-rays are also correctly reconstructed.

This new model has now been implemented in the synthetic diagnostic module and assists the analysis of the hard X-ray measurements in the TCV tokamak for the study of high-energy electron physics.

3 Suprathermal electron dynamics during ECCD

3.1 Introduction

As introduced in chapter 1.2.1, the suprathermal electron dynamics, in particular their response to ECCD, is studied in this chapter. The ECCD experiment has been conducted on the TCV tokamak [14] using second harmonic X-mode (X2) EC waves from a 750 kW source. A state-of-the-art hard X-ray spectrometer [27], equipped with high-resolution digital pulse acquisition and processing [28], has allowed studying the evolution of the hard X-ray profiles with arbitrary energy and time binning. The experimental results are presented in section 3.2.

In order to describe the time-evolving hard X-ray profiles, a time-varying Fokker-Planck simulation has been conducted using the 3-D bounce-averaged relativistic code LUKE [77, 86], coupled with the hard X-ray synthetic diagnostic module R5-X2 [57]. A key advantage of the time-varying version of the code is that it permits modeling non-steady-state scenarios such as modulation experiments. This in turn makes it possible to probe the plasma response whilst minimizing the steady-state perturbation. In the Fokker-Planck simulation, the suprathermal electron transport has been adjusted not only in the radial space but also in the momentum space, based on the time-evolving RF quasilinear diffusion coefficient. This has made it possible to assess various diffusion models by comparing the radial profile and energy spectrum of the hard X-ray measurement over time. The simulation results are presented and discussed in section 3.3. Conclusions can be found in section 3.4.

3.2 Hard X-ray measurements during ECCD discharges

3.2.1 Experimental setup

In the present work, two ECCD discharges are analyzed: on-axis ECCD in section 3.2.2 and off-axis ECCD in section 3.2.3. All other experimental conditions were identical but the poloidal injection angle was changed slightly to move the EC wave deposition position. The EC wave trajectories and absorption locations are presented in Figure 3.1. The toroidal injection angle

was in the direction such as to drive counter-ECCD. Indeed, an equivalent co-ECCD case was found to exhibit sawtooth oscillations (Figures 3.2 and 3.3), which compete with the imposed EC modulation and hamper its analysis.

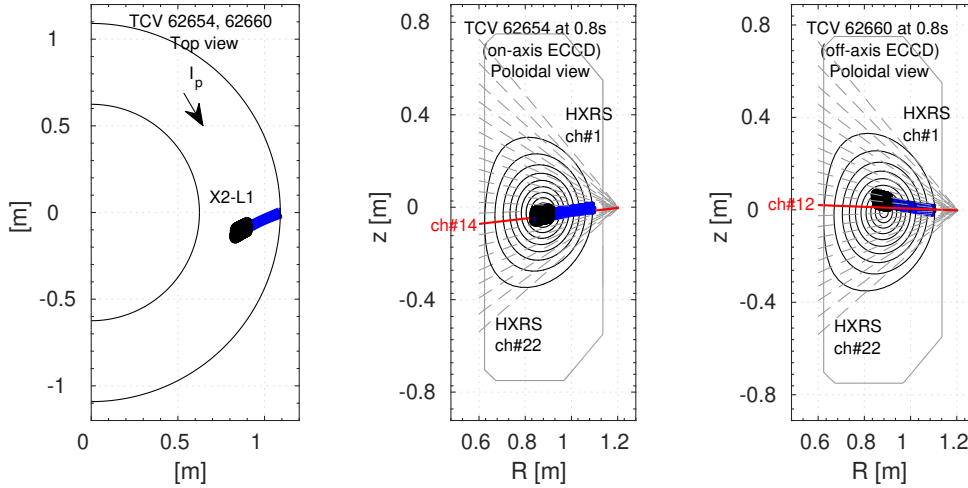


Figure 3.1 – Top view (left) and poloidal views of the on-axis ECCD (mid) and off-axis ECCD (right) cases. EC rays are shown in blue lines and their 99.9% absorption region in thick black lines. Hard X-ray lines of sight are shown in dashed lines.

An EC wave modulation technique was used to enhance the hard X-ray data statistics by means of conditional averaging, while keeping the perturbation to the plasma bulk properties to a minimum. During each square modulation cycle of 11 ms, the EC power was ramped-up for 1 ms and kept at 750 kW for 2 ms, followed by a ramp-down of 1 ms and a 7-ms low-power

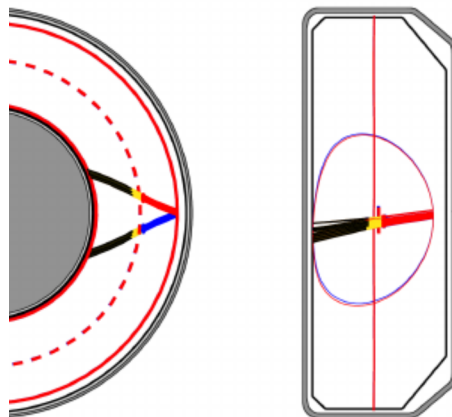


Figure 3.2 – Top view and poloidal view of TCV with ray tracing results. Red and blue rays correspond to co- and counter- ECCD.

3.2. Hard X-ray measurements during ECCD discharges

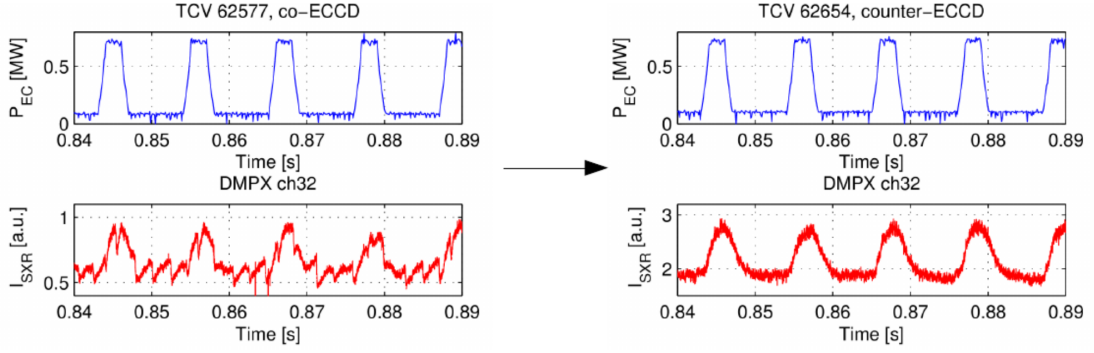


Figure 3.3 – The EC wave power and central soft X-ray signal. (Left) sawtooth oscillation synchronized with co-ECCD pulses, (right) sawtooth-free soft X-ray signal with counter-ECCD pulses.

phase at 100 kW (Figures 3.4 and 3.5). The gyrotron's characteristics preclude returning the power to zero after each high-power pulse.

The flat-top duration of 2 ms was determined empirically to allow sufficient photon statistics to observe the evolution of the hard X-ray profiles without perturbing the plasma significantly. If the EC pulse is shorter than the current diffusion time, a back electromotive force (EMF) can compensate the current change induced by ECCD [111, 112], so that the perturbation on the plasma equilibrium can be neglected. This plasma reaction time can be estimated using the resistive time $\tau_\rho = (\Delta\rho)^2 \tau_R$ where $\tau_R = a^2 \mu_0 \sigma$, σ is the electrical conductivity and $\Delta\rho$ is the current source's normalized width [111]. In this TCV discharge, $\tau_\rho \sim 11.4$ ms with $\Delta\rho \sim 0.1$. This is about 5 times longer than the pulse length of 2 ms, thus no significant change of the current profile is expected during the ECCD period.

The EC modulation period of 11 ms was set to be long enough for the relaxation of the suprathermal electron after turning off the EC power, and short enough to guarantee a sufficiently large number of EC cycles for the conditional averaging. In both the on-axis and off-axis ECCD discharges, 49 pulses were used for the conditional averaging of the hard X-ray data. The hard X-ray profile on the poloidal plane was measured using the equatorial hard X-ray camera with 22 lines of sight (dashed lines in Figure 3.1).¹ After the digital pulse processing of the collected data, the detected hard X-ray photons were sorted into time bins of 0.4 ms and energy bins of 10 keV.

The plasma parameters used in this work are: plasma current $|Ip| \sim 0.1$ MA, toroidal magnetic field $|B_\phi| \sim 1.4$ T, central electron density $n_e \sim 2.0 \times 10^{19}/m^3$ and effective charge $Z_{eff} \sim 1.2$. The electron temperature was modulated by the ECCD pulses from ~ 2 keV to ~ 3.5 keV in the on-axis ECCD case and from ~ 1.5 keV to ~ 2.1 keV in the off-axis ECCD case.

¹This experiment was repeated with the hard X-ray camera in the horizontal orientation, for a preliminary study of the effect of loop voltage on ECCD, and the results are presented in Appendix B.

3.2.2 On-axis ECCD

In the on-axis ECCD case, the EC beam absorption area was localized on-axis, according to the ray-tracing calculation using C3PO [86] (Figure 3.1). Figure 3.4 shows a modulation of the central electron temperature (T_e), obtained from a soft X-ray measurement based on the absorber foil technique. The hard X-ray emission (I_{HXR}) is modulated as well with ECCD. The time evolution of the line-integrated hard X-ray emission is analyzed in real space and energy space in the next section 2.2.1, and the local emissivity is obtained using the Abel-inversion technique in section 2.2.2.

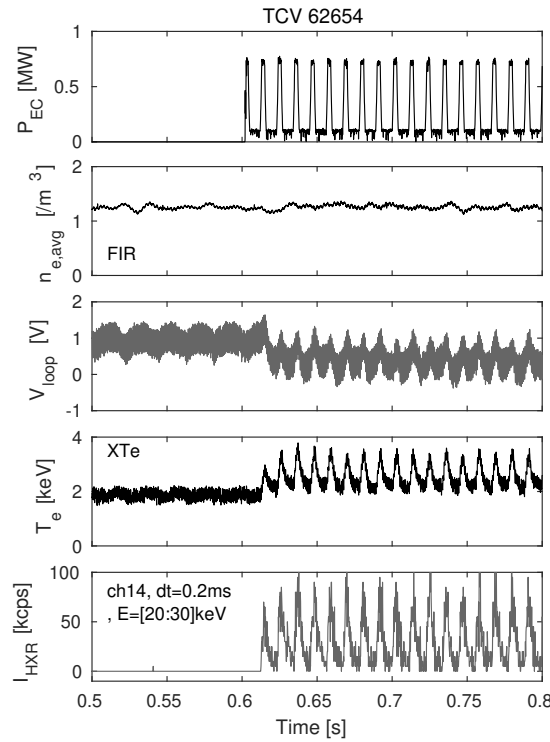


Figure 3.4 – Time traces of EC wave power, line-averaged electron density, loop voltage, central electron temperature from soft X-ray signals, hard X-ray count rate of channel 14.

No sawtooth activity was observed; however, a centrally localized frequency-chirping oscillation was found (Figure 3.5). The oscillation is localized near the magnetic axis and appears only during the EC ramp-down phase. The poloidally and toroidally distributed soft X-ray array is used to analyze the mode's spatial structure, which is characterized by $m = 1$ and $n = 1$, where m and n are the poloidal and toroidal mode numbers, respectively.² As the current profile is modified by both the ECCD and, indirectly, by the Ohmic current change

²A detailed analysis of determining the mode structure and the rotation direction are presented in Appendix A.

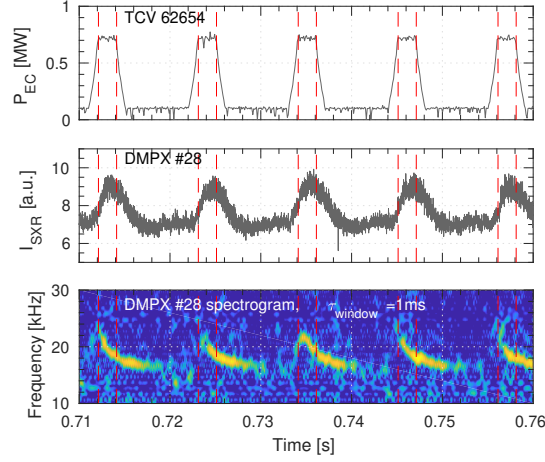


Figure 3.5 – Time trace of EC power, central soft X-ray emission, and a Fourier spectrogram of the latter.

induced by the temperature variation (as witnessed by the loop voltage swing, Fig. 2), it may be speculated that the conditions for destabilizing the internal kink mode are met transiently. This frequency-chirping mode may be an electron fishbone, which is destabilized by the energetic electrons [113]. This may induce a loss of suprathermal electrons and affect the hard X-ray measurement. The nature of this mode activity related to energetic electrons will be investigated further in the future.

Conditional averaging of hard X-ray data

In order to enhance the statistics of the hard X-ray data, the count rates sorted into the time and energy bins are conditionally averaged over ECCD pulses as presented in Figure 3.6. For the time trace of the central electron temperature (T_{e0}), each Thomson scattering measurement point is mapped into the modulation cycle. The electron temperature increases and decreases in response to the change of the EC power.

The response of I_{HXR} (hard X-ray photon count rate) to ECCD varies as a function of location and energy. Firstly the reaction of the outer channel (ch16) is slower than the central channel (ch14): for the first 1 ms during the ramp-up, only the central channel count rate increases significantly ($E=[20:30]$ keV). This can be also seen in the time evolution of the hard X-ray emission profiles in Figure 3.7. For a quantitative comparison, the ratio of the central to the outer count rate is plotted versus time in Figure 3.8. At the start of the ECCD pulse, the ratio increases as the I_{HXR} profile forms a narrow peak. Then the ratio drops as the EC power increases, and the broader shape is kept until the end of the modulation cycle. This suggests a radial diffusion of suprathermal electrons, which will be further studied in the following

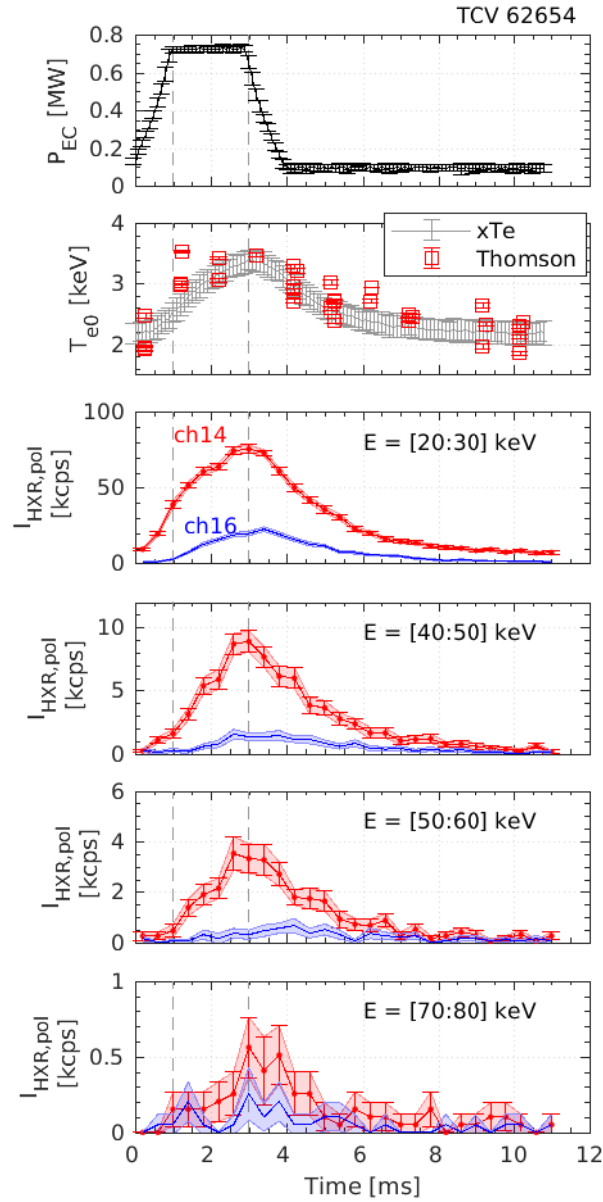


Figure 3.6 – Time trace of EC power, electron temperature and hard X-ray emission (I_{HXR}) on two chords from different energy bins denoted by E, averaged over EC modulation cycles.

section through an Abel-inversion.

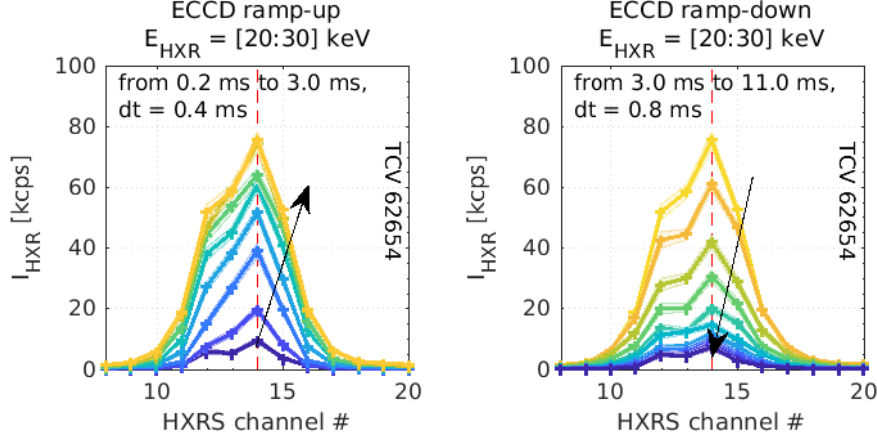


Figure 3.7 – Time evolution of the line-integrated profile of I_{HXR} .

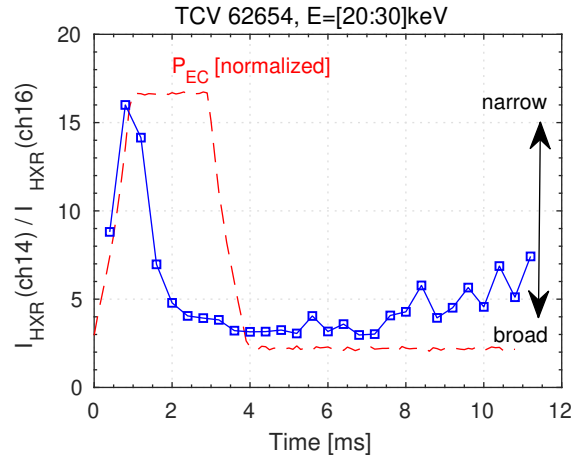


Figure 3.8 – Blue squares: the ratio of ch14 to ch16 count rate. Red dashed line: EC power time trace (arbitrary units).

For a fixed hard X-ray channel, the I_{HXR} response varies in different energy bins as well: higher energy emission responds more slowly to the EC power increase (Figure 3.6). As an example, the $E=[50:60]$ keV emission increases significantly only after 1 ms, when its $E=[20:30]$ keV counterpart has already reached half of its maximum. As a working hypothesis, we may attribute this to the quasilinear diffusion of the electron distribution function in momentum space, from lower to higher energy. In order to further understand the dynamics in phase space, the experiment will be modeled using a time-dependent Fokker-Planck simulation in section 3, with the aid of a hard X-ray synthetic diagnostic.

Abel-inversion of hard X-ray profiles

To derive the local hard X-ray emissivity from the line-integrated measurement, an Abel-inversion method is used, assuming poloidally uniform hard X-ray emission at each flux surface. Although both the magnetic field helicity [57] and the conservation of the magnetic moment [104] can give rise to an asymmetry in the poloidal emission, this effect is negligible in tokamak plasmas with a centrally localized suprathermal electron population [57].

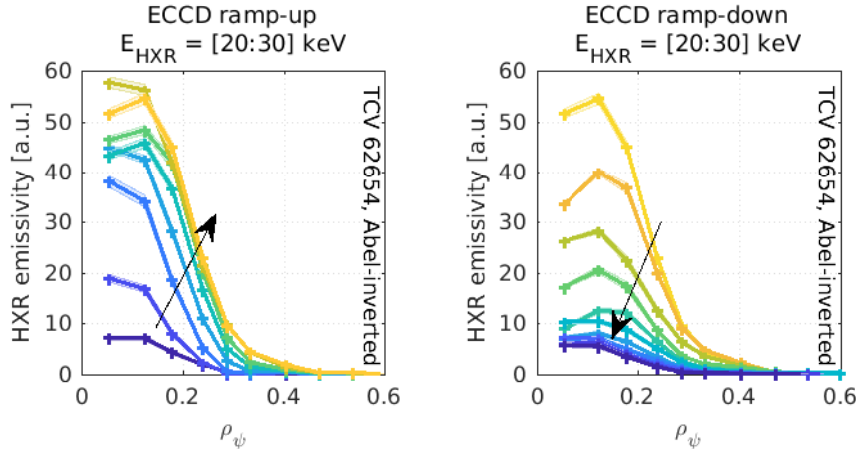


Figure 3.9 – Time evolution of hard X-ray emissivity profile in space, Abel-inverted from the line-integrated data in Figure 3.7. The time points are evenly spaced as indicated in Figure 3.7.

Figure 3.9 shows the Abel-inverted hard X-ray emissivity profiles in space as functions of ρ_ψ , which is the square root of the normalized poloidal flux. The temporal dynamics at different spatial locations are presented in Figure 3.10. The increase of the local hard X-ray emissivity is quicker in central locations (lower ρ_ψ) than in outer locations (higher ρ_ψ), as is especially clear in the normalized hard X-ray emissivity (bottom of Figure 3.10). This is indeed indicative of radial diffusion: the suprathermal electrons born on-axis can move outwards while the EC power increases. However, the possibility of EC wave scattering by fluctuations cannot be excluded: the birth function of suprathermal electrons can be broadened due to the scattered EC waves. In the next section, the effect of diffusion will be analyzed in the Fokker-Planck modeling and a possible contribution of the EC wave scattering will be discussed.

During the relaxation phase when only the minimum EC power is applied after 4 ms, however, no significant difference in temporal dynamics was found at varying locations. This suggests that the level of anomalous diffusion may vary as applied EC wave power changes, which will be investigated further in the following section by Fokker-Planck modeling. If the suprathermal electron diffusion varies with EC power, this may be due to the fact that the turbulence intensity depends on the EC power. Additionally, a localized MHD oscillation observed in this discharge (Figure 3.5) may be a candidate for suprathermal electron diffusion.

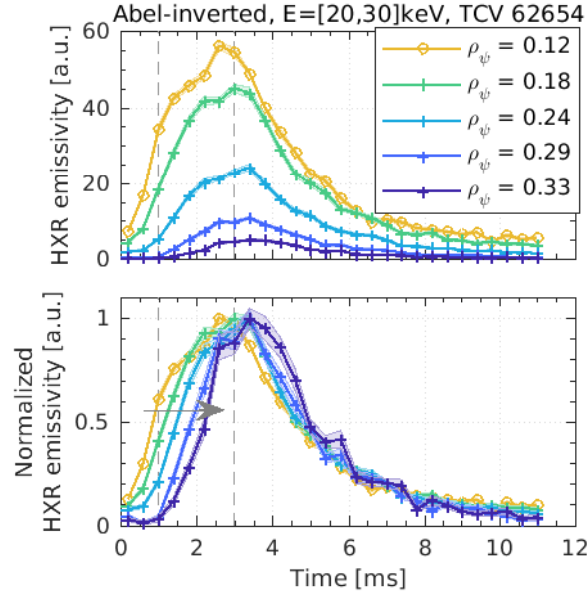


Figure 3.10 – Time traces of local hard X-ray emissivity at various spatial locations.

3.2.3 Off-axis ECCD

In order to see the effect of EC wave deposition location change, the poloidal angle of the EC wave was slightly moved from the on-axis ECCD discharge (Figure 3.1). The ray tracing calculation shows that the EC absorption is localized at $\rho_\psi \sim 0.2$. No MHD activity was detected in this discharge; neither the sawtooth nor the frequency-chirping internal kink mode appeared.

Conditional averaging of hard X-ray data

In the off-axis ECCD case, two peaks are observed in the line-integrated hard X-ray emission profiles (Figure 3.11). The two peaks correspond to the ECCD absorption locations. The height of the overall profile increases and decreases following the EC power change, keeping the two peaks. As observed in the on-axis ECCD case, the response of outer channels (ch9 in Figure 3.12) is slower than the response of the channel whose line of sight passes the EC absorption location (ch12 in Figure 3.12).

Compared to the on-axis ECCD case, the overall hard X-ray count rate was lower, as well as the electron temperature. Thus the hard X-ray energy spectrum cannot be resolved at high energies. However, the temporal behaviour of I_{HXR} can still be seen to vary with energy, likely due to the RF quasilinear diffusion in the momentum space.

In addition, it should be noticed that at the end of the relaxation phase, the count rate at the lower energies does not drop down to zero, in both on-axis and off-axis ECCD cases. This is because the EC wave power is kept at 100 kW after the ramp-down. Although the power is

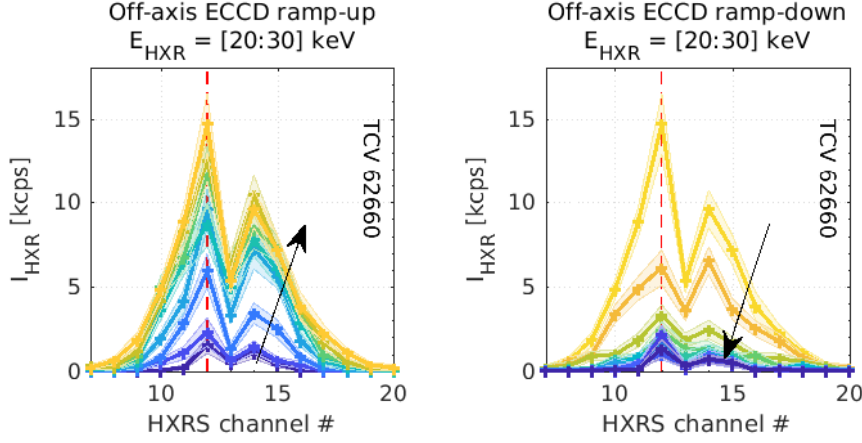


Figure 3.11 – Time evolution of line-integrated hard X-ray emission profile with EC power modulation. The time points are evenly spaced as indicated in Figure 3.7.

much lower than the maximum value (750 kW), the plasma is not completely ohmic and the suprathermal electron population is not negligible. This is an important consideration for the initial setup of the electron distribution function in the Fokker-Planck modeling, which will be discussed in section 3.

Abel-inversion of hard X-ray profiles

The Abel-inverted hard X-ray emissivity in Figure 3.13 shows a peak at the EC wave deposition location, $\rho_\psi \sim 0.2$, as observed in the line-integrated profiles. A broadening of the hard X-ray emissivity profile is observed, possibly due to radial diffusion or EC wave scattering, as discussed for the on-axis ECCD case. The time traces of the local hard X-ray emissivity at different locations in Figure 3.14 suggests that the suprathermal electrons generated at the localized ECCD location may be transported outwards over time; however, the low count rates make it difficult to observe the behavior clearly, unlike in the on-axis ECCD case.

It should be noticed that the broadening of the hard X-ray profile is not symmetric about the EC wave absorption location: the profile broadens only outwards, i.e. $\rho_\psi > 0.2$. This suggests that the suprathermal electron diffusion might not be uniform in space. This will be further investigated by the Fokker-Planck modeling with various diffusion models.

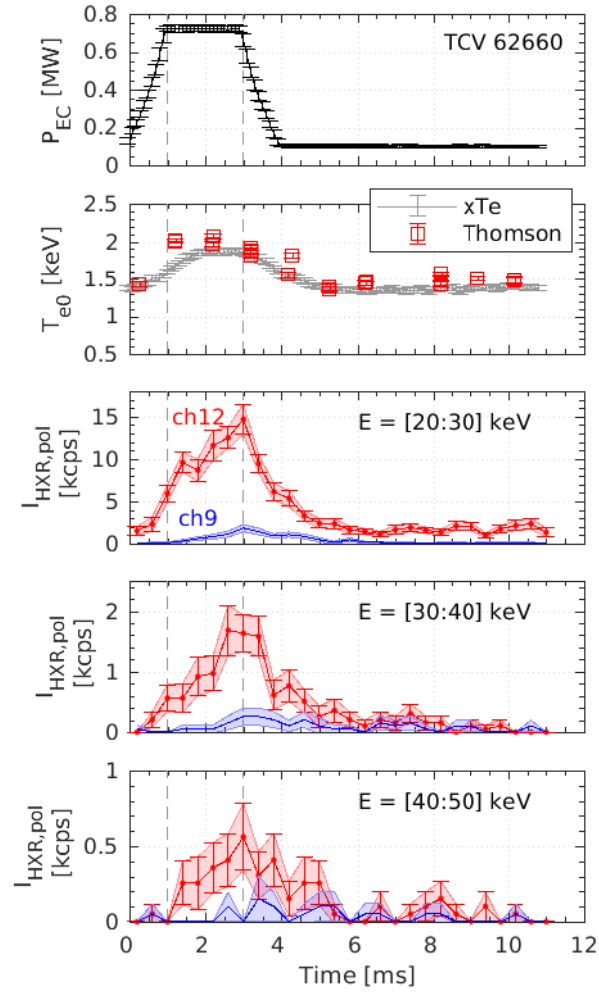


Figure 3.12 – Time traces of EC power, electron temperature and hard X-ray emission (I_{HXR}) in different energy bins (indicated as E in keV), averaged over EC modulation cycles.

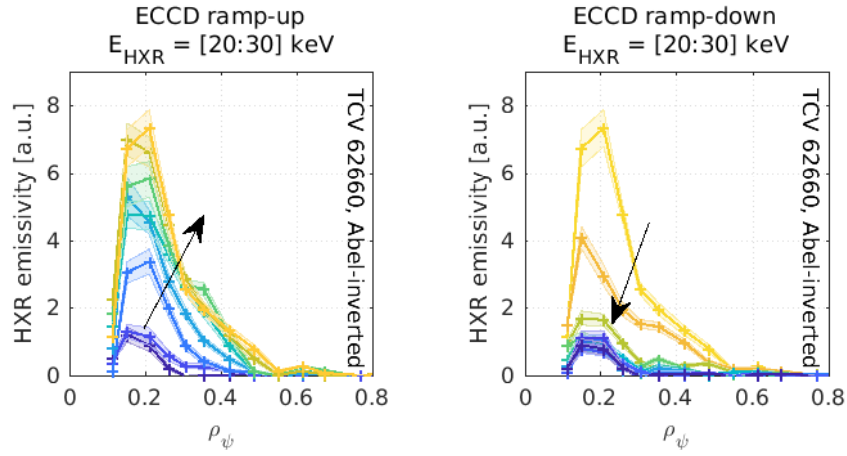


Figure 3.13 – Time evolution of local hard X-ray emissivity profiles, Abel-inverted from the line-integrated data in Figure 3.11.

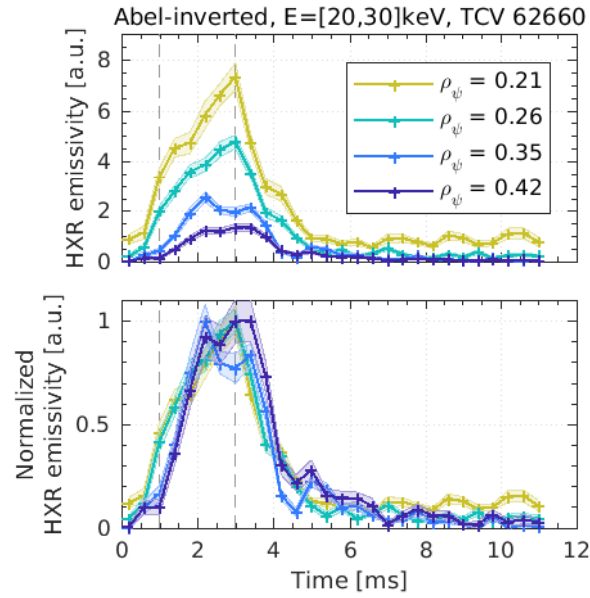


Figure 3.14 – Time traces of the local hard X-ray emissivity at various spatial locations.

3.3 Time-dependent Fokker-Planck modeling

3.3.1 Simulation setup

For the time-dependent modeling of the ECCD plasma, the 3-D bounce-averaged relativistic Fokker-Planck equation solver LUKE [77, 114] has been used in the present work. The code includes the relativistic collision operator, the RF wave quasilinear operator, the ohmic electric field operator, and the anomalous transport operator. The ray-tracing code C3PO [86] is coupled to the code LUKE to self-consistently calculate the ray damping and the electron distribution function. The simulation is followed by the hard X-ray synthetic diagnostic module [57], allowing a direct comparison between simulation and experiment.

The electron distribution function is calculated every 0.4 ms, which corresponds to the hard X-ray time bin length. Each cycle of the simulation consists of 28 consecutive runs, thus 11 ms of the experimental cycle is reproduced. At the beginning of the simulation, it is difficult to set the initial distribution function analytically, since the electron distribution function at the relaxed state is not a Maxwellian as observed in the experiment. Instead, the electron distribution function is evolved from a Maxwellian in the first simulation cycle, and continued through further simulation cycles until the relaxed state distribution function converges (i.e., the final state at the end of the cycle is the same for each cycle). In general the electron distribution function converged after a couple of cycles.

Since the loop voltage profile cannot be considered to be spatially uniform unlike in a steady-state simulation, the total plasma current profile (j_{tot}) is assumed to be fixed and the back-EMF is calculated at each simulation to compensate the change made in the current profile during ECCD. The total plasma current profile is the sum of the Ohmic, RF-driven, and bootstrap current profiles ($j_{tot} = j_{ohm} + j_{RF} + j_{BS}$). The Fokker-Planck simulation calculates the sum of Ohmic and RF-driven current profiles ($j_{ohm} + j_{RF}$), while the bootstrap current profile (j_{BS}) can be calculated from the measured plasma profiles [115, 116].

As TCV lacks a current profile measurement, the total current profile is prepared before the time-dependent simulation. Since the hard X-ray profiles were observed to saturate at the end of the modulation cycle, a spatially uniform loop voltage, whose value is measured by a flux loop, is initially assumed for the sole purpose of calculating the current profile. From this, a steady-state solution of the Fokker-Planck equation is calculated with the minimum EC power (100 kW). A spatially uniform radial diffusivity is assumed, and adjusted to match the experimental current value. The resulting profile ($j_{ohm} + j_{RF}$) is added to the bootstrap current profile (j_{BS}) of the end of the modulation cycle (0 ms in Figure 3.15) to obtain the fixed total plasma current profile (j_{tot}).

As presented in Figure 3.15, the bootstrap current profile changes during the modulation following the change in the electron temperature; the bootstrap current value I_{BS} varies from 27 kA to 48 kA, from 0 ms to 3 ms. At each simulation, the loop voltage profile is adjusted iteratively, so the simulated current profile ($j_{ohm} + j_{RF}$) matches the difference between the

total and bootstrap current profiles ($j_{tot} - j_{BS}$). The simulation is based on the TCV magnetic equilibrium calculated by the equilibrium solver LIUQE [22].

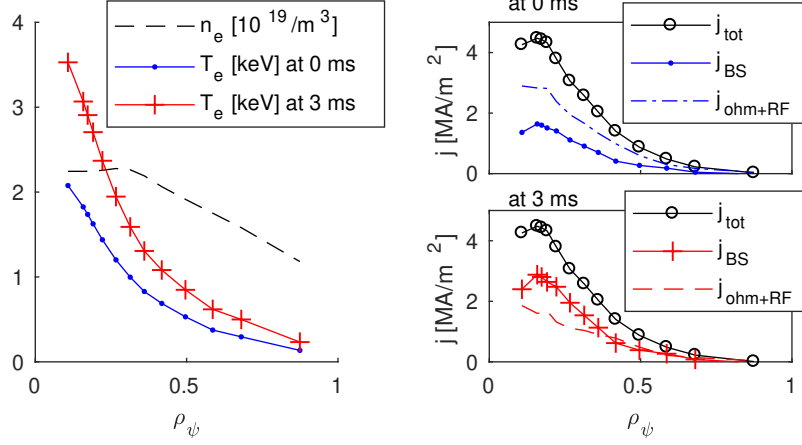


Figure 3.15 – (Left) Electron density and temperature. (Right) Current density profiles at 0 ms (top) and 3 ms (bottom). This is the on-axis ECCD case (TCV shot 62654).

3.3.2 On-axis ECCD simulation

Figures 3.16 and 3.17 show the Fokker-Planck simulation and the synthetic diagnostic results for the on-axis ECCD discharge. Since I_{HXR} of the central channel (ch14) is overestimated without any suprathermal electron transport ($Dr = 0$), the suprathermal electron transport operator is modified in this work to match the measurement data. Firstly, a spatially uniform diffusion model is used ($Dr = 1$ and Step Dr in Figures 3.16 and 3.17), for suprathermal electrons whose energy is higher than the bulk electron temperature.

When the diffusion is constant in time during the modulation cycle ($Dr = 1$), I_{HXR} is well estimated during the ramp-up phase but the calculated I_{HXR} drops too rapidly during the relaxation phase. This suggests that the suprathermal electron diffusion may be negligible during the relaxation phase. Thus a step diffusion model (Step Dr in Figures 3.16 and 3.17) is introduced, in which the level of spatially uniform diffusion changes following the EC power change: $Dr(t) = 1.2 \cdot (P_{EC}(t)/P_{EC,max})^5$. The coefficient is adjusted to match the count rate prediction with the measured value. This step diffusion model describes well the measurement, suggesting a dependency of the suprathermal electron transport on the EC power level.

The change of the EC power level is in fact only experienced by the resonant electrons in momentum space. To reflect this consideration, a new, momentum- and space-dependent diffusion model is introduced based on the RF quasilinear diffusion coefficient. As illustrated by Figure 3.18 for two selected spatial locations, the diffusion model is constructed by first normalizing the RF quasilinear diffusion coefficient in momentum space and then multiplying it by an appropriate diffusion coefficient. Since the RF quasilinear diffusion is localized at the

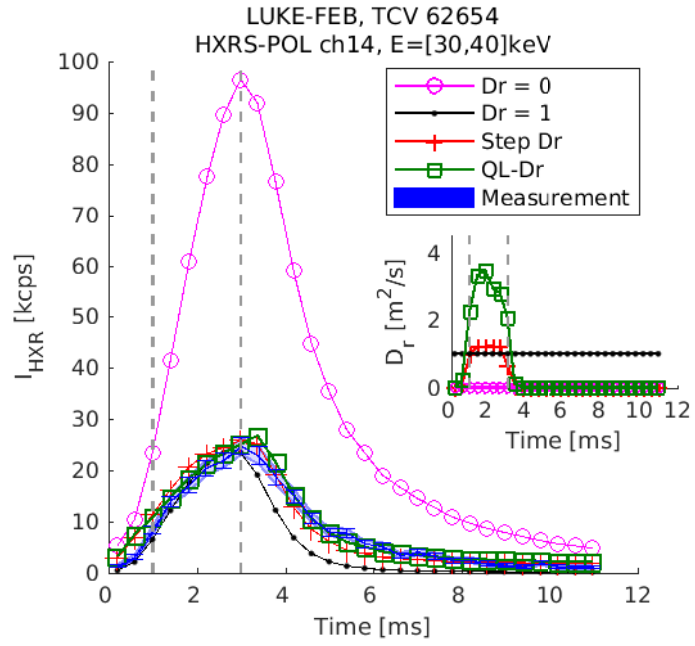


Figure 3.16 – Simulation and experimental results for hard X-ray emission at ch14 (I_{HXR}). Different diffusion models are also presented.

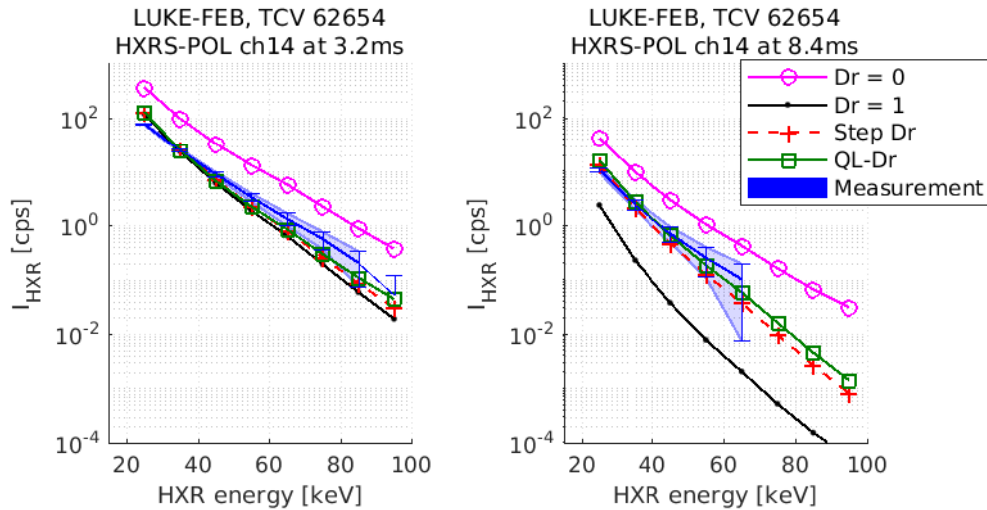


Figure 3.17 – Energy spectrum of ch14 at selected time steps.

EC absorption area in space, the modeled radial diffusion coefficient is also significant only near the magnetic axis (low ρ_ψ in Figure 3.18).

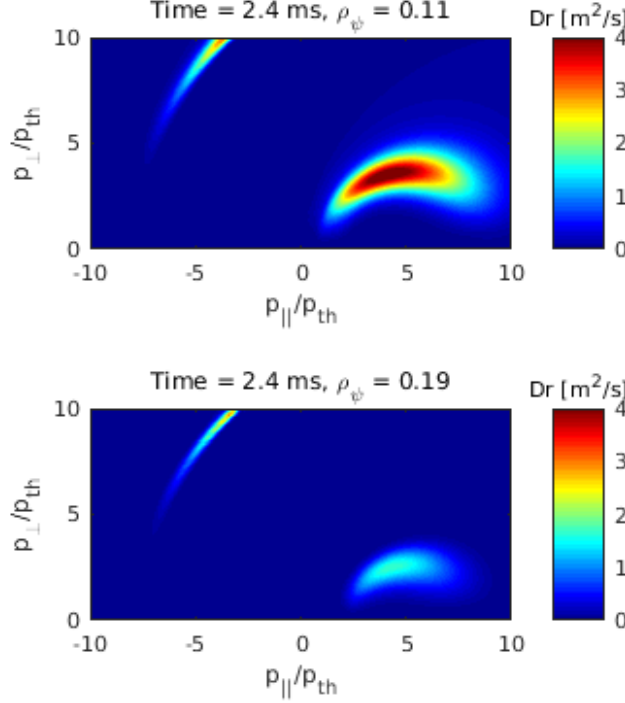


Figure 3.18 – Radial diffusion coefficient (QL-Dr) modeled in momentum space.

This new diffusion model based on the RF quasilinear diffusion coefficient (QL-Dr in Figures 3.16 and 3.17) predicts I_{HXR} as well as the step diffusion model (Step Dr) does. However, the hard X-ray profile in Figure 3.19 shows that the I_{HXR} profile predicted by this model (QL-Dr) is narrower than the measurement. And at the end of the relaxation phase, at 10.8 ms in Figure 3.19, both transport models (Step Dr and QL-Dr) fail to predict the broad I_{HXR} profile; this is indeed a natural consequence of positing a small radial diffusion coefficient when there is no power. It should, however, be remembered that in this relaxation state the EC power is not completely turned off but stays at the minimum level, 100 kW, so that a low level hard X-ray signal is still detectable. This result shows that it is difficult to model the ECCD plasma only by including the radial diffusion of suprathermal electrons. At least in the relaxed state, the EC wave scattering can therefore be a possible candidate for the hard X-ray profile broadening without inducing diffusive losses.

In this time-dependent Fokker-Planck simulation, the loop voltage profile has been calculated at each time step to compensate the change of ohmic and RF currents. Therefore, when no suprathermal electron transport is considered (Figure 3.20), the absolute value of the toroidal electric field increases as the EC power increases, due to the increase of the counter-ECCD current. When the QL-Dr transport model is used, the resonant electrons (A in Figure 3.21) diffuse out radially, so the ECCD current decreases. Then the ohmic current increase due to the

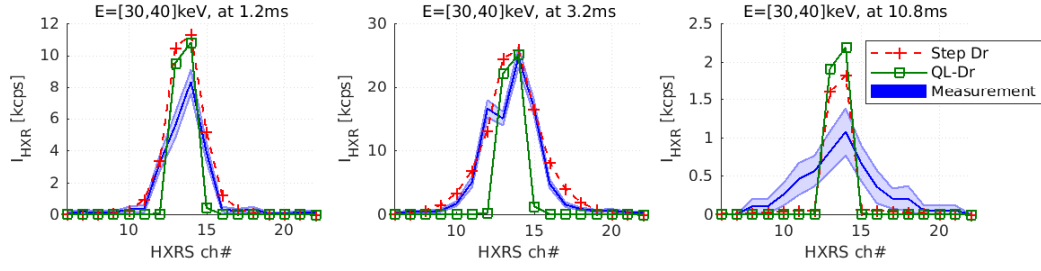


Figure 3.19 – Hard X-ray emission profiles from measurement and simulations.

electron temperature increase is dominant, so the absolute electric field decreases. However, when the spatially uniform diffusion coefficient is used (Step Dr), the suprathermal electron diffusion reduces the ohmic current contribution as well (B in Figure 3.21), so the change in the toroidal electric field is not significant. This analysis indicates that the suprathermal electron dynamics plays a role in the determination of the wave driven current, and therefore an accurate modeling of the suprathermal electron transport is important to estimate the RF current correctly.

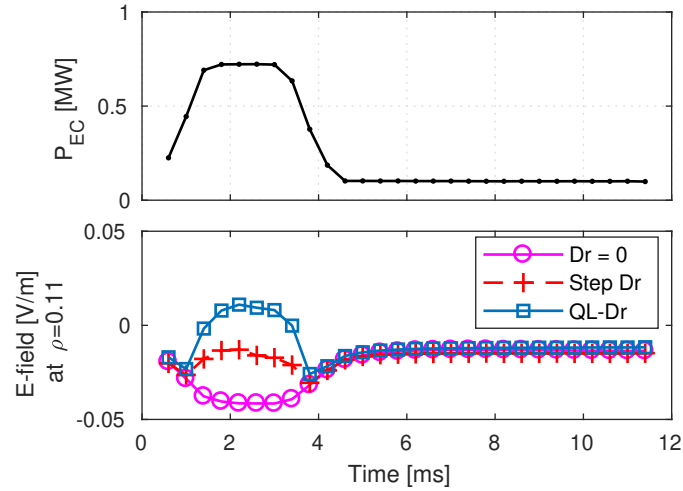


Figure 3.20 – (Top) Time trace of EC power. (Bottom) Central toroidal electric field calculated by LUKE with different transport models.

3.3.3 Off-axis ECCD

The off-axis ECCD discharge analyzed in section 2.3 showed two distinct ECCD peaks in the hard X-ray emission profiles. In Figure 3.22, the LUKE-FEB simulation without including any radial diffusion ($Dr = 0$) shows two peaks as the measurement does, but the absolute emission level is overestimated. The spatially flat diffusion model (Step Dr) is not able to reproduce the two peaks, as the profile is smoothed into a broad peak.

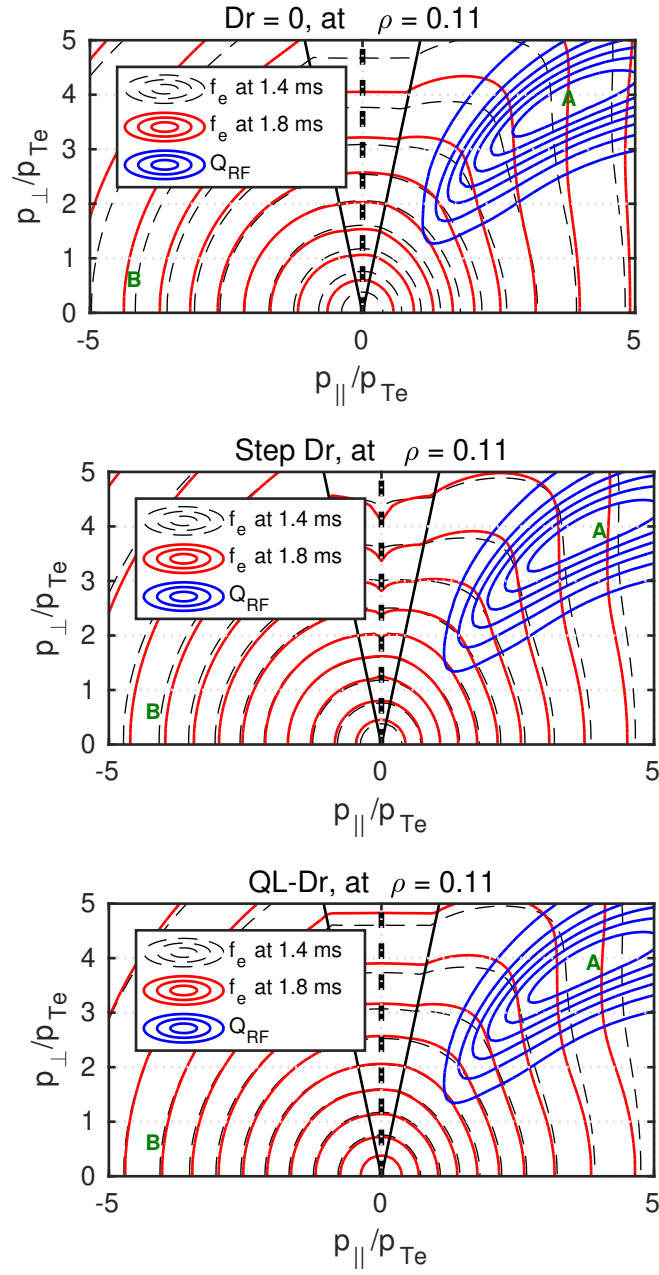


Figure 3.21 – The electron distribution function at two consecutive time steps, as well as the RF quasilinear diffusion coefficient, calculated by LUKE with different transport models.

In this case, introducing the RF quasilinear diffusion based radial diffusion model (QL-Dr, presented in Figure 3.18) gives a far better prediction as presented in Figures 3.22 and 3.23: the two ECCD peaks are reproduced and the time trace of I_{HXR} agrees with the measurement. Since only the resonant electrons experience the radial diffusion, the majority of electrons are not lost in this diffusion model and the broadening of the profile is prevented.

However, even in this case a minor discrepancy persists, in that I_{HXR} outside the ECCD peak is underestimated, as indicated with arrows in Figure 3.22. This is related to the discussion of section 2.3.2: the hard X-ray profile broadens only outwards, keeping the ECCD peak. Then an additional EC wave scattering may explain the discrepancy between the measurement and the simulation, without inducing a diffusive broadening at the core. This is, however, outside the scope of this thesis.

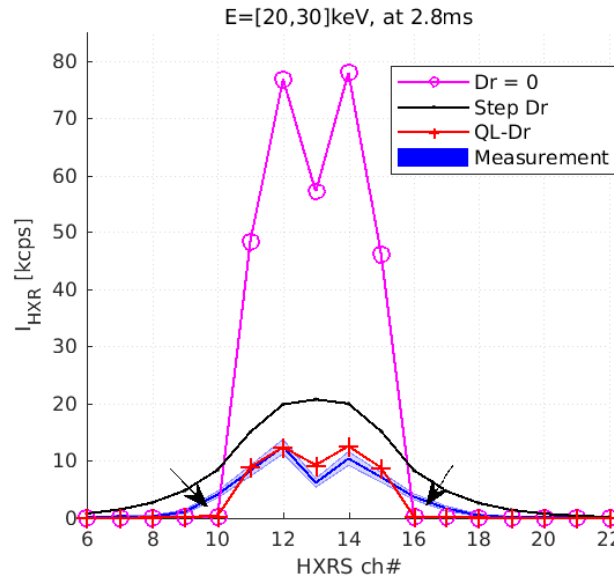


Figure 3.22 – Hard X-ray emission profiles from measurement and simulations.

3.4 Conclusions

In the present work a state-of-the-art hard X-ray spectrometer in TCV has been used to analyze the time evolution of the suprathermal electron population generated by ECCD. The results have shown that the hard X-ray profile broadens significantly when the EC power reaches its maximum value, suggesting that the level of broadening depends on the EC power.

Fokker-Planck modeling coupled to a hard X-ray synthetic diagnostic has shown that the radial diffusion coefficient needs to be monotonically increasing with EC power to explain the time-trace measurement. In particular, a radial transport model based on the RF quasilinear diffusion coefficient provides a satisfactory estimation without overly smoothing the hard X-ray profiles, in both on- and off- axis ECCD discharges. This suggests that the anomalous

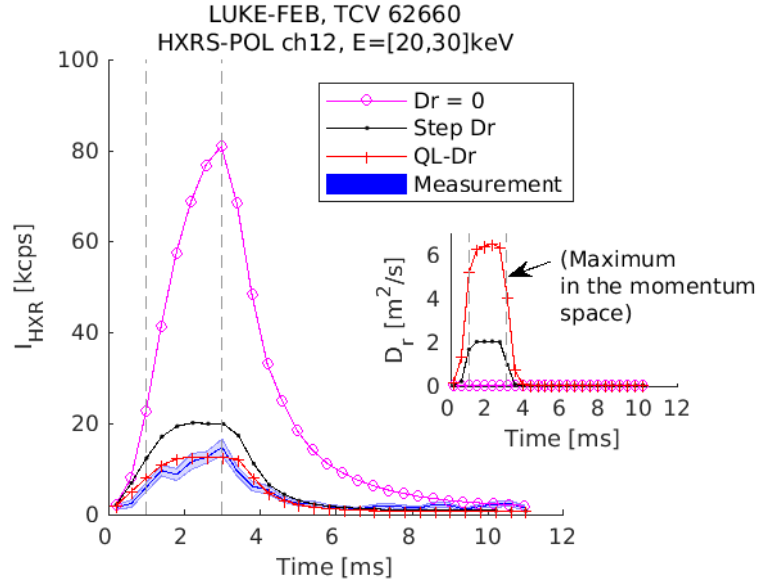


Figure 3.23 – Simulation and experimental results of I_{HXR} at ch12. Different diffusion models are also presented.

transport may be concentrated on the suprathermal electrons that interact resonantly with the EC waves, whereas the majority of electrons may not experience significant diffusive loss. The analysis performed in the 3-D space is encouraging evidence that the suprathermal electron dynamics plays an important role in determining the wave driven current.

Although the various diffusive transport models reproduced the measurements well, an additional mechanism appears to still be required to estimate the hard X-ray profile broadening outside the EC absorption area. EC wave scattering due to edge density fluctuations may be just such a mechanism.

4 Suprathermal electron driven fishbone instability

4.1 Introduction

In this work, new experimental data on the fishbone instability are reported, which is driven by suprathermal electrons during ECCD discharges in the TCV tokamak. A newly developed ECCD scenario enables collecting hard X-ray photons over regular electron fishbone bursts. Thus the temporal resolution of the hard X-ray measurement is enhanced to resolve the observed mode frequency. The kink mode structure is observed in the hard X-ray profiles, as well as in the soft X-ray profiles and the electron temperature profiles measured by the Thomson scattering system. In addition, the hard X-ray camera that can rotate on its axis permits a study of the different responses of trapped and passing electrons to the $m/n = 1/1$ mode. The stability of the mode is assessed by solving the linear fishbone dispersion relation, using a realistic electron distribution function modeled by solving the Fokker-Planck equation, with the aid of a hard X-ray synthetic diagnostic.

This chapter is arranged as follows: in section 4.2 the experimental setup and diagnostics used in this chapter are described. The experimental observation of the electron fishbones and detailed analysis are presented in section 4.3. In section 4.4, electron fishbone characteristics with varying ECCD power and location are analyzed. The experimental observations are compared to the solution of the linear fishbone dispersion equation, coupled with the Fokker-Planck simulation, in section 4.5. Conclusions can be found in section 4.6.

4.2 Experimental setup

In the discharges analyzed in this chapter, one 82.7 GHz gyrotron was applied with a power of up to 750 kW, heating at the second (X2) harmonic of the electron cyclotron resonance. The typical plasma parameters used in this work are: plasma current $|I_p| \sim 0.2$ MA, toroidal magnetic field $|B_\phi| \sim 1.34$ T, electron density $n_e \sim 2.2 \times 10^{19}/m^3$, electron temperature $T_e \sim 2.4$ keV, ion temperature $T_i \sim 0.45$ keV, plasma toroidal rotation frequency $|f_\phi| \sim 4.5$ kHz and effective charge $Z_{eff} \sim 1.2$. The common direction of I_p , B_ϕ , and f_ϕ (v_ϕ) is indicated in Figure

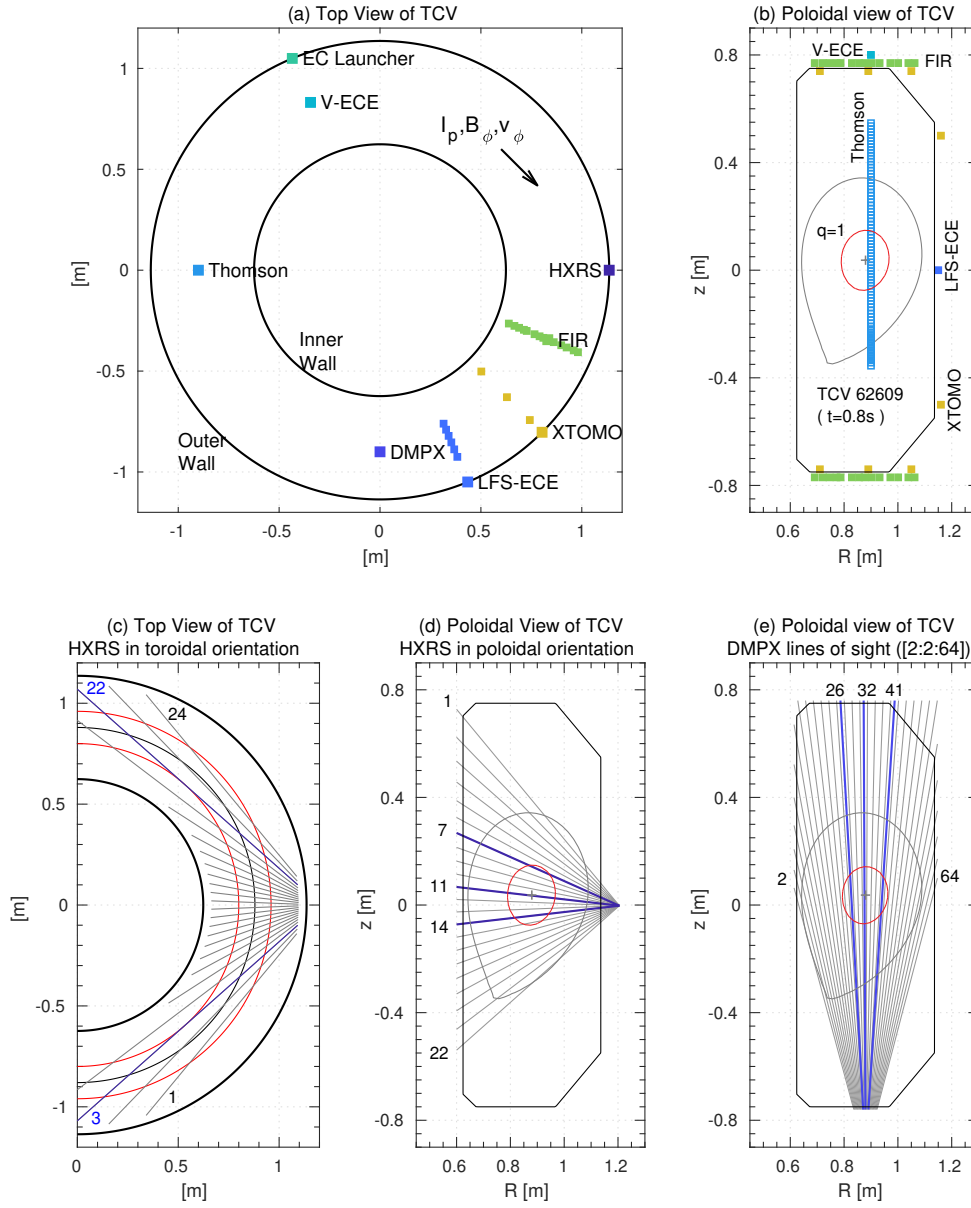


Figure 4.1 – (a) Top view of the diagnostic set in TCV. (b) Poloidal view of the diagnostics. The last closed flux surface and the $q = 1$ surface are presented from TCV shot 62609. (c,d) Lines of sight of HXRS equatorial camera in the toroidal and poloidal orientations. (e) Lines of sight of DMPX.

4.1 (a): in the clockwise direction on the top view of TCV. No neutral beam injection system was used. The plasma equilibrium is reconstructed from magnetic measurements, by solving the Grad-Shafranov equation with the code LIUQE [22].

A toroidal magnetic probe array and a soft X-ray tomographic system (XTOMO) are used to

analyze toroidal and poloidal mode structures, respectively. The toroidal magnetic probe array [25] comprises three ($z = -0.23$ m, $z = 0$ m, $z = 0.23$ m) high-field-side arrays of 8 probes each at the inner wall and three ($z = -0.23$ m, $z = 0$ m, $z = 0.23$ m) low-field-side arrays of 16 probes each at the outer wall. The magnetic pick-up coils acquire data at 250 kHz. The soft X-ray tomographic system (XTOMO) consists of 8 pinhole cameras with 20 p-n junction silicon photodiodes each, acquiring data at 100 kHz. The measured signal is used for the tomographic inversion of soft X-ray emission using a finite element grid discretization on the flux surfaces and the minimum Fisher regularization inversion method [23]. The data from both diagnostics are analyzed using the singular value decomposition (SVD) technique to study the time evolution (chronos) of the spatial mode structure (topos) [23, 24]. The mode frequency measured in the laboratory frame is converted to the frequency in the plasma frame using plasma toroidal rotation data acquired from Charge Exchange Recombination Spectroscopy (CXRS), which uses the C_{6+} impurity line assuming $\nu_\phi = \nu_{C_{6+}}$. The CXRS also provides T_i and Z_{eff} .

The fishbone fluctuation of thermal electrons is analyzed in detail using the multi-channel soft X-ray detector (DMPX) and the low field side ECE diagnostic (LFS-ECE). DMPX [117] has a high time resolution of 5 μ s and a high spatial resolution defined by 7.9 mm mean distance between two lines of sight, which allows observing changes in the soft X-ray profile in the plasma core far inside the $q = 1$ surface. One-half of the lines of sight (every other chord) are plotted in Figure 4.1(e), out of a total of 64 channels. Observations of the small scale mode structure inside the $q = 1$ surface are complemented by a recently upgraded Thomson scattering system, which provides a high spatial resolution (6-12 mm) vertical profile of n_e and T_e at $R = 0.9$ m. The measurement points are plotted in 4.1(b). For the analysis of the electron temperature fluctuations, the second harmonic X-mode LFS-ECE diagnostic is used, with 24 channels from 65 to 99 GHz [26]. The data is acquired at 200 kHz. Another ECE system, vertical ECE, that is positioned at the top of the tokamak (Figure 4.1 (a,b), V-ECE) can receive electron cyclotron radiation emitted by suprathermal electrons at the third harmonic of the electron cyclotron frequency, with 12 channels from 89 GHz to 114 GHz.

In this work, a single HXRS camera located at the midplane ($z = 0$ m) has been used. The camera can be rotated by 90 degrees, thus the lines of sight are able to cover either the toroidal plane, parallel to the magnetic field lines (Figure 4.1 (c)), or the poloidal plane, perpendicular to the magnetic field lines (Figure 4.1 (d)). Since energetic electrons emit hard X-ray radiation preferentially in the direction of travel (relativistic headlight effect [58]), trapped and passing electrons contribute differently to the hard X-ray photons received by the camera in different orientations. This fact is used in section 4.3.4, where the response of trapped electrons is studied separately from that of passing electrons.

The TCV hard X-ray system features digital pulse processing [28], which enables up to 600,000 photon counts per second. After the pulse processing, the photon counts are sorted into user-set energy and time bins. In this work, photon counts are conditionally averaged over repetitive fishbone bursts, in order to enhance the photon statistics in short time bins. This

has enabled a mode oscillation of a few kHz frequency to be directly observed in hard X-ray profiles for the first time.

Each photon impinging on a HXRS detector generates a charge pulse through photon-matter interaction, which is recorded by the associated electronics; the height of the pulse can then be translated into an energy value, based on the calibration performed using radioactive sources. While the photo-electric effect has the largest influence on the detected signal, the low energy contribution from the Compton effect needs to be considered as well. Because of this and, even more importantly, the continuous energy spectrum of the bremsstrahlung radiation, the electron distribution function cannot be reconstructed directly from the hard X-ray measurement. This limitation can be compensated by numerical modeling: in particular, Fokker-Planck modeling and a hard X-ray synthetic diagnostic have been used for this purpose. The modeled distribution function can also be used to solve the linear fishbone dispersion relation to assess the stability of the mode. The numerical modeling approach is described in detail in section 4.5.

4.3 Experimental observation of the fishbone oscillation

In this section we present the experimental observations and detailed analysis of the electron fishbone oscillation. An overview of the experimental conditions and observations is presented in section 4.3.1. Conditional averaging results of the hard X-ray and other diagnostics over regular fishbone bursts are presented in section 4.3.2, and the Abel-inversion of the hard X-ray and soft X-ray profiles is discussed in section 4.3.3. The different behavior of passing and trapped electrons is investigated from the hard X-ray data in section 4.3.4.

4.3.1 The $m/n = 1/1$ mode excitation during ECCD

Regular frequency chirping bursts such as those shown in Figure 4.2 have appeared in the magnetic probe, soft X-ray and ECE data during the ECCD phase in the discharge #62609, from 0.5 s to 1.9 s. In this discharge, 530 kW of co-ECCD power was injected obliquely with a toroidal angle of 20° (0° corresponds to pure ECH) with absorption localized at $\rho_\psi \sim 0.25$ (ρ_ψ is the square root of the normalized poloidal flux) on the high field side, according to the C3PO ray tracing calculations [86]. The $q = 1$ surface is located at $\rho_\psi \sim 0.44$ [22].

Figure 4.2 (b) shows the Fourier spectrogram of the $n = 1$ mode amplitude (n is the toroidal mode number), which corresponds to the dominant component (Chronos 1, Figure 4.2 (a)) from the SVD analysis of the toroidal magnetic probe array signal. The mode rotates in the precessional drift direction of deeply trapped electrons, which is opposite to the plasma current direction. The SVD analysis of the tomographically inverted soft X-ray emission from XTOMO has shown that the mode has a poloidal $m = 1$ structure (m is the poloidal mode number), rotating near the $q = 1$ surface in the electron diamagnetic drift direction.¹

¹A detailed analysis of determining the mode structure and the rotation direction are presented in Appendix A.

4.3. Experimental observation of the fishbone oscillation

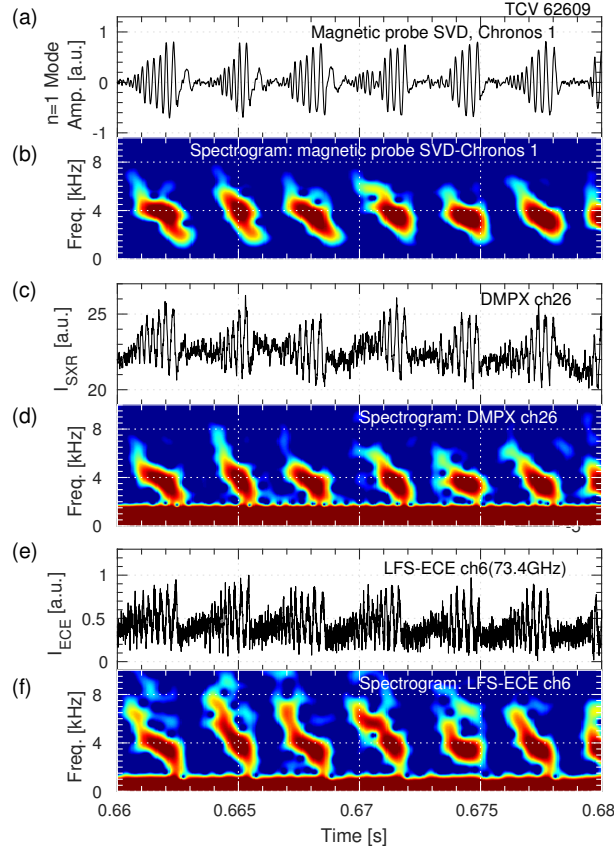


Figure 4.2 – Fishbone shaped oscillations and the Fourier spectrogram of (a,b) magnetic field fluctuation, (c,d) soft X-ray signal, and (e,f) ECE signal.

The spectrograms in Figure 4.2 show that the mode frequency chirps down from ~ 5 kHz to ~ 2 kHz, during ~ 2 ms, every ~ 3 ms. The toroidal rotation frequency in this discharge is 4.5 ± 0.6 kHz in the plasma current direction, which is opposite to the mode rotation direction. Therefore the mode frequency in the plasma frame chirps down from ~ 9.5 kHz to ~ 6.5 kHz. The regular burst time points are recorded for the conditional averaging of the results.

The time history of soft X-ray profiles in Figure 4.3 shows that the fishbone-shaped perturbation appear in the off-axis channels, whose lines of sight are parallel to the flux surfaces near the $q = 1$ surface. The lines of sight of DMPX are presented in Figure 4.1 (e) with the $q = 1$ surface of this discharge. The oscillations are accompanied by a central plasma relaxation, as seen in the central soft X-ray signal, I_{SXR} of ch32, taking the form of so-called non-standard sawtooth, classified as saturated or inverted [118].

The first investigations into the non-standard sawtooth [118] found that the sawtooth shape changed during EC heating, depending on EC heating conditions and plasma parameters, such as plasma shape or safety factor. The non-standard sawtooth activity was further studied about

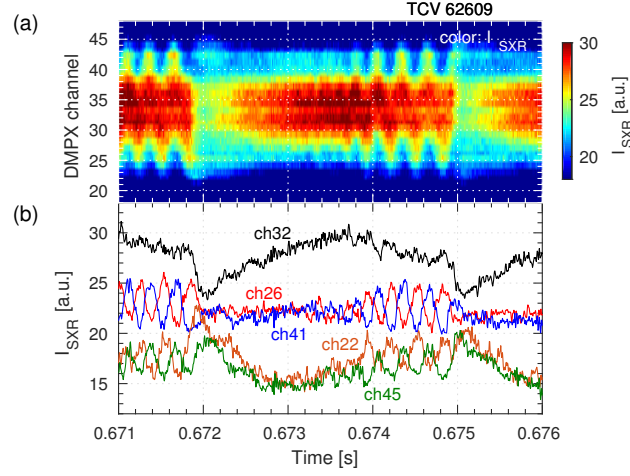


Figure 4.3 – Time history of (a) soft X-ray profiles and (b) the signal of selected channels.

20 years ago to simulate the electron temperature evolution using a magnetic island model in the presence of localized heat sources [119]; however, the spatial mode structure during the plasma relaxation was supported by limited experimental evidence. The mechanism behind the onset of the phenomena remained uncertain. In the present work, experimental evidence for the $m/n=1/1$ mode structure is provided in section 4.3.2, and a link between the central plasma relaxation and the mode oscillation is investigated in section 4.3.3.

At the end of the oscillation phase in Figure 4.3, there is a collapse of the central soft X-ray profile, resembling a standard sawtooth crash. Since the fishbone-like oscillation exists before the crash, no distinctive sawtooth precursor is observed. Then one must question whether this fishbone-like oscillation is actually an extended sawtooth precursor or whether this instability induces the sawtooth crash at the end of its oscillation. The possibility of the extended sawtooth precursor can be excluded because this fishbone-like oscillation is sometimes observed separately from a sawtooth precursor depending on the ECCD location, as can be seen in section 4.4.2, Figure 4.15. Thus it is possible that a small-amplitude sawtooth precursor overlaps with the fishbone-like oscillation. In section 4.5, we solve the linear fishbone dispersion relation, to study the stability of the fishbone mode of this discharge.

4.3.2 Conditional averaging of data

In order to observe the high frequency suprathermal electron dynamics, the hard X-ray photon counts have been collected over regular fishbone-like bursts. Although the fishbone-like bursts appear regularly, the amplitudes and the lengths of the oscillations vary; thus bursts that have similar amplitude and length have been selected in order to reduce the statistical error.

Conditionally averaged magnetic field fluctuations, ECE signal I_{ECE} , soft X-ray intensity I_{SXR} and hard X-ray count rate I_{HXR} are presented in Figure 4.4. In the discharge #62609, the

4.3. Experimental observation of the fishbone oscillation

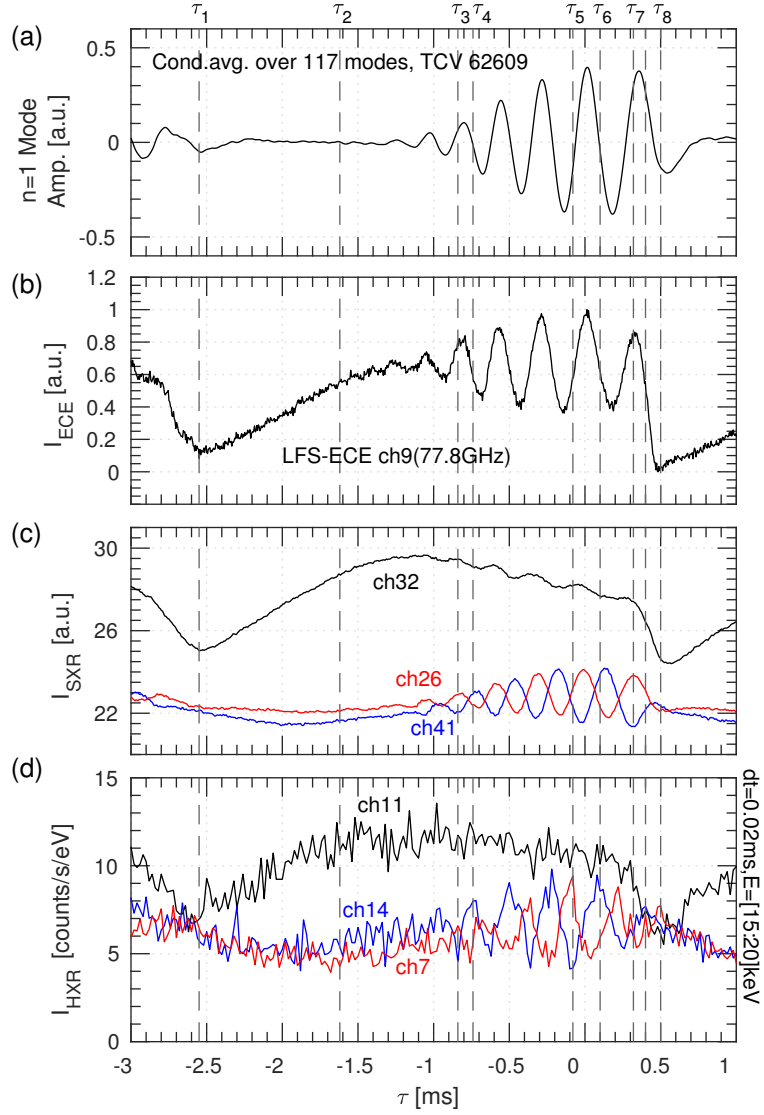


Figure 4.4 – Conditionally averaged (a) magnetic field fluctuation, (b) thermal ECE signal, (c) soft X-ray intensity, and (d) hard X-ray count rate. Selected relative time points are indicated as dashed lines at: $\tau_1 = -2.55\text{ms}$, $\tau_2 = -1.62\text{ms}$, $\tau_3 = -0.84\text{ms}$, $\tau_4 = -0.74\text{ms}$, $\tau_5 = -0.08\text{ms}$, $\tau_6 = 0.10\text{ms}$, $\tau_7 = 0.32\text{ms}$, $\tau_8 = 0.50\text{ms}$.

time points of 117 bursts are collected. The relative time variable τ is introduced such that at $\tau = 0$ the mode amplitude from the magnetic probe analysis has a maximum value. I_{SXR} shows the same behavior described in section 4.3.1 for the raw data: after ~ 1 ms of the plasma ramp-up phase, I_{SXR} on the central channel decreases gradually ($\Delta I_{SXR} \sim -2.4$) during ~ 2 ms of fishbone-like oscillations. Then the cycle ends with a sudden crash ($\Delta I_{SXR} \sim -2.1$) that appears between τ_7 and τ_8 .

In the conditionally averaged hard X-ray count rate plot (Figure 4.4 (d)), the same behavior is observed. This analysis refers to the 15-20 keV energy bin with an integration time of 0.02 ms. The lines of sight of the hard x-ray camera in the poloidal orientation are plotted in Figure 4.1 (d). The central channel (ch11) shows that the central hard X-ray signal also increases during the ramp-up phase and gradually decreases during the fishbone oscillation period. During this oscillation period, the fishbone oscillation in the hard X-ray data is observed in the channels whose line of sight is parallel to the $q = 1$ surface, such as ch7 and ch14. The frequency of the oscillation in I_{HXR} matches the frequency of the $m/n = 1/1$ oscillation, and a nearly π -phase difference is found between the two channels due to the $m = 1$ mode structure.

For the study of the spatial mode structure, the spatial profiles of I_{SXR} and I_{HXR} for the selected time points are presented in Figure 4.5. The Thomson scattering measurements of the electron temperature and density profiles at several relative time points (τ) are plotted in Figure 4.6. The $q = 1$ surface locations calculated by the LIUQE equilibrium reconstruction are indicated as red dashed lines.

During the ramp-up phase, the central intensity of both I_{SXR} and I_{HXR} increases (Figure 4.5 (a,e)). Profiles that are initially flat become peaked at the end of the ramp-up phase. Two peaks inside the $q = 1$ surface are observed due to the off-axis localized ECCD. These peaks can also be observed in the electron temperature profile (Figure 4.6 (a)), while the electron density profile remains constant during the ramp-up phase.

In the early phase of the $m = 1$ oscillation, fluctuation occurs only in a small region inside $q = 1$ (Figure 4.5 (b,f)). Towards the end of the oscillation phase, the I_{SXR} and I_{HXR} profiles show a broader fluctuation region and a larger fluctuation level (Figure 4.5 (c,g)). The localized region of fluctuation is also observed in the electron temperature profiles, indicated with red arrows in Figure 4.6 (b-d). This local flattening of the electron temperature is similar to the observation of the $m/n=1/1$ island in MAST [120] during the standard sawtooth crash on a much shorter time scale, for about 0.15 ms. This observation on TCV may be also attributed to the magnetic island structure. However, due to the lack of internal magnetic field measurement, another possible explanation for this is the formation of helical core, without magnetic reconnection [121]. Further research is required to investigate the nature of the $m/n=1/1$ helical structure. In Figure 4.6 (b-d), since the rotating crescent-shaped helical structure travels past the fixed view-line of the Thomson scattering system, the size and location of the partial flattening changes.

During the oscillation phase, hollow profiles are observed in the electron density (indicated

4.3. Experimental observation of the fishbone oscillation

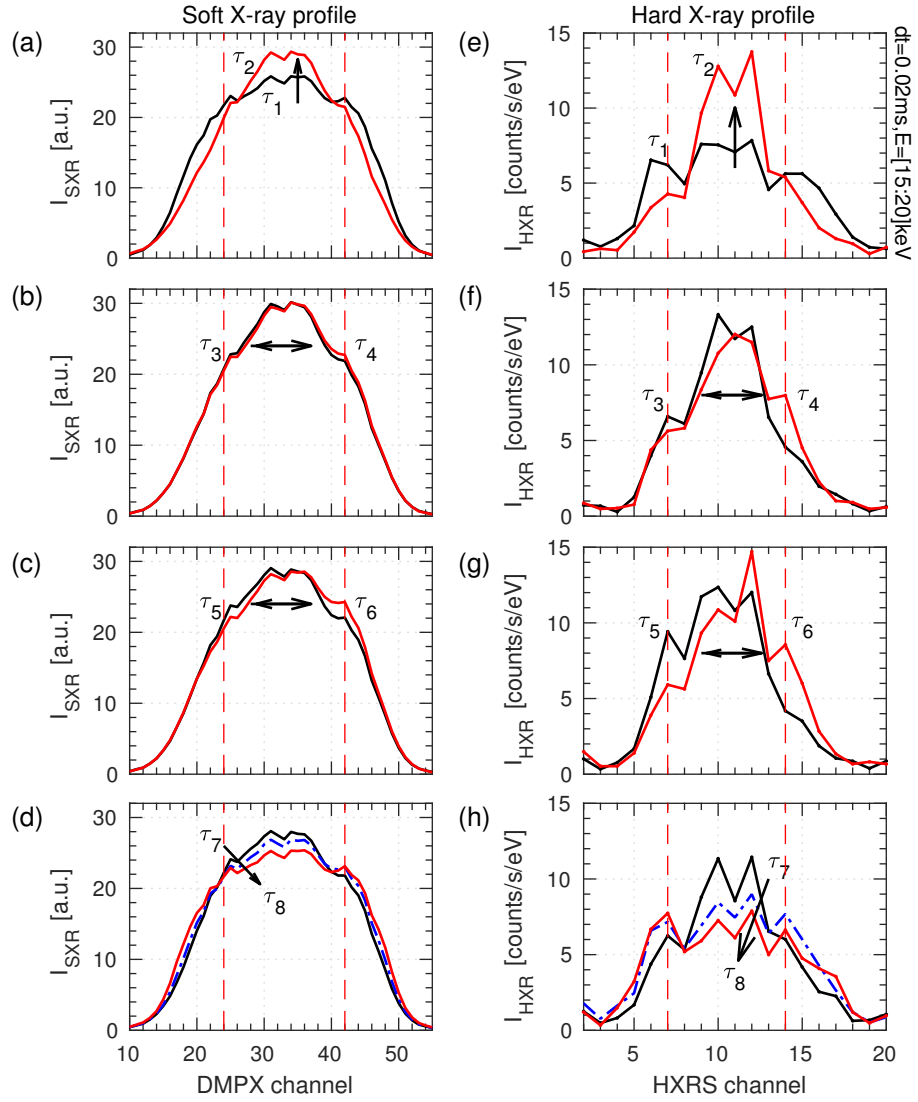


Figure 4.5 – Soft X-ray and hard X-ray profiles at selected times, as indicated in Figure 4.4.

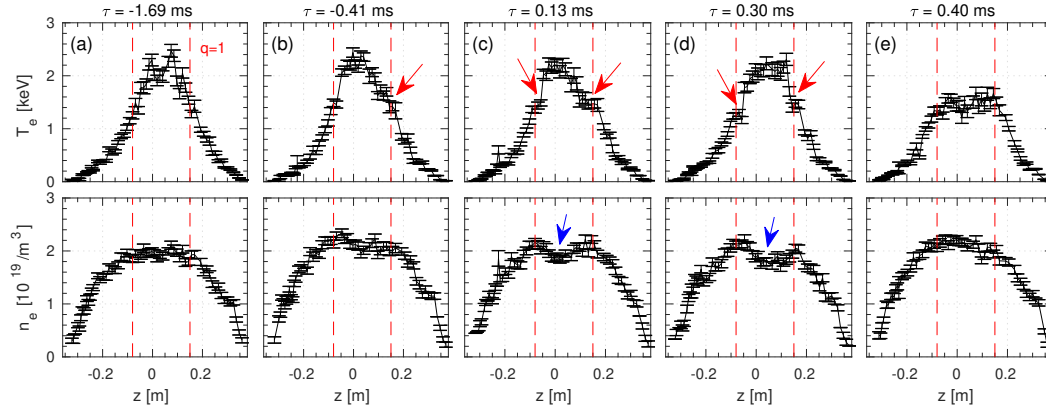


Figure 4.6 – Electron temperature and density profiles measured by the Thomson scattering system, at selected relative times (τ): (a) during the ramp-up phase, (b-d) during the fishbone-like oscillation, (e) after the crash.

with blue arrows in Figure 4.6), increasingly so towards the end of the fishbone oscillation phase. In Figure 4.6 (d), the difference of the density in between the core and the $q = 1$ surface is 19% of the density at the $q = 1$ surface. This is possibly due to the electron loss during the oscillation phase. The I_{SXR} and I_{HXR} of the central channels also show a decrease during the oscillation phase. However, since the I_{SXR} and I_{HXR} are line-integrated data, it is not possible to directly compare these profiles to the localized Thomson scattering measurement. The line-integrated I_{SXR} and I_{HXR} profiles are inverted using the Abel-inversion scheme in the next section 4.3.3.

At the end of the oscillation phase, in Figure 4.5 (d,h), the central I_{SXR} and I_{HXR} drop at the same time, similar to the behavior expected for a standard sawtooth crash. During the crash, both I_{SXR} and I_{HXR} profiles in the core decrease in amplitude and the signals of the outer channels increase, possibly because of the expelled electrons during the crash. The ECCD peaks decrease as well but remain distinctively visible. After the crash, the electron temperature inside the $q = 1$ surface drops and the electron density profile is no longer hollow (Figure 4.6 (e)).

The time evolution of I_{HXR} for the higher energy bins is presented in Figure 4.7 (a-d) for channels 11 and 14. The fishbone-like oscillation, as well as the ramp-up and relaxation of the central I_{HXR} , can be observed in the lower energy range but it becomes more difficult to distinguish these from the noise as the energy increases, since the number of ECCD-accelerated electrons decreases as their energy increases. The statistics thus become insufficient to determine whether these higher-energy electrons also undergo the fishbone-like oscillation. This diagnostic limitation can be compensated by the vertical ECE diagnostic, which receives ECE from suprathermal electrons at the third harmonic, directly above the magnetic axis location at the top of the tokamak. Although the measurement is integrated in space along the vertical

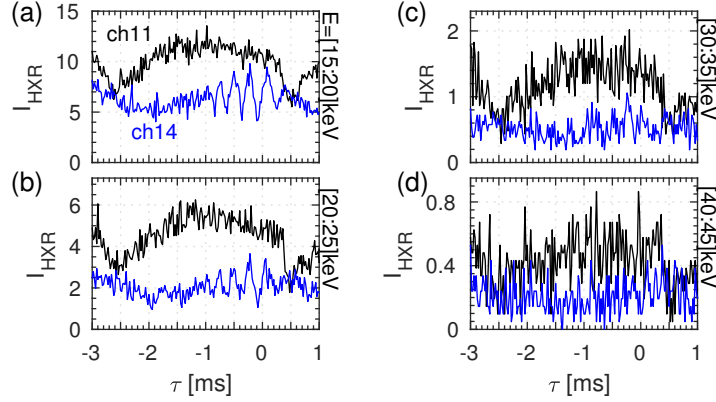


Figure 4.7 – (left) Time evolution of the hard X-ray signal at different energy bins: (a) $E = [15:20]$ keV, (b) $E = [20:25]$ keV, (c) $E = [30:35]$ keV, (d) $E = [40:45]$ keV. The time bin is 0.02 ms.

line, the received ECE radiation at each frequency is exclusively emitted from electrons with a specific energy, unlike the continuum bremsstrahlung radiation emitted in the hard X-ray range.

The vertical-ECE diagnostic was operational in the discharge #62962, which is a repeat of #62609 with higher density: the average density measured by FIR at $R = 0.9$ m is up from $1.78 \times 10^{19}/m^3$ to $1.99 \times 10^{19}/m^3$. The LIUQE equilibrium reconstruction shows that the $q = 1$ surface is located at the same location as #62609. In Figure 4.8, conditionally averaged fishbone-like oscillations observed in several diagnostics are presented for the discharge #62962, similarly to the data shown in Figure 4.4. In this discharge, the electron fishbone lasted 900 ms, which is shorter than in #62609 (1400 ms), reducing the statistics. Also because of the increased electron density, the hard X-ray count rate is lower than for #62609. Therefore the time bin length for the conditional averaging is larger in #62962 than #62609 (0.03 ms compared to 0.02 ms), as presented in Figure 4.8 (e). The fishbone-like oscillation is also observed in the several channels of the vertical ECE system, which correspond to different energetic electron energy ranges, as indicated in Figure 4.8 (d). This shows that electrons up to ~ 100 keV exhibit the fluctuation as observed in other diagnostics.

4.3.3 Abel-inversion of the soft X-ray and hard X-ray profiles

In order to study the redistribution of electrons over flux surfaces, the line-integrated soft X-ray and hard X-ray measurements need to be inverted. In both I_{SXR} and I_{HXR} measurements presented in section 4.3.2, no lines of sight cross one another because only a single camera is used in each measurement to receive the line-integrated signals. In this case Abel-inversion can be used to invert the data [80], with the assumption of uniform emissivity of I_{SXR} or I_{HXR}

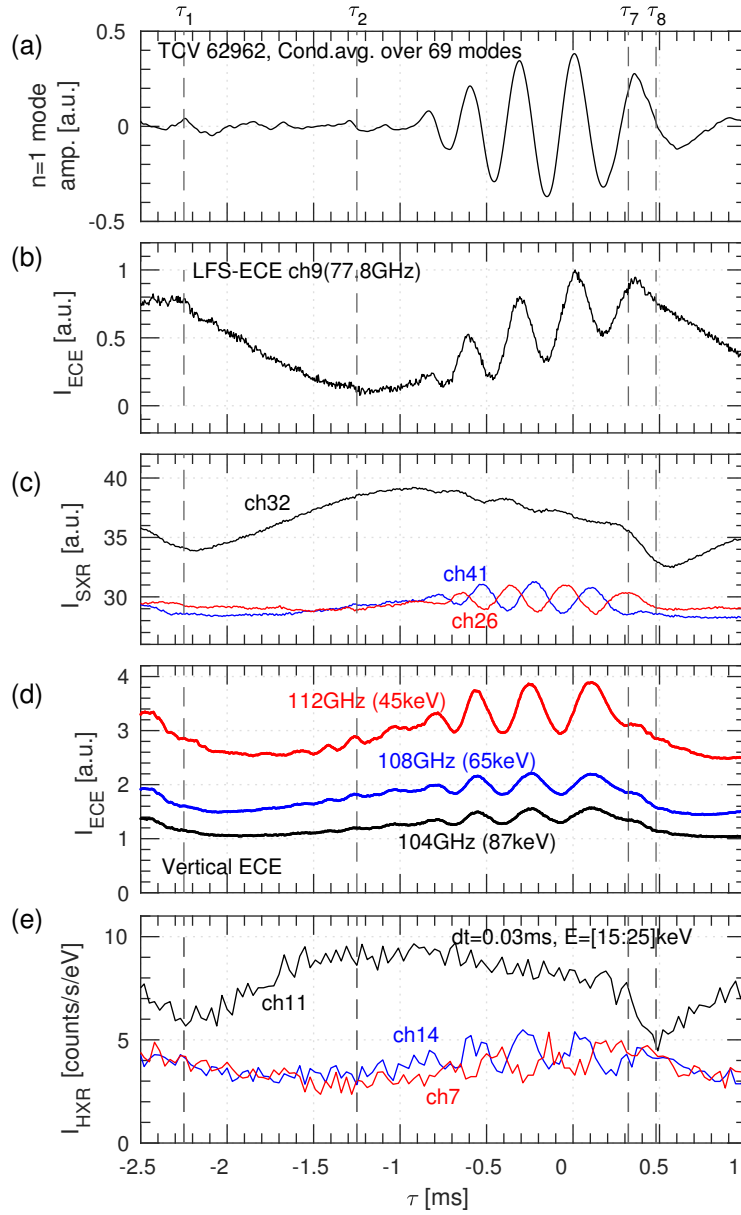


Figure 4.8 – Conditional averaging of fishbone-like perturbations in (a) the $n = 1$ mode amplitude from the SVD analysis of the magnetic probe array, (b) ECE from thermal electrons, (c) soft X-ray, (d) ECE from suprathermal electrons, (e) hard X-ray count rate. Relative time points shown as dashed lines are: $\tau_1 = -2.25\text{ms}$, $\tau_2 = -1.25\text{ms}$, $\tau_7 = 0.32\text{ms}$, $\tau_8 = 0.48\text{ms}$.

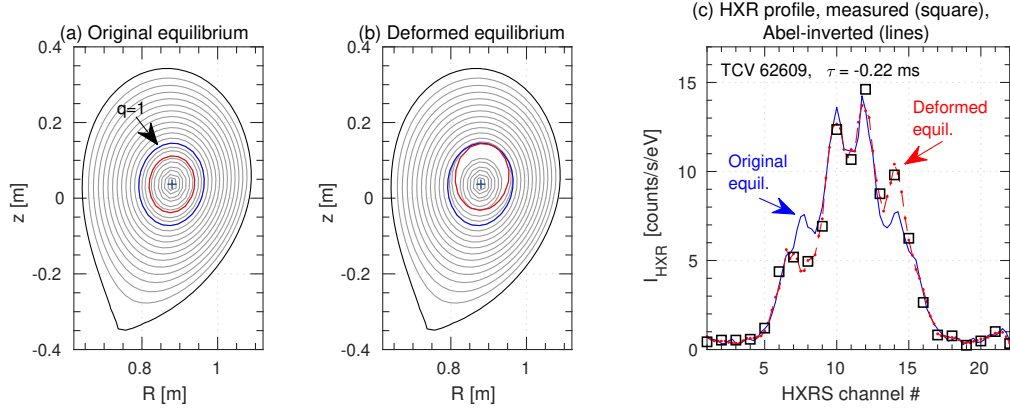


Figure 4.9 – (a) Equilibrium reconstructed by LIUQE, (b) deformed equilibrium model used in the Abel-inversion. (c) Experimental hard X-ray profile (square) and reconstructed profiles obtained by line-integrating the Abel-inverted profiles, using the default equilibrium model (blue solid line) and the helical equilibrium model (red dashed line).

over the poloidal angle at each flux surface.

When the hard X-ray lines of sight cover the poloidal plane, trapped electrons are the main contributors to the detected hard X-rays, due to their preferred radiation pattern towards the propagation direction [58]. In the discharge #62609, the bounce frequency of trapped electrons (at $|p_{\parallel}|/p|_{\theta=0} = 0.2$) near the $q = 1$ surface was 2.2 MHz for the thermal electrons at 2.4 keV, and 6.4 MHz and 14.4 MHz for the suprathermal electrons at 20 keV and 100 keV, respectively. Thus we may assume that we measure the orbit-averaged hard X-ray emission.

In fact the hard X-ray emission in the poloidal plane exhibits an asymmetry from high field side to low field side due to conservation of the magnetic moment over a collisionless particle orbit, which reduces the parallel energy on the high field side [104]. Another possibility that can give rise to an asymmetry is the helicity of the magnetic field, but in tokamak plasmas, this effect is negligible [57]. A previous study of these effects, using a vertically viewing hard X-ray camera and using Fokker-Planck modeling, showed that the assumption of poloidal symmetry in the hard X-ray emission for Abel-inversion is justified except in extremely off-axis RF deposition cases [57]. This effect is studied for this discharge as well in section 4.5.1, in the Fokker-Planck modeling of this discharge.

Since the emission is assumed to be uniform at each flux surface, it is important to have an appropriate magnetic equilibrium that reflects the observed mode structure. In section 4.3.2, during the fishbone oscillation phase, localized flattening of the electron temperature profile is observed (Figure 4.6), due to the helical mode structure. As the rotating crescent-shaped mode moves past the view-line of the Thomson scattering system, the width of the locally

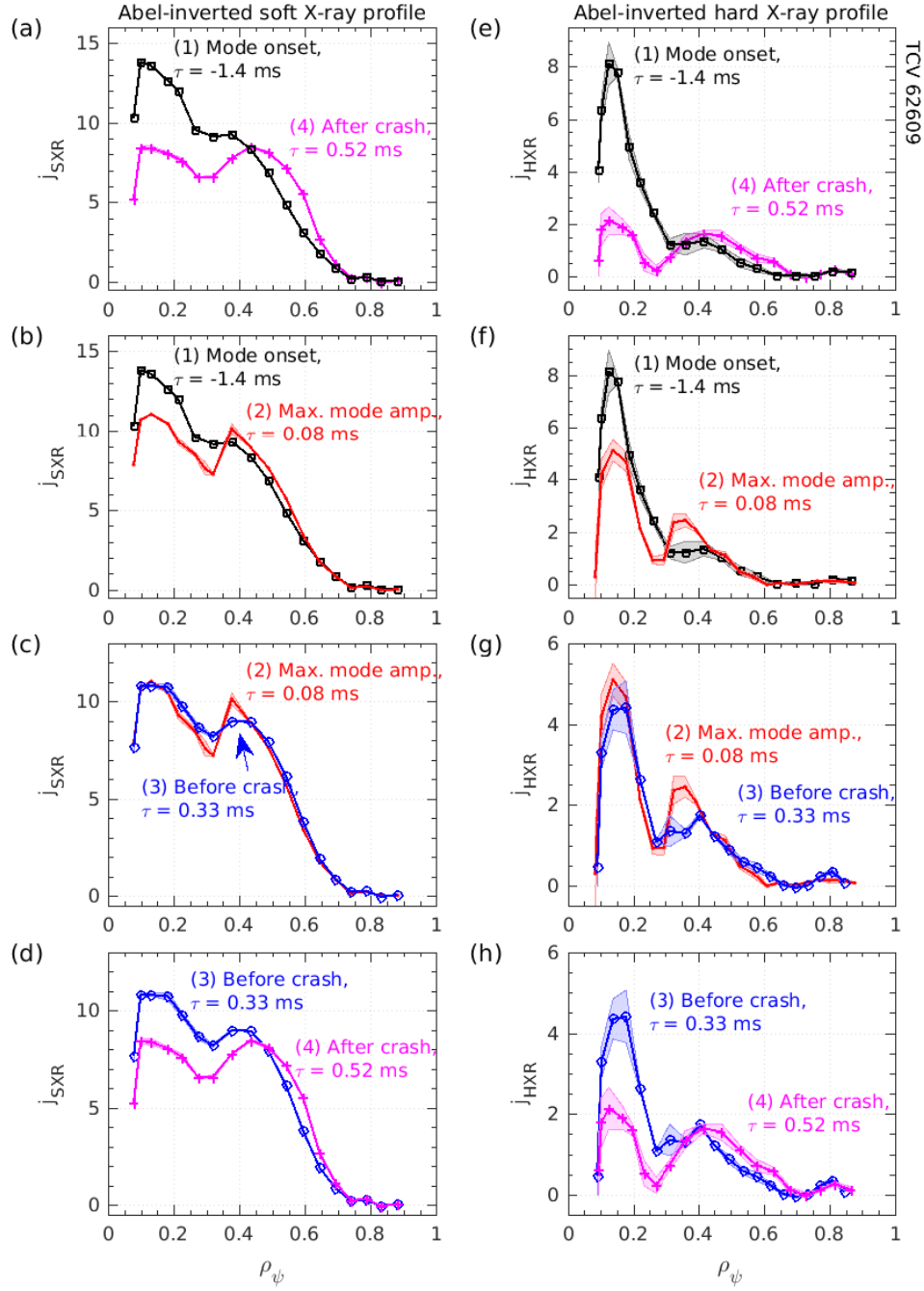


Figure 4.10 – Abel-inverted soft X-ray and hard X-ray profiles for selected time points.

4.3. Experimental observation of the fishbone oscillation

flattened temperature region changes. This observation has been reflected in the modeling of a deformed magnetic equilibrium profile with accurate phasing. Figure 4.9 (a) shows the original equilibrium reconstructed by the code LIUQE and Figure 4.9 (b) shows an example of deformed equilibrium. In Figure 4.9 (b), the crescent-shaped structure is positioned at $\rho_\psi = 0.26$ (red line) and the x-point is rotated by 261° from the low field side, in order to match the width and the phase of the oscillation in the measured hard X-ray profile in Figure 4.9 (c). The flux surfaces inside $\rho_\psi = 0.26$ are unchanged.

In order to assess the inversion result, the line-integrated I_{HXR} data are reconstructed from the Abel-inverted hard X-ray profiles, in Figure 4.9 (c). It is clear that both models can reconstruct the symmetric signals near the magnetic axis. However, in the fluctuation region near the $q = 1$ surface, near channels 7 and 14, the experimental hard X-ray profile can be reconstructed only using the deformed equilibrium. The root-mean-square errors are 0.97 and 0.44, for the original equilibrium and deformed equilibrium, respectively. In this reconstruction, 22 flux surfaces are included in the equilibrium. Since the hard X-ray camera has fewer measurement points (24 channels in total) than the soft X-ray measurement (64 channels in total), virtual lines of sight are added in between real lines of sight, and the measured data are interpolated on these virtual channels. A least-squares method is used to find a solution.

Figure 4.10 presents the Abel-inverted soft X-ray and hard X-ray profiles, j_{SXR} and j_{HXR} , for four selected time points: (1) at the onset of the oscillation, which is at the end of the ramp-up phase, (2) in the middle of the fishbone oscillation phase, around the maximum of the oscillation amplitude, (3) at the end of the oscillation phase, right before the sudden crash, (4) after the sudden crash. The data are plotted for pairs of adjacent time points, to allow direct comparisons and an assessment of the time evolution. The relative time τ is identical to that given in Figure 4.4.

During the ramp-up phase, the ECCD peaks in j_{SXR} and j_{HXR} near $\rho_\psi \sim 0.1$ increase (Figure 4.10 (a,e)). The intensity outside $\rho_\psi \sim 0.4$ decreases as the electrons outside the ECCD deposition area, which accumulated during the previous crash, are lost. Since the $m/n = 1/1$ mode grows at this point, (1), the fishbone stability study in section 4.5 will be based on the electron distribution function of this point.

During the first half of the fishbone oscillation phase, the ECCD peak in both j_{SXR} and j_{HXR} decreases in Figure 4.10 (b,f). The outer peak increases at $\rho_\psi \sim 0.36$, with the change in j_{HXR} (99%) more significant than that of j_{SXR} (13%). In the oscillation phase, the Abel-inversion is based on the deformed equilibrium model, as presented in Figure 4.9. The helical mode structure is positioned at $\rho_\psi = 0.26$, between the two peaks. This shows that the core population decreases during the mode rotation, and the expelled electrons accumulate outside the rotating helical structure. The radial displacement of the electrons can be related to the energy loss of the electrons as a result of a resonant interaction with the mode [122]. In section 4.5, the possibility of the resonant destabilization will be demonstrated by solving a linear fishbone dispersion relation. A further simulation during the non-linear phase is needed in

the future in order to investigate the redistribution of the electrons.

During the second half of the fishbone oscillation phase (Figure 4.10 (c,g)), there is no significant change in the ECCD peaks, but the other peak at $\rho_\psi \sim 0.36$ is reduced to the initial level of (1). This may be explained by the decreased ECCD peak at (2), compared to (1): the effective electron source is smaller than in (1), thus the transport loss of the accumulated electrons at $\rho_\psi \sim 0.36$ can no longer be fully compensated. This suprathermal loss outside the mode structure can be attributed to either collisional slowing down or anomalous transport [41, 46], depending on the level of turbulent driven fluctuations.

The end of the oscillation is followed by the sudden loss of the central pressure, as indicated in Figure 4.10 (d,h). The ECCD peaks in both j_{SXR} and j_{HXR} decrease significantly but the central value ($\rho_\psi \sim 0$) of j_{SXR} does not drop to zero because of the thermal electron contribution. In j_{HXR} , the central value does drop to nearly zero but the ECCD peak still exists, because the EC wave is constantly applied during the discharge. The other peak outside $\rho_\psi \sim 0.26$ still remains, due to the loss of the central electrons.

4.3.4 The different response of passing and trapped electrons

Since suprathermal electrons emit bremsstrahlung radiation preferentially in the direction of their propagation, in the hard X-ray measurement with a poloidally oriented camera, forward emission of the bouncing trapped electrons is the main contributor to the collected hard X-ray photons, along with the perpendicular bremsstrahlung emission of passing electrons. As presented in Figure 4.1 (c), the TCV hard X-ray camera can be rotated toroidally so some lines of sight can be parallel to the toroidal magnetic field lines. The TCV discharge #62609 analyzed so far was repeated with the hard X-ray camera in the toroidal orientation, as shown in Figure 4.11 (c). In this case forward bremsstrahlung emission of passing electrons is the main contributor to the photon detection of channel 3 (Tor-ch3), as well as perpendicular emission of trapped electrons. Since the intensity of backward bremsstrahlung emission is negligible compared to that of forward or perpendicular emission, the perpendicular emission of trapped electrons is expected to be dominant in the photon detection of channel 22 (Tor-ch22).

During the fishbone oscillation phase, I_{HXR} of Tor-ch3 stays relatively constant while Tor-ch22 exhibits a fishbone oscillation as observed in the poloidal orientation (Figure 4.11 (b)). The constant signal observed in Tor-ch3 can be attributed to the fact that there is no significant loss of passing electrons and no accumulation of passing electrons outside the helical structure. If passing electrons were also expelled during this phase, I_{HXR} would have shown even stronger fluctuation than that of Tor-ch22. This is possibly due to the highly constrained conditions for effective passing electron resonant interaction [123] (see also section 4.5.2).

4.3. Experimental observation of the fishbone oscillation

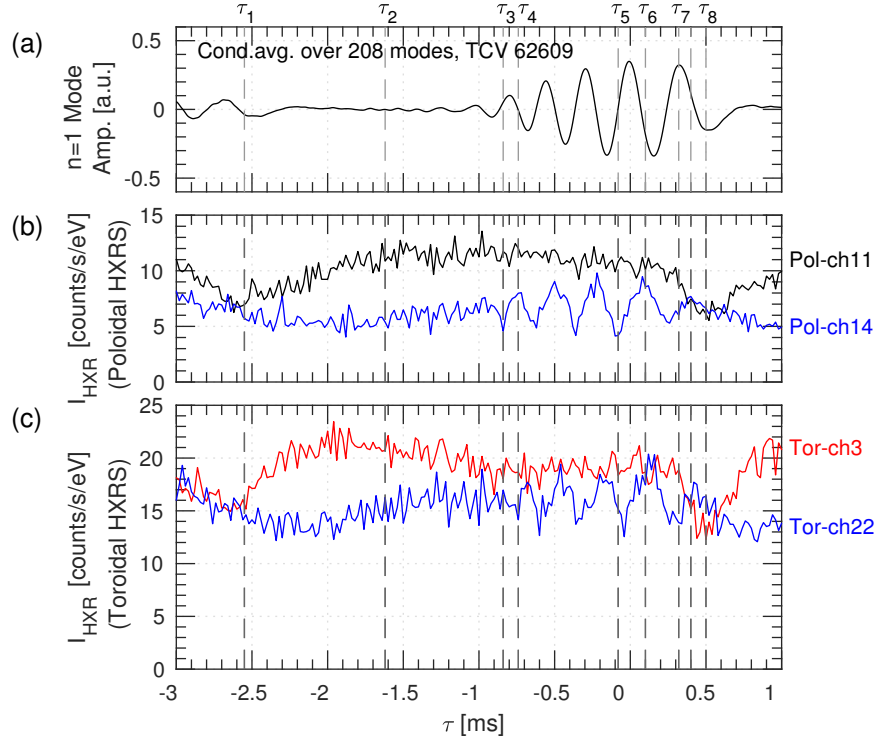


Figure 4.11 – Conditional averaging results of (a) magnetic field perturbation, (b) hard X-ray signals in channels 11 and 14 in the poloidal orientation, (c) hard X-ray signals in channels 3 and 22 in the toroidal orientation. In the hard X-ray analysis, $dt = 0.02$ ms and $E = [15:20]$ keV. The relative time points from τ_1 to τ_8 are identical to those in Figure 4.4.

4.4 The effect of ECCD parameters on the onset of the fishbone instability

In the previous section, we have seen that during the fishbone oscillation phase, core electrons are expelled and the mode frequency chirps down. The non-linear growth of the $m/n = 1/1$ mode can be closely related to the redistribution of the suprathermal electrons. In this section, we study the behavior of the fishbone oscillation in globally varying experimental conditions: we present results from an ECCD power scan in section 4.4.1, and from a magnetic field scan in section 4.4.2.

4.4.1 ECCD power scan

Based on the discharge #62609 analyzed in the previous section, the ECCD power was scanned in #62755, as shown in Figure 4.12 (a). The EC power of 750 kW is turned on at 0.4 s, then from 0.6 s at each 0.1 s, the power is decreased by 50 kW, keeping the injection angle fixed. The power transition at each step takes about 4 ms. The plasma current is kept constant at 210 kA and the LIUQE equilibrium reconstruction shows that the $q = 1$ surface is located at $\rho_\psi = 0.48 \pm 0.01$ throughout the discharge. The toroidal magnetic field is kept constant at 1.34 T from 0.5 s. The plasma toroidal rotation frequency near the $q = 1$ surface is measured to be 4.1 ± 0.8 kHz during ECCD, in the plasma current direction. The directions of the plasma current, toroidal magnetic field, and toroidal plasma rotation are identical as indicated in Figure 4.1 (a). The suprathermal electron population can be detected in the hard X-ray camera, as shown in Figure 4.12 (d). The suprathermal population decreases as the EC power decreases. The hard X-ray camera was in the poloidal orientation, so the line of sight of channel 11 goes through the magnetic axis.

In this discharge, the $m/n = 1/1$ mode oscillation is also observed near the $q = 1$ surface during the ECCD phase. Figure 4.12 (e) shows the spectrogram of the $n = 1$ mode, obtained from the SVD analysis of the magnetic probe data from the toroidal array. As the EC power is turned on, the mode appears with relatively high frequency in the beginning, and the mode frequency decreases as the ECCD power decreases. The amplitude of the mode oscillation, which can be seen from the power of the Fourier spectrum indicated in color (blue and red correspond to low and high spectral power, respectively), shows that the mode amplitude also changes over time, but does not decrease monotonically as the frequency does: the mode amplitude has a maximum value at ~ 1.0 s.

The $m/n = 1/1$ perturbation and the spectrogram are presented in detail in Figure 4.13, for three selected time windows with different EC powers. In all time windows, the fishbone-like bursts are accompanied by the non-standard sawtooth (I_{SXR} of DMPX ch32). The mode frequency is confirmed to decrease, following the decrease in EC power from 750 kW to 350 kW, from the first to the third column. In the first column, distinctive sawtooth precursors at ~ 5 kHz are observed at the end of the non-standard cycle. This supports the conclusion that

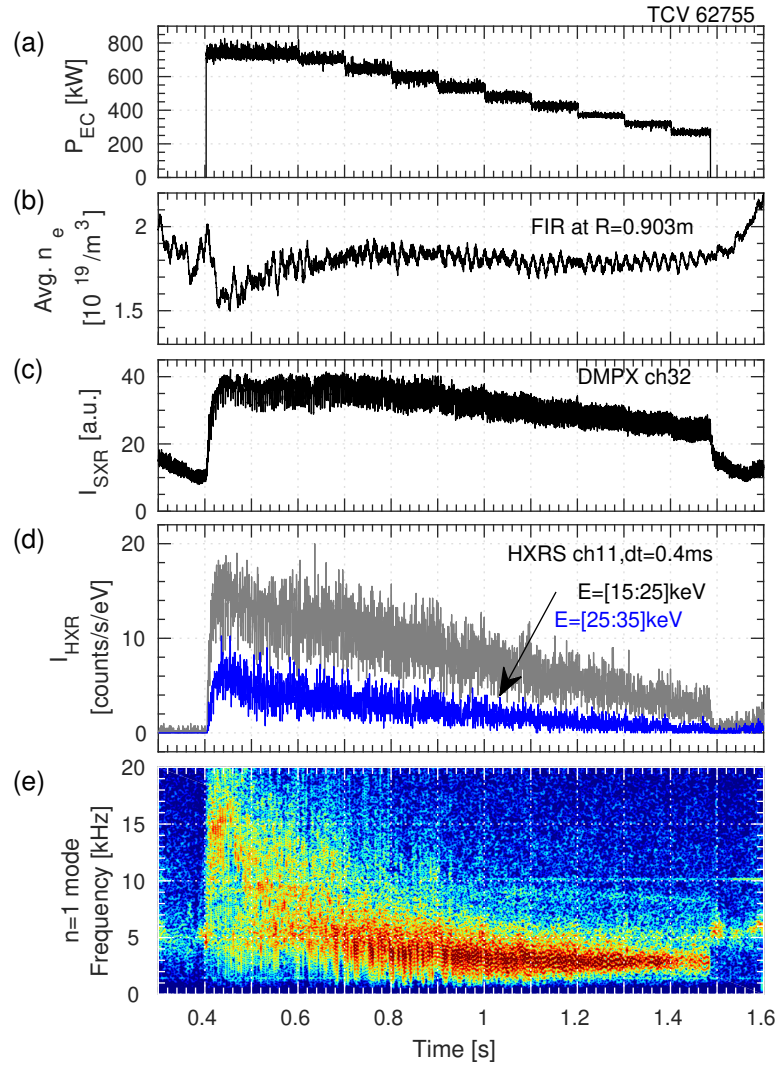


Figure 4.12 – Time evolution of plasma parameters in #62755: (a) ECCD power, (b) line-averaged electron density, (c) central soft X-ray, (d) hard X-ray count rate, (e) spectrogram of the $n = 1$ mode detected by the toroidal magnetic probe array.

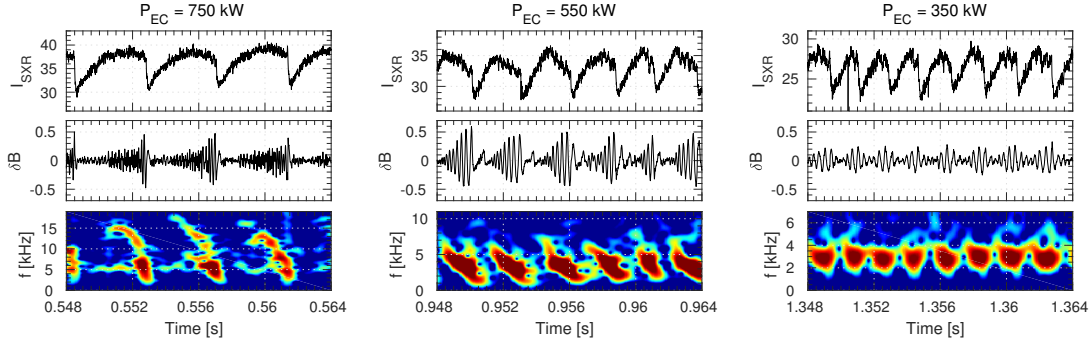


Figure 4.13 – Soft X-ray signal I_{SXR} of channel 32, the $n = 1$ mode amplitude in the magnetic probe (δB), and Fourier spectrogram of δB are plotted.

the observed fishbone modes are distinct from the standard sawtooth precursors, which have the same $m/n = 1/1$ mode structure. The stability properties of this discharge at varying EC power are assessed in section 4.5 by solving the linear fishbone dispersion relation.

The period of the non-standard sawtooth cycle decreases with diminishing ECCD power. As analyzed in section 4.3, the non-standard sawtooth period is directly related to the fishbone oscillation duration: after the ramp-up phase, the central I_{SXR} saturates or decreases during the mode oscillation, then the cycle ends with a sudden crash at the end of the fishbone oscillation. The suprathermal electron population, which depends on the EC power level, destabilizes the mode but at the same time is ejected by interacting with the mode. Therefore a balance between the acceleration and loss of suprathermal electrons determines the fishbone period, as for ion fishbones [124]. A further analysis that considers the non-linear growth of the fishbone mode is needed to predict the mode cycle.

4.4.2 Magnetic field scan

In order to study the effect of the ECCD location on the behavior of the $m/n = 1/1$ mode oscillation, we have scanned the localized ECCD (750 kW) deposition location from the high field side to the low field side, by varying the toroidal magnetic field, as presented in Figure 4.14. In the discharge #62927, the magnetic field intensity was ramped down from 1.42 T to 1.32 T by 0.01 T at every 0.1 s, thus the ECCD location is moved towards the high field side. The ray tracing calculation shows that the absorbed EC power (P_{EC}) has a gaussian shape and the full width half maximum (FWHM) is ~ 0.25 . In Figure 4.14 the localized ECCD location corresponds to the peak position of the EC power profile. As the ECCD location moves out, the suprathermal population and the mode frequency decrease. This relation between the suprathermal population and the mode behavior is similar to the result obtained in the previous section during the ECCD power scan.

In the discharge #62925, the magnetic field was ramped up from 1.42 T to 1.52 T by 0.01 T at

4.4. The effect of ECCD parameters on the onset of the fishbone instability

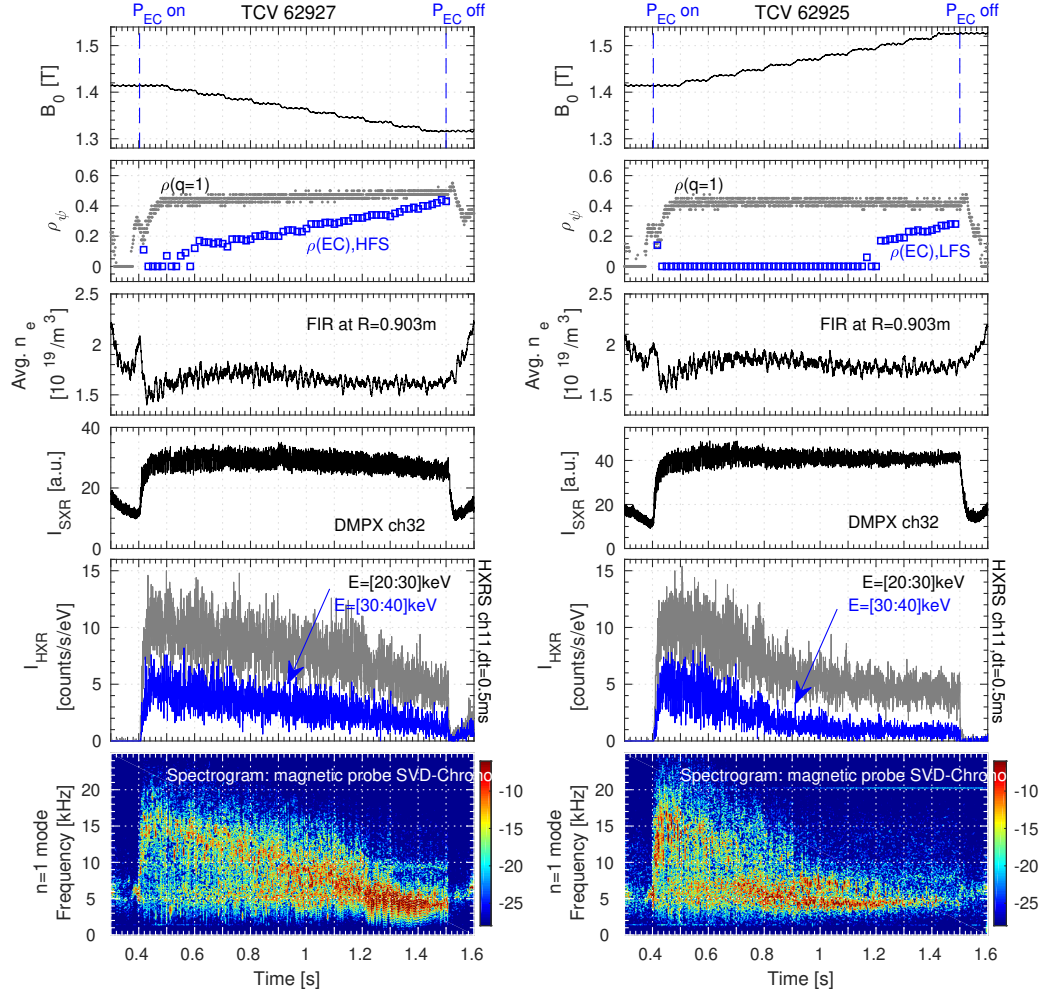


Figure 4.14 – Toroidal magnetic field ramp-down discharge #62927 (left) and ramp-up discharge #62925 (right). From top to bottom, each row corresponds to: toroidal magnetic field, the $q = 1$ surface location and the peak P_{EC} location, line-averaged electron density, central soft X-ray intensity, hard X-ray count rates from different energy bins, and the spectrogram of the $n = 1$ mode oscillation.

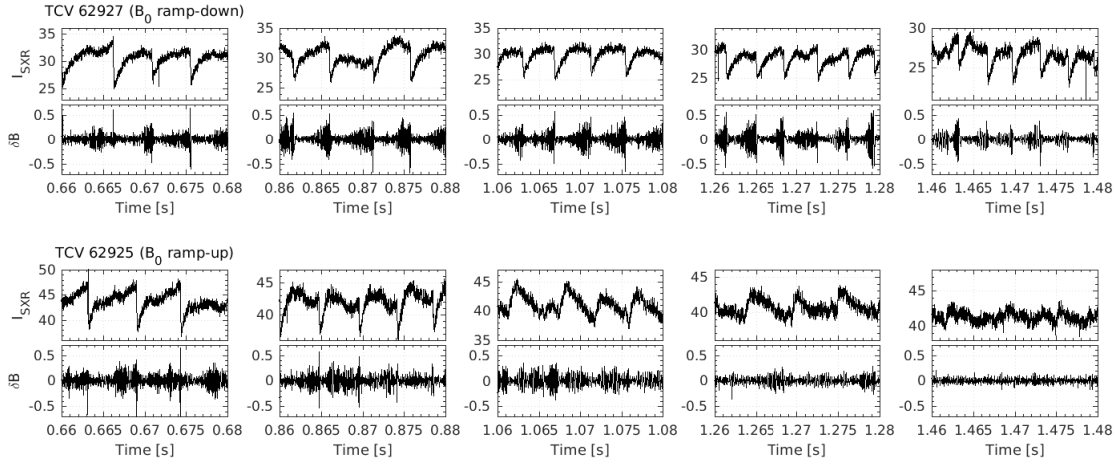


Figure 4.15 – Central soft X-ray intensity I_{SXR} , from DMPX channel 32, and the $n = 1$ mode perturbation from the SVD analysis of the toroidal magnetic probe array, for selected time windows of #62927, B-field ramp-down discharge, and #62925, B-field ramp-up discharge.

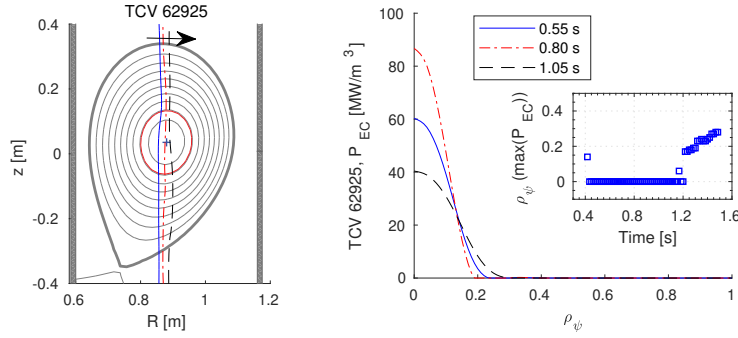


Figure 4.16 – (Left) EC resonance layer shifts and (right) absorbed EC power profiles at selected times of discharge # 62925.

every 0.1 s, thus the ECCD location moves towards the low field side. As one can see in Figure 4.16, the EC resonance layer passes the magnetic axis, thus the EC power peak is concentrated at the magnetic axis from ~ 0.4 s to ~ 1.2 s. Nevertheless, it should be kept in mind that the EC resonance layer shifts, as can be seen from the changing width of P_{EC} in Figure 4.16. The absolute level of I_{SXR} changes compared to #62927 because the measurement gain is different in the two discharges. The hard X-ray data shows that the suprathermal electron population also decreases, in the same way as in the B-field ramp-down case, but at a faster rate: I_{HXR} of $E = [20:30]$ keV drops down to 5 at only 0.8 s when the ECCD is still localized near the magnetic axis, while in #62927 I_{HXR} reaches 5 at 1.4 s, when ECCD is localized at $\rho_\psi \sim 0.4$. As the suprathermal electron population decreases, the mode frequency also decreases as observed in the B-field ramp-down discharge, and the mode almost disappears after 1.3 s.

4.4. The effect of ECCD parameters on the onset of the fishbone instability

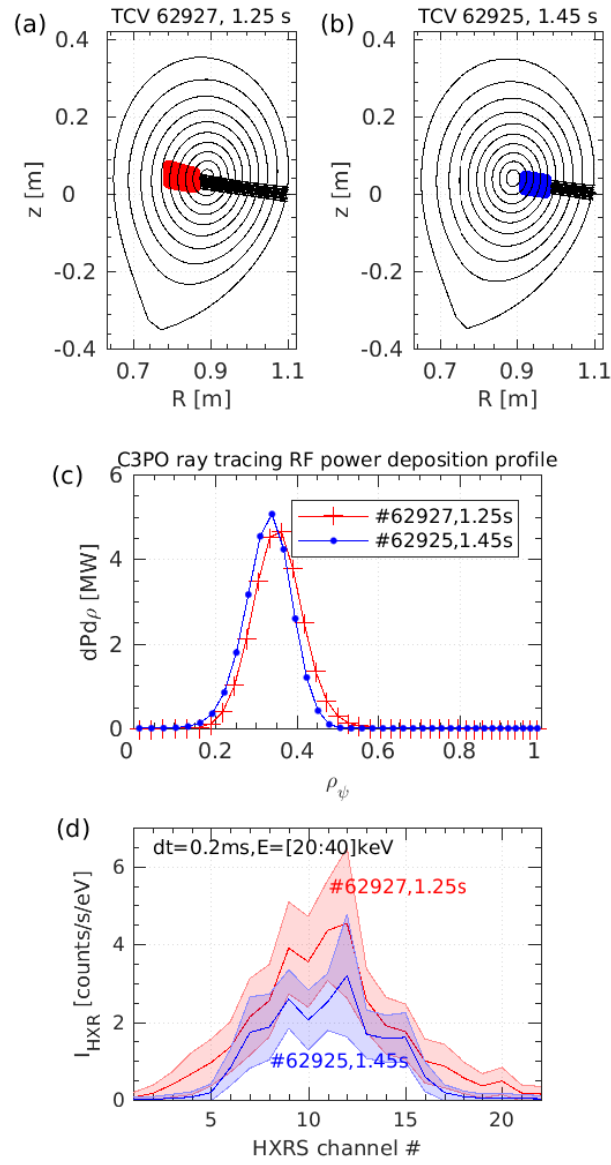


Figure 4.17 – Poloidal ray tracing trajectories of (a) high field side ECCD and (b) low field side ECCD. (c) The RF power deposition profiles. (d) Averaged hard X-ray count rate profiles for the two time points shown in (a) and (b).

The changing mode behavior, as well as the ECCD location scan, has an effect on the central plasma relaxation, as presented in Figure 4.15. In the high field side ECCD case (B_0 ramp-down), the central plasma relaxation keeps the saturated-sawtooth shape [118], and the standard sawtooth precursor is often separated from the fishbone-like perturbation. In the low field side ECCD case (B_0 ramp-up), the saturated shape transitions to an inverted shape, and then no significant central plasma relaxation is found when the ECCD is located at the outermost location.²

In Figure 4.17, an example of the asymmetric suprathermal electron distribution is presented for the low field side and the high field side ECCD cases. At 1.25 s of #62927 (Figure 4.17 (a)), the ECCD is localized at $\rho_\psi \sim 0.35$ on the high field side and at 1.45 s of #62925 (Figure 4.17 (b)), the ECCD is localized also at $\rho_\psi \sim 0.35$ but on the low field side. In Figure 4.17 (d), the hard X-ray profiles collected at every 0.2 ms are averaged at 1.25 ± 0.5 s in #62927 and at 1.45 ± 0.5 s in #62925, in the energy bin of $E = [20:40]$ keV. The two profiles show similar peak positions near hard X-ray channels 9 and 12, because the ECCD is localized at $\rho_\psi \sim 0.35$ in both cases. However, the core I_{HXR} from the high field side ECCD is higher than that from the low field side ECCD. This can be attributed to the electron trapping effect, which decreases the ECCD efficiency due to the fast bounce motion of the trapped electron fraction [43, 125, 126], which hinders electrons from absorbing energy from the EC beam. This effect is stronger on the low field side because of the higher trapped electron fraction. In addition, the I_{HXR} profile of the high field side case is broader than that of the low field side, as seen on the channels outside 7 and 15. This can be due to the stronger $m/n = 1/1$ mode activity in the high field side ECCD case, which regularly expels electrons, as observed in section 4.3.

4.5 Numerical analysis of the $m/n = 1/1$ mode

In order to assess the stability of the fishbone mode during the ECCD discharges in TCV, the plasma is modeled using the three-dimensional relativistic bounce-averaged Fokker-Planck solver LUKE [77], with the aid of a hard X-ray synthetic diagnostic [57], in section 4.5.1. The electron distribution function is used to solve the linear fishbone dispersion relation using the code MIKE [18], in section 4.5.2. The effect of the electron distribution function change on the mode behavior is studied as well.

4.5.1 Fokker-Planck modeling of the experiment

Fokker-Planck modeling of the plasma has been performed at the mode onset of the discharge #62609, which corresponds to the relative time point τ_2 in Figure 4.4 at the end of the ramp-up phase, when the $m/n = 1/1$ mode oscillation starts to grow. The electron temperature and density profiles from the Thomson scattering system, the plasma equilibrium structure from the LIUQE equilibrium reconstruction, the effective charge from the CXRS diagnostic, and

²A detailed study of non-standard sawtooth oscillations is presented in Appendix C.

the loop voltage measurement are used as input data in the Fokker-Planck solver LUKE [77]. The ray-tracing code C3PO [86] is coupled to LUKE to model the EC wave propagation, and the modeled ray properties are used to build the quasilinear RF diffusion coefficient in the Fokker-Planck calculation. The simulation time and suprathermal electron transport terms are used as free parameters, so the hard X-ray synthetic diagnostic result matches both the amplitude and width of the hard X-ray measurement.

Unlike other Fokker-Planck studies on ECCD discharges where the steady-state solution is considered, a finite Fokker-Planck calculation time is applied in this modeling. If the plasma can be described as a Maxwellian after the collapse, we can apply the ramp-up duration as a simulation time and calculate the electron distribution function from the Maxwellian distribution determined by the given temperature. However, the hard X-ray measurements presented in section 4.2 have shown that the plasma after the crash is in fact not in a Maxwellian state due to the significant fraction of suprathermal electrons remaining after the crash. Therefore the simulation time is adjusted to be longer than the ramp-up period and is set to $\tau_{FP} = 9.6ms$. This is found to be enough to create high energy electrons so the synthetic diagnostic can match the experimental hard X-ray measurement.

The suprathermal electron transport term is left as a free parameter, which plays an important role in modeling the ECCD plasma [41, 46]. The choice of an appropriate transport term is aided by the hard X-ray synthetic diagnostic, using the Fast Electron Bremsstrahlung (FEB) module in the LUKE code [57]. It calculates the bremsstrahlung radiation from the electron distribution considering the magnetic equilibrium, and the photons collected at each detector are calculated by integration along their line of sight for the specific geometry of the diagnostic. Finally, the response function of the CdTe detector is used to transform the received photon spectrum to the pulse spectrum, which can be directly compared to the experimentally measured hard X-ray data.

When no suprathermal electron transport is assumed (T_0 in Figure 4.18 (a)), the reconstructed hard X-ray profiles have two localized ECCD peaks that are larger in absolute value than the measured I_{HXR} . The calculated plasma current $I_{p,T_0} = -230$ kA is also larger than the experimental value $I_{p,exp} = -211$ kA. The broad I_{HXR} profile outside the ECCD area (outside HXRS channels 7 and 14) is not reproduced by the simulation, due to the transport of the suprathermals. The broad I_{HXR} profiles are reconstructed when we introduce a spatially flat transport model (T_{flat} in Figure 4.18 (a)). The radial diffusion parameter is set to $D_{r0} = 1.5m^2/s$, so the calculated $I_{p,T_{flat}} = -211$ kA also matches the experimental value. However, in this case the transport term smoothes out the localized ECCD peaks, such that the core I_{HXR} profiles cannot be reproduced. In addition, the central I_{HXR} shows that the high energy electrons are predicted to be lost more rapidly than in reality, see Figure 4.18 (b).

The Abel-inversion of the soft X-ray and hard X-ray profiles in section 4.3.3 showed that electron transport is enhanced near the helical mode structure during the fishbone oscillation and the sawtooth-like crash. At the onset of the mode, the electrons expelled before the

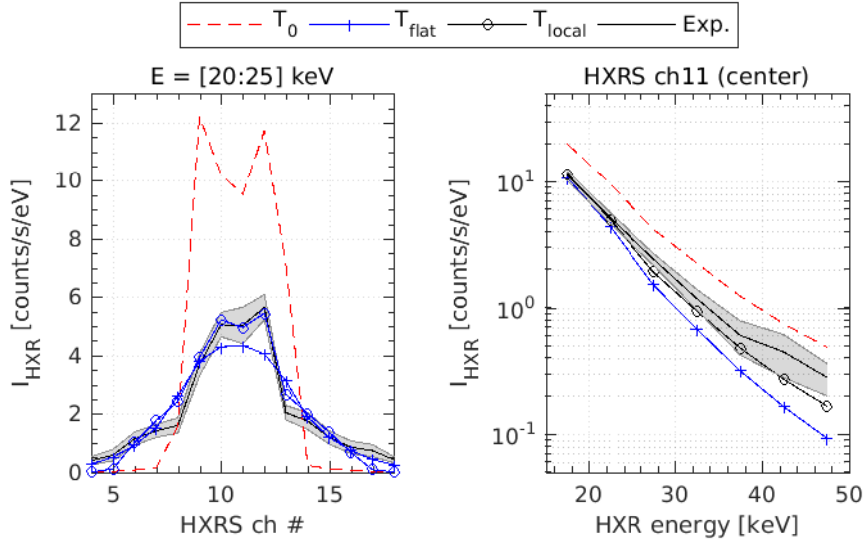


Figure 4.18 – (a) Line-integrated hard X-ray emissivity (count rate) profile from the experimental measurement and from LUKE-FEB, using no transport (T_0), spatially flat transport (T_{flat}), localized transport near the helical mode structure (T_{local}). (b) Energy spectrum of I_{HXR} from the experiment and simulations using different transport models.

ramp-up phase are still not lost, as experimentally observed. Thus a transport channel that is localized at the location of the helical mode structure is implemented. The radial diffusion coefficient is modeled as a Gaussian peak, $D_r(\rho_\psi) = D_{r0} \exp(-(\rho_\psi - \rho_0)/2\sigma^2)$, with $D_{r0} = 5.0$, $\rho_0 = 0.28$, and $\sigma = 0.06$. ρ_0 and σ are determined from the transport channel around $q = 1$, which was observed in Figure 4.10. Then the height of the Gaussian D_{r0} is adjusted, so the calculated $I_{p, T_{local}} = -211$ kA also matches the experimental value. The reconstructed hard X-ray profile using this model (T_{local} in Figure 4.18 (a)) matches well the experimental I_{HXR} , both ECCD peaks and the broad profile outside the $q = 1$ surface. Figure 4.18 (b) shows that the FEB result from the localized transport model agrees well also with the experimental energy spectrum of the central I_{HXR} .

An example of the electron distribution function in velocity space is presented in Figure 4.19 (a). Since ECCD is added in the direction of enhancing plasma current (co-ECCD), where $I_p < 0$, the electron distribution function is significantly distorted in the direction of positive momentum ($p_\parallel > 0$). The radial distributions of suprathermal electrons are presented in Figure 4.19 (b,c), at different positions in the velocity phase space. As observed in the hard X-ray emission, the suprathermal electrons have a peak due to the localized ECCD, and this peak is more distinguished in the higher energy electrons, due to their lower collisionality. The spatial gradient of the electron distribution function is negative ($\partial f_e / \partial \rho < 0$) except inside the ECCD peak, which is localized near the magnetic axis.

This electron distribution function is used to compute the bremsstrahlung radiation in the hard X-ray synthetic diagnostic module [57]. The bremsstrahlung emission in the perpendicular

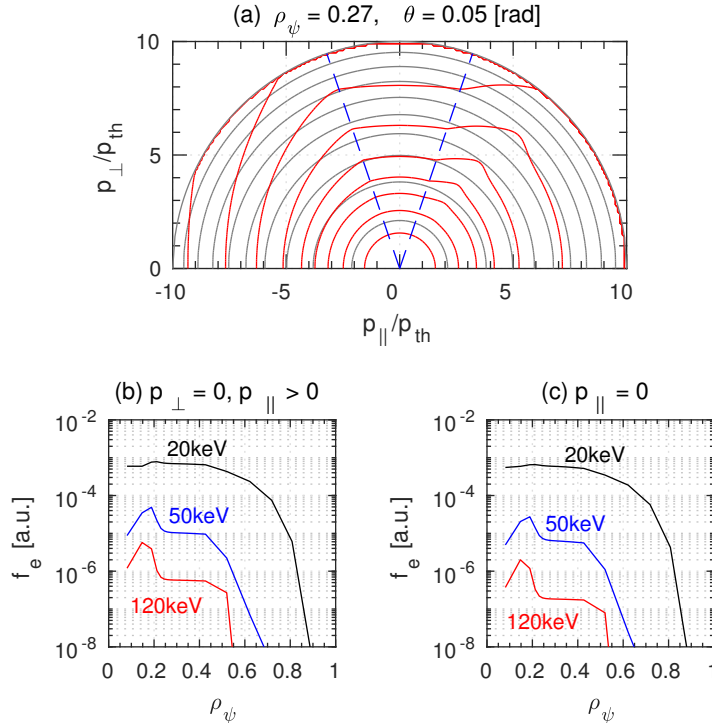


Figure 4.19 – (a) 2-D contour plot of the electron distribution at $\rho_{\psi} = 0.27$ and $\theta = 0.05$. The concentric circles in grey correspond to the Maxwellian distribution. Radial profile of the electron distribution for different energies, selected along (b) $p_{\perp} = 0$, $p_{\parallel} > 0$ and (c) $p_{\parallel} = 0$, of the 2-D distribution.

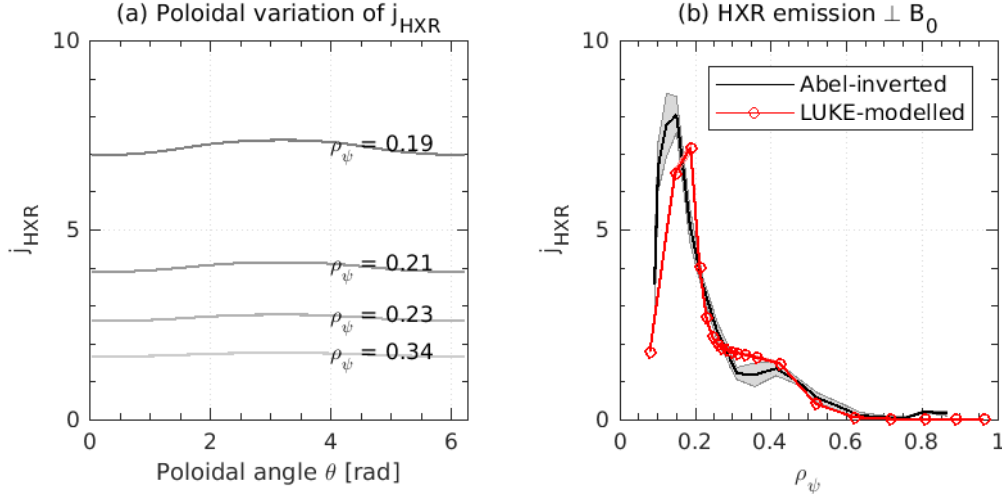


Figure 4.20 – (a) The hard X-ray emission perpendicular to the magnetic field, (b) the modeled hard X-ray emission and Abel-inversion result comparison

direction to the magnetic field, which is emitted in the poloidal plane, is presented in Figure 4.20 (a) as a function of the poloidal angle. The perpendicular hard X-ray emission is stronger at the high-field-side ($\theta = \pi$) because of the magnetic moment as discussed in section 4.3.3, but the poloidal variation in θ is smaller than the variation in between different radial points in ρ_ψ . Thus it can be reasonable to use the Abel-inversion method in section 4.3.3, assuming a uniform emissivity at each flux surface. In Figure 4.20 (b), the modeled hard X-ray emission profile j_{HXR} agrees well with the Abel-inverted profile from Figure 4.10.

4.5.2 Solving the linear fishbone dispersion relation

The Fokker-Planck modeled electron distribution function is used to solve the linear fishbone dispersion relation, $\delta \hat{W}_f + \delta \hat{W}_k(\omega) = \delta I(\omega)$, where ω is the complex frequency of the mode, $\delta \hat{W}_f$ and $\delta \hat{W}_k$ describe the fluid and kinetic components of the potential energy, respectively, and δI includes the physics inside the inertial layer. The code MIKE is used [18], which was developed to solve the linear fishbone dispersion relation. This code is coupled to the Fokker-Planck code LUKE, such that the equilibrium profile and the numerical results from LUKE can be used in solving the linear dispersion relation. In practice, a free parameter $\delta \hat{W}_c$ is added to the dispersion relation to modify the fluid term; this parameter acts as a proxy for the ideal MHD $\delta \hat{W}$. $\delta \hat{W}_f$ and $\delta \hat{W}_k$ are decomposed into thermal and suprathermal particle parts.

For the fixed $\delta \hat{W}_c$ value of 0.004, the result of the calculation is presented in Figure 4.21 (a,b).³ In order to study the effect of the suprathermal electron population on the stability

³A detailed process of solving the dispersion relation is described in Appendix D.

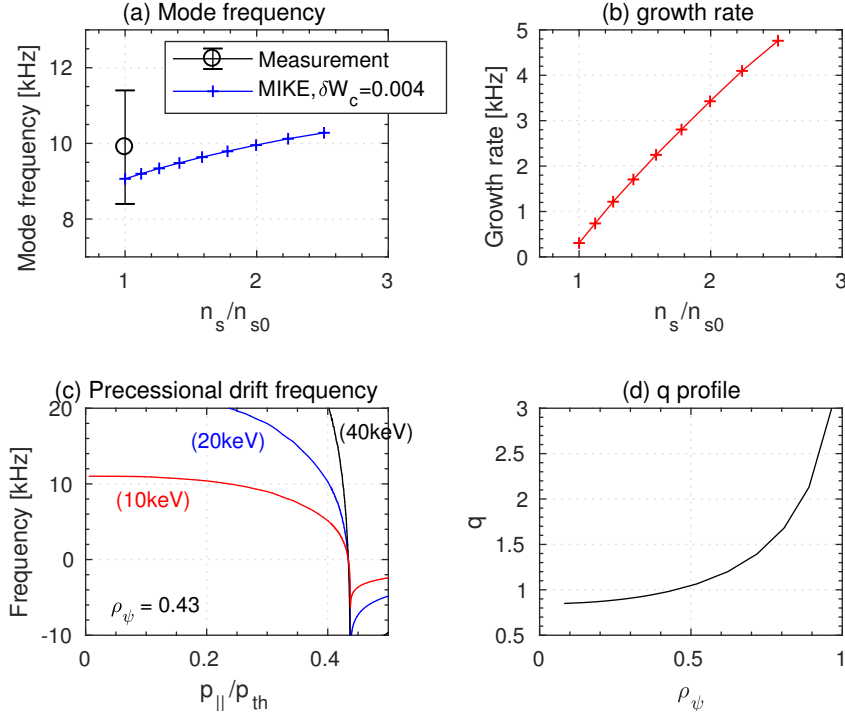


Figure 4.21 – (a) mode frequency and (b) growth rate, are obtained for fixed $\delta\hat{W}_c = 0.004$ and varying suprathermal electron population n_s . (c) Toroidal precessional drift frequency of suprathermal electrons near the $q = 1$ surface, as a function of pitch angle, $p_{||}/p_{th}$. (d) q profile of #62609.

of the mode, the suprathermal electron density n_s is scanned from n_{s0} , which corresponds to the Fokker-Planck modeled electron distribution based on the experiment. In $\delta\hat{W}_k$, these suprathermal electrons are considered collisionless. The predicted mode frequency lies within the error range of the measured mode frequency, and the mode growth rate is positive and increases with n_s . Thus it is clear that the suprathermal electron population destabilizes the fishbone mode. Here the experimentally measured mode frequency is shifted related to the toroidal plasma rotation. Thus the measured mode frequency in the plasma frame can be compared to the frequency predicted by the simulation.

Previously the excitation of the internal kink was attributed to the resonant interaction of barely trapped/passing electrons [17, 66, 70, 73] or deeply trapped electrons [68, 69, 127] with the mode. In the TCV experiment, the mode rotation directions obtained in the experiment and obtained in the simulation are in the electron diamagnetic drift direction. The calculation of the toroidal precessional drift frequency of suprathermal electrons near the $q = 1$ surface, in Figure 4.21 (c), shows that the deeply and moderately trapped electrons rotate in the same direction as the mode. In addition, the q profile (4.21 (d)) is not flat in the $q < 1$ region. It is noted in [123] that although passing and trapped drift precession can be similar in order of magnitude, the passing electron contribution to the dispersion relation is significant only

if $\Delta q \omega_b \sim \langle \omega_{d\psi} \rangle$, where ω_b and $\omega_{d\psi}$ are the bounce frequency and toroidal drift frequency, respectively. This for electrons is true only very close to $q = 1$, while the mode structure is not zero for $0 < r < r_{q=1}$. For that reason we can neglect the role of passing electron (see page 9 of [123] for more details).

In Figure 4.22, the ion diamagnetic drift frequency ω_{*i} in the inertia term of the fishbone dispersion relation is scanned, with different $\delta \hat{W}_c$ values. The suprathermal electron density is set to n_{s0} , the value based on the experiment. This shows that the electron fishbone mode that rotates opposite to the ion diamagnetic drift direction is stabilized by enhancing the ratio ω_{*i}/ω_{*e} , where ω_{*e} is the electron diamagnetic drift frequency. In the TCV experiment, the ratio ω_{*i}/ω_{*e} is small ($\sim 1/4$), and as a result the electron-diamagnetic-drift-directed fishbone is not stabilized by ion finite Larmor radius (FLR) effects. In contrast, the DIII-D electron fishbone reported earlier [17], where ECCD and NBI were used, could be stable to these electron-directed fishbones. The only channel available is the ion-diamagnetic-drift-directed fishbone mode that resonates with barely trapped electrons. In the DIII-D case an inverted spatial gradient of suprathermal electrons ($\partial f_e / \partial \rho > 0$) at $q = 1$ assists the mode drive.

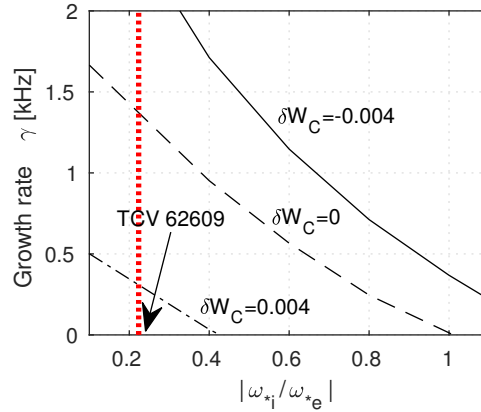


Figure 4.22 – Growth rate obtained for varying ω_{*i} and $\delta \hat{W}_c$

In order to study the ECCD power effect on the onset of the fishbone mode, three time windows during the ECCD power scan experiment (#62755, Figure 4.13), are selected for the analysis. Since the equilibrium and the electron density are kept constant throughout the discharge, the electron temperature and RF power are varied according to the experimentally measured values. The Fokker-Planck modeling is based on the analysis in section 4.5.1, using the localized transport model. The modeled electron distribution function at different energies is presented in Figure 4.23, for the three time windows. As the ECCD power decreases with time, as observed in the hard X-ray profiles, the suprathermal electron population decreases in every energy bin.

The solution of the linear fishbone dispersion relation is compared with the experimentally observed mode frequencies during the ECCD power scan, in Figure 4.24 (a). The calculated mode frequencies are Doppler-shifted considering the toroidal mode rotation frequency, 4.1 kHz in

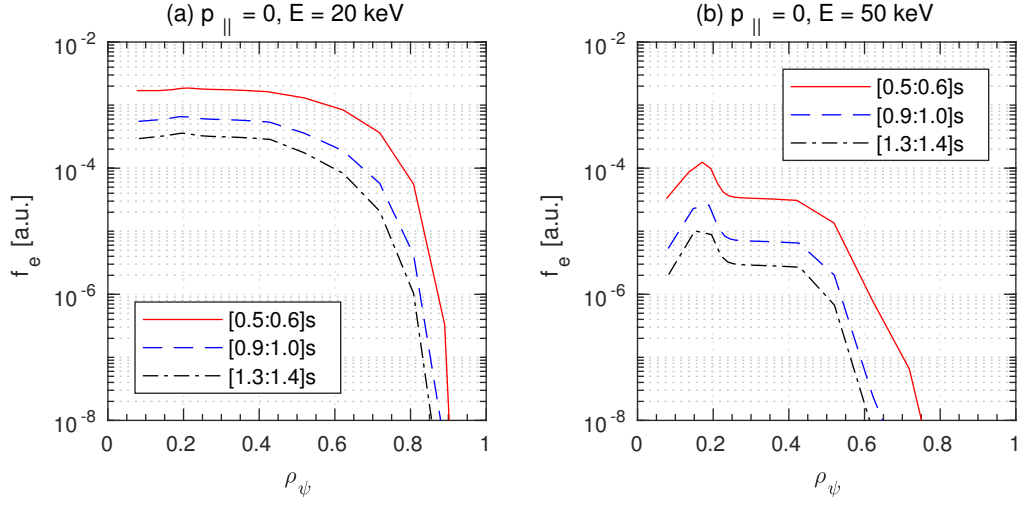


Figure 4.23 – Radial profile of Fokker-Planck modeled electron distribution function, for $\theta = 0$ and $p_{\parallel} = 0$, at three time windows, from 0.5 s to 0.6 s when $P_{EC} = 750 kW$, from 0.9 s to 1.0 s when $P_{EC} = 550 kW$, from 1.3 s to 1.4 s when $P_{EC} = 350 kW$.

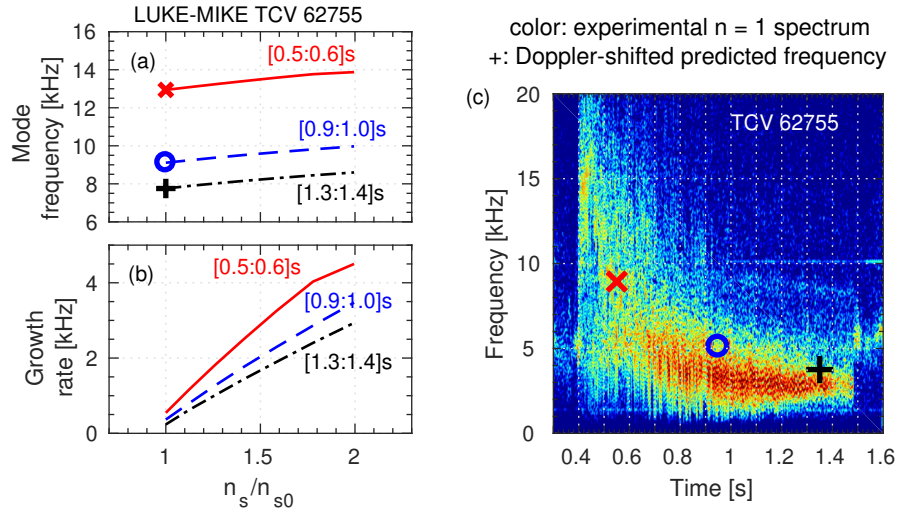


Figure 4.24 – (a,b) The predicted mode frequency and growth rate in three time windows. (c) The Doppler-shifted mode frequency prediction is plotted on the $n = 1$ mode spectrogram from the experiment.

the plasma current direction, and they agree well with the experiment. In all time windows, the growth rate is positive and the mode frequency increases when the suprathermal electron population n_s increases. Thus it is clear that in this experiment the suprathermal electron population plays a destabilizing role and the mode frequency decreases as the population decreases owing to the ECCD power ramp-down.

4.6 Conclusions

During ECCD injection in the TCV tokamak, fishbone-like bursts accompanied by central plasma relaxation are observed. The $m/n = 1/1$ mode structure in the soft X-ray and hard X-ray profiles have been shown for the first time with a high temporal resolution comparable with the observed mode frequency. The soft X-ray and hard X-ray profiles are Abel-inverted, based on an equilibrium that includes a mode structure. The rotatable hard X-ray camera has enabled a study of different responses of trapped and passing electrons to the mode, separately.

The results have allowed us to see the evolution of the electron distribution related to the fishbone oscillations. The mode is destabilized after the ramp-up of suprathermal electrons. Then trapped suprathermal electrons preferentially interact with the mode and are expelled during the mode oscillation phase. The solution of the linear fishbone dispersion relation, based on the Fokker-Planck modeling of the electron distribution function coupled with the hard X-ray synthetic diagnostic, confirms the destabilization of the fishbone mode by deeply and moderately (not barely) trapped suprathermal electrons' resonant interaction with the mode. This explains the observed mode rotation in the electron diamagnetic drift direction. The ECCD power scanning experiment and modeling have shown the mode frequency dependency on the electron distribution function, which can support the idea that the frequency chirping of a single fishbone burst is induced by the redistribution of the resonant electrons during the oscillation.

Many questions regarding the stability of the trapped electron fishbone and its impact on the plasma remain. A systematic study of the non-linear growth phase is necessary to assess and predict the effect of the instability on the electron distribution, which may degrade the ECCD efficiency and impose constraints on ECCD scenarios. In the current experiment, the trapped electron fishbone has been obtained with monotonic pressure profile and relatively low ion temperature without NBI. However, this instability may be stabilized by the NBI-heated ion population, as suggested by Figure 4.22, in which case it may not be a serious obstacle in future tokamak operation with high ion temperature. Future experiments in TCV will add NBI to the ECCD plasma with electron fishbones, in order to investigate the effect of ions on the instability. It might be expected that with the increase in ion temperature, the electron fishbone will no longer propagate in the electron diamagnetic direction, and the other branch of electron fishbones [17] may be generated due to resonance with barely trapped electrons.

5 Summary, conclusions, and future work

5.1 Summary

- Development and maintenance of diagnostics and related software tools
 - Re-installation and commissioning of HXRS third and fourth cameras have been carried out, in addition to retrofitting the first camera with motorized energy filter controls (chapter 2.1).
 - The maximum likelihood method and the Bessel method have been implemented for the hard X-ray tomography, for a variety of physics scenarios (chapter 2.2).
 - A conditional averaging tool for regular (chapter 3) and irregular (chapter 4) events has been developed.
- Development of modeling software
 - Based on the calibration of the camera with various radioactive sources, a realistic response function has been modeled for the CdTe detectors used in HXRS. The response function is implemented in the hard X-ray synthetic diagnostic, which is coupled to the Fokker-Planck code LUKE (chapter 2.3).
 - An optimized simulation scheme for a time-varying Fokker-Planck calculation has been developed for the ECCD modulation study, which includes a change of experimental conditions as well as various suprathermal electron diffusion models (chapter 3.3).
 - A spatially localized transport model for the Fokker-Planck simulation was designed and implemented, for the modeling of the plasma with internal kink modes (chapter 4.5).
- Experimental study and numerical modeling and analysis
 - Study of the suprathermal electron population response to ECCD (chapter 3)
 - * A series of sawtooth-free ECCD modulation scenarios with various ECCD conditions has been developed.

- * The time evolution of the hard X-ray emission profiles has been measured with high temporal resolution ($\sim 10^{-4}$ s). Changes of the spatial emissivity profile have been analyzed using an Abel-inversion scheme.
- * The time evolution of the suprathermal electrons has been modeled using the time-varying Fokker-Planck simulation, which is coupled to the hard X-ray synthetic diagnostic. For the first time, EC wave power dependent suprathermal electron transport parameters, which are asymmetric in momentum space, have been implemented in the simulation and compared to the experimental results.
- Study of the interaction between MHD modes and suprathermal electrons (chapter 4)
 - * Electron fishbone scenarios with various ECCD conditions have been developed.
 - * The redistribution of ECCD-created suprathermal electrons at high temporal resolution (comparable to the mode time scale) has been analyzed using HXRS. For the first time, the response of hard X-ray profiles to the internal kink mode is observed, at the frequency of the mode, suggesting the role of suprathermal electrons in destabilizing the fishbone mode.
 - * The electron distribution function has been modeled using the Fokker-Planck code coupled with the hard X-ray synthetic diagnostic, and a linear fishbone dispersion relation is solved to study the stability of the mode.

5.2 Conclusions

This thesis work has advanced the understanding of the dynamics of suprathermal electrons and their interaction with MHD modes. Considerable progress has been made with regard to the use of a hard X-ray diagnostic as a tool for the study of suprathermal electrons in real and velocity spaces. Comprehensive results have been obtained from Fokker-Planck modeling coupled with a hard X-ray synthetic diagnostic, enhancing the modeling methodology of the electron distribution function in ECCD plasmas.

In the study of the suprathermal electron population's response to ECCD, the experimental and simulation results indicate that a broadening of the suprathermal electron population depends on the injected EC wave power, and a collisional slowing down of the suprathermal electrons dominates over their diffusive transport during the relaxation phase. The present findings have important implications for research into ECCD, for plasma profile control and NTM control: the broadening of the suprathermal electrons and the following reduction of ECCD efficiency should be considered in the estimation of the ECCD driven current profile. A simple ray-tracing estimation of the ECCD driven current profile, which is generally used nowadays, might overestimate the ECCD efficiency. Thus a further research is required to systematically characterize the broadening and develop a model in various physics scenarios.

Detailed suggestions for future works are presented in the next section.

In the study of the interaction between MHD modes and suprathermal electrons, the hard X-ray analysis and the solution of a linear fishbone dispersion relation have demonstrated the role of suprathermal electrons in destabilizing the fishbone mode and their redistribution during the evolution of this instability. This indicates that the suprathermal electron population can be lost periodically under this instability condition. This degrades the quality of the ECCD current drive, giving a new constraint for ECCD operation. A systematic study of the non-linear growth phase is necessary to assess and predict the effect of the instability on the electron distribution. Further suggestions for the improvement of this research are presented in the next section.

Taken together, these findings from both studies conducted during this thesis work highlight the importance of suprathermal electron dynamics in the use of ECCD. The two studies are closely related in the sense that the dynamics of the suprathermal electrons affects the MHD stability, and the interaction with MHD modes redistributes the suprathermal electron population. Therefore, this thesis work provides the framework for a comprehensive understanding of this physics, aiming at efficient use of ECCD in tokamak plasmas.

5.3 Future work

There are several additional improvements that could be made to the analysis of suprathermal electron dynamics. A possible roadmap is as follows:

- Study of the suprathermal electron population response to ECCD
 - Based on the sawtooth-free ECCD discharge designed in this thesis work, the EC wave deposition location and the EC wave power could be scanned. In the poloidal plane, moving the ECCD location towards far off-axis would be also used for the study of the Ohkawa current drive mechanism. Changing the EC wave power might affect the stability of the plasma by modifying the plasma temperature and ECCD current profiles. With a systematic characterization, one could model an empirical formula for the estimation of the ECCD current profile in various plasma scenarios.
 - Based on the tomography methods implemented in this thesis, a complete set of HXRS cameras should be used to reproduce the 2-D distribution of hard X-ray emissivity. Along with the ECCD location scan, the tomographic inversion might be able to show the effect of trapped electrons on the asymmetric hard X-ray emission. The poloidal emission asymmetry could be documented for various ECCD locations and provide the limits of applicability of the Abel-inversion of hard X-ray measurements.
 - During this thesis work, a preliminary study of the toroidal asymmetry has been

conducted (see appendix B). Further measurements are required to characterize the hard X-ray emission asymmetry in the toroidal plane, utilizing the equatorial and upper-lateral hard X-ray cameras in the horizontal orientation. Fully understanding the effect of loop voltage on the acceleration of the ECCD-generated suprathermal electrons would improve the quality of ECCD plasma modeling with a Fokker-Planck code.

- In the time-varying Fokker-Planck simulation conducted during this thesis work, the total plasma current profile has been assumed to be fixed in space and time, based on the estimation of the current diffusion time. However, the flux loop measurement has suggested a possible change of the current profile during the ECCD modulation phase. Therefore, a coupling of a plasma transport code to the time-varying Fokker-Planck simulation could clarify the effect of the ECCD pulse on the plasma current profile. In addition, by using a plasma transport code, the ECCD modulation study could be extended to the study of the effect of ECCD on the current diffusion, which might be important in the NTM stabilization application where the magnetic island rotates at high frequency.
 - The Fokker-Planck modeling with various diffusive transport models has indicated that an additional mechanism is still required to explain the hard X-ray profile broadening outside the EC absorption area. EC wave scattering due to the edge density fluctuation might explain this, with reduced diffusive losses of suprathermal electrons. The effect of the wave scattering in a fluctuating equilibrium could be studied based on the discharge obtained during this thesis work, using the Fokker-Planck code LUKE.
- Study of the interaction between MHD modes and suprathermal electrons
 - This thesis work has shown the dependency of the electron fishbone frequency and intensity on the ECCD power and the ECCD location (B-field). However, during the scanning experiments, the experimental conditions were kept only for 100 ms, which was not long enough for the conditional averaging of the hard X-ray data. Therefore, further experiments with fixed ECCD parameters would give an extended data set of hard X-ray emission response to the fishbone mode, and this would characterize an impact of electron fishbones on the redistribution of suprathermal electrons.
 - In this thesis work, a deformed magnetic equilibrium profile is modeled for an Abel-inversion of the hard X-ray emission profiles, assuming a poloidal emission symmetry. Although the Fokker-Planck simulation has confirmed that the emission is symmetric in the discharge analyzed in this thesis, a 2-D tomographic inversion of the hard X-ray emission would be required for various ECCD scenarios, in particular during the off-axis ECCD discharges. This study could be conducted together with the study of suprathermal electron response to ECCD.

- In this thesis work, a linear fishbone dispersion relation has been solved based on the electron distribution function modeled using the Fokker-Planck simulation, in order to assess the stability of the plasma. In the future work on the electron fishbones, a systematic study of the non-linear growth phase would be necessary to assess and predict the effect of the instability on the electron distribution.
- As analyzed at the end of chapter 4, the electron fishbone instability observed in TCV might be stabilized by the NBI heated ion population. Future experiments adding NBI to the ECCD plasma with electron fishbones would demonstrate the effect of ions on this instability. Firstly a constant NBI could be added to the ECCD power scan or B-field scan discharges obtained in this thesis work, then an optimum plasma scenario could be designed based on the scan.

A Analysis of time-varying MHD mode structure

In this thesis, the $m/n = 1/1$ modes have been observed in different ECCD discharges: in chapter 3, the mode has been observed only during the co-ECCD discharge, synchronized with modulated ECCD pulses. In chapter 4, the mode behavior has been the main topic of the analysis. The effect of the electron fishbones on the distribution of electrons has been analyzed and the role of trapped and passing electrons has been analyzed separately.

In this type of analysis, it is important to know not only the mode structures but also their time evolution, with a time resolution sufficiently high to resolve the physics of interest. Singular value decomposition (SVD) has been used for this purpose [23, 24]: when there is a $(m \times n)$ matrix \mathbf{X} , which contains the temporal and spatial distribution of the measured data, the SVD method decomposes \mathbf{X} into:

$$\mathbf{X} = \mathbf{S} \mathbf{V} \mathbf{D}^*, \quad (\text{A.1})$$

where \mathbf{S} , \mathbf{V} , and \mathbf{D} are $(m \times m)$, $(m \times n)$, and $(n \times n)$ matrices, respectively. \mathbf{D}^* is the conjugate transpose of \mathbf{D} .

\mathbf{S} contains spatial information on the modes, and its columns are called *topos*. \mathbf{V} is a diagonal matrix with the singular values in descending order. \mathbf{D} contains temporal information on each *topo*, and the columns are called *chronos*. In general, the first *topo/chrono* pair shows the dominant structure in the plasma, the background thermal plasma. Then the second and third pairs show the dominant MHD mode structure with a spatial phase shift. By combining the two pairs, the toroidal and poloidal rotation of the mode structure can be reconstructed.

In this appendix, the SVD analysis used in this thesis is presented in detail. Although the magnetic probe array is the main diagnostic for the mode analysis in tokamak plasmas in general, in the case of the internal kink mode which is located near the plasma core, it is not always possible to obtain a sufficiently large signal from the magnetic probes which are placed outside the plasma. Therefore, depending on the plasma condition, either the magnetic probe array or the soft X-ray array has been used in this thesis work.

In section A.1, the magnetic probe analysis results for the toroidal mode analysis are presented. The poloidal mode is analyzed using XTOMO in section A.2 and the toroidal mode analysis with soft X-ray diagnostics is presented in A.3. A summary is provided in section A.4.

A.1 Toroidal mode analysis with magnetic probes

In TCV, the toroidal magnetic probe array [25] comprises three ($z = -0.23$ m, $z = 0$ m, $z = 0.23$ m) high-field-side arrays of 8 probes each at the inner wall and three ($z = -0.23$ m, $z = 0$ m, $z = 0.23$ m) low-field-side arrays of 16 probes each at the outer wall. The magnetic pick-up coils acquire data typically at 250 kHz.

Figure A.1 shows the first two topo/chrono pair of the SVD analysis of the magnetic probe signal of TCV # 52269. In this discharge, electron fishbones appeared as ECCD was applied from 0.3 s. A high-pass-filter is used to remove low frequency noise, so the background magnetic signal is not included. The first two topo/chrono pairs correspond to the $n = 1$ mode, as can be seen from the structure of topos 1 and topos 2.

The first two pairs can be combined to reproduce the rotation of the $n = 1$ mode. Figure A.2 shows combinations of the two at consecutive time steps. It is clear that the perturbed signal is moving in the negative ϕ direction. In this discharge, the plasma current was in the positive ϕ direction, so the toroidal mode rotation was opposite to the plasma current direction, in the electron's diamagnetic drift direction. The TCV coordinate system used in this work is presented in Figure A.3.

In order to analyze the direction of the toroidal diamagnetic drift, the diamagnetic flow can be written as [128]:

$$\bar{v}_d = -\frac{1}{q_j n_j B^2} \nabla p_j \times \bar{B}, \quad (\text{A.2})$$

where q_j, n_j, p_j are the charge, density, and pressure of a species j , and $\hat{b} = \bar{B}/|B|$.

Using $\bar{B} = F(\psi)\nabla\phi + \nabla\phi \times \nabla\psi$ and $\nabla p_j = \frac{dp_j}{dr} \frac{\nabla\psi}{d\psi/dr} = \frac{p'_j}{\psi'} \nabla\psi$, one obtains

$$\begin{aligned} \bar{v}_d &= -\frac{1}{q_j n_j B^2} \frac{p'_j}{\psi'} \nabla\psi \times (F\nabla\phi + \nabla\phi \times \nabla\psi) \\ &= -\frac{1}{q_j n_j B^2} \left(\frac{p'_j}{\psi'} \nabla\psi \times F\nabla\phi \right) - \frac{1}{q_j n_j B^2} \frac{p'_j}{\psi'} (\nabla\psi)^2 \nabla\phi \\ &= -\frac{1}{q_j n_j B^2} (\nabla p_j \times \bar{B}_t) - \frac{1}{q_j n_j B^2} \frac{p'_j}{\psi'} (\nabla\psi)^2 \nabla\phi \\ &= \bar{v}_{d\theta} + \bar{v}_{d\phi}. \end{aligned} \quad (\text{A.3})$$

A.1. Toroidal mode analysis with magnetic probes

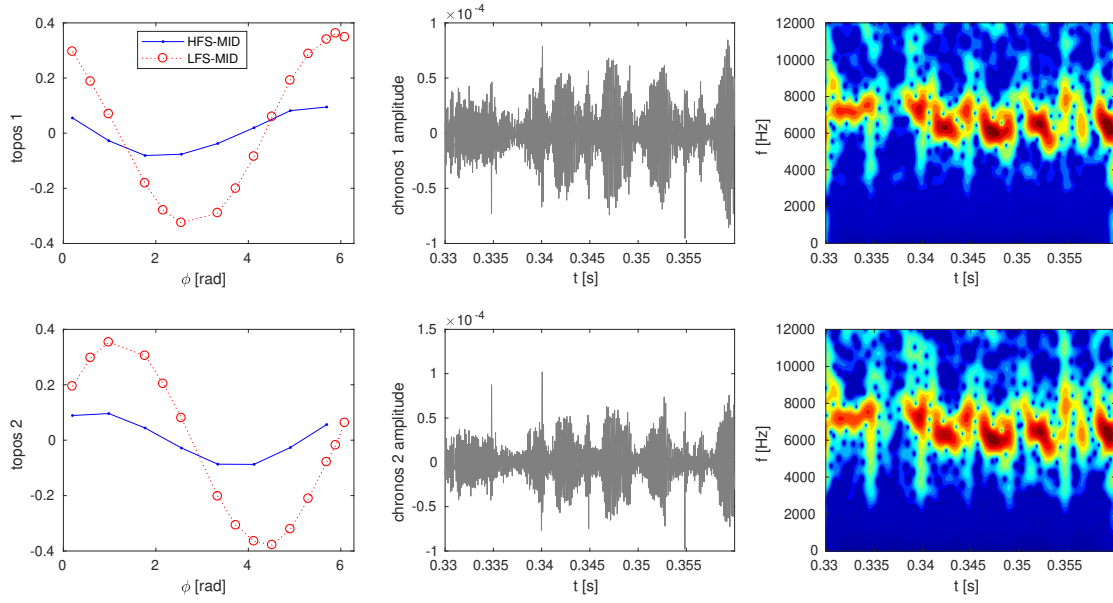


Figure A.1 – SVD analysis of the magnetic probe data of TCV 52269. (Left) Topos of the high-field-side array at $z = 0$ (HFS-MID) and of the low-field-side array at $z = 0$ (LFS-MID). (Middle) Chronos and (right) its spectrogram.

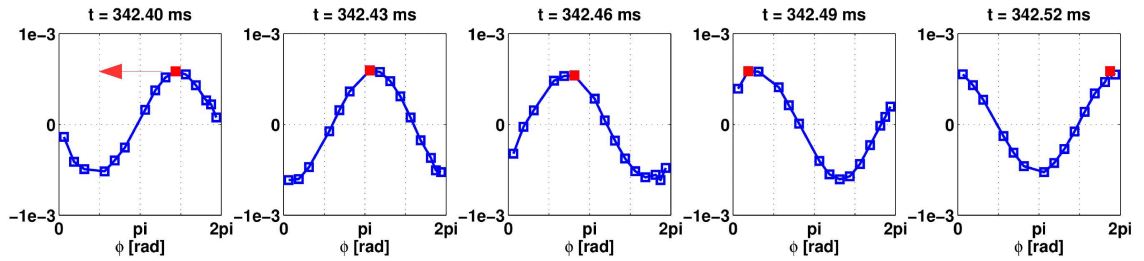


Figure A.2 – Rotation of the $n = 1$ mode based on the analysis in Figure A.1.

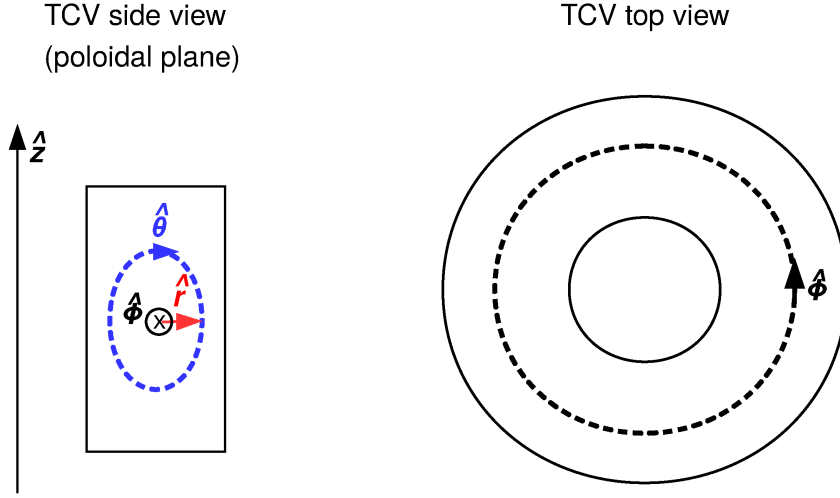


Figure A.3 – TCV coordinate system (r, θ, ϕ) .

Therefore the toroidal diamagnetic flow is

$$\bar{v}_{d\phi} = -\frac{1}{q_j n_j B^2} \frac{p'_j}{\psi'} (\nabla \psi)^2 \nabla \phi. \quad (\text{A.4})$$

Using $q = \frac{\bar{B} \cdot \nabla \phi}{B \cdot \nabla \theta}$, i.e. $\psi' = \frac{rF}{qR}$, the sign is

$$\begin{aligned} \text{sign}(v_{d\phi}) &= -\text{sign}(q_j) \cdot \text{sign}(p'_j) \cdot \text{sign}(\psi') \\ &= -\text{sign}(q_j) \cdot \text{sign}(p'_j) \cdot \text{sign}(F) \cdot \text{sign}(q) \\ &= -\text{sign}(q_j) \cdot \text{sign}(p'_j) \cdot \text{sign}(B_t) \cdot \text{sign}(B_t) \cdot \text{sign}(I_p) \\ &= -\text{sign}(q_j) \cdot \text{sign}(p'_j) \cdot \text{sign}(I_p). \end{aligned} \quad (\text{A.5})$$

Therefore, for a centrally peaked electron distribution, the diamagnetic flow direction is opposite to the plasma current direction,

$$\text{sign}(v_{d\phi}) = -\text{sign}(I_p). \quad (\text{A.6})$$

A.2 Poloidal mode analysis with soft X-ray array

TCV features multiple poloidal arrays of magnetic probes, which provide a measurement of magnetic field fluctuation around each poloidal plane. However, due to the highly elongated shape of the TCV tokamak vessel, it is difficult to use the poloidal magnetic probe array for the

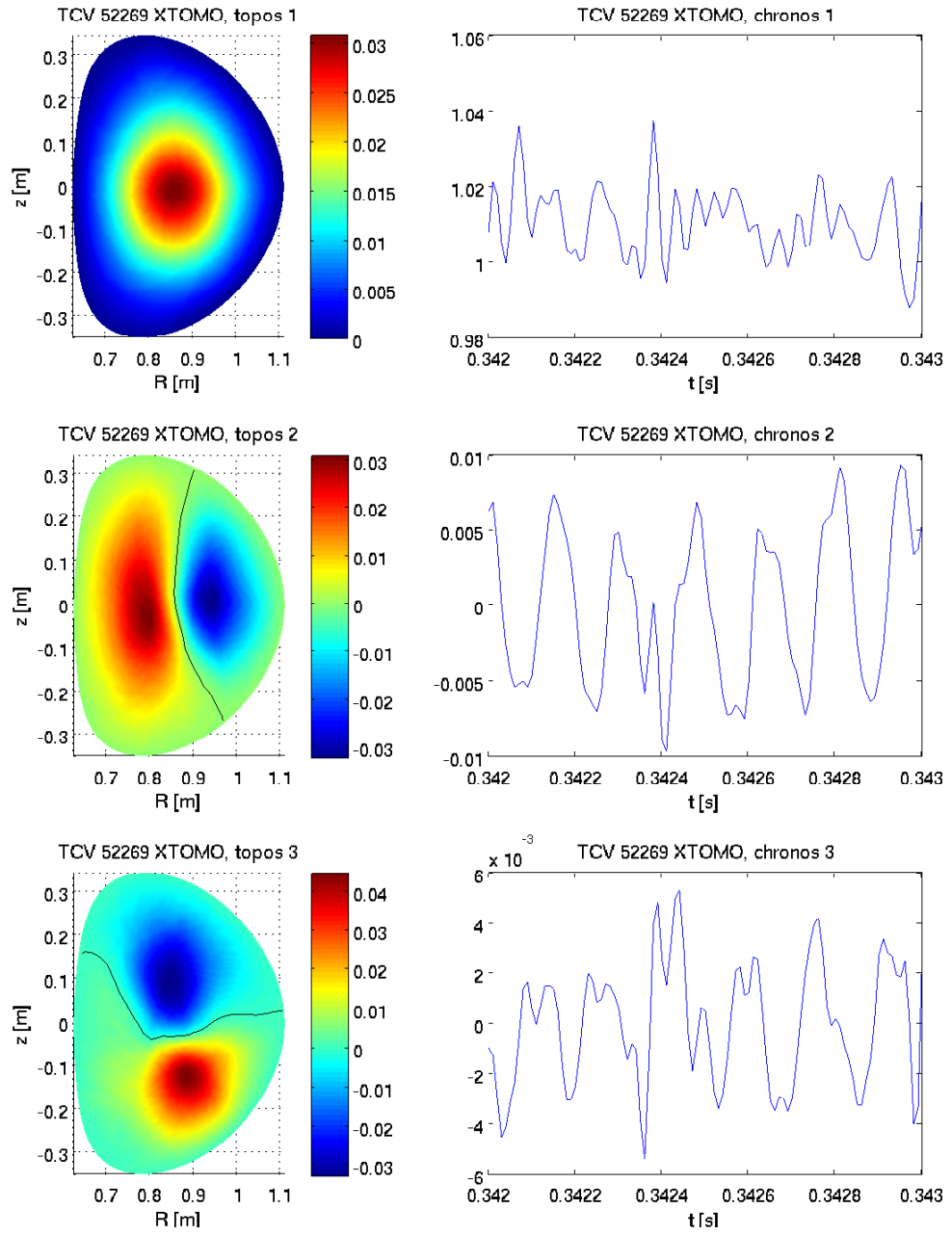


Figure A.4 – First three pairs of topo/chrono of XTOMO SVD analysis of TCV 52269.

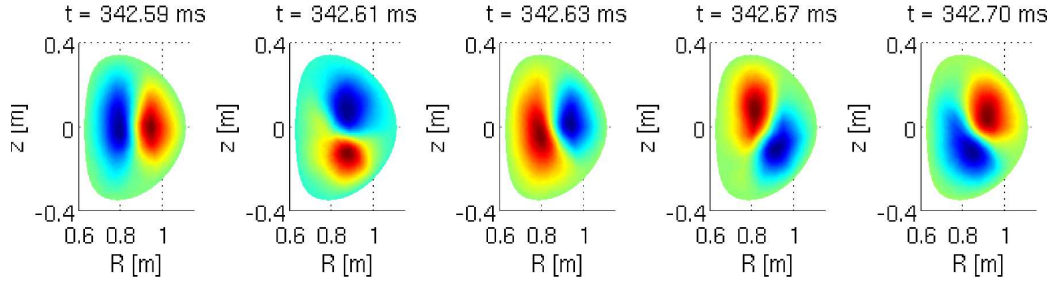


Figure A.5 – Rotation of the $m = 1$ mode based on the analysis in Figure A.4.

mode analysis of fluctuations occurring near the magnetic axis.

Thus for the analysis of the $m = 1$ mode in this thesis, the soft X-ray array of XTOMO around the tokamak is mainly used. The soft X-ray tomographic system (XTOMO) consists of 10 pinhole cameras with 20 p-n junction silicon photodiodes each, acquiring data at 100 kHz. The measured signal is used for the tomographic inversion of soft X-ray emission using a finite element grid discretization on the flux surfaces and the minimum Fisher regularization inversion method [23].

After the tomographic inversion, the 2-D emissivity data are analyzed using the singular value decomposition (SVD) technique as shown in Figure A.4. The first topo/chrono pair shows the background soft X-ray emissivity by the thermal electrons. Then the next two topo/chrono pairs correspond to the $m = 1$ mode, which has a positive peak and a negative peak on a flux surface.

As analyzed in the previous section, the two pairs of the $m = 1$ mode are used to reproduce the rotation of the mode structure at consecutive time steps. Figure A.5 shows the rotation in the clockwise direction, which is in the electron's diamagnetic drift direction. In this discharge, the toroidal magnetic field was in the negative direction ($B_t < 0$) and the electron pressure profile was centrally peaked ($\nabla p < 0$). Thus the diamagnetic drift (equation A.3)

$$\bar{v}_{d\theta} = \frac{1}{qB^2} \left(-\frac{\nabla p}{n} \times B_t \right), \quad (\text{A.7})$$

where q is an electron charge $q = -e$, becomes positive (Figure A.3).

In the discharge # 49502 presented in Figure A.6, the magnetic field was in the negative direction (Figure A.3), i.e. $B_t < 0$. Thus the electron diamagnetic drift direction in the poloidal plane is in the negative direction. The $m = 1$ mode rotation analyzed in Figure A.6 shows that the mode is rotating in the counter-clockwise direction, which corresponds to the electron diamagnetic drift direction.

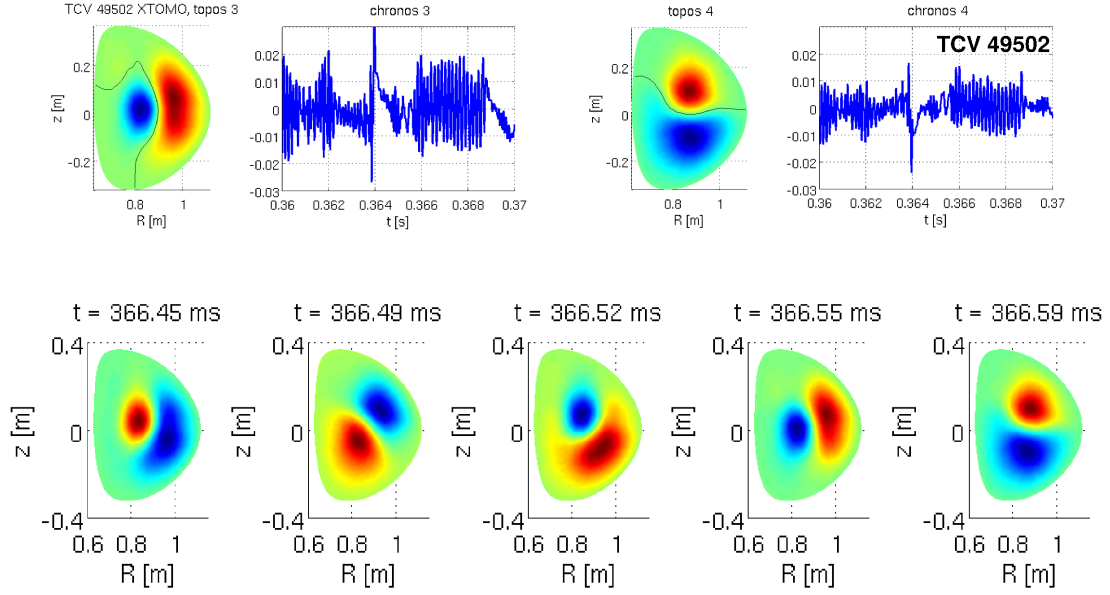


Figure A.6 – Topos and Chronos and the reconstructed $m = 1$ mode rotation, from the SVD analysis of XTOMO data of TCV 49502.

A.3 Toroidal mode analysis with soft X-ray array

In the on-axis counter-ECCD modulation discharge analyzed in chapter 3, frequency-chirping modes were observed, synchronized with the ECCD pulses. As can be observed in Figure A.7, the oscillation is concentrated near the magnetic axis. Ch 32 of DMPX corresponds to the central chord. Compared to the previous discharges analyzed in this appendix, this mode was located closer to the magnetic axis and the mode intensity was weaker. Thus it is difficult to use the magnetic probe signals for the toroidal and the poloidal mode analysis.

In this case, two soft X-ray array diagnostics, DMPX and XTOMO are used to analyze the mode structure. For each measurement, the data is Fourier-analyzed and the spectral power is conditionally averaged over multiple ECCD pulses. Figure A.8 indicates the frequency chirping signal and the spectral power growth over frequency and time. For the poloidal mode number analysis, the two channels located at opposite sides of the magnetic axis (Figure A.9 (left)) are selected and their phases are compared. One can notice that in Figure A.9 the phase difference of the mode at the two location is π . This suggests that the poloidal mode structure is $m = 1$. Unfortunately during this experimental campaign, the central cameras of XTOMO were removed for another diagnostic as can be seen in Figure A.10, thus the quality of the tomographic inversion is not good enough to observe the mode rotation direction.

For the toroidal mode analysis, the soft X-ray signal of DMPX and XTOMO are cross-checked, since they are toroidally displaced by $\pi/4$, as can be seen in Figure A.10. The phase difference

Appendix A. Analysis of time-varying MHD mode structure

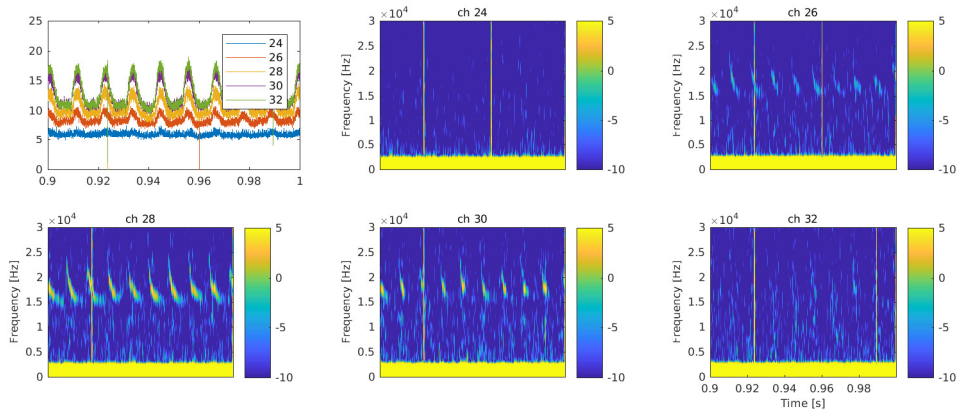


Figure A.7 – Frequency-chirping signals observed in the soft X-ray signals (DMPX) near the magnetic axis in TCV 62653.

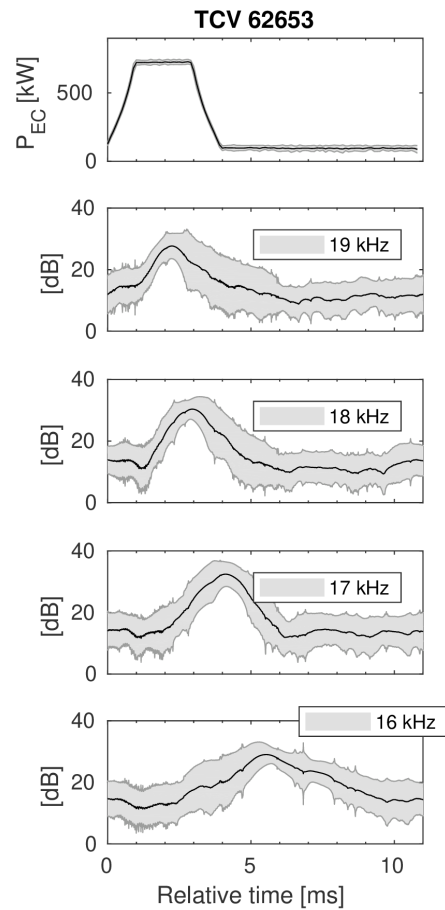


Figure A.8 – Conditionally-averaged spectral power at each frequency, from the data of ch 28 of DMPX.

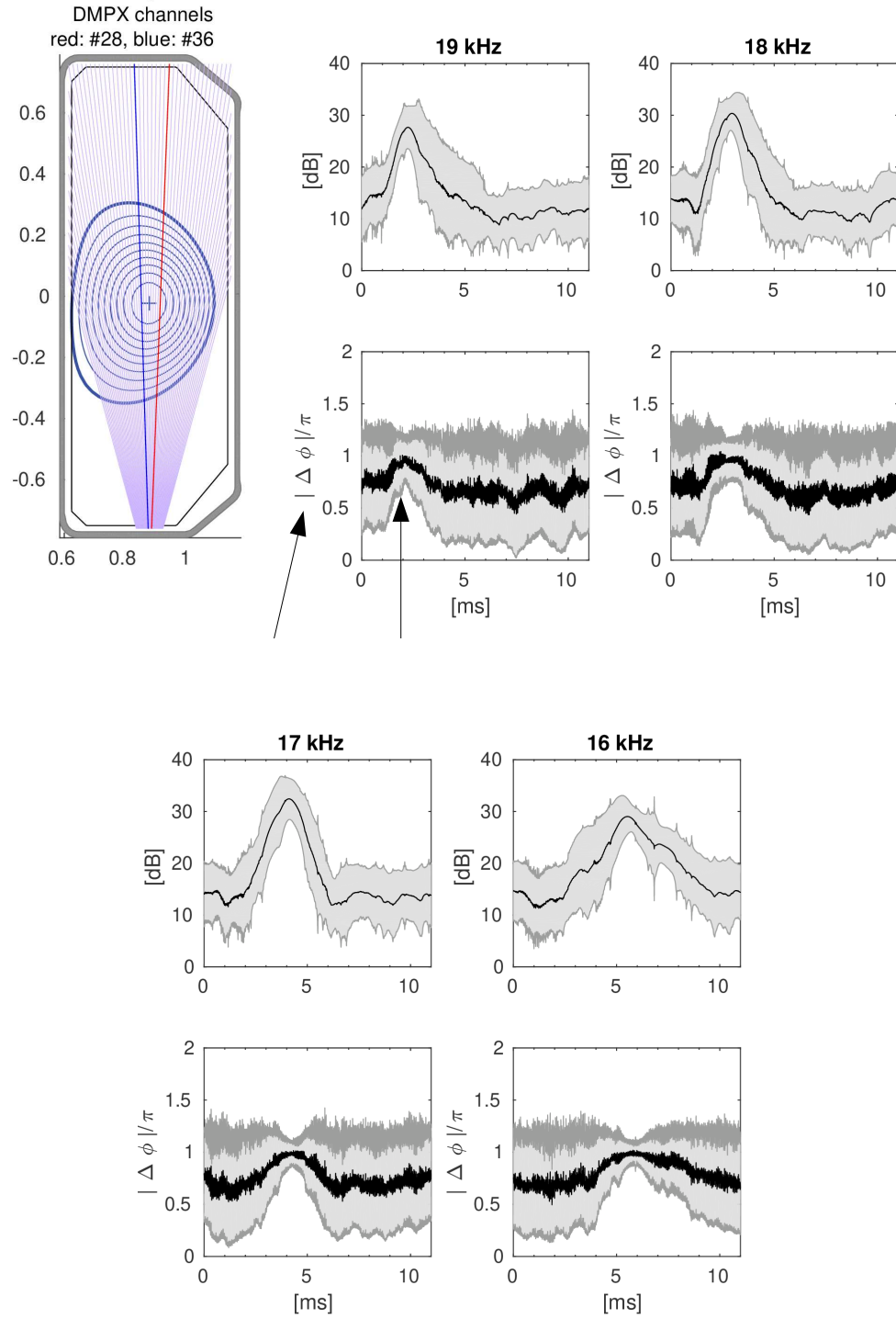


Figure A.9 – (Top left) DMPX lines of sight, x-axis: R [m], y-axis: z [m]. Spectral power of the mode at each frequency and the phase difference between channels 28 and 36. The phase difference is indicated with arrows.

Appendix A. Analysis of time-varying MHD mode structure

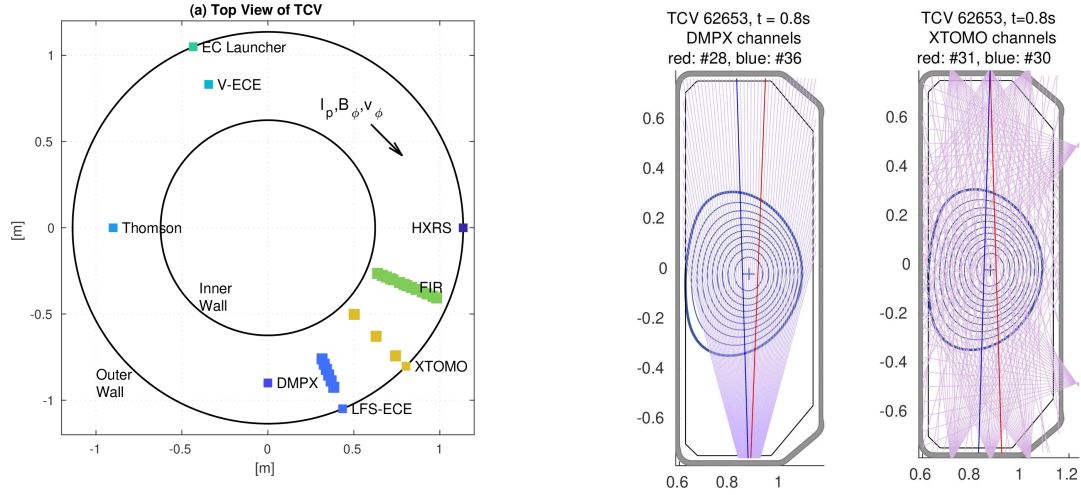


Figure A.10 – (Left) Toroidal locations of diagnostics. (Middle) DMPX lines of sight with channels 28 and 36 in red and blue lines, respectively. (Right) XTOMO lines of sight with channels 31 and 30 in red and blue lines, respectively.

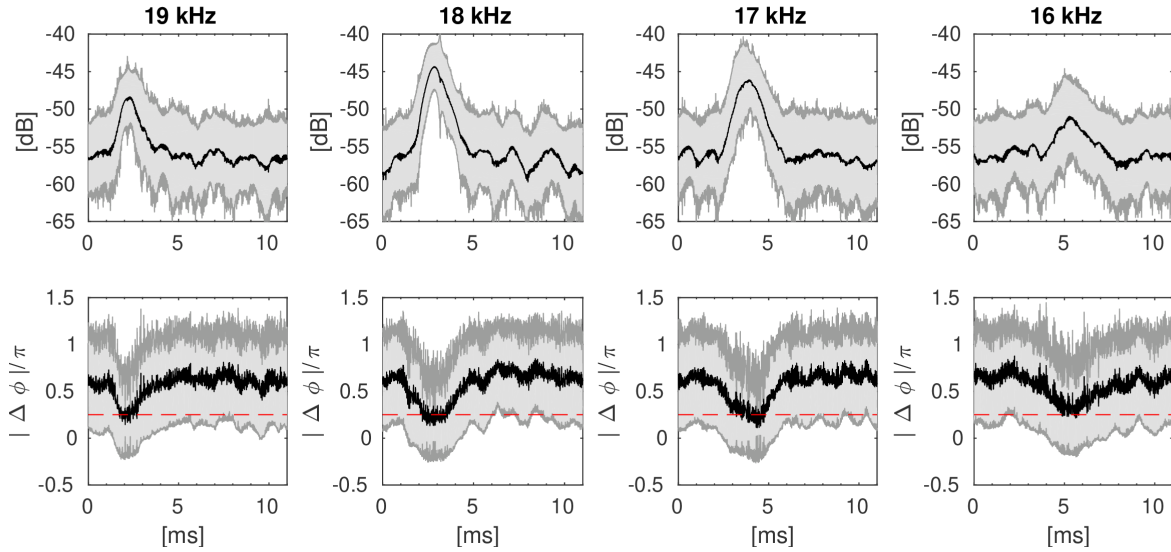


Figure A.11 – (Top) time evolution of the spectral power of the mode. (Bottom) phase difference between toroidally displaced soft X-ray measurements (see Figure A.10).

analyzed in Figure A.11 corresponds to the difference between DMPX ch28 and XTOMO ch30 (or DMPX ch36 and XTOMO ch30). The phase difference is $\pi/4$, which indicates that the toroidal mode has the $n = 1$ structure. However, it is not possible to obtain the direction of the toroidal mode rotation from this two point analysis.

A.4 Summary

In this appendix, various mode structure analysis methods used in this thesis work have been presented. Since the experimental condition varies depending on the physics scenario, it is suggested that one needs to check various diagnostics and select appropriate methods to analyze the mode structure.

B Study of toroidal asymmetry in the hard X-ray emission

The response of suprathermal electrons to ECCD has been studied in chapter 3, using the hard X-ray diagnostic. In chapter 3, the analysis has been conducted using the equatorial camera in the vertical orientation. With the vertical orientation, the lines of sight cover the poloidal plane, thus a spatial distribution of the hard X-ray emissivity can be obtained by means of Abel-inversion. In TCV, the equatorial camera can be rotated by 90 degrees, so the lines of sight can cover the toroidal plane, as presented in Figure B.1. The lines of sight are geometrically symmetric; for example, the length of channels 3 and 22 in Figure B.1 are identical. In this case, a comparison of signals from the two channels can provide information on suprathermal electron dynamics in the toroidal direction, due to the headlight effect of the bremsstrahlung radiation.

The on-axis ECCD case analyzed in chapter 3 is repeated with the equatorial hard X-ray camera in the horizontal orientation, as presented in Figure B.1. The hard X-ray data are conditionally averaged over the ECCD pulses as presented in chapter 3. The time traces of channels 22 and 3 in Figure B.2 show a significant difference, which increases as the photon energy increases. This clearly demonstrates a toroidal asymmetry of the hard X-ray emission due to the toroidally asymmetric dynamics of suprathermal electrons.

In this appendix, various factors that can affect the toroidal hard X-ray measurement are investigated, using the Fokker-Planck code LUKE coupled with a hard X-ray synthetic diagnostic. In section B.1, the effects of the magnetic equilibrium are analyzed, when the equilibrium is not kept constant throughout a discharge. In section B.2, the effects of a balance between the RF wave power and the loop voltage are studied.

B.1 Effect of magnetic equilibrium

Figure B.3 presents the radial and vertical locations of the magnetic axis during the ECCD modulation discharge. It is clear that the radial location (R_0) is modulated with the ECCD pulses, as can be also seen from the conditionally averaged data. The vertical location (z_0)

Appendix B. Study of toroidal asymmetry in the hard X-ray emission

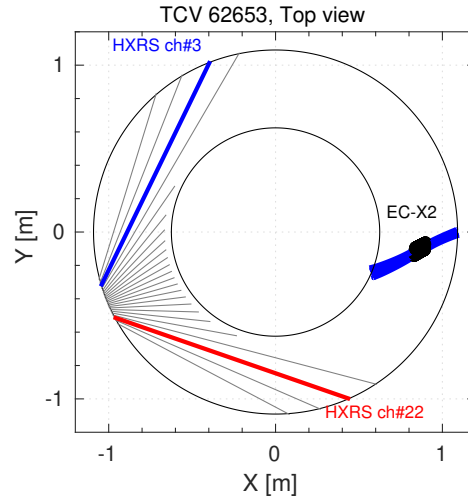


Figure B.1 – Top view of the TCV tokamak. The equatorial camera of HXRS in the horizontal orientation.

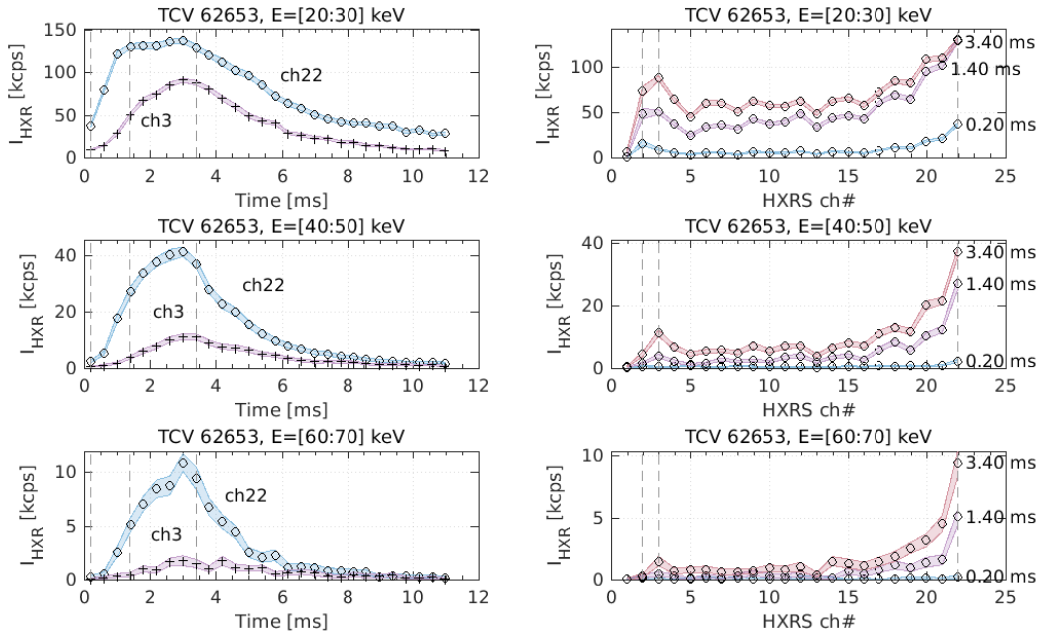


Figure B.2 – (Left) Time trace of the hard X-ray emission at ch3 and ch22, at different energy bins. (Right) Hard X-ray emission profiles at selected times, at different energy bins. In this discharge, only channels from 1 to 22 of the hard X-ray camera were connected, thus there is no data from channels 23 and 24.

changes slowly over time, about 10 mm in total.

Based on the experimental parameters obtained from the TCV discharge #62653, the magnetic

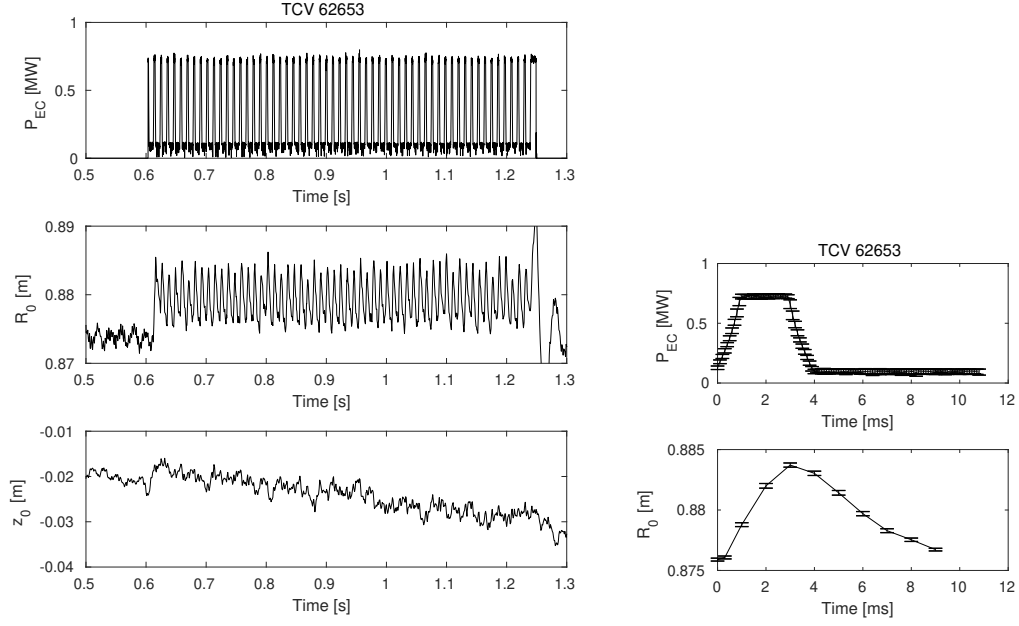


Figure B.3 – (Left) Time trace of EC wave power, radial (R_0) and vertical (z_0) locations of the magnetic axis. (Right) Conditionally averaged R_0 .

equilibrium is scanned radially and vertically in the simulations presented in Figure B.4. The default equilibrium ($\Delta R = 0$ mm and $\Delta z = 0$ mm) is selected from the LIUQE equilibrium at 0.8 s. A spatially uniform loop voltage profile is assumed. The radial diffusion of suprathermal electrons is not considered here to simplify the simulation. The EC wave power is set to 200 kW and the steady state solution of the Fokker-Planck equation is calculated.

Figure B.4 shows that the maximum peaks appear at channels 2 and 23 in most cases. However, when the radial position is shifted by -20 mm ($\Delta R = -20$ mm), the maximum peaks are found in channels 3 and 22. This may explain the effect shown in Figure B.2, where the maximum peak position shifts from channel 2 to 3 over time. Unfortunately channels 23 and 24 were disconnected from the acquisition system during the experiment.

Figure B.5 presents the poloidal profile of the hard X-ray emission calculated by LUKE-FEB, with the identical simulation conditions used in the previous figure. This shows that the poloidal profile shifts slightly as the vertical position is scanned; however, the overall shape hardly changes with the radial position scan. This indicates that the poloidal hard X-ray profiles are not as sensitive as the toroidal hard X-ray profiles to a shift in the magnetic equilibrium.

Appendix B. Study of toroidal asymmetry in the hard X-ray emission

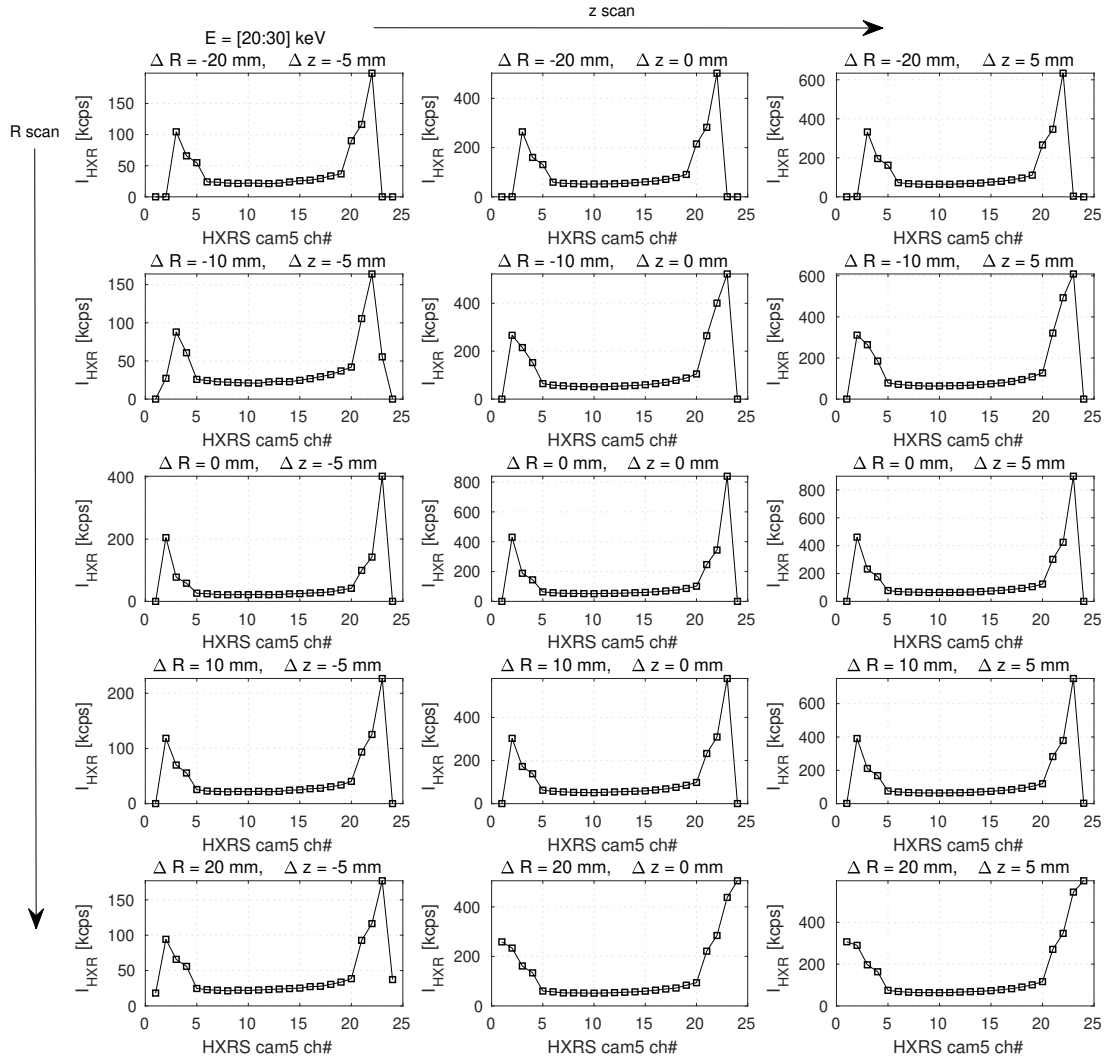


Figure B.4 – Vertical (z) and radial (R) scan of the magnetic equilibrium. Hard X-ray emission data in the energy bin $E=[20:30]$ keV are presented.

B.2. Competition between RF waves and toroidal electric field

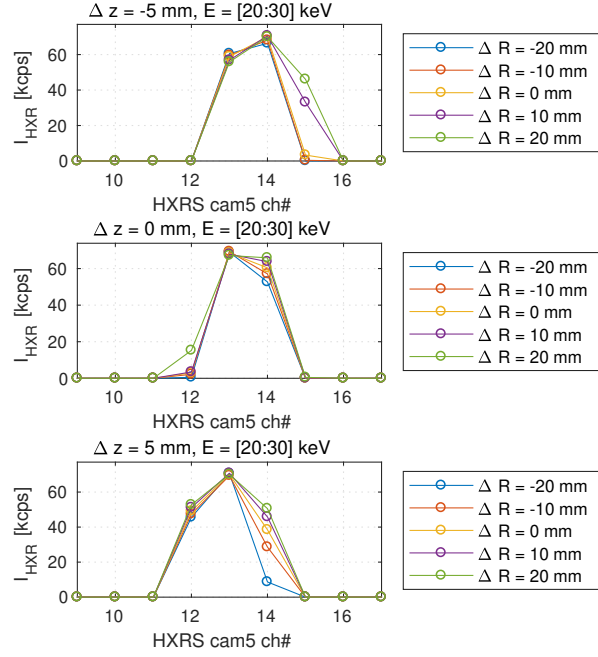


Figure B.5 – The poloidal hard X-ray emission profiles from the scan of R_0 and z_0 .

B.2 Competition between RF waves and toroidal electric field

Due to the headlight effect of the bremsstrahlung radiation (see chapter 1), the toroidal measurement of the hard X-ray emission is sensitive to the change in loop voltage and in the EC wave angle and power. In the Fokker-Planck modeling for the analysis of the toroidal hard X-ray measurement, the loop voltage often needs to be calculated, while the EC wave angle and power can be obtained after the experiment. In chapter 3, in the time-transient Fokker-Planck simulation, only the edge loop voltage from the flux loop measurement was available to use, so the loop voltage profile change was calculated using the frozen current mode.

In this section, based on the experimental parameters used in the previous section, the EC wave power and the loop voltage are scanned. The magnetic equilibrium is fixed as $\Delta R = -20$ mm and $\Delta z = -10$ mm, which reproduces the hard X-ray profiles seen in the measurement. Figure B.6 presents the toroidal hard X-ray profiles calculated from LUKE-FEB. The negative and the positive P correspond to the counter-ECCD and co-ECCD, respectively.

When there is no RF power and no loop voltage added ($P=0$ and $V_l=0$), the plasma is in Maxwellian equilibrium, so no asymmetry is found in the toroidal hard X-ray profile. As the loop voltage increases, I_{HXR} near channel 3 becomes higher than that of channels near 22, due to the electrons accelerated by the loop voltage.

Appendix B. Study of toroidal asymmetry in the hard X-ray emission

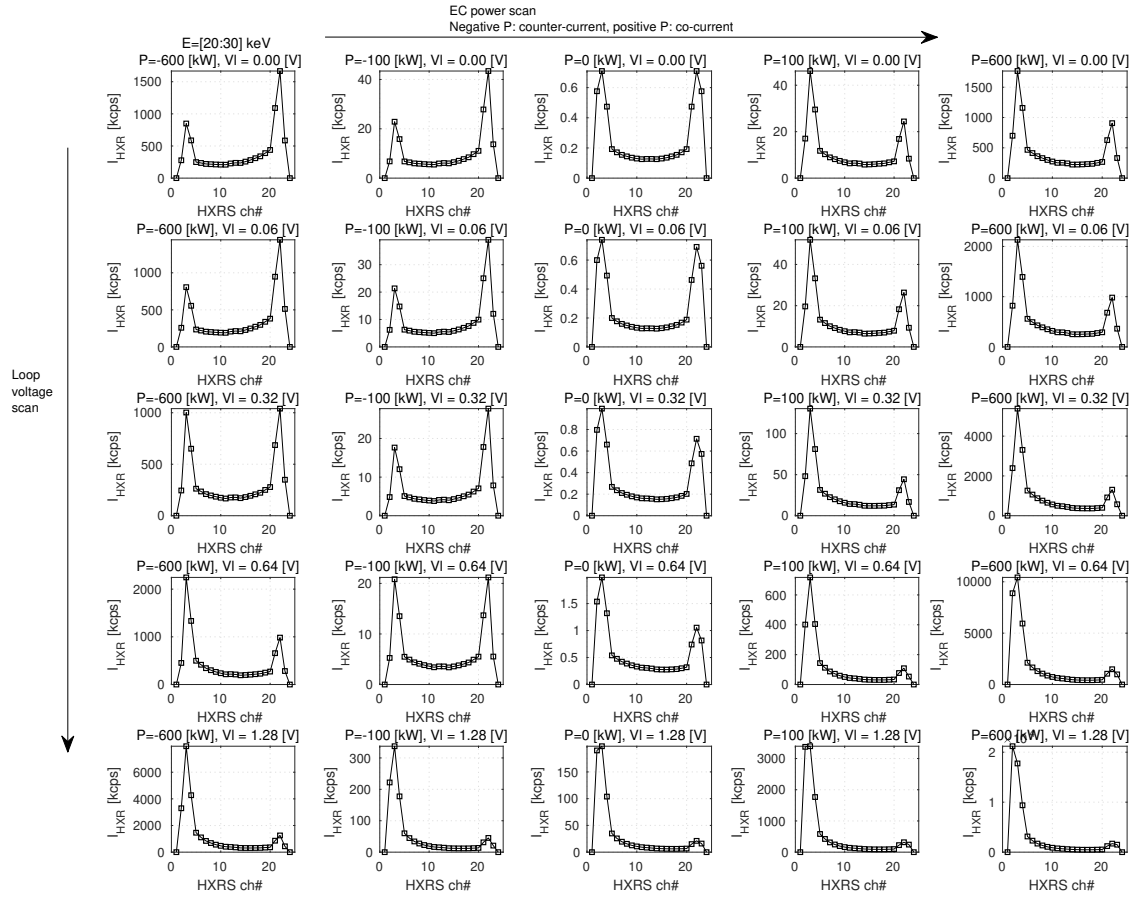


Figure B.6 – The toroidal hard X-ray profiles from the EC power and loop voltage scans. The negative and positive P correspond to the counter-ECCD and co-ECCD, respectively.

B.2. Competition between RF waves and toroidal electric field

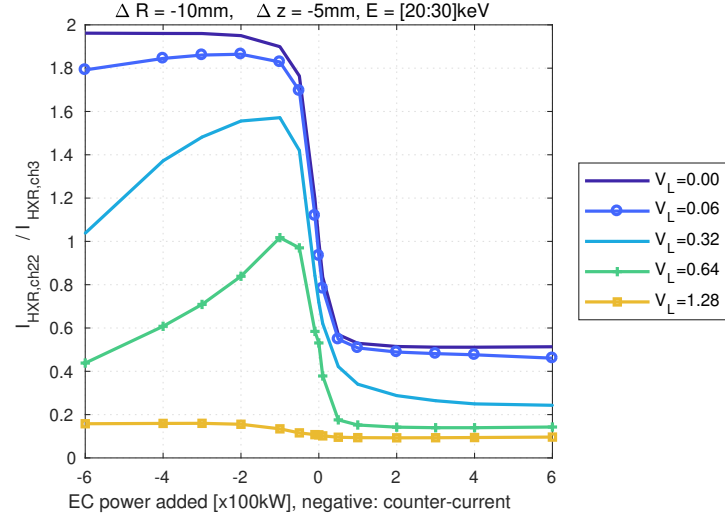


Figure B.7 – The ratio of I_{HXR} of channel 22 to channel 3, during the EC wave power and the loop voltage scans.

When the RF power is scanned with zero loop voltage, I_{HXR} of channel 3 is higher and lower than that of channel 22 in the case of co-ECCD and counter-ECCD, respectively, due to the asymmetry in the electron distribution induced by the resonant interaction between the electrons and the EC waves. This shows that the EC wave can increase or decrease the plasma current depending on its direction on the toroidal plane. In addition, one can notice that the absolute value of I_{HXR} increases significantly as the EC wave power increases.

When the loop voltage is not zero and co-current ECCD is applied (positive P), the suprathermal electron population increases in the direction enhancing I_{HXR} of channel 3. However, when the loop voltage is not zero and counter-ECCD is applied, I_{HXR} of channel 22 is not always dominant over that of channel 3. When the effect of the electron acceleration by the toroidal electric field is stronger than that caused by the wave-particle interaction, I_{HXR} of channel 3 is higher than that of channel 22 as observed in the co-ECCD case.

In order to compare the relative intensity of I_{HXR} between channels 22 and 3, the ratio between the two is presented in Figure B.7 for different EC wave power and loop voltage. It indicates again that during counter-ECCD the ratio falls below 1, when the effect of the loop voltage is dominant over that of the EC wave.

The change in the electron distribution function can be seen in Figure B.8. When there is no loop voltage, the Maxwellian distribution deforms into the toroidally asymmetric distribution as the toroidal direction of the EC wave changes. When the loop voltage is added, the electron population in the direction of the loop voltage increases.

Appendix B. Study of toroidal asymmetry in the hard X-ray emission

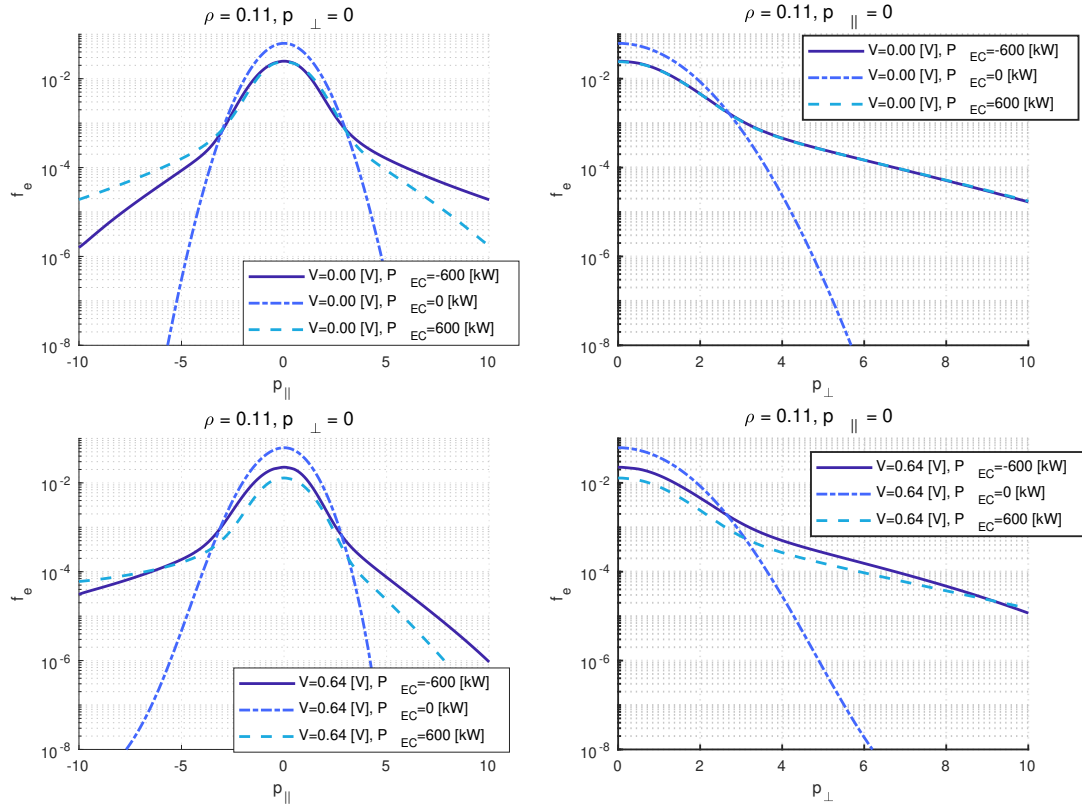


Figure B.8 – The electron distribution functions from the loop voltage and EC wave power scans. $p_{||}$ and p_{\perp} correspond to the parallel and perpendicular momentum normalized to the thermal electron momentum value.

B.3 Conclusions

Firstly, this appendix has shown that the toroidal measurement of the hard X-ray emission is sensitive to the change of the magnetic equilibrium, while the poloidal measurement is not. This indicates that a correct reconstruction of the magnetic equilibrium is important in the analysis of the toroidal hard X-ray profile analysis.

The scan of the loop voltage and the EC wave power has shown that the ratio of the two effects determines the asymmetry in the toroidal hard X-ray measurement. A further study based on more experimental data is required to clarify the sensitivity of the asymmetry to the loop voltage change. This will enhance the accuracy of the Fokker-Planck calculation, especially during the time-varying simulation.

C Study of non-standard sawtooth related to electron fishbones

Electron fishbones observed during the TCV ECCD discharges have been analyzed in chapter 4 of this thesis. The analysis in chapter 4 is focused on the fishbone oscillations, in order to investigate the nature of this suprathermal electron driven instability. In this appendix, the analysis is extended to quantities related to the thermal electron population, in particular related to the non-standard sawtooth oscillations [119, 129]. Different types of non-sawtooth oscillations are introduced and their relation to the electron fishbones is analyzed.

C.1 Observation of fishbone-like perturbations during non-standard sawteeth

Fishbone-like oscillations that are accompanied by non-standard sawteeth have been observed during ECRH and ECCD discharges in TCV. In the discharge analyzed in figure C.1, 440 kW of EC power is deposited around $\rho \simeq 0.13$ with a significant spatial dispersion, $w_{FWHM} \simeq 0.12$, from the low-field-side, at a plasma current 0.20 MA ($q_{95} \simeq 3.6$). The triangularity and elongation of the 95% poloidal flux surface are $\delta_{95} \simeq 0.32$ and $\kappa_{95} \simeq 1.37$, respectively. The co-ECCD drove a reduction in the loop voltage, $\Delta V_{loop} \simeq -0.3$ V below the ohmic loop voltage $V_{loop} \sim 1.1$ V. The $q = 1$ surface moves from $\rho \simeq 0.47$ at $t = 0.410$ s to $\rho \simeq 0.41$ at $t = 0.439$ s, as the plasma profile evolves with co-ECCD. T_e is higher than T_i , $T_e \sim 6T_i$, thus the effect of the fast ions on the MHD mode can be excluded. No neutral beam injection was used.

The soft X-ray emissivity I_{SXR} shows that the standard sawtooth shape changes to one of the non-standard sawteeth [130], the “humpback” sawtooth ((A) in Figure C.1) when ECCD is applied (“ P_{EC} on”): after the ramp-up, I_{SXR} decreases slightly for ~ 1 ms, then it continues increasing until it crashes as in a normal sawtooth termination. Four cycles of the humpback sawteeth appear for ~ 15 ms, then as the plasma profiles evolve, the “saturated” type appears ((B) in Figure C.1) : after the ramp-up, I_{SXR} saturates for 1-2 ms, then the cycle ends with a sudden sawtooth crash.

Appendix C. Study of non-standard sawtooth related to electron fishbones

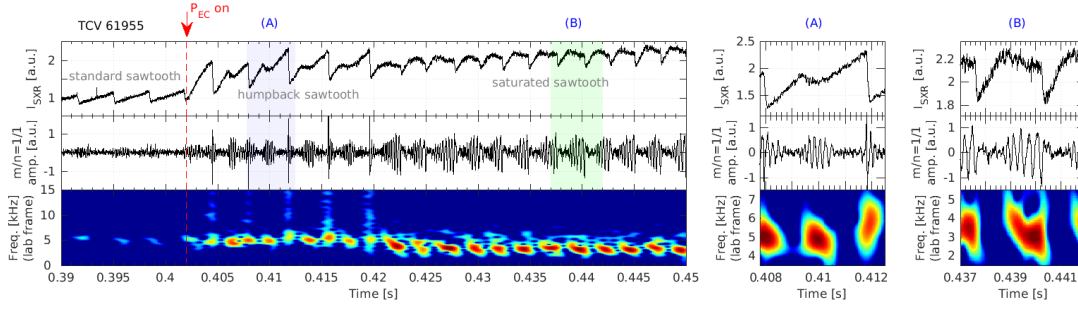


Figure C.1 – Transition of the sawtooth shape from standard to humpback (A) and saturated (B) sawtooth. (Top) Soft X-ray emissivity I_{SXR} of the channel passing through the magnetic axis, (mid) $m/n = 1/1$ mode amplitude from the SVD analysis of the magnetic probe array, (bot) spectrogram of the mode oscillations.

The SVD analysis of the magnetic probe array shows that the dominant mode has a spatial structure of $m/n = 1/1$ and exhibits fishbone-like bursts. These bursts are directly related to the shape of the non-standard sawtooth: as the fishbone-like oscillation grows, I_{SXR} decreases in the humpback sawtooth case (Fig.C.1(A)) or I_{SXR} saturates in the saturated sawtooth case (Fig.C.1(B)). Standard sawtooth precursor oscillations are also found when the humpback sawtooth terminates its cycle with the sudden crash, and the frequency is ~ 1 kHz higher than that of the fishbone-like oscillation. In the case of the saturated sawtooth, a relatively weaker sawtooth precursor may be overlapped with the fishbone-like burst, thus the mode frequency slightly increases after chirping-down (Fig.C.1(B)).

The $m/n = 1/1$ mode rotates near the $q = 1$ surface in the electron diamagnetic drift direction (counter-current direction), and the frequency is chirping down by 1-2 KHz for 1-2 ms, as presented in the spectrogram. The initial mode frequencies are ~ 5.5 kHz for the humpback sawtooth and ~ 4.5 kHz for the saturated sawtooth: this difference can be attributed to the change of plasma parameters such as I_p , n_e , T_e , or the change of the toroidal rotation velocity with ECCD. Since the typical toroidal rotation frequency in this ECCD condition is ~ 3 kHz in the ion diamagnetic direction, the Doppler-shifted mode frequency in the plasma frame is ~ 8 kHz in the electron diamagnetic drift direction.

In the discharge analyzed in figure C.2, 440 kW of EC power is deposited at $\rho \simeq 0.14$ ($w_{FWHM} \simeq 0.13$), from the low-field-side, at a plasma current 0.21 MA ($q_{95} \simeq 3.3$). Compared to the previous discharge (Fig.C.1), the toroidal angle of the EC launcher is moved ~ 5 degrees in the direction of increasing current-drive. The triangularity and elongation of the 95% poloidal flux surface are $\delta_{95} \simeq 0.14$ and $\kappa_{95} \simeq 1.42$, respectively. The co-ECCD drove a reduction in the loop voltage, $\Delta V_{loop} \simeq -0.5$ V below the ohmic loop voltage $V_{loop} \sim 1.1$ V. In this discharge, the “inverted” type of sawtooth appears: ~ 1 ms of ramp-up in I_{SXR} is followed by ~ 2 ms of steady decrease with the fishbone-like burst. The inverted sawtooth terminates its cycle when I_{SXR} is decreased to the initial value at the beginning of the ramp-up. No sudden crash of I_{SXR} is observed, unlike for the humpback and saturated sawteeth. The mode frequency, in

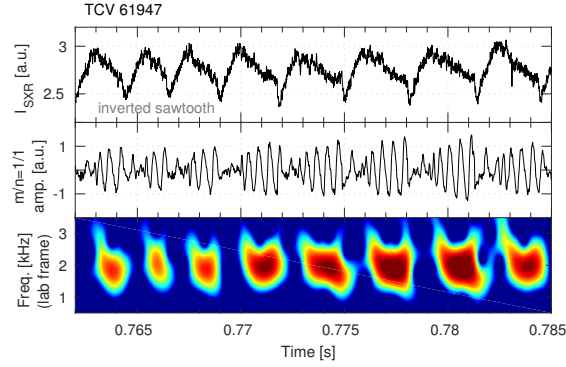


Figure C.2 – Example of the inverted sawtooth. (Top) soft X-ray emissivity of the channel passing through the magnetic axis, (mid) the $m/n = 1/1$ mode amplitude calculated from the SVD analysis of the magnetic probe array, (bot) the spectrogram of the mode oscillations.

the electron diamagnetic drift direction, is also chirping down. The plasma toroidal rotation frequency in this ECCD condition is ~ 5 kHz in the ion diamagnetic drift direction, thus the Doppler-shifted initial mode frequency in the plasma frame is ~ 7.5 kHz in the electron diamagnetic drift direction.

Figure C.3 displays the soft X-ray time traces of the channel passing through the (unperturbed) magnetic axis and adjacent channels inside the $q = 1$ surface, as well as the time evolution of the soft X-ray emissivity profiles. The soft X-ray emissivity profile increases during the ramp-up phase, keeping the axisymmetric structure, followed by the rotation inside the $q = 1$ surface during the fishbone-like oscillation phase.

The helical core structure is also observed in the T_e profiles measured by the Thomson scattering system. During the fishbone-like oscillations, the T_e profile is partially flattened inside the $q = 1$ surface and the maximum value of the T_e profile is shifted from the unperturbed core axis. In figure C.4, the $m = 1$ mode structure from the SVD analysis of a tomographically inverted soft X-ray emission image is presented with the T_e profile. The shifted core, which corresponds to the positive emissivity (red) in figure C.4(a), matches the T_e peak in figure C.4(b). The flattened T_e profile matches the negative phase of the $m = 1$ mode; however, it is unclear whether this is due to a magnetic island as observed in MAST during the standard sawtooth crash [120] or not, since at the moment there is no diagnostic in TCV that measures the q profile directly.

C.2 Analysis of the evolution of the electron distribution

In this section, the evolution of the electron distribution during the non-standard sawtooth activity, which is accompanied by the fishbone-like perturbations, is investigated. The Thomson scattering diagnostics data are used for the analysis of the thermal electrons and the hard

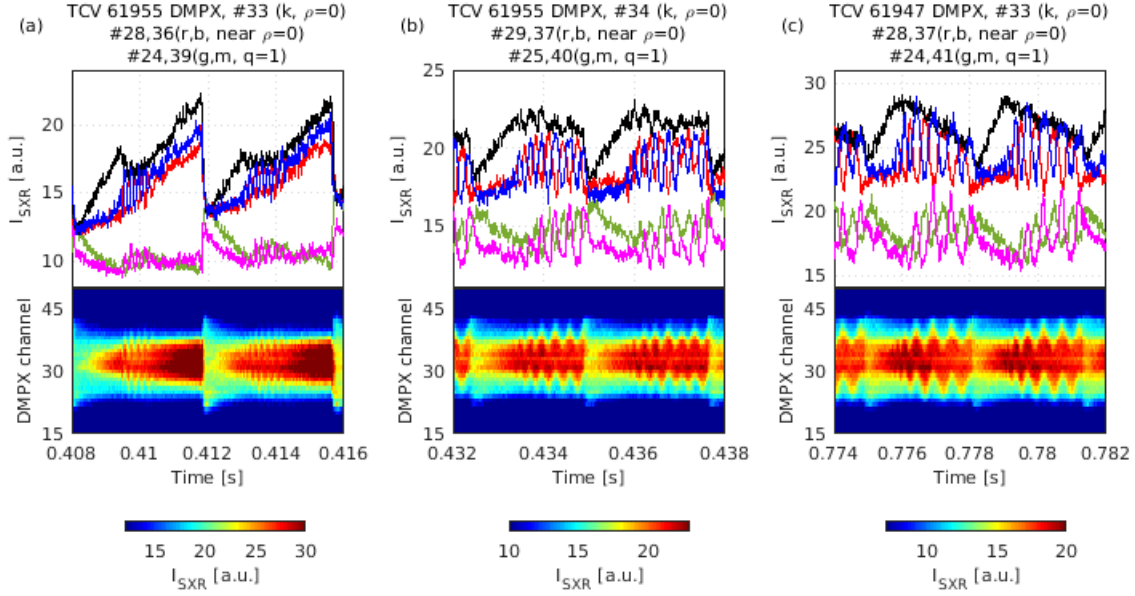


Figure C.3 – (Top) Soft X-ray emissivity traces for the channels inside the $q = 1$ surface, (bot) time evolution of the soft X-ray emissivity profiles of the (a) humpback, (b) saturated, and (c) inverted sawteeth.

X-ray data are used for the analysis of the suprathermal electrons. In this analysis, the hard X-ray statistics was not good enough for a detailed analysis of the mode oscillation near the $q = 1$ surface. Instead, only the hard X-ray data of the central channel, whose line of sight passes the magnetic axis, is presented. The electron distribution function, modeled using the Fokker-Planck code, is used to solve the fishbone dispersion relation to assess the role of the suprathermal electrons in the experimental observations.

C.2.1 Evolution of the electron density and temperature profiles: Thomson scattering data analysis

Figure C.5 displays the maximum values of the n_e and T_e profiles ($n_{e,max}$ and $T_{e,max}$, respectively) of two discharges, which have repetitive non-standard sawteeth. The inverted and saturated sawtooth cases, discussed earlier in relation with Figures C.2 and C.1, respectively, are shown in Figs. C.5(a) and (b). Compared to the inverted sawtooth case, the EC power is deposited farther from the magnetic axis in the saturated sawtooth case, but still inside the $q = 1$ surface. The ray-tracing calculation (TORAY) shows that the EC driven current is lower than the inverted sawtooth case; this can also be inferred from the lower loop voltage reduction with ECCD.

During the ramp-up phase, $n_{e,max}$ and $T_{e,max}$ correspond to the values at the magnetic axis.

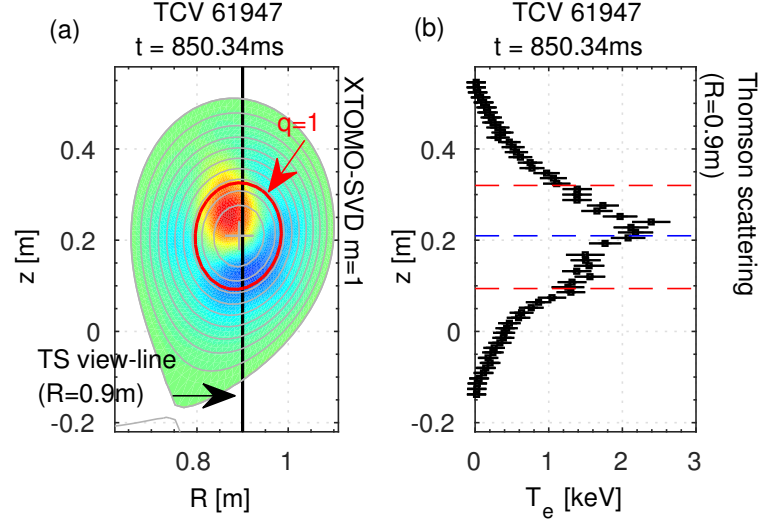


Figure C.4 – (a) $m = 1$ mode structure from the SVD analysis of the soft X-ray emission distribution inverted from XTOMO data. The $q = 1$ surface (red) and the vertical view-line of the Thomson scattering system at $R = 0.9$ m (black) are plotted. (b) T_e profile measured by the Thomson scattering system. Since the toroidal angle between XTOMO and the Thomson scattering system is $3\pi/4$, the corresponding phase shift is taken into account in determining the $m = 1$ mode phase.

However, during the fishbone-like oscillation phase, the center of the helical core can deviate from the view-line of the Thomson scattering system; therefore the measured $n_{e,max}$ and $T_{e,max}$ can be different from the actual values at the center of the helical core. For example, the helical core model in figure C.6(c) shows that the center of the helical core deviates from the view-line of the Thomson scattering system, whereas in figure C.6(a) the center of the helical core is on the view-line.

In figure C.5, while $n_{e,max}$ is quite constant over both the inverted and the saturated sawtooth cycles, $T_{e,max}$ follows the soft X-ray trace. However, during the fishbone-like oscillation phase, when I_{SXR} decreases or saturates after the ramp-up phase, $T_{e,max}$ sometimes deviates from the linearly decreasing or saturating trace; this can be attributed to the fact that the center of the helical core does not always pass the view-lines of the Thomson scattering system.

The n_e and T_e profiles measured by the Thomson scattering system during the fishbone-like oscillation phase is presented in figure C.6(b,d). As shown in figure C.4, the T_e profile is partially flattened inside the $q = 1$ surface due to the helical core structure. This is commonly observed during the fishbone-like oscillation phase, regardless of the type of the non-standard sawtooth. However, only in the inverted sawtooth case (Fig.C.6(b)), a hollow n_e profile inside the shifted core, where the T_e profile has a peak, is observed during the fishbone-like oscillation phase. This indicates that the core electron density drops when the helical core rotates during the inverted type central plasma relaxation. The shifted core density is decreased by up to 20 %

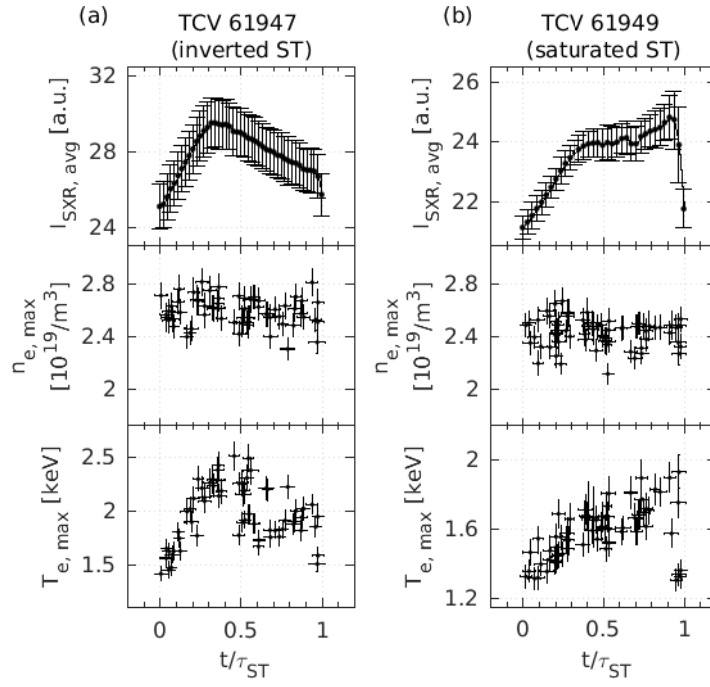


Figure C.5 – (Top) Averaged time trace of the soft X-ray emission of the channel passing through the magnetic axis. Maximum value of the (mid) n_e and (bot) T_e profiles at each Thomson measurement, mapped in time over the (a) inverted and (b) saturated sawtooth cycles, with the period τ_{ST} .

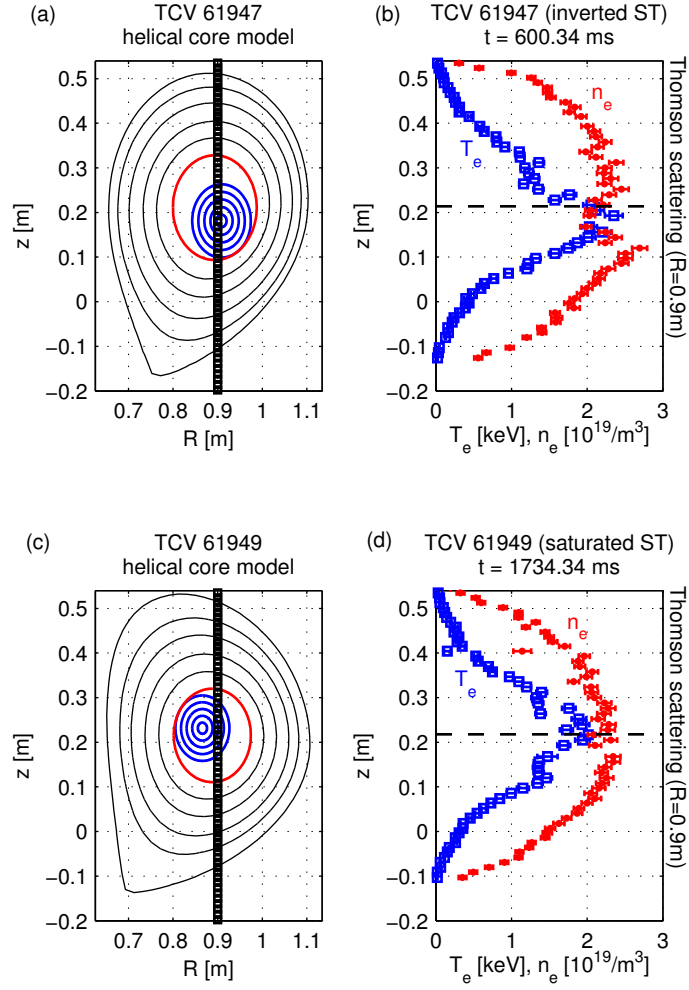


Figure C.6 – (a,c) Helical core model that matches the measurement of (b,d) the n_e and T_e profiles by the Thomson scattering system. In the helical core model, the center of the core is shifted $\sim 30\%$ of the length between $\rho = 0$ and the $q = 1$ surface.

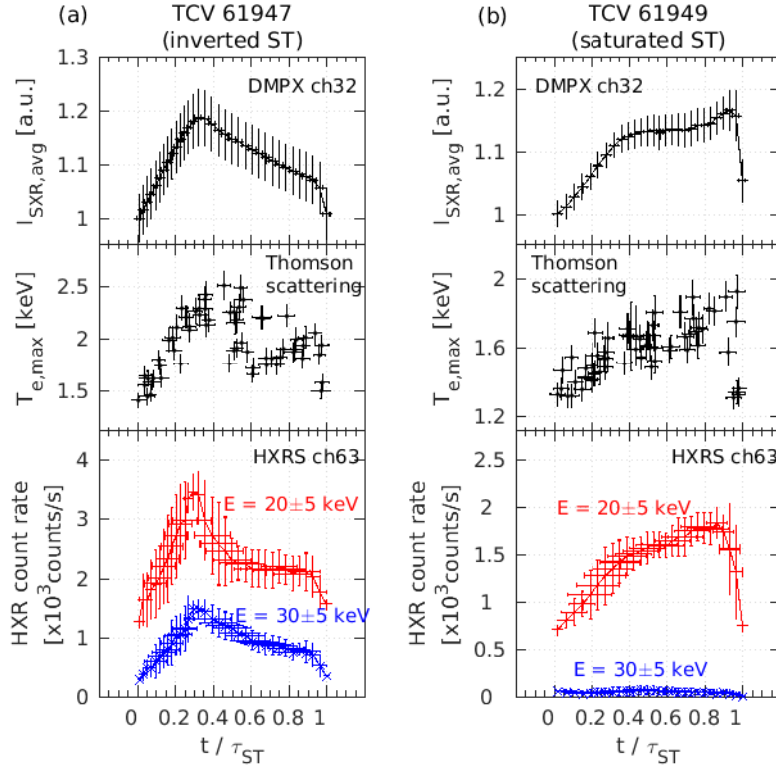


Figure C.7 – (Top) Averaged and normalized trace of the soft X-ray emission of the channel passing through the magnetic axis and (mid) the maximum value of the T_e profile presented in figure 4.4. (Bot) Hard X-ray count rates for different energy bins, $E = [15, 25]$ keV and $E = [25, 35]$ keV, measured by the channel, whose line-of-sight passes through the magnetic axis, for the (a) inverted and (b) saturated sawteeth.

of the density at the $q = 1$ surface and the drop is constant over the fishbone-like oscillation phase.

C.2.2 Suprathermal electron re-distribution: hard X-ray data analysis and numerical analysis

Figure C.7 displays the evolution of hard X-ray count rates as well as the soft X-ray intensity and the maximum value of the T_e profile, from the discharges shown in figure C.5. The soft X-ray trace is normalized to the initial value, I_{SXR} at $t / \tau_{ST} = 0$, where τ_{ST} is a non-standard sawtooth period. The relative change in the soft X-ray emissivity I_{SXR} can be described using the formula of the soft X-ray emission for the plasma in thermal equilibrium at temperature T_e , $I(\nu) = 1.54 \times 10^{-38} g_{ff}^- n_e n_Z Z^2 \exp(-h\nu / T_e) / \sqrt{T_e}$ [$W / m^3 / eV$], where g_{ff}^- is the the Maxwell-averaged Gaunt factor [80, 93].

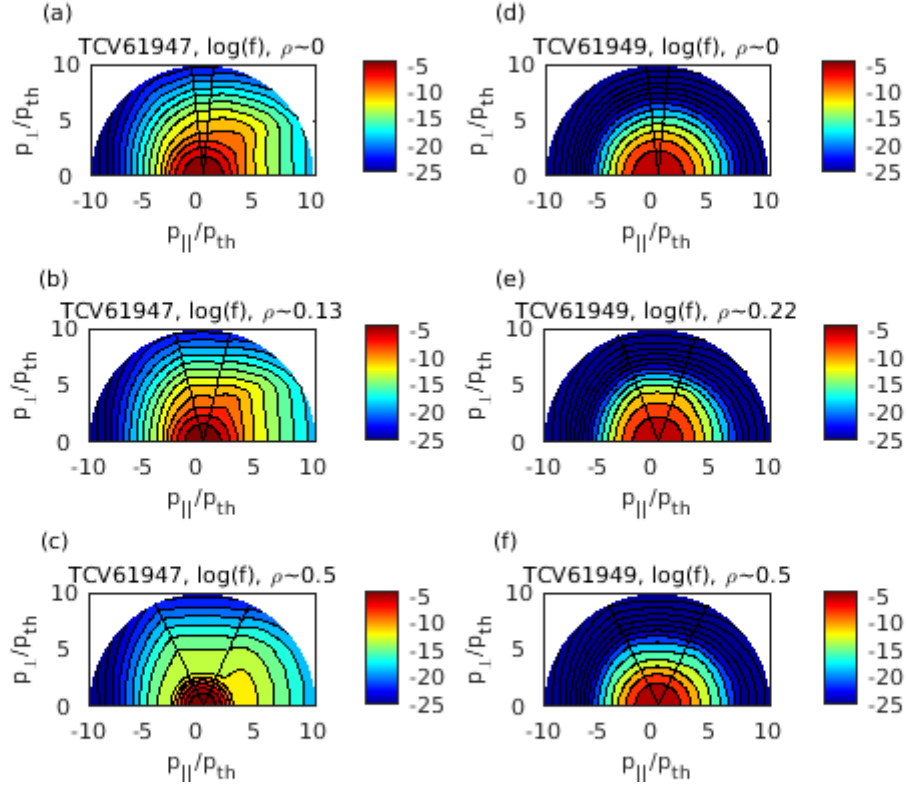


Figure C.8 – The electron distribution function modeled using the Fokker-Planck code LUKE for the (a-c) inverted and (d-f) saturated sawtooth cases, (a,d) near the magnetic axis, (b,e) near the EC power deposition location, and (c,f) near the $q = 1$ surface.

In both inverted and saturated sawteeth, the evolution of the photon count rate follows the trend of the observed soft X-ray trace, I_{SXR} , as T_e does. Figure C.7(a) shows that the suprathermal electron population increases during the ramp-up phase and decreases during the fishbone-like oscillation phase. In the beginning of the fishbone-like oscillation phase, at $t/\tau_{ST} \sim 0.3-0.4$, the lower energy photons ($E = 20 \pm 5$ keV) drop quickly and then slowly decrease during the rest of the cycle, while the higher energy photons ($E = 30 \pm 5$ keV) slowly decreases during the entire fishbone-like oscillation phase. This suggests that the lower energy suprathermal electrons may be lost quickly as the fishbone-like perturbation grows.

In the case of the saturated sawtooth (Fig.C.7(b)), the lower energy photon count rate ($E = 20 \pm 5$ keV) follows the soft X-ray emissivity trace, but the higher energy ($E = 30 \pm 5$ keV) photon count rate is too low to have enough statistics. This shows that the high energy suprathermal electron population was lower than that of the inverted sawtooth. In order to see the electron distribution function for the two discharges, both plasmas at the end of the ramp-up phase ($t/\tau_{ST} \sim 0.3$) are modeled by solving the Fokker-Planck equation using the code LUKE [77].

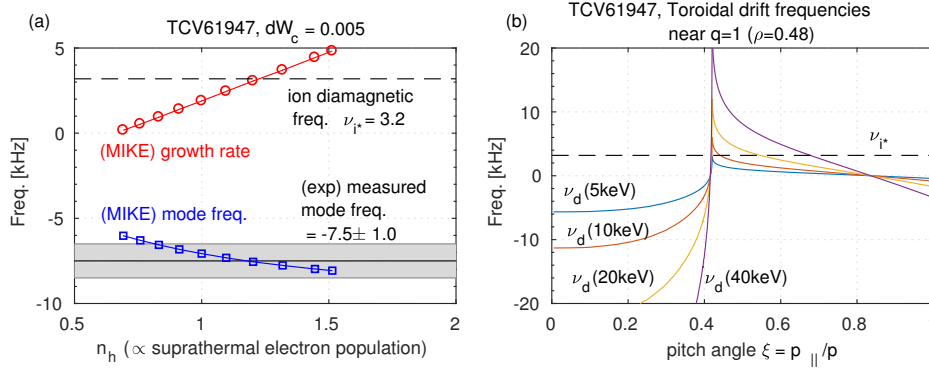


Figure C.9 – (a) Evolution of the mode frequency and growth rate over n_h , which is proportional to the energetic electron fraction. (b) Toroidal drift frequencies for different energy electrons near the $q = 1$ surface ($\rho \approx 0.48$).

The plasma parameters used in the simulation are: the n_e and T_e profiles measured by the Thomson scattering system, V_{loop} measured by flux loops, Z_{eff} measured by CXRS and the equilibrium profile reconstructed by the code LIUQE. Considering the anomalous transport of the fast electrons, the radial diffusion coefficient is set to $4 \text{ m}^2/\text{s}$, so that the simulated I_p matches the measured I_p . Figure C.8 displays the electron distribution functions in velocity space at different radial positions: at the magnetic axis, $\rho = 0$ (a,d), at the EC power deposition location, $\rho = 0.13$ for the inverted sawtooth (b) and $\rho = 0.24$ for the saturated sawtooth (e), and near the $q = 1$ surface, $\rho \approx 0.5$ (c,f). It is clear that the high energy electron population is higher in the inverted sawtooth case, as observed from the hard X-ray diagnostic. This electron distribution function is used to solve the fishbone dispersion relation (Fig.C.9).

The linear fishbone dispersion relation is solved using the code MIKE [18], based on the electron distribution function (Fig.C.8) modeled by the Fokker-Planck code LUKE. The T_e and n_e profiles at the end of the ramp-up phase, therefore at the onset of the fishbone-like burst, are used to assess the destabilization of the fishbone instability in the experimental condition. Figure C.9(a) shows the dependence of the mode frequency and growth rate on the suprathermal electron population: the suprathermal population destabilizes the mode and the mode frequency found in the simulation lies in the experimentally observed frequency range. The mode frequency is in the electron diamagnetic drift direction, as observed in the experiment. Stabilizing thermal ion FLR effects can be neglected, due to the low ion temperature, $T_e \sim 6T_i$.

Figure C.9(b) shows the toroidal drift frequencies computed from a TCV equilibrium for different energies, near the $q = 1$ surface. This indicates that trapped electrons in the energy range between 5 keV and 10 keV can resonate with the mode, rotating in the electron diamagnetic drift direction. The simulation on the saturated sawtooth case (Fig.C.8(d-f)) also yields a similar result: trapped electrons near 5-10 keV ($p/p_{th} \sim 2$) can destabilize the mode by the resonant interaction. This may explain why the fishbone mode is triggered in both inverted and saturated sawtooth cases despite the fact that the high energy population is quite different,

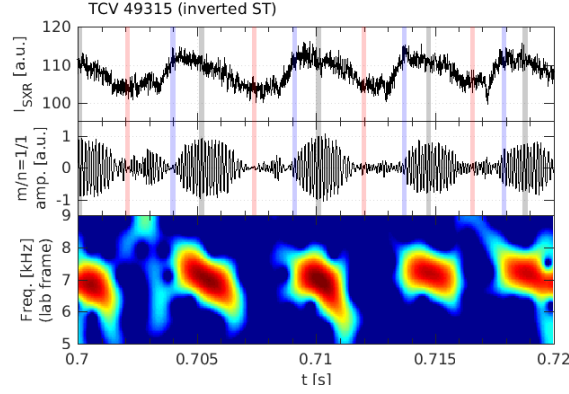


Figure C.10 – The soft X-ray emissivity of the central soft X-ray channel, the $m/n = 1/1$ mode amplitude from the SVD analysis of magnetic probe data, and spectrogram of the fishbone-like perturbation, for the inverted sawtooth discharge, whose HXRS data is inverted in figure 4.9. Vertical lines correspond to the conditional averaging points used in figure 4.9(c-e).

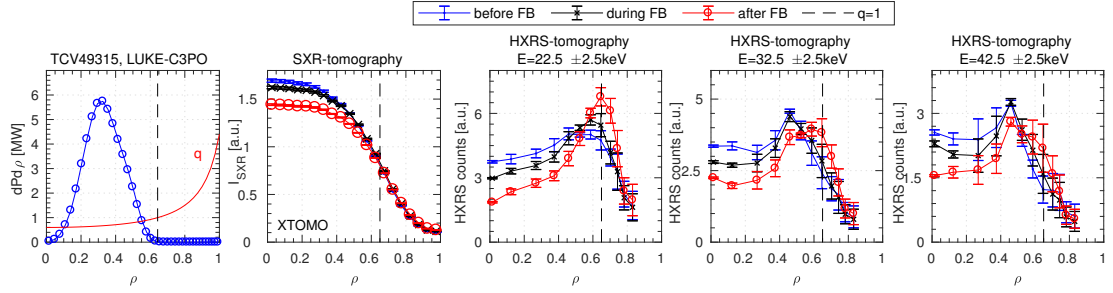


Figure C.11 – (a) EC power deposition and q profile, (b) radial distribution of the soft X-ray emissivity inverted from XTOMO measurement, and radial distribution of the hard X-ray photon counts inverted from the HXRS measurement for different energy bins: (c) $E = [20, 25]$ keV, (d) $E = [30, 35]$ keV, (e) $E = [40, 45]$ keV.

because the lower energy suprathermal electrons mainly resonate with the mode. In addition, the fast drop of the lower energy hard X-ray photons observed in figure C.7(a) can possibly be due to the resonant interaction of the lower energy suprathermal electrons with the mode.

In order to see the radial re-distribution of the suprathermal electrons with the fishbone-like burst, a tomographic inversion of conditionally-averaged hard X-ray data is performed for one of the inverted sawtooth discharges. Figure C.10 displays the soft X-ray trace, the $m/n = 1/1$ mode amplitude and spectrogram from this discharge. 1680 kW of EC power is deposited at $\rho = 0.33$ ($w_{FWHM} \approx 0.30$, Figure C.11(a)) from the low-field-side, at 0.24 MA ($q_{95} \sim 3.6$). The co-ECCD drove a reduction in the loop voltage, $\Delta V_{loop} \approx -1.0$ V below the ohmic loop voltage $V_{loop} \sim 1.3$ V. The inverted sawtooth of ~ 4 ms period appeared for ~ 1.7 s. As analyzed in the previous section, I_{SXR} decreases during the fishbone-like burst, after the ramp-up phase.

This discharge is chosen for the tomographic inversion due to its large $q = 1$ surface at $\rho = 0.65$. Thus the number of HXRS line-of-sights passing inside the $q = 1$ surface is large enough to see the hard X-ray emission distribution inside the $q = 1$ surface. The maximum likelihood method [94] is used to invert the hard X-ray emissivity distribution, which features an off-axis peak, near the $q = 1$ surface, with the square pixel discretization scheme. The hard X-ray emissivity profiles are presented in figure C.11 for three different energy bins and for three different times during the non-standard sawtooth: before the onset of the fishbone(FB)-like oscillation, thus at the end of the ramp-up phase (“before FB”), in the middle of the fishbone-like oscillation (“during FB”), and after the fishbone-like oscillation, thus at the end of the inverted sawtooth cycle (“after FB”). The intervals are partially shown in figure C.10, in blue, black and red colors, respectively.

As shown in Figure C.7, the core suprathermal population decreases during the fishbone-like burst, following the I_{SXR} trace. In addition, as the central HXR emissivity decreases, the emissivity at the $q = 1$ surface increases: this shows that the core suprathermal electrons may be expelled to the $q = 1$ surface during the fishbone-like oscillation phase. The hard X-ray photon count difference between $\rho = 0$ and $\rho = 0.65$ ($q = 1$) is larger for the lower energy suprathermal electrons, possibly due to the low resonant electron energy. The evolution of the electron distribution function with the resonant particle loss will be studied in the future, by adjusting the transport term in the Fokker-Planck calculation and taking the helical core structure into account. The modeled electron distribution function will be used to feed the synthetic diagnostic, which permits a direct comparison between the simulation and the measurement.

C.3 Summary

In this appendix, the observation of fishbone-like oscillations accompanied by a central plasma relaxation, taking the form of non-standard sawtooth, is presented. A detailed analysis of the soft X-ray data reveals a direct relation between the fishbone-like oscillation and the non-standard sawtooth: after the ramp-up phase, the sawtooth shape changes when the fishbone-like oscillation starts to grow. In addition, a partially flattened electron temperature profile inside the $q = 1$ surface is measured by the high spatial resolution Thomson scattering system, which supports the formation of a helical core observed in the soft X-ray measurements.

Hard X-ray analysis indicates a correlation between the suprathermal electron population and the onset of the instability. Furthermore, the re-distribution of the suprathermal electron profiles during the mode oscillation is observed from the hard X-ray tomography inversion. The experimental results are complemented by the solution of the linear fishbone dispersion relation, coupled with the Fokker-Planck modeling of the electron distribution function. A more detailed analysis on the internal kink is presented in chapter 4, based on this work.

D Solving the electron fishbone dispersion relation

In chapter 4, the electron fishbones observed during ECCD have been analyzed by solving the electron fishbone dispersion relation using the code MIKE. In this Appendix, a detailed procedure of solving the dispersion relation is presented.

D.1 ECCD discharge with fixed EC power

The Fokker-Planck modeled electron distribution function discussed in chapter 4 is used to solve the linear fishbone dispersion relation, $\delta\hat{W}_f + \delta\hat{W}_k(\omega) = \delta I(\omega)$, where ω is the complex frequency of the mode, $\delta\hat{W}_f$ and $\delta\hat{W}_k$ describe the fluid and kinetic components of the potential energy, respectively, and δI includes the physics inside the inertial layer [18]. The code MIKE is used [18], which was developed to solve the linear fishbone dispersion relation, considering the effect of both trapped and passing electrons on the resonant interaction. This code is coupled to the Fokker-Planck code LUKE, such that the equilibrium profiles and the numerical results from LUKE can be used in solving the linear dispersion relation. In practice, $\delta\hat{W}_c$ is added to the dispersion relation to modify the fluid term, and $\delta\hat{W}_f$ and $\delta\hat{W}_k$ are decomposed into thermal(th) and hot(h) particle parts. Therefore the dispersion relation can be written as: $\delta\hat{W}_c + \delta\hat{W}_{th,f} + \delta\hat{W}_{th,k}(\omega) + n_h(\delta\hat{W}_{h,f} + \delta\hat{W}_{h,k}(\omega)) = \delta I(\omega)$. Once every term is calculated, n_h is changed in order to study the effect of the suprathermal electron population on the stability of the mode.

The result of the calculation is presented in Figure D.1 (a), for $n_h = 1$ and varying δW_c . In this section, n_h corresponds to n_s/n_{s0} of chapter 4. The solutions of the dispersion relation, the real and imaginary frequencies that correspond to the mode frequency and the growth rate, are obtained at the intersection of the $\text{real}(\delta W_c)$ and $\text{imag}(\delta W_c)$ lines. For the fixed δW_c value of $4 \cdot 10^{-3}$, the real and imaginary parts of n_h are presented in Figure D.1 (b) and the corresponding solutions are presented in Figure D.1 (c,d). The predicted mode frequency lies within the error range of the measured mode frequency, and the mode growth rate is positive and grows as the suprathermal population grows, thus in this case the suprathermal electron population destabilizes the fishbone mode. Here the experimentally measured mode

Appendix D. Solving the electron fishbone dispersion relation

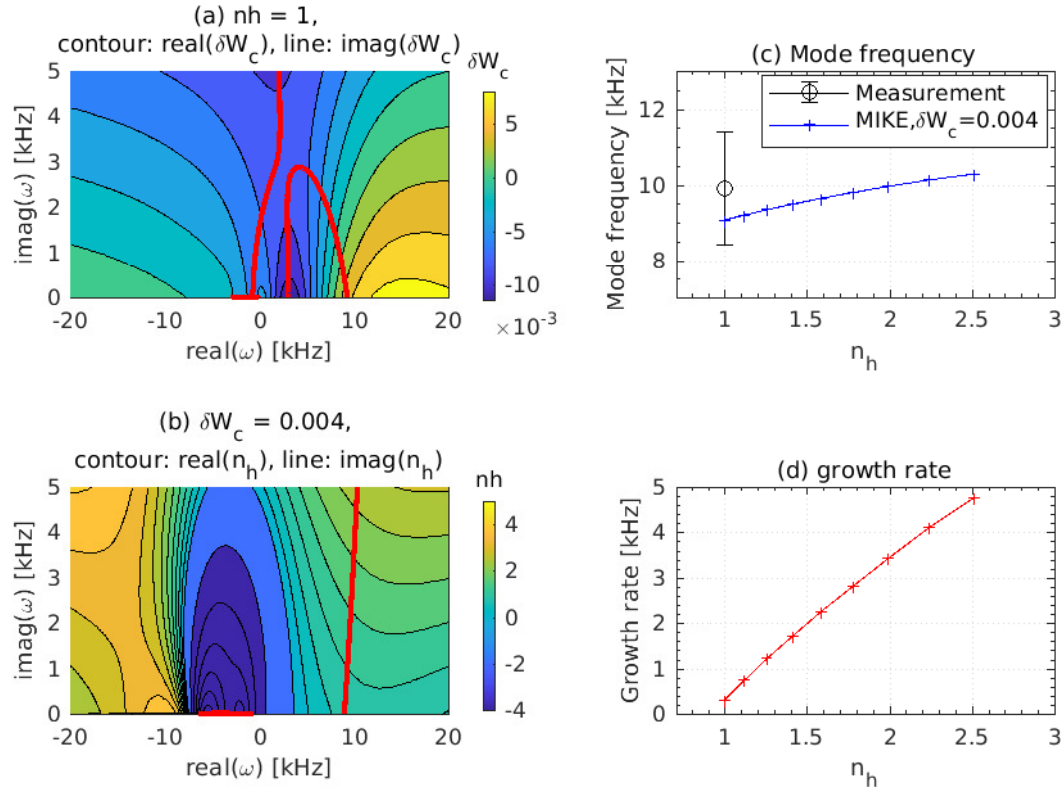


Figure D.1 – (a) Real (color-filled contour) and imaginary (red solid line) parts of δW_c for $n_h = 1$, (b) Real (color-filled contour) and imaginary (red solid line) parts of n_h for $\delta W_c = 0.004$. The solutions, (c) mode frequency ($\text{real}(\omega)$) and (d) growth rate ($\text{imag}(\omega)$), are obtained for fixed $\delta W_c = 0.004$ and varying n_h .

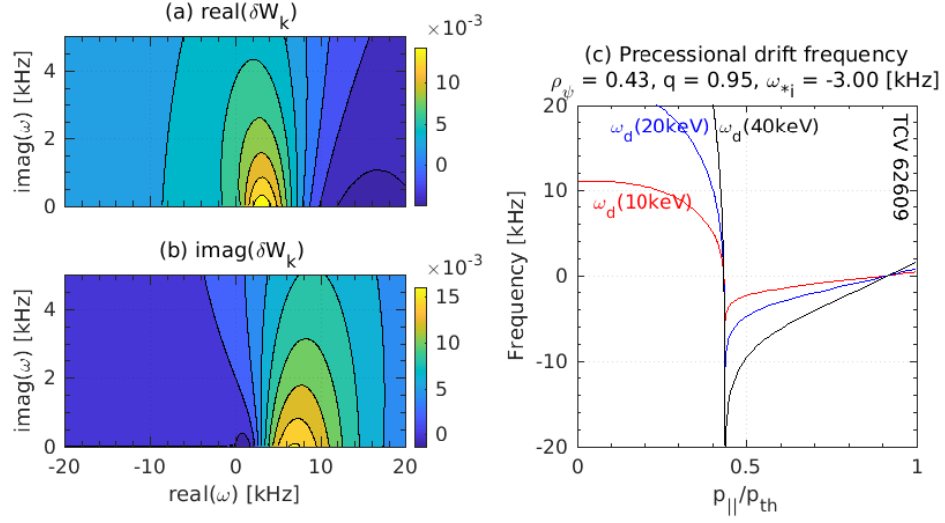


Figure D.2 – (a) Real and (b) imaginary parts of the kinetic potential energy term, δW_k . (c) Toroidal precessional drift frequency ω_d of suprathermal electrons near the $q = 1$ surface, as a function of pitch angle, $p_{||}/p_{th}$.

frequency is shifted according to the toroidal plasma rotation, thus the mode frequency in the plasma frame can be compared to the frequency predicted by the simulation.

The mode rotation directions from the experiment and from the simulation are both opposite to the plasma current direction, thus it is possible that the deeply trapped electron population interacts with the mode. The calculation of the toroidal precessional drift frequency of suprathermal electrons near the $q = 1$ surface, in Figure D.2 (c), shows that the drift of deeply trapped electrons is in the same direction as the mode rotation direction.

The role of trapped electrons in the resonant interaction may be checked further by solving the linear dispersion relation without including the passing electrons. In Figure D.3, the real and imaginary curves of the kinetic potential energy δW_c at $\gamma = 0$ show that there is almost no change in the result when the effect of the trapped electrons is included in the calculation. The root-mean-square error between the two curves is 8.7×10^{-6} in $\text{real}(\delta W_k)$ and 5.1×10^{-7} in $\text{imag}(\delta W_k)$, thus the differences are negligible in relative terms.

Appendix D. Solving the electron fishbone dispersion relation

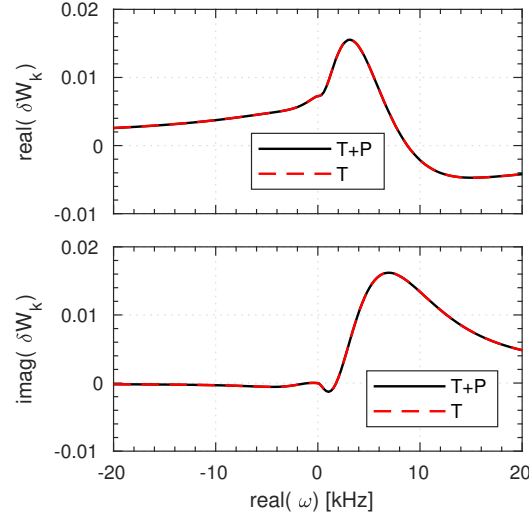


Figure D.3 – Real and imaginary parts of the kinetic potential energy δW_k , when $\gamma = \text{imag}(\omega) = 0$. Solid black lines, "T+P", correspond to the simulation including the full electron distribution function, both trapped and passing electrons, while red dashed lines, "T", correspond to the simulation including only the trapped electrons.

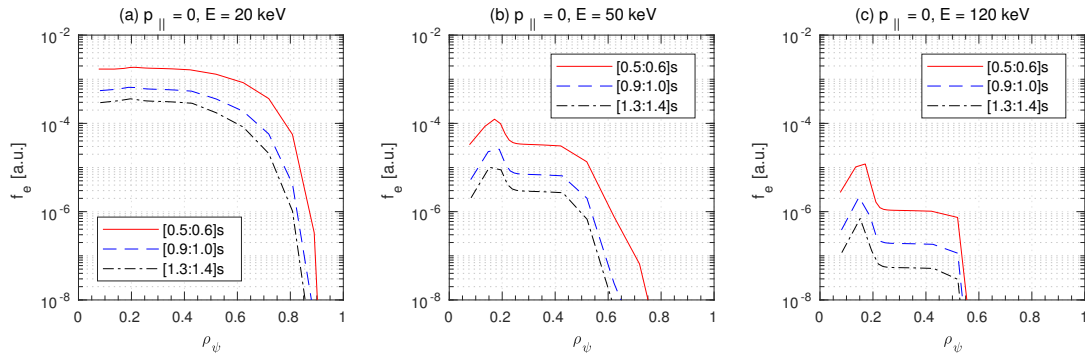


Figure D.4 – Radial profile of the Fokker-Planck modeled electron distribution function, for $\theta = 0$ and $p_{||} = 0$, at three time windows, from 0.5 s to 0.6 s when $P_{ECCD} = 750 \text{ kW}$, from 0.9 s to 1.0 s when $P_{ECCD} = 550 \text{ kW}$, from 1.3 s to 1.4 s when $P_{ECCD} = 350 \text{ kW}$.

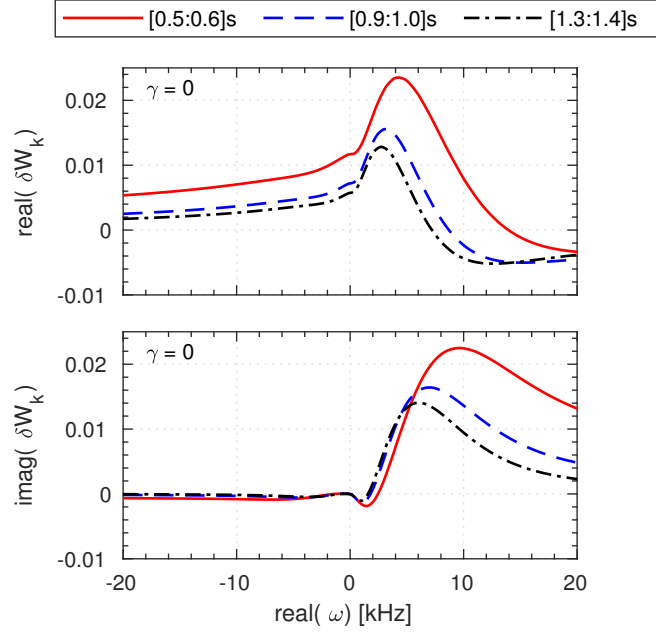


Figure D.5 – Real and imaginary parts of the kinetic potential energy δW_k , for $\gamma = \text{imag}(\omega) = 0$, at three time windows with different ECCD powers.

D.2 Study of the ECCD power effect on the onset of the fishbone mode

In chapter 4, the ECCD power scan experiment has shown that the electron temperature and the suprathermal electron population both decrease during the ECCD power ramp-down. The equilibrium reconstruction by the code LIUQE shows that the q profile is kept constant throughout the discharge. The constant equilibrium profile gives constant toroidal drift frequency profiles throughout the discharge, which in turn keeps the resonance condition fulfilled, as can be checked in the denominator of the kinetic potential energy part in the fishbone dispersion relation [18],

$$\delta \hat{W}_k = -\frac{\pi}{2} \frac{\mu_0}{B_0^2} \frac{1}{V} \int E^2 \bar{\Omega}_d^2 \frac{\omega \partial_E \ln F - \omega_* \partial_r \ln F}{\omega - (q-1)\omega_b \delta_p - \omega_d} F d^3 x d^3 p, \quad (\text{D.1})$$

where B_0, E, F, x and p are the magnetic field on axis, the energy of the particle, the electron distribution, the position in real space and in momentum space, respectively. $\omega, \omega_*, \omega_b, \omega_d$ are the mode, the ion diamagnetic, the bounce and the toroidal drift frequencies, respectively. $\bar{\Omega}_d$ is defined by $\omega_d = (qE\bar{\Omega}_d)/(eB_0R_p r)$, with e is the electron charge and R_p is the major radius. The integral is limited to the space inside the $q = 1$ surface of total volume $V = 2\pi^2 r_s^2 R_p$, where $q \simeq 1$ at $r = r_s$.

Appendix D. Solving the electron fishbone dispersion relation

During the ECCD power scan #62755, three time windows are selected for the analysis: from 0.5 s to 0.6 s with $P_{EC} = 750$ kW, from 0.9 s to 1.0 s with $P_{EC} = 550$ kW, and from 1.3 s to 1.4 s with $P_{EC} = 350$ kW. Since the equilibrium and the electron density are kept constant throughout the discharge, the electron temperature and RF power are varied according to the experimentally measured values. The Fokker-Planck modeling is based on the analysis in section 5.1, using the localized transport model. The modelled electron distribution function at different energies is presented in Figure D.4, for the three time windows. As the ECCD power decreases with time, as observed in the hard X-ray profiles, the suprathermal electron population decreases at every energy bin.

Since the equilibrium is kept constant, the resonance condition does not change but the numerator of the equation D.1 changes: the kinetic part of the potential energy δW_k is larger when the ECCD power is high, following the higher suprathermal electron population. Figure D.5 shows the real and imaginary parts of the kinetic portion of the potential energy, at $\gamma = \text{imag}(\omega) = 0$. Due to the constant equilibrium, the peak position is not varying during the ECCD power scanning but the overall level decreases as the ECCD power decreases, since δW_k is proportional to the electron distribution.

Bibliography

- [1] I Langmuir. *Proceedings of the National Academy of Sciences*, 14:627, 1928.
- [2] L Tonks and I Langmuir. *Physical Review*, 33:195, 1929.
- [3] F F Chen. *Introduction to plasma physics and controlled fusion*. Springer, 1984.
- [4] J Ongena et al. *Nature Physics*, 12:398, 2016.
- [5] A V Melnikov. *Nature physics*, 12:386, 2016.
- [6] J Jacquinot et al. *Plasma physics and controlled fusion*, 41:A13, 1999.
- [7] ITER Physics Basis Editors, ITER Physics Expert Group Chairs, Co-Chairs, ITER Joint Central Team, and Physics Unit. *Nuclear Fusion*, 39:2137, dec 1999.
- [8] EDA ITER. *International Atomic Energy Agency*, 24:257ff, 2002.
- [9] ITER Physics Expert Group on Energe Drive and ITER Physics Basis Editors. *Nuclear Fusion*, 39:2495, dec 1999.
- [10] V Erckmann and U Gasparino. *Plasma physics and controlled fusion*, 36:1869, 1994.
- [11] D Mazon et al. *Nature Physics*, 12:14, 2016.
- [12] M Porkolab. In *AIP Conference Proceedings*, volume 933, page 3. AIP, 2007.
- [13] J P Freidberg. *Plasma physics and fusion energy*. Cambridge university press, 2008.
- [14] S Coda et al. *Nuclear Fusion*, 59:112023, 2019.
- [15] J P Freidberg. *Ideal MHD*. Cambridge University Press, 2014.
- [16] K McGuire et al. *Physical Review Letters*, 50:891, 1983.
- [17] K L Wong et al. *Physical Review Letters*, 85:996, 2000.
- [18] A Merle et al. *Physics of Plasmas*, 19:072504, 2012.
- [19] C F F Karney. *Computer Physics Reports*, 4:183, 1986.

Bibliography

- [20] M Brambilla. *Kinetic theory of plasma waves: homogeneous plasmas*. Oxford University Press, 1998.
- [21] T H Stix. *Waves in plasmas*. Springer Science & Business Media, 1992.
- [22] F Hofmann et al. *Nuclear Fusion*, 28:1871, 1988.
- [23] M Anton et al. *Plasma Physics and Controlled Fusion*, 38:1849, 1996.
- [24] T Dudok de Wit et al. *Physics of Plasmas*, 1:3288, 1994.
- [25] J-M Moret et al. *Review of Scientific Instruments*, 69:2333, 1998.
- [26] V S Udintsev. In *EC-14: 14th Joint Workshop on Electron Cyclotron Emission and Electron Cyclotron Resonance Heating*, 2006.
- [27] S Coda et al. In *1st EPS conference on Plasma Diagnostics*, volume 240, page 139. SISSA Medialab, 2016.
- [28] J Kamleitner et al. *Nuclear Instruments and Methods in Physics Research Section A: Accelerators, Spectrometers, Detectors and Associated Equipment*, 736:88, 2014.
- [29] R Prater. *Physics of Plasmas*, 11:2349, 2004.
- [30] C F Kennel and F Engelmann. *The Physics of Fluids*, 9:2377, 1966.
- [31] I Lerche. *The Physics of Fluids*, 11:1720, 1968.
- [32] N J Fisch and A H Boozer. *Physical Review Letters*, 45:720, 1980.
- [33] T Ohkawa. *General Atomics Report GA-A13847*, 1976.
- [34] T C Luce et al. *Physical review letters*, 83:4550, 1999.
- [35] S Coda et al. *Plasma Physics and Controlled Fusion*, 42:B311, 2000.
- [36] H Zohm et al. *Nuclear Fusion*, 41:197, 2001.
- [37] R J La Haye. *Physics of Plasmas*, 13:055501, 2006.
- [38] T P Goodman et al. *Physical review letters*, 106:245002, 2011.
- [39] T C Hender et al. *Nuclear Fusion*, 47:S128, 2007.
- [40] R J La Haye. In *EPJ Web of Conferences*, volume 157, page 03027. EDP Sciences, 2017.
- [41] R W Harvey et al. *Physical review letters*, 88:205001, 2002.
- [42] P Nikkola et al. *Nuclear fusion*, 43:1343, 2003.
- [43] C C Petty et al. *Nuclear fusion*, 42:1366, 2002.

-
- [44] E Poli et al. *Nuclear Fusion*, 53:013011, 2012.
- [45] N Bertelli and E Westerhof. *Nuclear Fusion*, 49:095018, 2009.
- [46] S Coda et al. *Nuclear fusion*, 43:1361, 2003.
- [47] A Köhn et al. *Plasma Physics and Controlled Fusion*, 60:075006, 2018.
- [48] N Bertelli et al. In *Journal of Physics: Conference Series*, volume 260, page 012002. IOP Publishing, 2010.
- [49] C Tsironis et al. *Physics of Plasmas*, 16:112510, 2009.
- [50] K Hizanidis et al. *Physics of Plasmas*, 17:022505, 2010.
- [51] F J Casson et al. *Nuclear Fusion*, 55:012002, 2015.
- [52] O Chellaï et al. *Plasma Physics and Controlled Fusion*, 61:014001, 2018.
- [53] J Decker et al. In *EPJ Web of Conferences*, volume 32, page 01016. EDP Sciences, 2012.
- [54] Y Peysson et al. *Plasma Physics and Controlled Fusion*, 53:124028, 2011.
- [55] S Von Goeler et al. *Nuclear fusion*, 25:1515, 1985.
- [56] G Giruzzi et al. *Physical review letters*, 74:550, 1995.
- [57] Y Peysson and J Decker. *Physics of Plasmas*, 15:092509, 2008.
- [58] S Coda. *Review of Scientific Instruments*, 79:10F501, 2008.
- [59] F M Poli et al. *Plasma Physics and Controlled Fusion*, 58:095001, 2016.
- [60] A Schmidt et al. *Physics of Plasmas*, 18:056122, 2011.
- [61] M Valovic et al. *Nuclear Fusion*, 40:1569, 2000.
- [62] J A Snipes et al. *Nuclear Fusion*, 48:072001, 2008.
- [63] C B Deng et al. *Physical Review Letters*, 103:025003, 2009.
- [64] M Isobe et al. *Nuclear Fusion*, 50:084007, 2010.
- [65] X T Ding et al. *Nuclear Fusion*, 53:043015, 2013.
- [66] X T Ding et al. *Nuclear Fusion*, 42:491, 2002.
- [67] W Chen et al. *Nuclear Fusion*, 49:075022, 2009.
- [68] W Chen et al. *Nuclear Fusion*, 50:084008, 2010.
- [69] L M Yu et al. *Nuclear Fusion*, 57:036023, 2017.

Bibliography

- [70] F Zonca et al. *Nuclear Fusion*, 47:1588, 2007.
- [71] R Cesario et al. *Nuclear Fusion*, 49:075034, 2009.
- [72] A Macor et al. *Physical Review Letters*, 102:155005, 2009.
- [73] Z O Guimarães-Filho et al. *Nuclear Fusion*, 52:094009, 2012.
- [74] L Delgado-Aparicio et al. *Physics of Plasmas*, 22:050701, 2015.
- [75] L Sugiyama et al. *Physics of Plasmas*, 25:082120, 2018.
- [76] Y P Zhang et al. *Review of Scientific Instruments*, 81:103501, 2010.
- [77] J Decker et al. Tech. rep. No EUR-CEA-FC-1736, 2004.
- [78] R L Gluckstern and M H Hull Jr. *Physical Review*, 90:1030, 1953.
- [79] G Elwert and E Haug. *Physical Review*, 183:90, 1969.
- [80] I H Hutchinson. *Principles of plasma diagnostics*. Cambridge University Press, 2005.
- [81] J Stevens et al. *Nuclear fusion*, 25:1529, 1985.
- [82] G F Knoll. *Radiation detection and measurement*. John Wiley & Sons, 2010.
- [83] Y Peysson et al. *Nuclear Instruments and Methods in Physics Research Section A: Accelerators, Spectrometers, Detectors and Associated Equipment*, 458:269, 2001.
- [84] I Kawrakow and D W O Rogers. *NRC Report PIRS-701, NRC, Ottawa*, 2000.
- [85] Y Peysson and J Decker. *Fusion Science and Technology*, 65:22, 2014.
- [86] Y Peysson and J Decker. *Plasma Physics and Controlled Fusion*, 54:045003, 2012.
- [87] S Gnesin et al. In *AIP Conference Proceedings*, volume 988, page 222. AIP, 2008.
- [88] S Gnesin et al. *Review of scientific instruments*, 79:10F504, 2008.
- [89] S Gnesin. Electron cyclotron heating and suprathermal electron dynamics in the tcv tokamak. *EPFL Thesis 5181*, 2011.
- [90] J Kamleitner. Suprathermal electron studies in tokamak plasmas by means of diagnostic measurements and modeling. *EPFL Thesis 6523*, 2015.
- [91] J Kamleitner et al. *Plasma Physics and Controlled Fusion*, 57:104009, 2015.
- [92] L C Ingesson et al. *Fusion science and technology*, 53:528, 2008.
- [93] I Furno et al. *Nuclear Fusion*, 41:403, 2001.

-
- [94] T Craciunescu et al. *Nuclear Instruments and Methods in Physics Research Section A: Accelerators, Spectrometers, Detectors and Associated Equipment*, 595:623, 2008.
- [95] Y Nagayama and A W Edwards. *Review of scientific instruments*, 63:4757, 1992.
- [96] Y Nagayama. *Journal of applied physics*, 62:2702, 1987.
- [97] Y Dong et al. *Journal of the Korean Physical Society*, 49, 2006.
- [98] A M Cormack. *Journal of applied physics*, 34:2722, 1963.
- [99] R S Granetz and P Smeulders. *Nuclear fusion*, 28:457, 1988.
- [100] L Wang and R S Granetz. *Review of scientific instruments*, 62:1115, 1991.
- [101] A N Tikhonov and V I Arsenin. *Solutions of ill-posed problems*, volume 14. Winston, Washington, DC, 1977.
- [102] T Craciunescu et al. *Nuclear Instruments and Methods in Physics Research Section A: Accelerators, Spectrometers, Detectors and Associated Equipment*, 605:374, 2009.
- [103] L A Shepp and Y Vardi. *IEEE transactions on medical imaging*, 1:113, 1982.
- [104] S Texter et al. *Nuclear Fusion*, 26:1279, 1986.
- [105] M Odstreil et al. *Nuclear Instruments and Methods in Physics Research Section A: Accelerators, Spectrometers, Detectors and Associated Equipment*, 686:156, 2012.
- [106] G W Phillips and K W Marlow. *Nuclear Instruments and Methods*, 137:525, 1976.
- [107] J L Campbell et al. *Nuclear Instruments and Methods in Physics Research Section B: Beam Interactions with Materials and Atoms*, 9:71, 1985.
- [108] R H Redus et al. *IEEE Transactions on Nuclear Science*, 56:2524, 2009.
- [109] J E Fernández et al. *X-Ray Spectrometry*, 44:177, 2015.
- [110] SYF CHU et al. The Lund/LBNL Nuclear Data Search, Version 2.0, available at <http://nucleardata.nuclear.lu.se/toi/> (accessed on September 25th, 2018).
- [111] G Giruzzi et al. *Nuclear Fusion*, 39:107, 1999.
- [112] N J Fisch. *Reviews of Modern Physics*, 59:175, 1987.
- [113] D Choi et al. *Plasma Physics and Controlled Fusion*, 62:025006, 2020.
- [114] Y Peysson and J Decker. In *AIP Conference Proceedings*, volume 1069, page 176. AIP, 2008.
- [115] O Sauter et al. *Physics of Plasmas*, 6:2834, 1999.

Bibliography

- [116] O Sauter et al. *Physics of Plasmas*, 9:5140, 2002.
- [117] A Sushkov et al. *Review of Scientific Instruments*, 79:023506, 2008.
- [118] Z A Pietrzyk et al. *Nuclear Fusion*, 39:587, 1999.
- [119] I Furno et al. *Nuclear Fusion*, 41:403, 2001.
- [120] I T Chapman et al. *Physical Review Letters*, 105:255002, 2010.
- [121] J P Graves et al. *Plasma Physics and Controlled Fusion*, 55:014005, 2012.
- [122] R B White. *The theory of toroidally confined plasmas*. World Scientific Publishing Company, 2013.
- [123] J P Graves. *Plasma Physics and Controlled Fusion*, 55:074009, 2013.
- [124] L Chen et al. *Physical Review Letters*, 52:1122, 1984.
- [125] T Suzuki et al. *Nuclear Fusion*, 44:699, 2004.
- [126] J Decker. In *AIP Conference proceedings*, volume 694, page 447. AIP, 2003.
- [127] H He et al. *Nuclear Fusion*, 54:114001, 2014.
- [128] J P Graves. Private Communication.
- [129] I Furno et al. *Nuclear Fusion*, 41:403, 2001.
- [130] Z A Pietrzyk et al. *Nuclear Fusion*, 39:587, 1999.

Acknowledgements

Foremost, I would like to express my sincere gratitude to my supervisor Stefano Coda, for his support, patient guidance, and helpful comments of this research work over the years. My grateful thanks are also extended to Jonathan Graves for his help in MHD analysis and for many discussions of MHD theory, to Joan Decker for his assistance with the Fokker-Planck analysis and for his technical support with the code LUKE, and to Antoine Merle for his support in the electron fishbone analysis and for his help with the code MIKE.

Thanks to all of the TCV team¹ for keeping the tokamak running. I wish to acknowledge the technical help with HXRS provided by Severino Antonioni, Stefano Barberis, Pierre-François Isoz, and Blaise Marlétaz. Thanks to Miguel Silva for the gyrotron operation. In particular, I would like to thank Xavier Llobet for his help with the HXRS acquisition.

It has been a great privilege to work with the scientists of the TCV team, without whom I could not have understood and utilized multiple diagnostics. My gratitude goes to Patrick Blanchard and Hugo Arnichand with Thomson scattering system, Claudio Marini, Alexander Karpushov, and Filippo Bagnato with CXRS, Matteo Fontana, Laurie Porte, and Arsène Tema Biwole with ECE. In addition, I would like to thank the HXRS ancestors, Silvano Gnesin and Josef Kamleitner, for their help at the beginning of this thesis work. I would also like to thank Jean Cazabonne for the useful discussions at the end of this thesis work, and for translating the abstract in French.

In addition, I would like to thank the people who helped me begin my journey in plasma physics with their enthusiastic encouragement: Prof. Yong-Seok Hwang and Prof. Kyoung-Jae Chung at Seoul National University and Dr. Christopher Watts at ITER. Thanks to Yeong-Shin Park, YoungHwa An, Jisung Kang, and Yuna Lee for their support.

I am grateful to all of the Ph.D. students and postdocs at the Swiss Plasma Center, in particular my PPH office-mates, Lorenzo, Arsène, Himank, Matteo, Jérémy, and Mengdi, with whom I have had the pleasure to share many discussions, as well as the occasion of a glass of wine. Finally, I wish to thank Florian, Christa, Elisa, Michael, Raphael, Laura, Simon and Linda. My deepest gratitude goes to my parents and brothers for their support and patience over the duration of this endeavor. And to Sam, whose constant support has made this thesis possible.

¹ See author list of S. Coda et al 2019 Nucl. Fusion **59** 112023

Acknowledgements

This work was supported in part by the Swiss National Science Foundation. This work has been carried out within the framework of the EUROfusion Consortium and has received funding from the Euratom research and training programme 2014 - 2018 and 2019 - 2020 under grant agreement No 633053. The views and opinions expressed herein do not necessarily reflect those of the European Commission.

Curriculum Vitae

Personal data

Name: Dahye CHOI

Date of Birth: January 24, 1988

e-mail: d.choi245@gmail.com

Education

Ph.D. in Physics, EPFL, Switzerland (2015 - 2020)

M.S. in Nuclear Engineering, Seoul National University, South Korea (2012)

Thesis title: Development of interferometer system for Versatile Experiment Spherical Torus

B.S. in Nuclear Engineering, Seoul National University, South Korea (2010)

Thesis title: Study on bipolar flow in plasma electron sheath using PIC code simulation

Peer-reviewed articles

D. Choi et al., Suprathermal electron driven fishbone instability in the TCV tokamak, *Plasma Phys. Control. Fusion* **62** 025006 (2020).

D. Choi et al., Study of suprathermal electron dynamics during ECCD using hard X-ray measurements in the TCV tokamak, *To be submitted*

D. Choi et al., Modeling of the response function of CdTe detectors for a hard X-ray synthetic diagnostic of the TCV tokamak, *To be submitted*

Conference presentations

D. Choi et al., Hard X-ray tomographic spectroscopy and suprathermal electron physics studies in the TCV Tokamak, Annual Meeting of the Swiss Physical Society, 2016.

D. Choi et al., Investigation of suprathermal electron dynamics with ECCD in the TCV tokamak, 44th European Physical Society Conference on Plasma Physics, 2017.

D. Choi et al., Investigation of the coupling between energetic electrons and the $m/n=1/1$ mode in the TCV tokamak, 60th Annual Meeting of the APS Division of Plasma Physics, 2018.